Title
The MINIS Balloon Campaign: Duskside Relativistic Electron Precipitation

Author
Sample, John Glen

Publication Date
2013

Peer reviewed|Thesis/dissertation

The MINIS Balloon Campaign: Duskside Relativistic Electron Precipitation

By

John Glen Sample

A dissertation submitted in partial satisfaction of the

requirements for the degree of

Doctor of Philosophy

In

Physics

In the

Graduate Division

Of the

University of California, Berkeley

Committee in charge:

Robert P. Lin co-chair
David M. Smith co-chair
Steven E. Boggs co-chair
Stuart Bale
Imke de Pater

Spring 2013

Abstract

The MINIS Balloon Campaign:
Duskside Relativistic Electron Precipitation

by

John Glen Sample

Doctor of Philosophy in Physics

University of California, Berkeley

Professor Robert Lin, Co-Chair
Professor David Smith, Co-Chair
Professor Steven Boggs, Co-Chair

The Earth's radiation belts are a dynamic population of highly-energetic (> MeV) electrons and ions trapped in the dipole geometry of the Earth’s magnetic field . These particles can strongly influence atmospheric chemistry, satellite operations, human explorers, long distance communications and even the electrical grid. The belts are also the most accessible laboratory for study of the particle acceleration that we see taking place throughout the universe. This dissertation presents the results from the MINIS balloon campaign, a January 2005 effort to observe the loss of relativistic electrons from the belts through relativistic electron precipitation (REP). MINIS launched 6 balloon payloads equipped with X-ray spectrometers into high-altitude, high-latitude, long-duration flights. These flights took place during a dramatic series of solar activity that set off a -99 Dst geomagnetic storm. During the storm sudden commencement phase, three payloads measured bremsstrahlung X-rays from electrons hitting the top of the atmosphere, making MINIS the first multi-point measurement of relativistic electron precipitation. The observations took place at dusk local times, consistent with other high energy precipitation observations from single point balloons. Measuring the scale size and motions of the precipitation region as well as its energy and intensity allow improved measurement of the average loss rate as well as more tightly constraining the instantaneous loss rate from the belts. Scale sizes and motions can also be better tied to the physical structures in the belts which lead to these particle losses. During the MINIS observed precipitation, the scale size was at least 0.6 L (a unit of Earth radii when mapped to the magnetic equator) by 1 hour of magnetic local time, and expansion rates of the precipitation were well faster than the drift rate for ~MeV electrons. The MINIS balloons also served as a proof of concept for a much larger balloon campaign that began in January 2013 and will continue at least until February 2014. That campaign, BARREL, and estimates of what it will observe as well as a possible satellite mission to observe REP are also detailed here.

Dedicated to:

Robert Lin (1942-2012), who made it better

Michael Revers (1978-2007), who would have made it fun

Miriam Sample (1920-2008), who would have made it look great.

Table of Contents

Acknowledgements

You do not take this long to graduate without racking up a longer list of people to acknowledge than you could possibly address, so to any feeling left out I apologize.

I would like to start out by thanking my advisors David Smith and posthumously Bob Lin. I joined the Space Sciences Lab mostly with the goal of going on an adventure to Antarctica *once*, but it didn't take long for Bob's excitement to infect me. Despite telling me he didn't particularly like magnetospheric physics, he was still an amazing mentor in the field. He treated graduate students as true colleagues, and I will dearly miss the opportunity to bounce ideas around with him again. David, as an advisor and a friend, has provided great support from afar and I count myself lucky to collaborate with him as we go forward. The trust he showed in me early on made me feel comfortable and drove me to my best. I don't know why Bob and David hired me, but I am grateful to them for teaching me that the knowledge was the adventure and Antarctica just the means.

I would also like to thank my other original committee members Imke De Pater and Stuart Bale for their long service, quick reading, and helpful comments. Thanks also to Jonathan Wurtele for his participation in my qualifying exam. Special thanks go to Steve Boggs who stepped in to make this happen on short notice and made mind and schedule bending contributions to whip this dissertation into shape in so little time.

Thanks to Robyn Millan, whose footsteps I followed and for being a friend who was always the best place to go for getting a science focused chat in amidst all the project based noise. Thanks to Nadir Jeevanjee and Gavi Begtrup for their years as roommates and their ability to be silly and smart. Thanks to Jess, for years of climbing and friendship, thanks to Albert for being the luckiest cubicle placement in all parallel universes ever. Thanks to Michael Kokorowski for being the anti-IW and making the adventure worthy of its goals. Thanks to George Parks for his perspective and his table tennis. I believe I once promised to say thanks to the BLFC and the Psi Stars, the greatest intramural softball team to never win a championship (perhaps because I was always in Antarctica for the finals?).

Thanks to Anne Takizawa and the physics department administrators who kept the wheels turning on this process despite my remove from campus. Thanks to Marsha Colby for teaching me to solder and making me laugh through my early years here and to Steve McBride for his patience and remarkable ability to teach me about electronics and physics while always saying he didn't care and it wasn't his thesis. Thanks to Kate Harps for her assistance and persistent reminders on 'How's that thesis coming?"

Thanks to my parents for their willingness to support me while I let this draw on so long, their forgiveness for chemistry sets used inappropriately, and their love of people and nature that will always inspire me. Thanks to my brothers and sister for everything, I couldn't imagine a better

group. James, thanks for the constant nagging/support that helped push me to the finish line. You will always give the best advice I may seem not to follow, but trust me, I learn from you.

Thank you, most of all, to my love, Claire. I am not a bad husband, but you are a great wife. I know that I am luckier than I know, but at least I know that much. Thank you to Owen, Declan and Cole, without you my sun wouldn't rise (but please, just give me five more minutes' sleep).

1. Introduction

The Earth's radiation belts are a population of high-energy particles, primarily electrons and protons, that are magnetically confined inside the first seven Earth radii (R_e) by the Earth's roughly dipolar magnetic field. This region is embedded within the larger magnetosphere, the volume carved out of the solar wind by the influence of the Earth's magnetic field. The radiation belts spatially overlap several other particle populations, notably the ring current and plasmasphere, and are primarily distinguished by the high energy of the particles, greater than several hundred keV. The radiation belts are of particular interest because the energetic particles can affect spacecraft, astronauts, atmospheric chemistry, and long-range communications. The belts have been studied since the earliest days of the space age (1958), but still questions remain unanswered. The electron population in particular is highly dynamic, changing in flux by more than three orders of magnitude on day-long timescales. The volatility of the electron belt is the result of competing acceleration and loss processes. This acceleration is a poorly understood process that can happen rapidly and occurs local to the magnetosphere. Understanding these acceleration processes in our local "laboratory" has implications for general particle acceleration throughout the observed universe. Understanding the acceleration of particles into this population requires understanding the competing and sometimes related loss process which removes particles from the population.

This dissertation presents observations from the MINIS high-altitude, long-duration balloon (LDB) campaign that occurred in January 2005 from the South African Antarctic station SANAE IV. The campaign set out to measure high energy (>500 keV) electron precipitation from the Earth's radiation belts using NaI scintillators to observe bremsstrahlung X-rays. Four identical, small (40 kg), payloads were launched successively to achieve spatially separated observation points as the balloons drifted. In addition these payloads carried instruments for measuring the electric and magnetic field at ~1 Hz, 1 kHz, 5 kHz and ~20 kHz. There were also two payloads, lacking the field measurements, launched from Fort Churchill, Canada. These latter two payloads were launched in hopes of making magnetically conjugate observations of electron precipitation.

Three MINIS balloons were aloft and returning data during the January 21st, 2005 geomagnetic storm. The data from this time period represents the focus of this research effort. I will begin with a brief tour of the earth's magnetosphere, highlighting those regions and processes which are important to understanding the MINIS observations. A brief history of previous, related observations and the details of the MINIS systems will follow. The data from this geomagnetic storm and conclusions that can be drawn from it constitute the bulk of this effort. Finally I will discuss future experiments, both in progress and proposed, to answer unresolved questions regarding the high-energy electrons in the Earth's radiation belts.

MINIS set out to study relativistic electron precipitation (REP) from multiple points primarily to establish a spatial extent of the precipitation and separate out some spatial and temporal aspects of the precipitation. The spatial extent of a single precipitation event strongly influences how effective that event is at depleting the radiation belts of energetic electrons and this can place additional limits on various acceleration processes.

1.1 The Magnetosphere and Geomagnetic Activity

1.1.1 From the bowshock to the magnetotail

The magnetosphere is the volume of space carved out of the solar wind by the Earth's roughly dipolar magnetic field. The region extends from ~10 R_e in the sunward direction to hundreds of R_e in the anti-sunward direction. Inside this region particle motion is dominated by the Earth's magnetic field. The magnetosphere is further subdivided into regions with common field and particle properties, some of those are detailed below and pictured in figure 1.1.

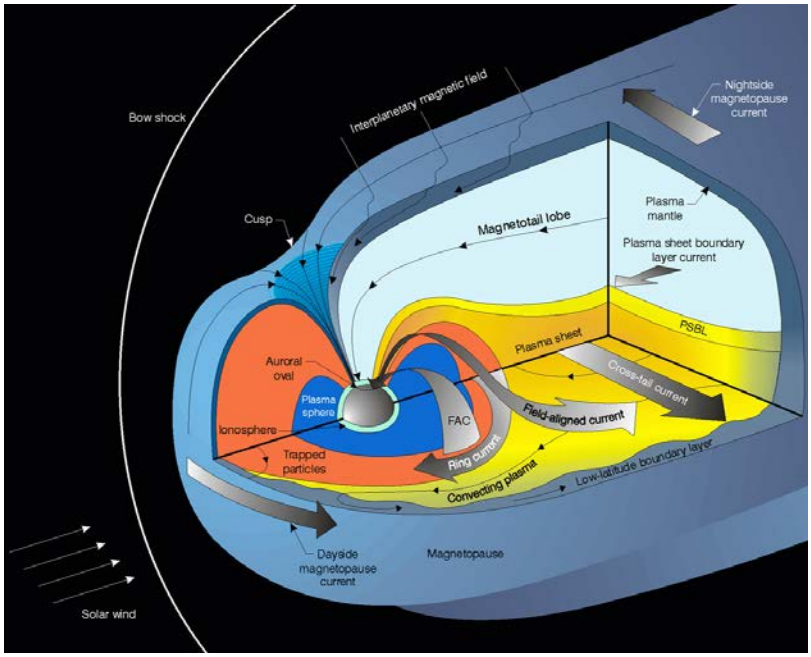

Figure1.1: An overview of regions of the magnetosphere. (Adapted from [Kivelson and Russell, 1995])

1.1.1.1 The solar wind

The solar wind is a tenuous plasma with an average ion density of less than 10 per cc. At Earth's orbit (1 AU from the Sun) the solar wind typically travels at ~400 km/s approximately radially outward from the Sun, but faster wind speeds can occur at ~1000 km/s from coronal holes, connected solar polar regions, and fast moving CMEs (Coronal Mass Ejections, detailed later). Frozen into this flowing plasma is a magnetic field of solar origin referred to as the Interplanetary Magnetic Field or IMF. By the time the solar wind reaches earth at 1 AU the IMF lies mostly in the ecliptic plane at ~45 degrees to the Earth-Sun line (The Parker spiral, arising from the ~27 day period rotation of the sun). The IMF does have an out-of-ecliptic component, which substantially influences how the solar wind influences the Earth's magnetosphere. This component is referred to as IMF B_z and is sometimes referred to as northward ($B_z > 0$) or southward ($B_z < 0$), where northward and southward are consistent with the Earth's sense of geographic north.

MINIS observations of REP occurred during a time when the solar wind dramatically impacted the magnetosphere. A fast moving, 1000 km/s, shock with densities 25x the quiet time level that preceded them struck the earth and strongly influenced the shape and structure of the magnetosphere.

1.1.1.2 The bow shock

Even the slow solar wind is faster than the local wave speeds (in this case the fast-mode magnetosonic wave), resulting in a detached shock standing several R_e in front of the magnetopause. This shock, called the bow shock, converts some of the energy of the solar-wind flow into thermal energy. A model of the bow-shock location by Farris and Russel [1994] takes into account the solar-wind Mach number and density to determine the standoff distance of the bow shock. Usually this location is >10 R_e upstream of the Earth. The region behind the bow shock is referred to as the *magnetosheath* and is characterized by an increase in density, magnetic-field strength, and temperature over the solar wind. The shocked plasma is then able to be deflected around the Earth's magnetosphere (or transferred into it in some cases).

1.1.1.3 The magnetopause

The boundary between the magnetosphere and the magnetosheath is referred to as the magnetopause. The magnetopause occurs roughly where the magnetic pressure of the Earth's magnetic field balances the dynamic pressure (momentum flux) of the solar wind. Thus the magnetopause location is subject to variations in the solar-wind dynamic pressure. Increases in density and/or velocity of the solar wind can reduce the size of the magnetosphere. An approximate magnetopause standoff distance in the sunward direction, measured in Earth radii is given by [Kivelson and Russell, 1995]:

$$L_{mp}(R_e) = 107.4(n_{sw} * u_{sw}^2)^{-1/6}$$

A typical value for the magnetopause location is ~10 Re upstream of the earth, but the location does vary. Variations in magnetopause location can have significant effects on the particle populations of interest to this dissertation. A more thorough discussion of magnetopause location during the MINIS balloon campaign is deferred to later chapters.

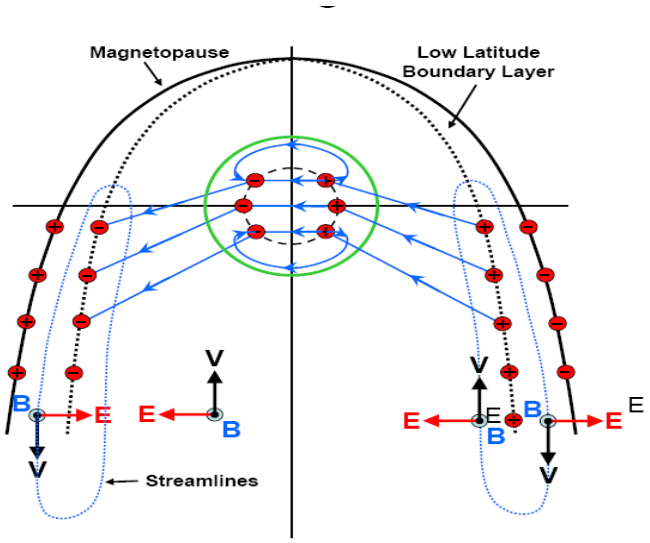

Figure 1.2: The magnetopause is stretched into a long tail configuration by the solar wind. The cross-tail electric field, in the center of this equatorial representative drawing, with red E vectors, points from local dawn to local dusk (right to left in the above picture), which, with a weak Earth's B-field pointing out of the page results in an ExB flow in the center of the tail that is towards the Earth. This field controls the dynamics of cold plasma in the inner magnetosphere.

The magnetopause is also the location of an eastward-flowing current sheet which compresses the Earth's magnetic field on the dayside. As the shocked solar wind flows around the magnetosphere, momentum is transferred tangentially to the magnetosphere. This

drags the magnetopause into a long tail-like configuration, a shape maintained by a large cross-tail current sheet that runs across Earth's nightside equatorial region(from the "dawn" side to the"dusk" side, where dawn and dusk are naturally defined by the Earth's rotation) as pictured in Fig 1.2. The cross-tail current is maintained by a cross-tail electric field (a dawn to dusk electric field) the strength of which strongly depends on the parameters of the solar wind. Variations in the cross-tail field can significantly affect inner magnetospheric particle populations. One consequence of the large cross-tail current sheet is a small radius of curvature for tail magnetic field lines as they cross the equator. The cross-tail current closes around the northern and southern lobes of the magnetosphere.

1.1.1.4 The plasma sheet

Embedded in this cross-tail current is a region of relatively hotter and denser plasma referred to as the plasma sheet. The plasma sheet extends ~100 Re from earth in the anti-sunward direction and separates the lower-density and colder tail lobes. Plasma-sheet thermal pressure from the ~keV plasma balances the magnetic pressure of the lobes. This plasma sheet is an important source population for energetic particles that are convected into the inner magnetosphere (<8 R_e) by **E**x**B** drifts from the dawn-dusk E-field and the locally northward B-field.

1.1.1.5 The inner magnetosphere

Inside ~6-8 Earth radii, the magnetic field is dominated by the Earth's dipole field, and many plasma structures naturally define themselves along magnetic boundaries. Thus it is useful to set up an appropriate coordinate system for describing regions within this space based on the local field. Although many refinements are possible, the simplest coordinate system for discussing radial profiles is the system of L-shells where the L parameter is depicted in Fig. 1.3a. L=4 is the locus of all points connected along the magnetic field that intersects the plane of the magnetic equator at 4 Earth radii (geocentric). It is an oversimplification, but intuition-building to consider

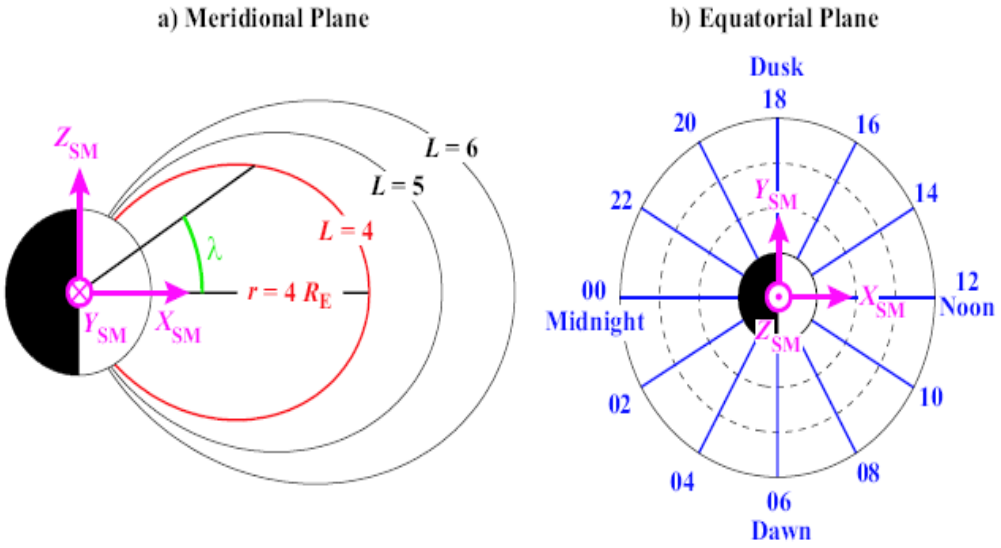

Figure 1.3: Shows the coordinate system used most often in describing locations within the Radiation belts.

the surfaces of revolution that would be created if Figure 1.3a were spun about the magnetic pole. These are referred to as L-shells, and in the absence of waves, high-energy particles will remain trapped on a particular shell if the fields remain static on timescales comparable to a particle circumnavigating the planet.

For discussing position along these shells, we will use latitude (lambda in the Figure 1.3a) and eventually pitch angle to describe positions away from the magnetic equator, and to describe phase around the earth we will use the concept of Magnetic Local Time (MLT) [1.3b]. The local-time coordinate system is a 24-hr clock angle with noon in the sunward direction, midnight in the anti-sunward, and 6 AM (or dawn) in the direction of the Earth's orbit about the Sun, i.e., as expected for these terms on the ground as defined by the rotation of the Earth.

1.1.1.6 The ionosphere

The plasma population from approximately 60 or 100km above the Earth and extending to ~1000 km altitude is referred to as the ionosphere. Planetary ionospheres are formed from the ionization of the planet's neutral atmosphere. Two processes can occur in which sufficient energy is deposited to exceed the binding potential of the neutral-atmosphere atomic or molecular components: photoionization mostly from solar input and particle-impact ionization from the precipitation of energetic particles1.4. Photoionization is dominated by UV light and occurs primarily on the dayside. Both sources of ionization can have important implications for atmospheric chemistry: for instance, medium-energy electrons of ~100 keV can strongly influence the production of NOx at high altitude and, if the NOx is transported to lower altitudes in the polar vortex, lead to the subsequent destruction of atmospheric ozone [Randall et al. 2007]. Higher-energy electrons such as those that form the focus of this manuscript could have the same effect at even more damaging lower altitudes because of their deeper penetration [Baker et al., 1993].However the intensity of fluxes at these higher energies is not often thought significant enough to contribute to ozone depletion.

The ionosphere ends up being an important source of cold plasma (eV energies) for the rest of the magnetosphere, including singly ionized oxygen which is important in determining the strength of geomagnetic storms (discussed later) and its significant effects on spacecraft operation. Ionospheric outflows also contribute to the particle population known as the plasmasphere which can strongly influence the wave particle resonance conditions that end up accelerating sand scattering relativistic electrons.

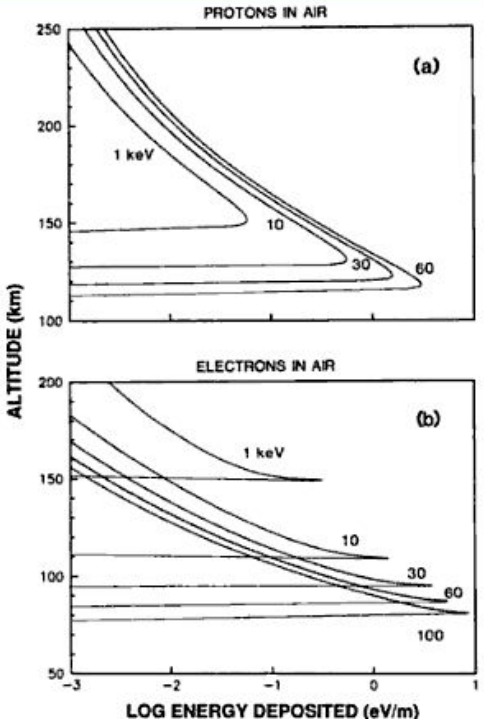

Figure 1.4: Energy deposition profiles for electrons and protons of various energies incident on the Earth's atmosphere. [Kivelson and Russel, 1995]

1.1.1.7 The plasmasphere

Above the ionosphere is the plasmasphere, a region of cold, dense (up to 10^4 per cc) plasma whose outer boundary is referred to as the plasmapause. The ionosphere is the source of plasma in the plasmasphere via ionospheric outflows. The few-eV plasma here follows contours of constant potential set up by two electric fields, that caused by the rotation of the Earth and the cross-tail electric field mentioned earlier. The sum of these two electric fields and illustrative equatorial ExB drift paths are depicted in Fig. 1.5 (particles follow surfaces of constant potential in the bottom figure).

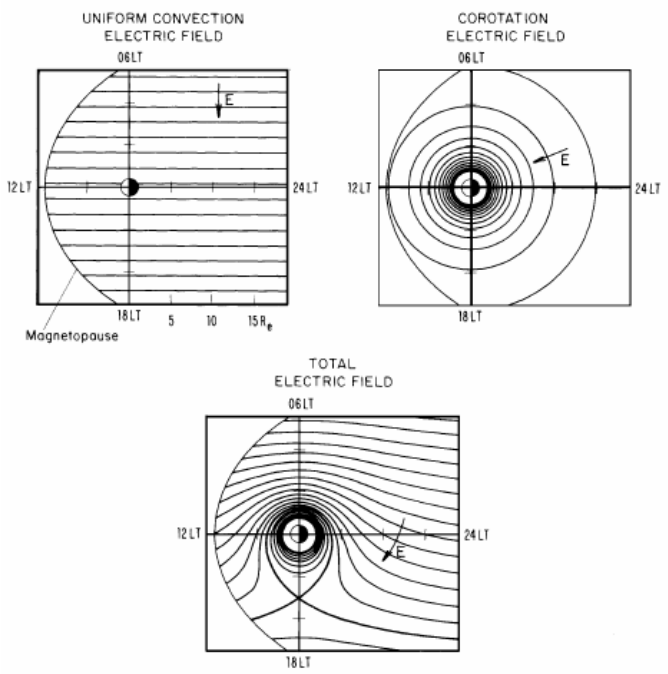

Figure 1.5: Solid lines are constant potentials. The plasmapause is, to first order, the region defined by closed drift paths set up by the corotation electric field and the convection electric field. Changes in the convection electric field move the plasmapause boundary radially, which sometimes leaves detached plumes of plasma free to convect towards the dayside magnetopause. [Lyons and Williams, 1984]

It is important to notice the existence of both closed (close to the Earth) and open (higher altitude) drift shells. The separatrix between these two classes of drifts is a good first order explanation of the plasmapause. The plasmapause location is thus a function of the strength of the cross-tail electric field described earlier. Increases in the convection electric field result in shrinking plasmapause and plasma that was previously trapped near the Earth is convected sunward. Empirically the plasmapause location is found to be a function of K_p (a magnetic index that averages over many ground based magnetometers and ranges from 1=least disturbed to 9+= most disturbed magnetosphere, the index is computed hourly) as shown in Fig. 1.6 and as described by the following equation from Moldwin et al. 2002.

$$L_{pp} = (5.99 \pm 0.072) - (0.382 \pm 0.019)K_p(max)$$

(units are the L-shells described earlier)

It is also critical to note the bulge in the plasmasphere that occurs on the dusk side of the magnetosphere which brings plasmaspheric densities to larger radii where other particle populations can be found. Further, changes in magnetospheric convection can result in the stripping off of this bulge to form plasmaspheric plumes which can temporarily extend the high densities of the plasmasphere to even larger radii, while the main plasmasphere itself shrinks. Significant advances in understanding plasmaspheric dynamics have been made in the last ten

years through the use of UV images from the IMAGE spacecraft. An example of one such image showing a recently formed plasmaspheric plume is shown in Figure 1.7.

The high densities of cold plasma trapped in the plasmasphere actually play a critical role in the wave particle interactions which heat and scatter relativistic electrons into the Earth's atmosphere (REP). The density and composition of the plasmasphere plays a strong role in controlling the growth of waves and the energies at which those waves are resonant with higher energy particles. Long term studies of satellite data show that the location of the inner edge of the outer radiation belt is almost always tied to the plasmapause because enhanced losses at the plasmapause significantly deplete high energy electrons [Li, 2006].

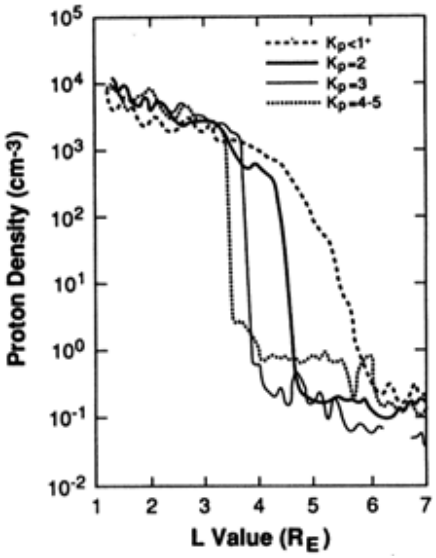

Figure 1.6: As the dawn dusk electric field increases (here a magnetic activity index, K_p, is used as a proxy) the plasmasphere moves inward, but does not compress. Outer layers are eroded away. [Chappell, 1972]

1.1.1.8 The Ring Current & Radiation Belts

Overlapping the plasmasphere, but extending to higher altitudes (up to ~6 R_e), are the radiation belts, sometimes called Van Allen belts after their discoverer, and the ring current. Both populations are magnetic-field-aligned structures of trapped energetic particles. The higher energies of these particles imply that the magnetic field, and not the electric field, primarily determines particle trajectories. Ring-current particles are so named because they can constitute a large westward-flowing current which is measurable as a decrease in the Earth's equatorial magnetic field. The

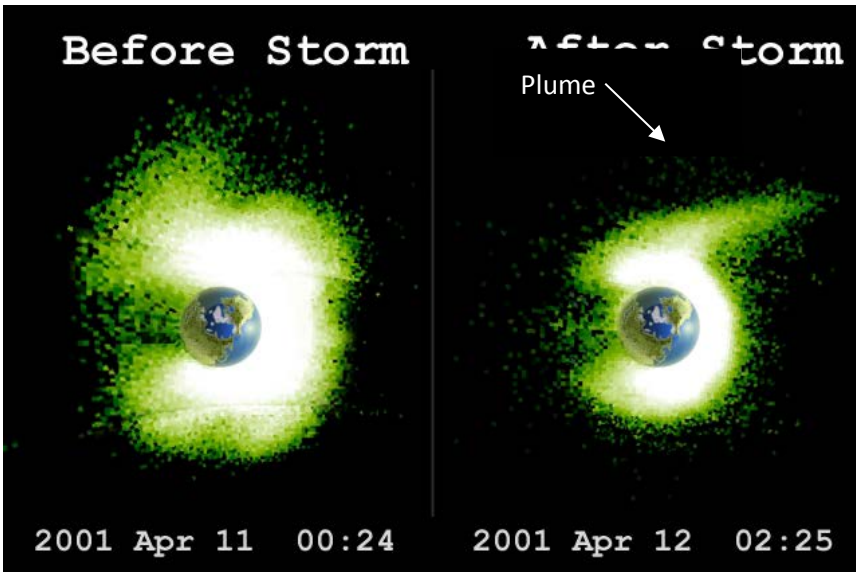

Figure 1.7. A characteristic plume is formed when the plasmasphere is eroded. Depending on conditions, the plume can connect directly to the dayside magnetopause or can "wrap" substantially around the Earth. In these images from the IMAGE satellite, the high densities of the plasmasphere are shown in white-green (from measurement of He emission) (courtesy J. Goldstein).

strength of the current is variable and can lead to field depressions of several hundred nT during times referred to as magnetic storms (described later). Greater than 90% of the current is carried by ions below 300 keV. The ions are principally O+ of ionospheric origin and protons from both the solar wind and the ionosphere. Ions above this energy and similarly high-energy electrons are referred to as radiation-belt particles, although there is significant overlap in the terminology.

1.1.2 Magnetic Storms and Substorms

Up until now the magnetosphere has been described as relatively static. The magnetosphere, though, is far from still. Variations in the speed, density, and magnetic-field orientation of the solar wind can have dramatic consequences for the magnetosphere, moving boundaries described above by multiple Earth radii (e.g., a reduction in plasmasphere volume of up to 80%), changing flux levels (high-energy electrons can vary by up to 4 orders of magnitude in a matter of hours), and lighting up the high-latitude sky with bright auroral features. These events are broadly categorized as "space weather" or referred to as "geomagnetic activity."

1.1.2.1 Substorms

When the Z-component of the IMF turns from northward to southward (i.e., from parallel with the Earth's field to anti-parallel), the transfer of energy and material from the solar wind to the magnetosphere is made far more efficiently. The process of anti-parallel magnetic fields merging is called magnetic reconnection, and this process is often invoked as a way of converting energy stored in the magnetic field into particle energy. Independent of the conversion of field energy to particle energy, the southward turning of the IMF makes a topological change in the magnetic fields that constitute the boundary of the magnetosphere. The reconnection process results in increased energy transfer to the magnetosphere and is well correlated with the initiation of a substorm.

A substorm is a significant process of reorganization in the magnetosphere as the increased solar-wind input is temporarily stored and then dramatically released. Substorms were first identified

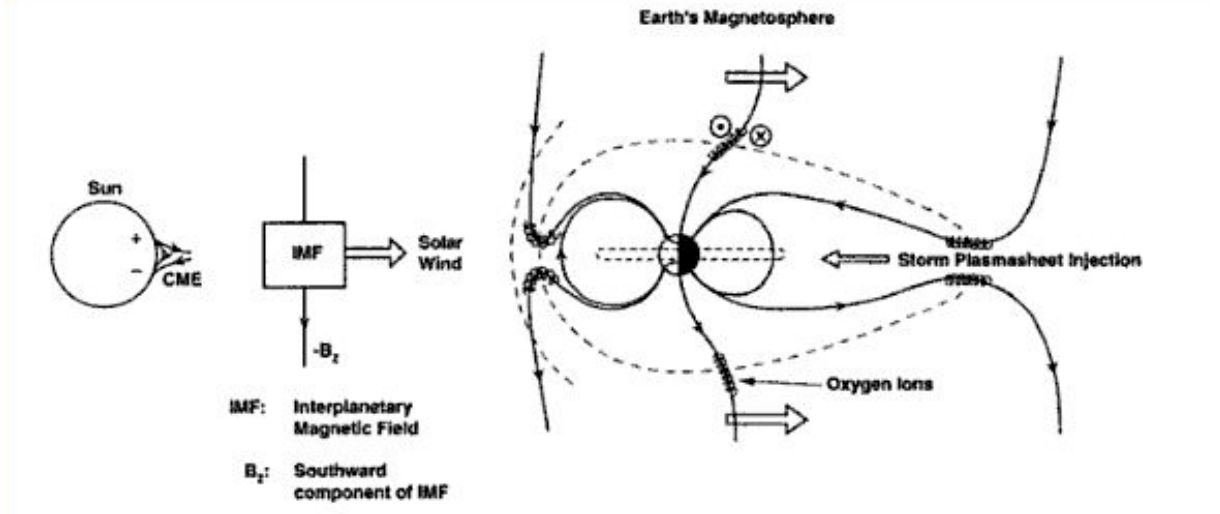

Figure 1.8: Showing the sequence of a magnetospheric substorm. From Tsuratani, 2001

by their bright auroral signatures, but the processes, causes, consequences, and even signatures of substorms are hotly debated. A cartoon of some key substorm processes is included in Figure 1.8. Following the southward turning of the IMF, magnetic flux is transferred to the tail lobes (above and below the plasma sheet). The increased magnetic pressure squeezes the plasmasheet and stores energy in the magnetotail. This is referred to as the growth phase and is sometimes identified by a change in the slope of the AL index, AL represents a combination of various ground-based magnetic-field measurements in the near-polar regions. "Magnetic bays" are measureable at Earth as a depression in the local field, the size of the polar cap (field lines which do not close on the Earth) increases, and spacecraft that were once measuring trapped particles may find themselves observing a substorm "dropout" even if particle fluxes have not yet changed substantially (Figure 1.9). Following the stretched phase, the field lines can return to a more dipolar orientation, which usually carries with it an injection of ~100 keV ions and electrons 1.10.

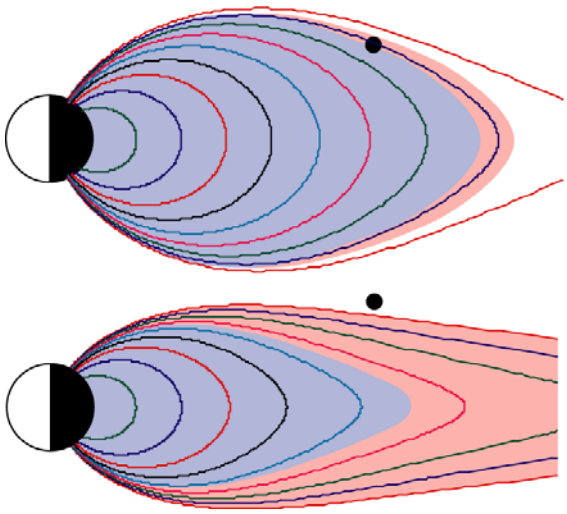

Figure 1.9: Using a magnetic-field model to depict how dramatically the measured flux at a geosynchronous satellite (the black dot) near midnight (note the **magnetic latitude** of geosynchronous orbit is NOT 0) can change in response to the stretching of nightside field lines in a magnetic substorm [modified from G. Reeves, personal communication].

Substorms are most often considered in the realm of 10s of keV particles that they inject directly, but they can strongly impact higher energy particles as well. Some previous observations of REP from balloons found ~MeV electrons scattered into the atmosphere whenever there was a substorm. This is likely an indirect effect, due to the lower energy electrons and ions exciting waves that can resonate with higher energy particles.

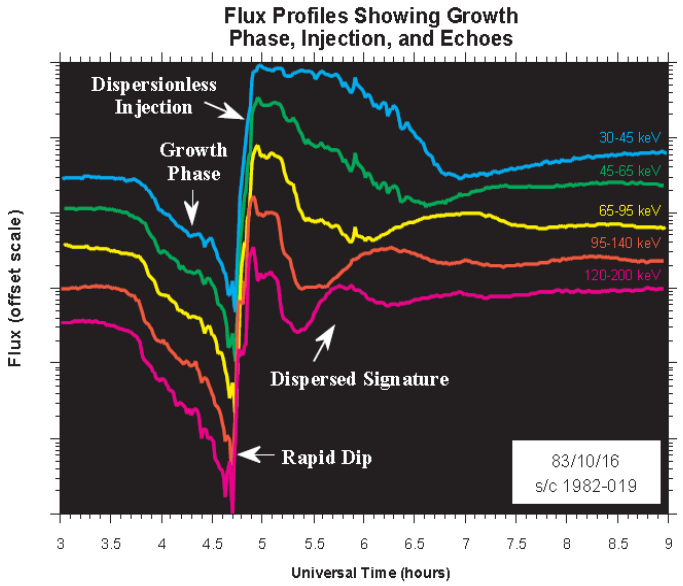

Figure 1.10: Ion data from the LANL-1982 geosynchronous spacecraft during a substorm injection.

1.1.2.2 Geomagnetic Storms

If the IMF remains southward for an extended period of time, or if large shockwaves in the solar wind strike the magnetopause, the result is usually a geomagnetic storm. Magnetic storms are identifiable by a characteristic reduction in the measured equatorial magnetic field. This effect is captured in the Dst index. A plot of the Dst index showing the evolution of a magnetic storm is shown in Fig. 1.11. The decrease in the equatorial field is the result of a large ring current carried by ~tens of keV ions injected into the inner magnetosphere from the tail. This injection process takes up to a few hours and is referred to as the main phase of the storm. Shown is an equatorial decrease of ~100 nT, typical in intensity, but both smaller and significantly larger storms are possible.

When the driving force in the solar wind subsides, a period of typically several days called the recovery phase occurs. Gradually the magnetic field returns to its equilibrium state as ring-current particles are lost. Some ions are lost to the atmosphere via scattering into the loss cone (discussed for electrons in following sections), lost to the magnetopause through outward radial diffusion, de-energized, or lost by charge-exchanging with the neutral exosphere. This last loss process turns the ions into Energetic Neutral Atoms (ENAs) which are no longer confined by the magnetic field and can be sensed remotely as a way to image plasmas. In some cases, particularly magnetic storms initiated by large shock waves in the solar wind, the main phase of the storm can be preceded by an increase in the equatorial field. This is usually due to a compressing of the magnetosphere

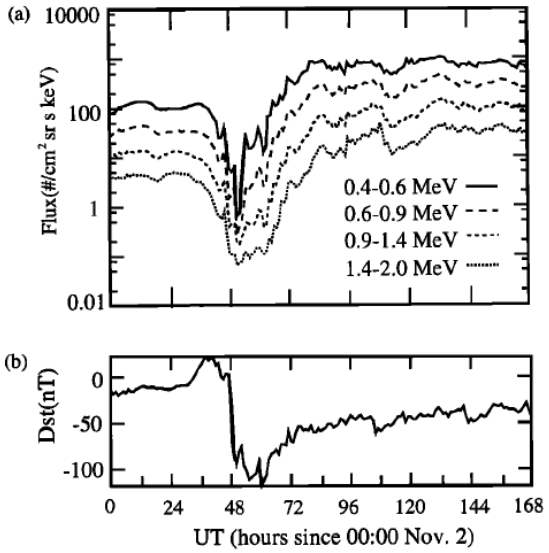

Figure 1.11: A geomagnetic storm as captured by a geosynchronous energetic electron detector (a) and the Dst index (b). The SSC is the initial 10-hour increase in Dst, followed by the few-hour main phase (sharp decrease in Dst) and the days-long recovery phase (gradual increase). Figure from [Kim and Chan, 1997]

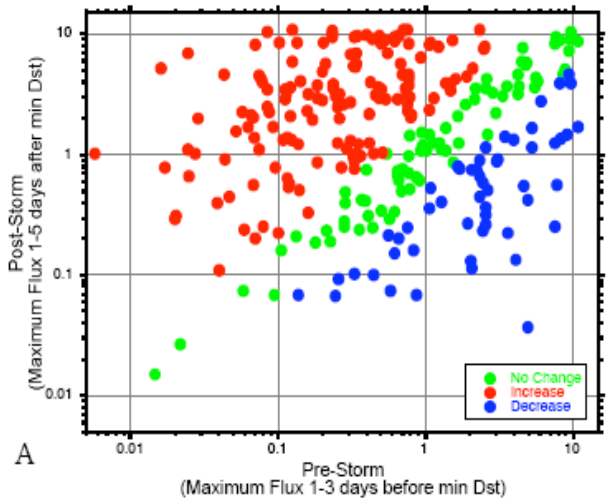

Figure 1.12: Shows the wide possible response of the electron radiation belt to the action of a magnetic storm. [Reeves et al., 2003]

(or equivalently an increase in the magnetopause current), before the ring current subsequently builds up. This time period is referred to as a Storm Sudden Commencement (SSC) or occasionally as an initial phase.

Magnetic storms are highly dynamic and dramatically change the magnetosphere. Because most particle orbits follow the magnetic field, particle populations reorganize throughout the course of the magnetic storm. Further, particles can gain or lose energy due to field changes. Thus, a spacecraft making measurements in a fixed energy range and at a single point can have a difficult time tracking specific particle populations during the storm. When the ring current has decayed, pre-storm and post-storm particle populations can be compared. It is found that there is almost no relationship between pre-storm and post-storm fluxes (see Figure 1.12).

1.2 The Earth's Radiation Belts

As described before, the first 6 R_e above the Earth are populated by magnetically confined electrons and protons of remarkably high energy. This region has been studied since the earliest days of the space age, beginning with the Geiger counter aboard Explorer 1. In this region, the inner magnetosphere, the Earth's field is roughly dipolar and particles are organized along the magnetic L-shells described earlier.

The radiation belts are divided into electron and ion belts. The spatial distributions taken on by these belts are a result of the competing source and sink terms that play on each population. The ion belt is principally found below 3 R_e altitude. Ion populations are relatively stable, resulting from Cosmic Ray Albedo Neutron Decay (CRAND) or inward radial diffusion (and thus energization) of plasmasheet ions. Ions are lost by collisions with the Earth's exospheric atmosphere.

The electron population is further divided into a relatively stable inner belt and a more dynamic outer belt. The region separating these two belts is referred to as the "slot" and is the result of enhanced losses to the

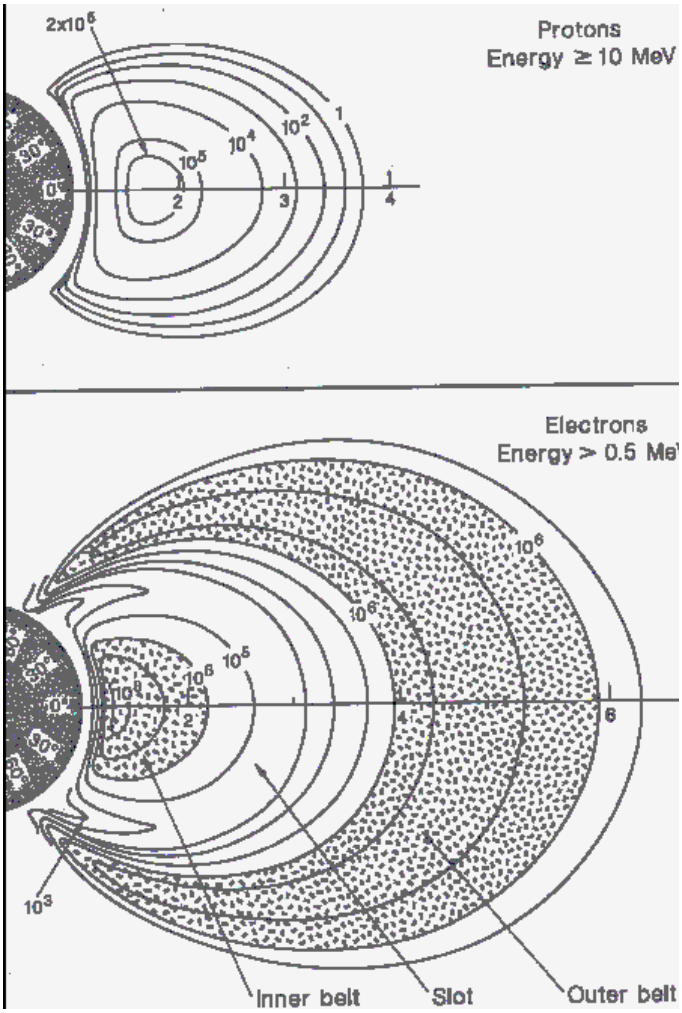

Figure 1.13: Average radial profiles of the electron and proton radiation belts. This static picture is more accurate for the protons than for the electrons, which vary more in flux and extent [schulz and lanzerotti]

atmosphere that occur in the slot by wave-particle interaction [Lyons et al. 1972]. The slot is occasionally filled by strong inward injections of outer-belt electrons, but these "new radiation belts", as they are often called, will typically decay away with lifetimes of tens of days. Occasionally, the slot will remain filled longer because of a pitch-angle distribution that is sharply peaked near equatorial trapping. This distribution is the result of acceleration/transport mechanisms (discussed later) that can fill the slot. Average radial profiles for both electrons and protons are shown in Fig. 1.13.

1.2.1 Motion of Trapped Particles in the Radiation Belts

Motion of charged particles in the Earth's magnetic field is controlled by the Lorentz force equation. For a magnetic field **B**, electric field **E** and external non-electromagnetic force **F**

$$\frac{d}{dt}\left(m\frac{d\boldsymbol{r}}{dt}\right) = q\left(\frac{d\boldsymbol{r}}{dt}\times\boldsymbol{B}+\boldsymbol{E}\right)+\boldsymbol{F}$$

In the approximately dipole magnetic-field geometry of the inner magnetosphere and at energies relevant to the radiation belt and ring current, this force leads to periodic motions on three timescales which are usually well separated. The motions are often referred to as gyration, bounce, and drift in order of highest to lowest frequency. Associated with each timescale (and related spatial scale) is an invariant of the motion which is conserved provided the background field does not change on timescales comparable to the period associated with each invariant. A similar requirement on the spatial variation is necessary. The frequencies of gyration, bounce, and drift are shown in Figure 1.14 for both protons and electrons. While there are a number of ways of deriving the three adiabatic invariants, see e.g. textbooks by Roederer [1970], Parks[2004], Schulz and Lanzerotti [1974], Nicholson [1983] and Kivelson and Russell [1995] with surprisingly little overlap, the simplest physical argument involves the path integral of the canonical momentum around the approximate orbit path, which is a conserved quantity.

$$J = \oint[\vec{p}+\frac{q}{c}\vec{A}]\cdot\overrightarrow{dl}$$

The invariants end up defining the radiation belts during quiet times and the breaking of these invariants is the story of magnetically disturbed times when particles are forced off their usual trajectories and among other things can encounter the atmosphere as REP.

1.2.2 The 1st invariant: M or μ: Gyration

The first invariant is associated with the fastest periodic motion, and the relevant path integral is simply the circular gyration about the local magnetic field. Given a particle with velocity v in the presence of a magnetic field B, the velocity can be separated into motion parallel to the magnetic field ($v_{\|}$) and motion perpendicular to the field ($v_{\perp}$), with the angle between the field and the original velocity vector referred to as the pitch angle (α). Thus:

$$v_{\perp} = v\sin\alpha$$

$$v_{\|} = v\cos\alpha$$

With frequency:

$$\Omega_e = \frac{qB}{\gamma m_o c}$$

And the Larmor radius of:

$$R_l = \frac{p_\perp c}{|q|B}$$

Protons and electrons gyrate in opposite directions, with electrons being "'Right- handed" and protons "Left-handed." An electron orbit (with some $v_\parallel$) is pictured below in Figure 1.15. The conserved quantity becomes:

$$J_1 = 2\pi p_\perp R_l + B\pi R_l^2$$

$$= \frac{\pi p_\perp^2 c}{qB}$$

This is usually rewritten (adding and dropping constant factors) as:

$$\mu = \frac{p_\perp^2}{2m_0 B}$$

which highlights the invariant as conserving the ratio of the particle's energy perpendicular to the field to the strength of the local magnetic field.

1.2.3 The 2nd invariant: I, J, or K:Bounce

A particle gyrating about the magnetic field will experience a "mirror" force in the presence of a convergent magnetic field which applies a force to the particle opposite the gradient in $B_\parallel$. The geometry of relevance here is the convergent magnetic field found in the Earth's ~dipolar near-Earth region. For a given line of magnetic force, the weakest field intensity is found at the equator, while tracing the line of force towards the Earth's surface at high latitude i.e. in Figure 1.3 one finds significantly higher field intensities. For example, the field intensity along a field line at L=6 changes by a factor of $\sim \frac{1}{2 \cdot 6^3} \approx 0.002$, and a charged particle found on this field line is repelled by the strong field at northern and southern latitudes and bounces between "mirror points" (i.e., points where its $v_\parallel \rightarrow 0$).

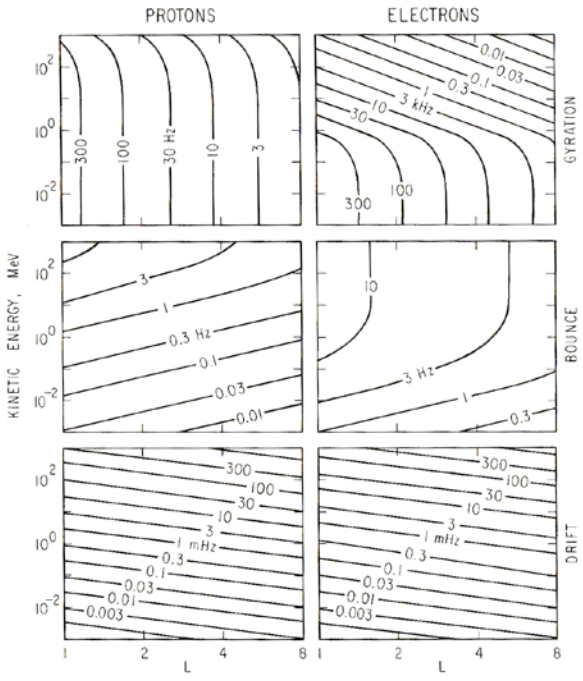

Figure 1.14: shows timescales as a function of L and energy for the three adiabatic invariants described in the text for equatorially mirroring particles. [Schulz and Lanzerotti 1974]]

This can be seen from the equating the first adiabatic invariant at two points along the field line and requiring conservation of energy as well. The result relates the local pitch angle at point s, α_s, to the pitch angle at the equator, α_0:

$$\frac{\sin^2 \alpha_s}{B(s)} = \frac{\sin^2 \alpha_0}{B(0)}$$

Again using energy conservation, we can express the parallel velocity as a function of position:

$$v_{\|}(s) = v \cos \alpha_s = v \left[1 - \frac{B(s)}{B(0)} \sin^2 \alpha_0\right]^{\frac{1}{2}}$$

Which clearly goes to zero since B(s) > B(0) for a dipole, this is the particle mirror point. The solution in a perfect dipole is symmetric, since B(s, $\lambda > 0$)=B(s,$\lambda < 0$). The particle is trapped between these two points, and "bounces" between them.

This second periodic motion between the mirror points defines the path integrated over to find the second adiabatic invariant of the motion. $J_2 = J = \oint p_{||} \cdot \overrightarrow{dl}$ Assuming the first invariant is not violated (a tighter constraint than those placed on the second invariant as it is) and expressing $p_{\|}$ in terms of $v_{\|}$, J_2 can be rewritten:

$$\mathrm{I} = \int_{mirror}^{mirror} \left[1 - \frac{B(s)}{B_m}\right]^{\frac{1}{2}} ds$$

Note: $J = 2pI$, B_m is the magnetic field at the mirror point

I only depends on the length of the field line bounce, as determined by the location of the mirror points, and is independent of particle energy. It is conserved only if there are no parallel-acting forces. If external forces are present which at all times act perpendicular to the magnetic field this is expressed as:

$$K = I\sqrt{B_m} = \int_{mirror}^{mirror} [B_m - B(s)]^{\frac{1}{2}} ds$$

K is the most common choice of representing the 2nd invariant for high energy particles of interest here. Particles whose mirror points are close to the equator (small values of the second invariant) have equatorial pitch angles near 90º or are "equatorially mirroring," while particles with much smaller equatorial pitch angles are called "field aligned."

1.2.4 The 3rd invariant: Φ or L: Drift

Energetic particles also experience a more gradual drift motion about the Earth. This motion is due to the radial gradient in field intensity and, for particles with substantial second invariants, the curvature of the field line. In a perfect, static dipole, this orbit would maintain a constant radial distance from the Earth when passing through the magnetic equator (or at all times for an equatorially mirroring particle). In such a field geometry, L-shell, as defined earlier the McIllwain L, is proportional to the conserved quantity. The particle orbits the earth at a relatively

low velocity, and the conserved quantity is equal to the line integral of **A** along this orbit, which is easily transformed to be proportional to the magnetic flux contained within the orbit path $J_3 = \Phi$.

Because the Earth's field is not static or dipolar, but L-shells are useful systems for organizing particle populations, a quantity L* or the Roederer L-value is defined through Φ as:

$$L^* = -\frac{2\pi k_0}{\Phi R_e}$$

and is very close to the L-value defined from dipole geometry, particularly at smaller radii in the inner magnetosphere and/or during quiet geomagnetic conditions. Throughout this dissertation the differences between L and L* will be largely ignored. Determining L* can be computationally intensive as it depends on tracing out an entire drift shell in a model field. For the low-altitude measurements used in this effort, the accuracy of the field model dominates over the error in definition. I will use L and L* interchangeably, but usually specify the field model used in determining the parameter. When unspecified, L refers to the Internal Geomagnetic Reference Field (IGRF-2005). The reader is cautioned that in the larger literature, L* is the more physical quantity and when possible should be used for organizing particle measurements.

In addition to the plot [invarianttimescales] which shows drift frequencies for equatorial particles, a useful equation for estimating the drift-time periods in a dipole field is from Parks [2004] with ε in MeV and the period is in minutes:

$$\langle T_D \rangle = \begin{cases} \frac{43.8}{L\varepsilon}, & \alpha = 90 \\ \frac{62.7}{L\varepsilon}, & \alpha = 0 \end{cases}$$

Which highlights the increased drift period for particles which are closer to field aligned.

1.3 Acceleration and Loss of Energetic Electrons in the Earth's Radiation Belt

Interest in understanding the source of the high-energy electrons found in the radiation belts has increased significantly over the last 20 years [Friedel et al. 2002]. The interest in this population arises in part because of the correlation between the occurrence of high fluxes in the ~MeV energy range and of subsequent spacecraft operating anomalies or failures, especially at altitudes important for communications (geosynchronous) and GPS (~4R_e, 60° incl.) near the heart of the dynamic outer radiation belt. In addition, the understanding of these mechanisms will contribute to the knowledge of transport and heating processes of more general astrophysical and laboratory plasmas.

Since spacecraft measure flux at a single location and time, it is often impossible to directly observe the processes which are energizing the electron population. The difficulty in observing the physical processes which act on the particle population is compounded by the fact that the adiabatic invariants described earlier are not measured directly. While μ, K, and L are more closely related to the phase-space density of the electrons, spacecraft measurements are actually made of flux, pitch angle, and energy. Calculating μ is relatively easy if one knows energy, pitch angle, and the local magnetic field. K, however, depends on the magnetic field along the entire bounce path of the particle, and thus is not a local measurement, and L (actually L*, the use of which is more important when near the equator) depends on the magnetic field over the entire

drift orbit. To understand the electron radiation belts it is essential to make multipoint observations of the particle population, tie them together with accurate magnetic-field models, and understand the source and loss terms that modulate the *in situ* measurements that can be made. Different magnetic-field models disagree most during the most interesting times, magnetic storms [Reeves et al. 1996], so it is important to have as thorough a measurement set as possible.

The dynamics of the electron radiation belt represents the net result of competing acceleration and loss processes. The balance of these processes is not well understood. Reeves et al. [2003] showed that ~half of magnetic storms result in a net increase in electron flux, while almost 20% result in a net decrease. The causal differences between these storm classes is unknown, but is not simply captured by measured solar wind parameters, Dst, or storm-time satellite measurements yet made in the belts. The following sections will attempt to break down some of the processes which go into this balance and ultimately lead to the observations of the loss term (REP) that this dissertation discusses.

1.3.1 Radial Diffusion

One of the earliest proposed mechanisms for generating ~MeV electrons is the process broadly referred to as radial diffusion. Radial diffusion involves the movement of electrons from deep in the magnetotail to the inner magnetosphere while conserving the first (and usually the second) adiabatic invariant. If the first invariant is conserved while a particle is brought into a region of higher magnetic field, it must also gain in perpendicular energy (apparent from the definition of μ). For instance, a 90 degree 15 keV electron found at >12 R_e in the tail where the field is ~10 nT which is brought into L=4 where the field is ~800 nT will have 800 keV of energy. This process creates a 90-degree peaked distribution at high energies because it preferentially adds energy to the perpendicular component of the particle velocities.

The dawn-dusk electric field extending across the plasmasheet (as was shown in the model of the plasmasphere, Fig. 1.2, and the near-vertical (+Z in GSM coordinates) magnetic field gives rise to an **E** x **B** drift towards the Earth. Particles that move under the influence of this drift are said to be "convected" into the inner magnetosphere. Convection occurs for all particles, but is often thought of mostly as a process affecting low-energy particles. Fluxes of high-energy electrons in the inner magnetosphere cannot be explained by simple convection. Time scales for simple convection are too slow to explain the rapid rise of energetic electrons that can occur in the inner magnetosphere. However, radial diffusion can be accelerated by modulations of the geomagnetic field by Ultra Low Frequency waves. ULF waves (typically in the mHz) can act in drift resonance with electrons that have sufficient energy to ensure that the convective motion does not dominate their trajectory. For example, a seed population of tens of keV electrons in the near tail can rapidly be energized by ULF-driven radial diffusion [Elkington, 2006, Schulz and Lanzerotti 1974]. Indeed any modulation of the magnetopause standoff distance at timescales faster than the third invariant leads to a type of radial diffusion (and thus energy diffusion) where particles on the nightside at the time of the compression will move to larger L-shells and lower energies, while particles on the dayside move inward and gain energy [Roederer, 1970]. It is important to note that a symmetric, breathing-mode ULF wave in a dipole cannot drive radial diffusion, while azimuthal modes, higher m-number modes, and the asymmetry of the Earth's dipole all are sufficient to allow for radial diffusion to occur. It is also possible that ULF waves and some K-violating pitch-angle scatter process combine to allow for radial diffusion without any of these conditions [Friedel et al., 2000].

1.3.2 Local Wave Heating

In contrast to the very-large-scale process of radial diffusion, local wave heating is a process that can act on the scale of the electron gyroradius. Local wave heating is the process whereby the electric field of some plasma wave does work directly on the electron, violating either the first and/or second adiabatic invariant. In order to be effective at rapid energization (or scatter), the process invoked is usually a resonant interaction where the Doppler-shifted wave electric field has an extended opportunity to act on the electron. Although at lower energies, resonance with electrostatic waves is possible, most of this dissertation will focus on interaction of circularly polarized electromagnetic waves that are in gyroresonance with some part of the electron population. In this case the condition of resonance is:

$$\omega - k\|v_{\|}\| = \pm m\frac{\Omega}{\gamma}$$

where ω is the wave frequency, k the wave vector, v|| the electron velocity || to the background magnetic field, m an integer, Ω the electron cyclotron frequency, and γ the Lorentz factor for the electron. Fig. 1.15 shows an example interaction for m=+1. In this case, the electron and the wave are travelling in opposite directions (k||v||<0), so the electron sees an increased effective wave frequency.

The time for this interaction is small, and wave amplitudes are assumed to be reasonably small, and thus the energy gained or lost by the electron is also small. However, as the electron is bouncing between mirror points, it is thought to encounter a large number of wave packets, and each of the encounters will occur at a random phase. The above equation only describes resonance and phase determines whether the interaction will be a net positive change in energy and/or pitch angle, or a net negative. The evolution of the electron distribution under these conditions can be described as a diffusion process in energy and/or pitch angle. Most studies have separated out momentum and pitch-angle diffusion [e.g. Horne, 2003 and references therein], but cross terms do exist and may occasionally be large [Albert and Young, 2005] Much of the study of electron phase-

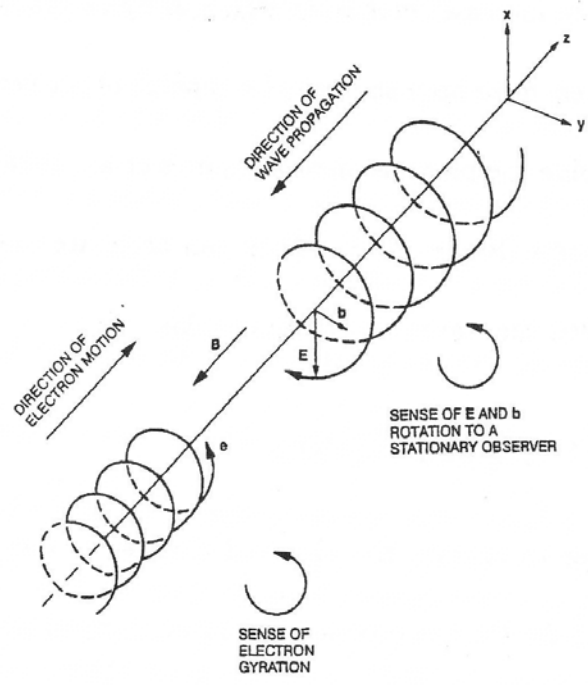

Figure 1.15 a right handed wave interacts with a gyrating electron as in the m=+1 case from equation 1.x This orientation allows the electron to see a ~constant E-field over the interaction time.

space evolution in the radiation belts by local heating has been confined to determination of "bounce-averaged" diffusion coefficients, referred to often (and broadly) as quasi-linear diffusion. However, the assumption of small wave amplitudes may not be valid in at least some cases [Cattell, 2008]. Large wave amplitudes, wave trapping and non-linear interactions may be behind many of the processes that were previously believed to be diffusive. New measurements at high time resolution capable of observing brief, strong fields (such as the RBSP mission described in Chapter 6) and improved Particle-In-Cell (PIC) modeling should resolve this question.

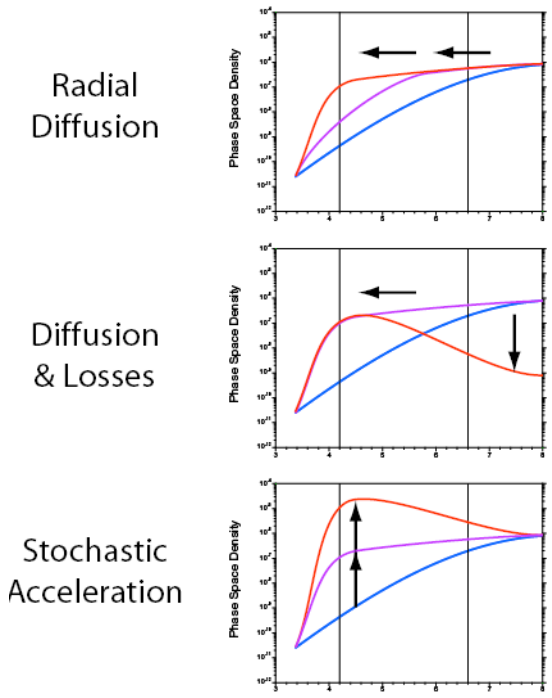

Figure 1.16: Radial diffusion (top) and local heating (stochastic acceleration, bottom), should produce very different phase-space density distributions shown here for fixed μ, K as a function of L. However, losses at large L can confuse the two (middle panel).[Green, 2004]

Diffusion need not be a slow process, and even consistent small wave amplitudes can be shown to be sufficient to explain the rapid heating of the electron population that occurs in some storms. This local heating will tend to create a peak in the phase-space density (PSD) at relevant energies around the L-shell where it occurs. This is in contrast to the PSD expected from radial diffusion which relies on a positive $\frac{\partial f}{\partial L}$ gradient in the source population at large L to bring particles into the inner magnetosphere. Schematically this difference is indicated in Figure 1.16 adapted from Green and Kivelson, 2004. As stated earlier though, the non-local nature of measuring adiabatic invariants and the required reliance on magnetic-field models make this measurement difficult. It has demonstrated relative success only in quiet magnetic conditions [Onsager, 2004, Chen, 2005]. Ultimately, acceleration of seed populations to relativistic energies is probably a combination of both local heating and radial diffusion [O'Brien,2003], but the relative importance and the conditions that make one or the other more effective for a particular storm are not well understood. Resolution of the question depends sensitively on understanding the sink term as well as the source [Summers, 2004]. Thus it is vitally important that measurements of REP are well quantified in a variety of conditions.

1.3.3 The Dst effect

We now turn our attention to loss of energetic particles out of the radiation belt, although we first look at changes in flux which are only apparent losses. During a magnetic storm, the flux enclosed by an undisturbed drift shell of a particle orbit around the radiation belt generally decreases (the Dst index is a measure of this decrease in field at the Earth's surface). If this

change in flux occurs slowly enough, i.e., slower than the drift period of the particles in question (recall that the drift period is inversely related to particle energy), the particle's drift path will change to conserve the 3rd adiabatic invariant (L*). This motion is outward for a decrease in magnetic flux in the inner magnetosphere caused by the ring current. It is important that this conservation is in response to a *global* change in the magnetic field, not a local one. The particle in fact moves to larger drift paths, and the *local* field it sees decreases, see Fig. 1.17

Conservation of the first invariant then implies that the particle's perpendicular momentum will decrease as well.

$$\mu = \frac{p_\perp^2}{2m_0 B}$$

This decreases the energy of the particle, so that a spacecraft making measurements at a fixed position and fixed energy will see a change of flux that is the convolution of the spatial gradient in flux and the energy spectrum, which is usually steeply falling. This effect has been known for a long time (e.g. Dessler and Karplus [1961], McIllwain [1966], and Roeder [1967]). How it affects spacecraft measurements in a particular storm is far less certain, and resolving the question depends on magnetic-field modeling of storm-time dynamics. It has been shown that in at least a few storms, much of the initial decrease in flux, as measured equatorially, is fully adiabatic [Kim and Chan, 1997].

1.3.4 Magnetopause Losses

A manner in which the radiation belts can actually lose relativistic electrons (and protons of similar gyroradius, but much lower energy) is out the magnetopause. Electrons at large L-values can intersect the magnetopause where they then precipitate at high latitude or are lost to the solar wind. When particles encounter the magnetopause the magnetic field can change dramatically on the order of a gyroradius, so the adiabatic tracking of particles is no longer valid . Magnetopause losses are typically thought of as important only at high L-shells, but several factors can make this process important into L~4. First, the magnetopause can be dramatically compressed, as when a sudden increase in solar-wind density and/or velocity (and thus pressure) impacts the magnetosphere. Li [1997] showed that magnetospheric compression was responsible for a three orders-of-magnitude flux drop down to L=4.5. A similar situation is detailed in Chapter 3 where the magnetopause is shown to compress inside of L=5.

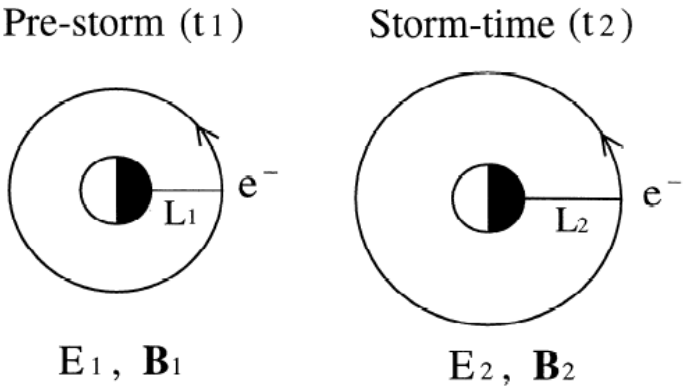

Figure 1.17: In response to a slow increase in the ring current, a particle will move to larger radii with weaker fields.

It is also the case that radial diffusion can act *outwards* towards the magnetopause. Radial diffusion acts any time there is a gradient in phase-space density. It is often assumed that this gradient is inward, from

high fluxes of moderate-energy particles at the inner edge of the plasmasheet, but a slowly modulated magnetopause will actually create a negative gradient in phase space, leading to effective radial diffusion outwards. This can be an essential loss mechanism as it can act across local times and rapidly [Shprits, 2006b and Ukhorskiy, 2006]. Because magnetopause losses should be gyroradius dependent more than any other parameter, this loss mechanism should show up in protons with comparable energies. However, this does not appear to be the case [Green, 2004b], at least for geosynchronous flux dropouts. Measuring magnetopause losses directly has not been achieved, and thus most work has been done through modeling efforts. The observational evidence for magnetopause losses is often a 'butterfly' pitch angle distribution [Gannon, 2007 and references therein] where flux is not peaked at 90° because equatorially mirroring particles have the largest gyroradius and will hit the magnetopause sooner than the more field aligned electrons on their L-shells.

1.3.5 Precipitation

The next two types of electron loss mechanisms both involve the precipitation of electrons into the Earth's atmosphere at high magnetic latitude. Trapped electrons undergo some process, often identified as a wave-particle interaction, that decreases their equatorial pitch angle to the point where the mirror point is at or below ~100 km. Once the particle reaches this approximate altitude, collisional losses with the dense atmosphere of the earth cause the particle to be "lost". The depth of penetration into the atmosphere depends on particle energy and incident angle, and some backscatter from the atmosphere does occur. While most of the energy of the particle goes into collisions, electrons also lose a small part of their energy by the generation of bremsstrahlung X-rays. These X-rays allow for remote sensing of electron precipitation as they are visible from balloon detectors below [Winckler, 1958], as well as from orbiting low-altitude spacecraft [e.g. Imhof, 1974].

Precipitation of ions, on the other hand, is visible in some energy ranges by the generation of line emission [e.g., Mende, 1999 and references therein] and by imaging of energetic neutral atoms that escape after the incident proton charge-exchanges (perhaps multiple times) with the cold

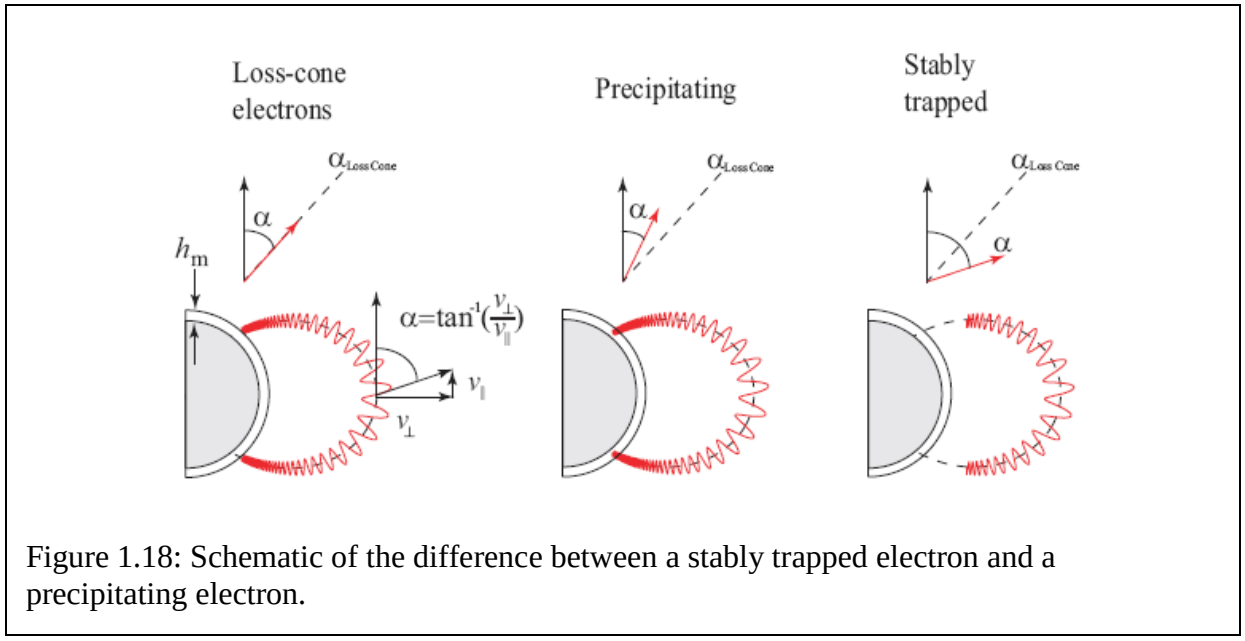

Figure 1.18: Schematic of the difference between a stably trapped electron and a precipitating electron.

neutral atmosphere [e.g. Roelof, 1997]. While most of this dissertation focuses on relativistic electron precipitation (REP) and observations of the associated bremsstrahlung, one important possible cause of REP should also precipitate non-relativistic ~10 keV ions.

A schematic representation of the various wave modes and regions that a particle will encounter during its orbit is included here as Figure 1.19. It is important to note that precipitation by wave particle interaction probably relies on the cumulative effect of multiple wave modes acting on the particle as it drifts around the Earth.

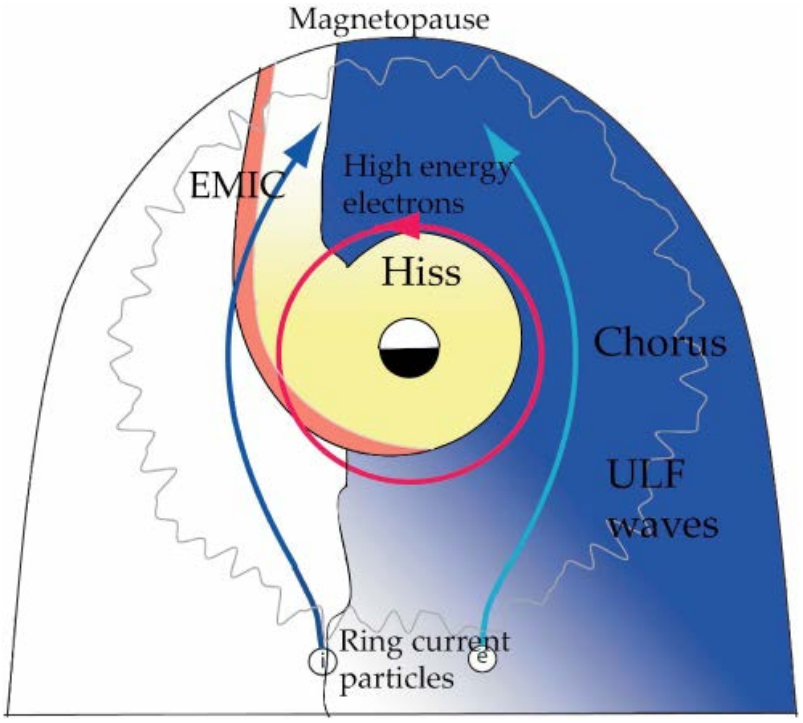

Figure 1.19: Shows the distinct wave regions encountered by a relativistic electron as it progresses around its drift path. [Shprits, 2006]

1.3.5.1 Microbursts

One type of REP that has gained considerable attention is the microburst. Microbursts are characterized by their ~0.25 s timescale. Microbursts extend from ~20keV [Datta, 1996] seen on rockets to >MeV [Imhof, 1978, Blake, 1996], seen on satellites [Fig. 1.20]. The low-energy cutoff, if present, is not well known as microburst-like structures are visible in FAST data down to 100s of eV [Carlson, private communication]. They occur primarily at dawn local times, but at higher L-shells can also be found around midnight

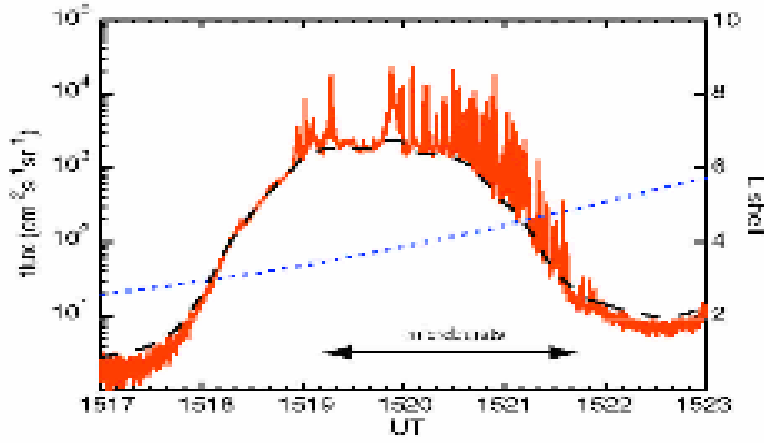

Figure 1.20: Counts above a 1MeV threshold in the large-area HILT detector aboard the polar orbiter SAMPEX. No additional spectral information on the microbursts is known. [Lorentzen, 2001]

[Fig.1.21]. The physical process for explaining microbursts is not well known [Parks 1993, Lee 2005], but an association with wave-particle pitch-angle scattering by VLF-chorus has been made [Lorentzen, 2001, Meredith, 2001].

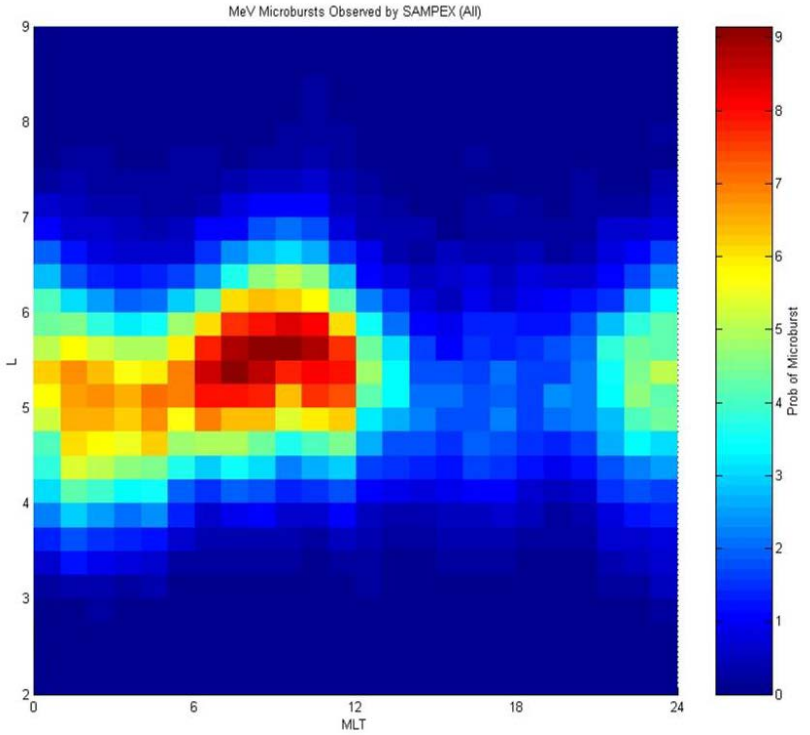

Figure 1.21: MLT (horizontal) vs. L-shell (vertical) distribution of microburst probability occurrence for MeV bursts on SAMPEX. [O'Brien, 2004]

While balloon-based measurements were some of the first to identify microbursts of ~100 keV [Parks, 1967] (shown in Fig. 1.22), there have been no reports of balloon-based observations of the ~MeV energy microbursts even though these have been identified as an important radiation-belt loss process capable of depleting the belts in just a few days [Lorentzen, 2001b, O'Brien, 2004]. This surprising fact may partly be explained by the apparent small spatial scale of MeV microbursts, >10 km, which is on the order of a few tens of gyroradii at precipitation altitudes. [Blake, 1996].

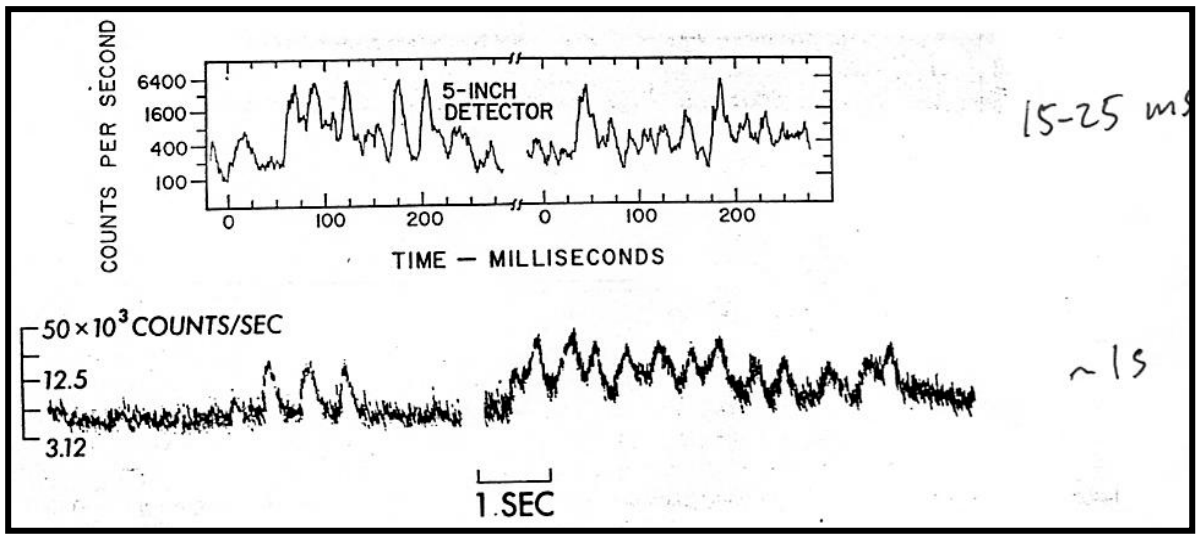

Figure 1.22: Early detection of microbursts from balloon based spectrometers.

1.3.5.2 Dusk-side Relativistic Electron Precipitation

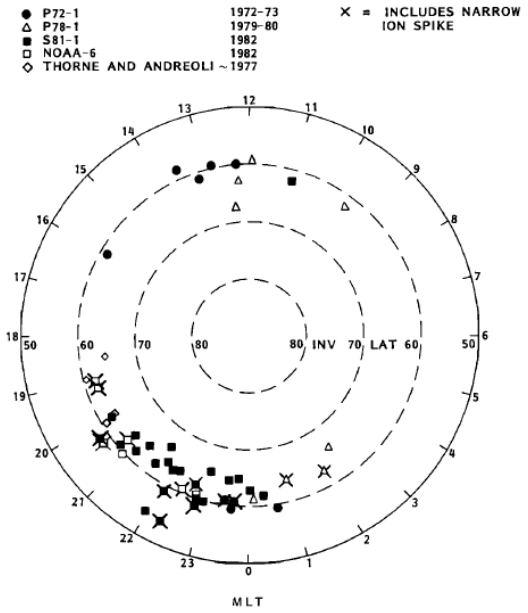

Figure 1.23: Precipitation location in latitude and MLT as observed by Imhof et al. 1986

While Microbursts occur mostly on the dawn side, a second type of REP occurs on the dusk side. This second category of precipitation, referred to as Dusk-side REP or DREP, has not been as well studied from orbit. Thorne and Andreoli [1980] observed only 3 events in 14 months of S3-3 data (1% of all precipitation events observed), which led them to conclude that high-energy precipitation on the dusk-side was rare. The local time coverage of S3-3 data was limited. They attributed these precipitation events which had very hard energy spectra to a cyclotron resonance between relativistic electrons and L-mode ElectroMagnetic Ion Cyclotron (EMIC) waves. In order for an electron to be resonant with such a wave it must have sufficient parallel velocity that it overtakes the wave (opposite of the orientation pictured in Figure1.15 and sees a Doppler-shifted E-field that rotates in the same direction as the electron gyration. This enforces a high minimum energy for resonance to occur which helps explain the observed precipitation spectral hardness.

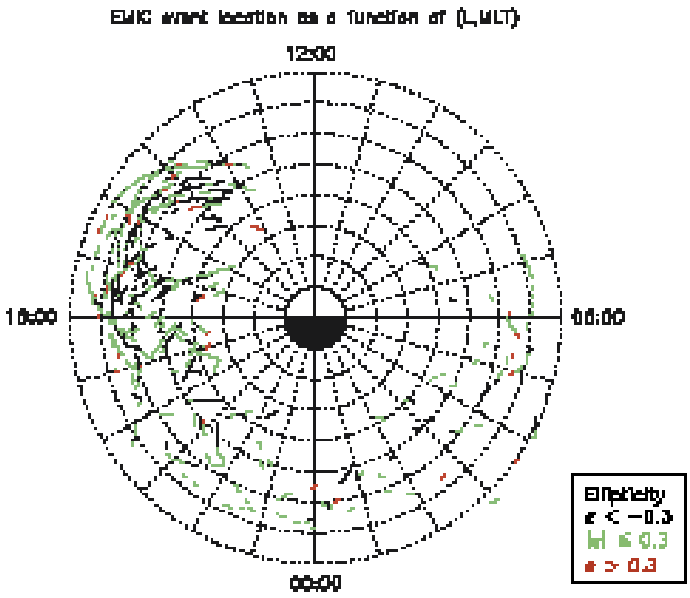

Figure 1.24: Showing the distribution of EMIC waves as observed on the CRRESS satellite. [Meredith et al. 2003]

Imhof [1986] analyzed 41 events using S-(72,78,81)-1 data. Some of these events were among the most intense observed in these satellites' lifetimes. In order to select the events, they filtered on narrow structures in L, i.e., transited rapidly by the polar-orbiting satellite (<10 seconds of observation time, corresponding to <100km). Thus, they were unable to study the time evolution of an event or determine its duration. They also would not have found broad structures that lacked sharp boundaries. Electron e-foldings were found to be >500keV and ~ 30% of the events

were found in association with the precipitation of few-keV protons. Figure 1.23] shows event locations (local time and magnetic latitude).

DREP was subsequently observed by balloon-borne spectrometers looking at bremsstrahlung from the precipitating electrons [Foat, 1998, Millan, 2002]. These observations are detailed in sections 1.6 and 1.7. Balloons may be better able to see DREP than they are microbursts because of the larger spatial scale of DREP. Even the narrow L-filtering of Imhof gives a latitudinal dimension an order of magnitude larger than an MeV microburst. Occasionally, with opportune orbit phasing, multiple satellites were able to observe what was assumed to be the same DREP region. In these cases the longitudinal extent was found to extend up to 47° [Imhof, 1986], or ~3000 km. The strong association of DREP with EMIC waves is due to the very hard spectra, the coincident local times (Figure 1.24), and the occasional associated ion measurements. Direct measurements of EMIC waves and well characterized DREP have not been observed in conjunction.

1.4 Observing the Energetic electron Population of the Belts

Observing relativistic electron loss is a non-trivial effort. While much of the understanding of the radiation belts is derived from near-equatorial-orbit spacecraft, it is impossible to look directly at the loss cone while at the heart of the radiation belts. At L=3.5, the loss cone at the equator varies between 6.5 and 8.5 degrees, depending on longitude (more on the longitudinal dependence in a moment). At higher L shells the loss cone is an even smaller angle near the equator. For geosynchronous orbit, where many observing satellites are stationed and knowledge of radiation-belt dynamics are extremely important for commercial spacecraft, the loss cone is always < 3°. In terms of solid angle, the loss cone is (1-cos(3°)). As a percentage of an omni-directional flux this is vanishingly small (.069%). A typical pitch-angle distribution at ~MeV energies is pictured in Fig. 1.25 and shows a peak at the locally mirroring 90 degrees. Thus in terms of actual electron counts, the loss cone is even harder to see than the solid-angle calculation would imply.

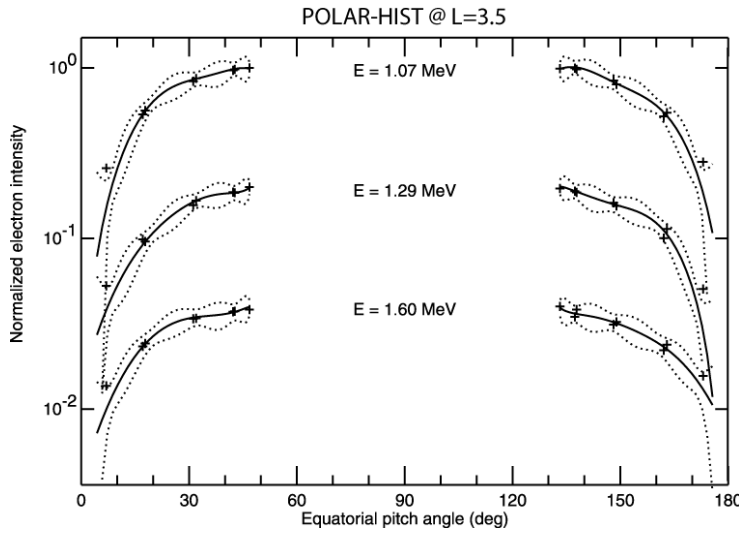

Figure 1.25: A measurement of pitch-angle distribution which has been mapped to the pitch-angle distribution as it would be at the magnetic equator. Very little flux is present at pitch angles close to the loss cone. Adapted from [Selesnick et al., 2003]

Measuring such a small signal in the presence of such a high-flux, hard-to-shield, easily-scattered background has not been accomplished, although continuing efforts are underway (e.g., RBSP uses a magnetic spectrometer with rapid sampling on a spinning spacecraft). Lacking direct measurements of the loss cone, most equatorial satellites only consider net changes in flux,

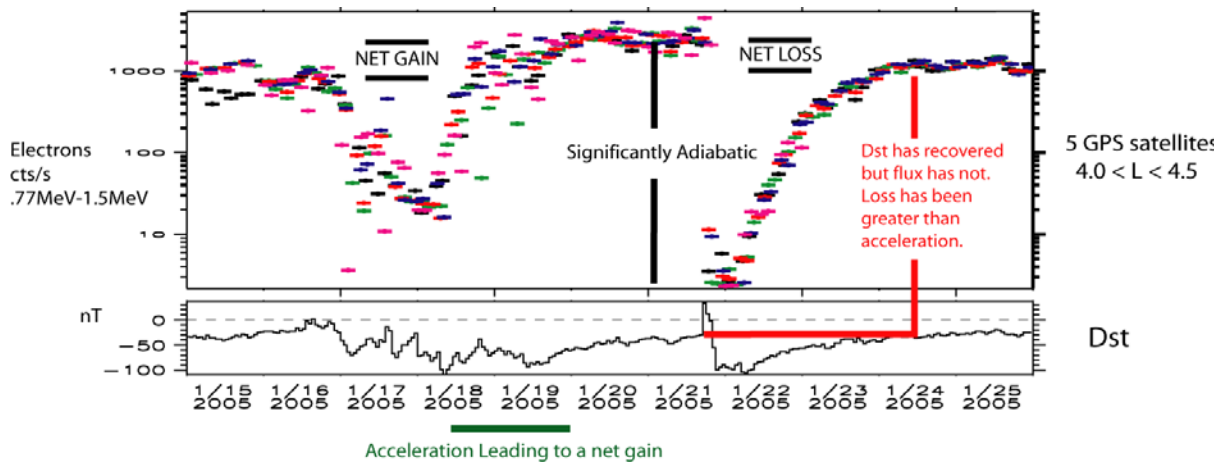

Figure 1.26: GPS satellites making measurements of ~MeV electrons in the heart of the radiation belts, near the magnetic equator see dramatic changes in flux on short time scales. The flux of particles can increase or decrease in association with magnetic storms (as represented by Dst in the bottom panel). The rapid dropout in flux associated with storm onset on 1/21/2005 is principally a result of a nearly adiabatic temporary reorganization of the radiation belts.

which is a convolution of adiabatic effects, losses, and newly accelerated populations. An example from GPS satellite observations relevant to this effort is shown here in Figure 1.26. This data is taken when the satellites are near the magnetic equator at L~4.

The second principal observation of relativistic electron loss from the radiation belts involves using low altitude satellites in highly inclined orbits. Numerous satellites have made observations in this region, and the advantages over equatorial observations are clear, since the loss cone at most longitudes at Low Earth Orbit (LEO ~600 km) is approximately 70° wide for outer electron belt L-shells. The opportunity to measure lost high-energy MeV electrons seems simple. However, LEO satellites are moving at a minimum of 7.5 km/s. For microbursts, this allows relatively complete observations of the temporal phenomenon, but not of the spatial, because the bursts are ~0.1 seconds in duration and ~10 km in scale size at MeV energies[Blake, 1996], and larger at lower energies [Parks et al,1965, 1967].

For more gradually varying phenomena, both spatially and temporally, such as DREP, the precipitation can be difficult to distinguish from the trapped and drift loss electrons found at the same position without significant effort. In these cases, even if the spatial extent can be determined (in latitude), the short-term temporal evolution cannot be followed, as it is convolved with any spatial variations across the latitude extent, while the long-term variation can be established only orbit timescales of ~90 minutes.

Low-altitude spacecraft additionally have to deal with strong variation of particle populations with local time, longitude, and latitude. Local-time variation is due to the aforementioned local-time variation in scattering processes which move particles towards the loss cone where they are able to be seen by low-altitude spacecraft. Strong latitude and longitude variation is due to the offset of the Earth's magnetic dipole axis from Earth center and from the tilt of that dipole axis.

The offset in the dipole axis means weaker magnetic fields in the southern hemisphere (as a function of altitude) for a given field line. The first equation in section 1.2.3 implies that this B-field asymmetry means a particle mirroring well above the atmosphere at 600 km in the northern hemisphere will sometimes mirror at <100 km when it bounces to the southern hemisphere. Thus the southern hemisphere is a more common, but not exclusive, precipitation location. This effect is captured in one month's data from SAMPEX shown here in Figure 1.27. This month long

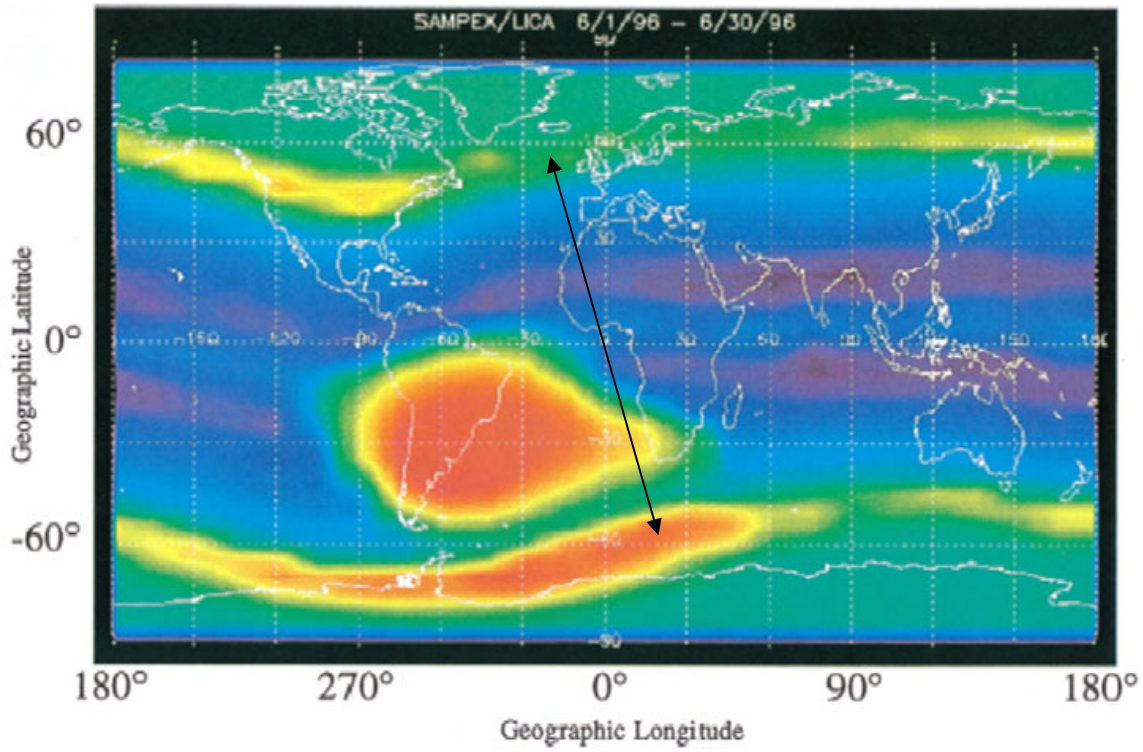

Figure 1.27: SAMPEX PET data showing the strong north-south asymmetry in precipitation as well as longitudinal variations at a given magnetic latitude. The brightness of the strip across the southern hemisphere relative to the northern strip is a real effect of the magnetic-dipole offset. The "wave" of this strip is because of the tilt in the magnetic dipole relative to the geographic coordinates plotted here. The bright blob over South America is the "South Atlantic Anomaly" (SAA) and is largely background in the electron channel (the increase in background is also an effect of the dipole offset, but the counts are mostly from very-high-energy inner-belt protons). Figure courtesy J. Mazur

average does not capture any local time variation because SAMPEX orbits precess in local time, and any such variation is smoothed out. For comparison, a combination of >300 keV data from 3 POES satellites [POESmap] shows the same spatial distribution convolved with local time "striping" because the POES spacecraft are in sun-synchronous orbits (~98 degree inclination), which spend most of their orbit at two particular local times (see also Chapter 3).

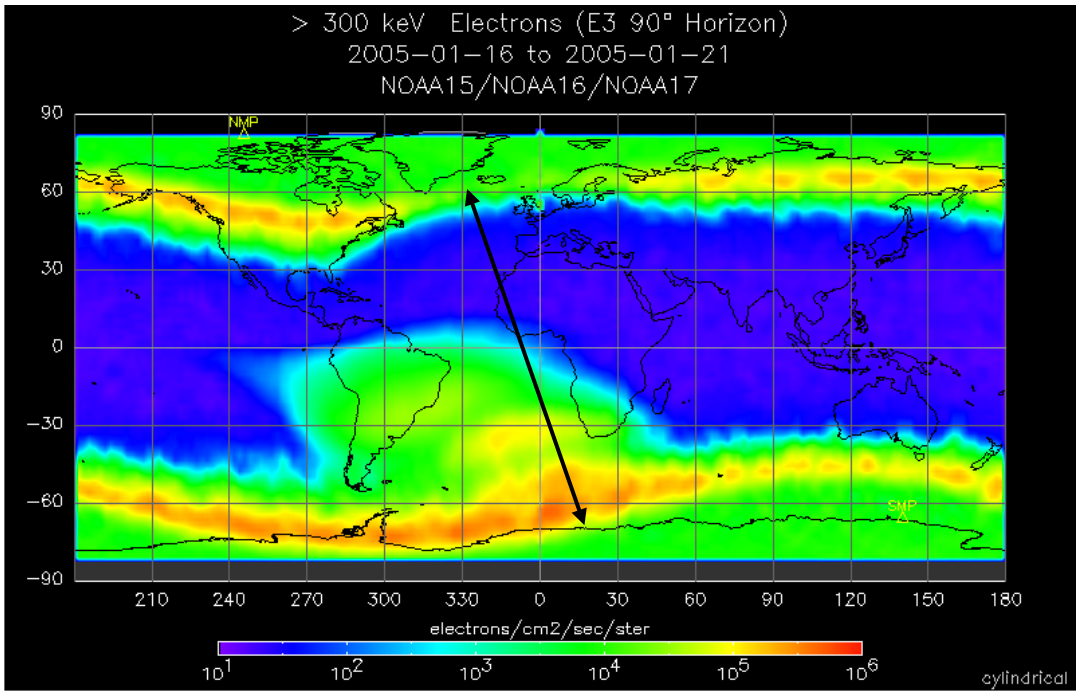

Figure 1.28: 6 days of POES >300keV electron data from N15, N16, and N17 satellites. The map retains some of the local-time variation that the SAMPEX map has integrated over, however reconstructing the local-time variation is rarely done, and separating local time and geographic distributions is the subject of ongoing research efforts [Chen et al. 2008]. The black arrow represents the prime meridian in dipole longitude.

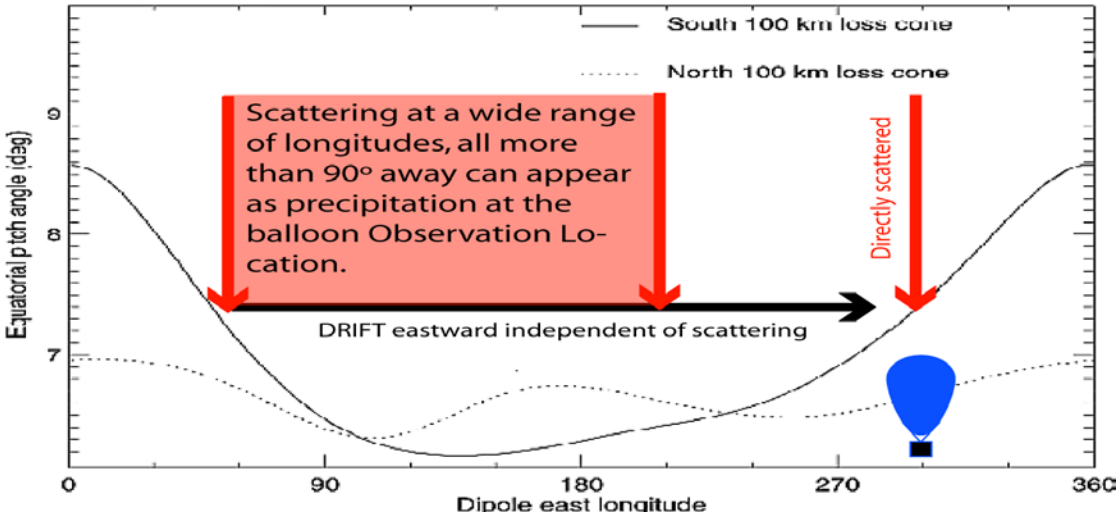

Figure 1.29: The equatorial loss cone as a function of longitude for northern and southern hemispheres. Note that this is a function of dipole longitude, while the maps before were in geographic coordinates.

Figure 1.28 and 1.27 also capture the effect of the longitudinal variation in the loss cone. Many of the counts at 0° longitude are precipitating out of the "Drift Loss Cone" (DLC) (note: throughout this dissertation, I will refer only to the DLC due to inherent asymmetry from the magnetic field of the earth, and not to the distinct drift loss cone that arises from L-shell splitting due to noon midnight asymmetry from compression of the magnetosphere by the solar wind as described in Roeder 1970). For particles precipitating in regions of the drift loss cone, the location of the pitch-angle scattering that caused them to precipitate could be substantially to the west (east for protons). This makes observations of precipitation in this region harder to connect to the process which scattered the electrons in the first place.

A simple way to look at the drift loss cone is to look at the size of the equatorial loss cone as a function of longitude (Fig. 1.29). A candidate balloon or observation at 300° East is shown schematically. The balloon observation will see both the electrons which scatter at its longitude, and electrons that drift into the local loss cone. A spacecraft above the atmosphere is similarly confused unless it has sufficient angular resolution in its detectors; a quality of measurement that has been lacking for high energy electrons and the geometric factors they require. During quiet times, simulations show that it is possible to use the longitudinal variation in spacecraft location with respect to the dipole offset to determine the rate of diffusion into the DLC [Selesnick, 2003]. To determine this quiet-time pitch angle diffusion rate one needs multiple, energy resolved observations at a given L-shell but separated in dipole longitude

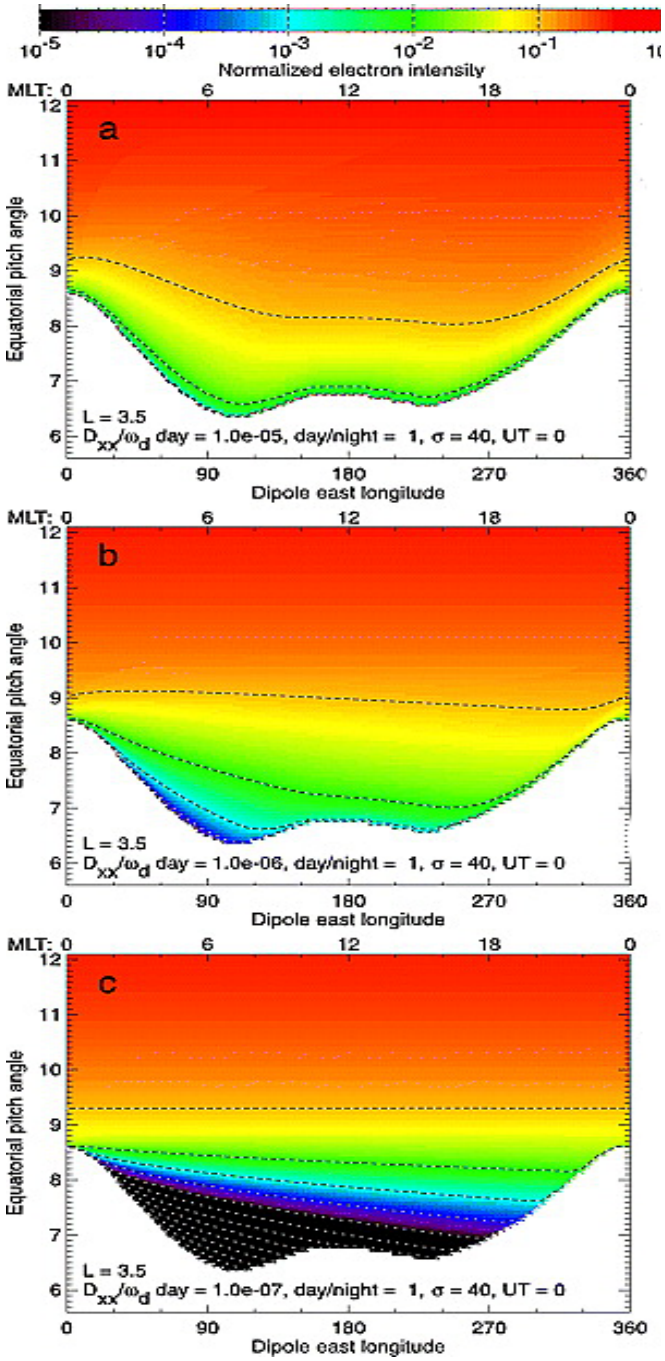

Figure 1.30: Flux in the drift loss cone will vary based on the ratio of pitch-angle diffusion rate to drift period (decreasing from top to bottom). For high energies with fast drifts, precipitation will occur most often between 270° and 360° E. dipole longitude. Adapted from [Selesnick, 03]

(e.g. along the rising slope from 270 E to ~360E in the simulation figure).

However this method will miss rapid variations in precipitation (including any bounce loss cone precipitation), and, because it relies so much on measurements in the DLC, it can only identify local-time variations in scattering by modeling and using long-term averages. The results of this type of model are shown in Figure 1.30. From top to bottom, the ratio of pitch-angle diffusion to drift rate is varied by an order of magnitude in each plot. This is equivalent to assuming a constant pitch-angle diffusion coefficient and moving up in electron energy, from top to bottom, by two orders because ω_d increases with energy as in Figure 1.14 [in prior section].

1.5 Discovery of Terrestrial MeV X-rays

In 1996 an X-ray burst with energies extending above 1 MeV was observed by a high-resolution Ge spectrometer launched from Kiruna, Sweden. The spectrometer was intended to study moderate energy X-rays generated by ~100 keV electrons, but was serendipitously outfitted to record energy spectra up to 1.36 MeV. These high energy X-rays could only have been created by comparably high-energy electrons striking the upper atmosphere. When an energetic electron hits the Earth's atmosphere, most of the energy is lost by Coulomb collisions with the neutral atmosphere. However, a small percentage of the energy goes into the generation of bremsstrahlung X-rays which can propagate to balloon altitudes. A detailed explanation of this process is in Chapter 2. The Kiruna observation was found to be consistent with a mono-energetic (ME) 1.7 MeV parent electron population. The event lasted ~20 minutes with a modeled electron loss rate in the field of view of $2x10^{17}$ electrons/s [Foat,1998]. The time profile of the Ge countrate is included here as Figure 1.31.

The balloon-borne spectrometer in the Kiruna case observed modulation of the precipitation rate at 10–20s periods as well as longer modulation on ~100–200s timescales. These modulation times are unlikely to be associated with the actual waves that are doing the scattering of the relativistic electrons because the resonant energies for such slow waves are far too high [Foat, 1998] in any reasonable plasmaspheric density. It was shown to be more likely that EMIC waves of ~Hz generated by substorm-injected protons of ~60keV drifting to the nightside [Lorentzen, 2000] were responsible for the scattering.

The balloon was at ~19MLT during the observations. Substorm-injected particles tend to have pitch-angle distributions peaked at 90°, a distribution unstable to the growth of EMIC waves [Cornwall, 1970], particularly in the region of increased density near the plasmapause [e.g., Jordanova, 2001, Fraser, 1996]. The source of the X-ray modulation on longer timescales was not resolved. A Field Line Resonance (FLR) [for description of FLRs, see Glassmeir, 1984] at ~200 s was observed nearby, but the mechanism for coupling this oscillation into the precipitation was not specified.

1.6 The MAXIS balloon experiment

Following the discovery of >MeV electrons precipitating into the atmosphere by the relatively short Kiruna flight described above, the MAXIS balloon campaign was instrumented to observe bremsstrahlung from these high energy precipitation events [Millan, 2002]. MAXIS was launched from McMurdo, Antarctica and saw a wide range of magnetic latitudes and local times over the course of an eighteen day flight. The flight path as well as indications of where nine

precipitation events like those seen by Foat, [1998] is shown here in figure1.32. A spectral comparison of one of the MAXIS events with the Kiruna event is shown in figure 1.33, as well as the x-ray lightcurve, in two channels, during this time range. This MeV event (D2a_sp as found in table 4.2) stands out as a brief, distinct precipitation from the surrounding, softer precipitation.

It is important to note that from a geographic perspective MAXIS saw MeV events both in and out of the drift loss cone. From a geomagnetic standpoint, MAXIS saw these same events only in association with substorms and only at duskside local times during 8 days of the flight when the balloon was located at L-values from 3.8 to 6.7. Softer precipitation was seen without the substorm or local time exclusive dependence. Events lasted ~38 minutes on average but with a significant variance. The 9 event durations have a standard deviation of 41 minutes. The longest event (145 minutes) which was also the brightest event above 500 keV ($8.7x10^{17}$ e^-/s in the field of view), though far from the hardest event (e-folding energy of 330keV) occurred on Jan. 19th at L=4.7 in a region where the drift loss cone extends for more than 12 hours. This event (B2a from table 4.2) accounts for 80% of the electron loss observed by MAXIS. This particular event occurred at the time of flux dropout at geosynchronous and GPS altitude [Millan, 2007] similar to those observed by Onsager [2002], and Green [2004a].

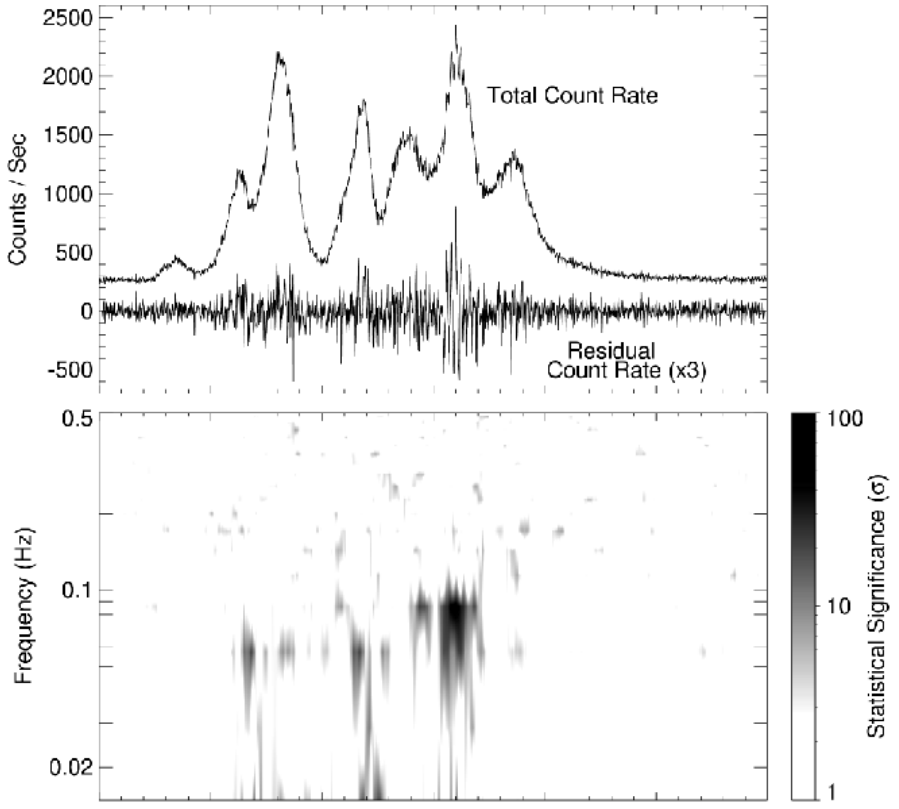

Figure 1.31: The count rate measured on the high-energy Ge detector during the Kiruna flight (top), and a power spectrum of oscillations embedded in the overall count rate as a function of time (bottom).

When the balloon was in an appropriate region of L, the average rate of precipitating >500 keV electrons was ~360 $e^-/cm^2/s$. Millan [2002] argue that the MAXIS observations are a representative sample of the precipitation over the area between 58° and 68° (magnetic) latitude. Multiplying this area by the average observed precipitation rate one obtains an average loss rate from this type of precipitation that will drain the radiation belts (as measured before the first high energy precipitation event) of high energy electrons in ~3 days. This timescale is comparable to observed decay times for the enhanced fluxes that sometimes occur in association with magnetic storms.

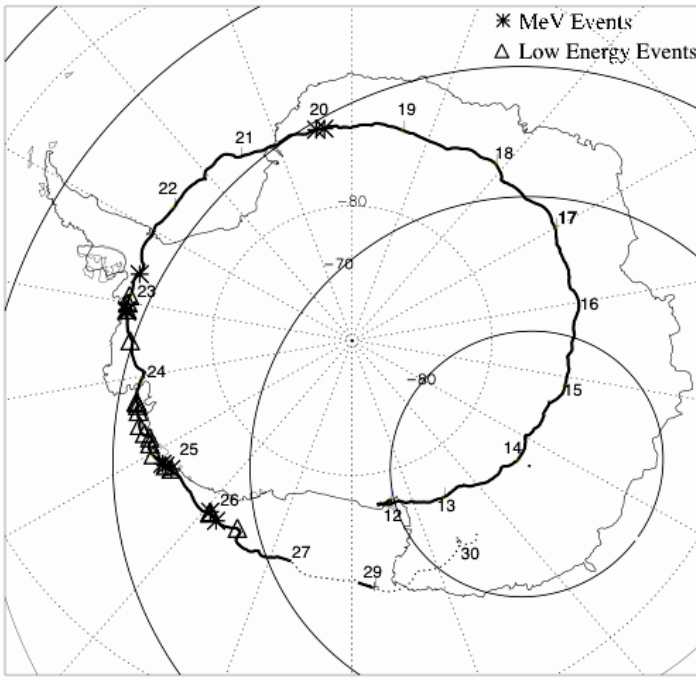

Figure 1.32: The flight path of MAXIS. Solid circles represent every ten degrees in magnetic latitude (IGRF), dashed lines are geographic: 0° lon at the top, 80°S and 60°S latitude about the center. Asterisks represent balloon location during high energy precipitation events.

While the timescale from average loss calculations for the MAXIS data show that DREP can be an essential loss mechanism for the radiation belts, unanswered questions about the high energy precipitation process remain. The importance of the event B2a in these calculations, that event's location in the DLC, and the high variance in fluence and timescale of the MeV events raises the question of how often this precipitation type is dominant. Similar loss timescales have been reported for MeV microbursts, but different observing periods. It is also unclear what the latitude scale and the local time scale are for an individual event. This unknown spatial scale has important implications for determining the instantaneous loss rate from DREP. The spatial scale and distribution should also shed light on the physical mechanism responsible for DREP. These questions represent the seed from which the MINIS balloon campaign sprouted. MINIS aimed to make the first multipoint measurement of MeV electron precipitation from an X-ray observing balloon.

1.7 Overview

This dissertation details the MINIS project (Chapter 2), places the MINIS observations in context with other measurements at the same time and compares those measurements to MAXIS (Chapter 3). We then go on to looking at generating high-time-resolution electron precipitation scaling (chapter 4) and compare the MINIS observations to other loss rates observed during the same time period, both space and ground based, and look at the time structure and spatial scale of the REP (chapter 5). Finally, a series of new experiments are detailed that will shed light on

the unanswered questions of MINIS (Chapter 6, 7). A summary of conclusions is given in chapter 8.

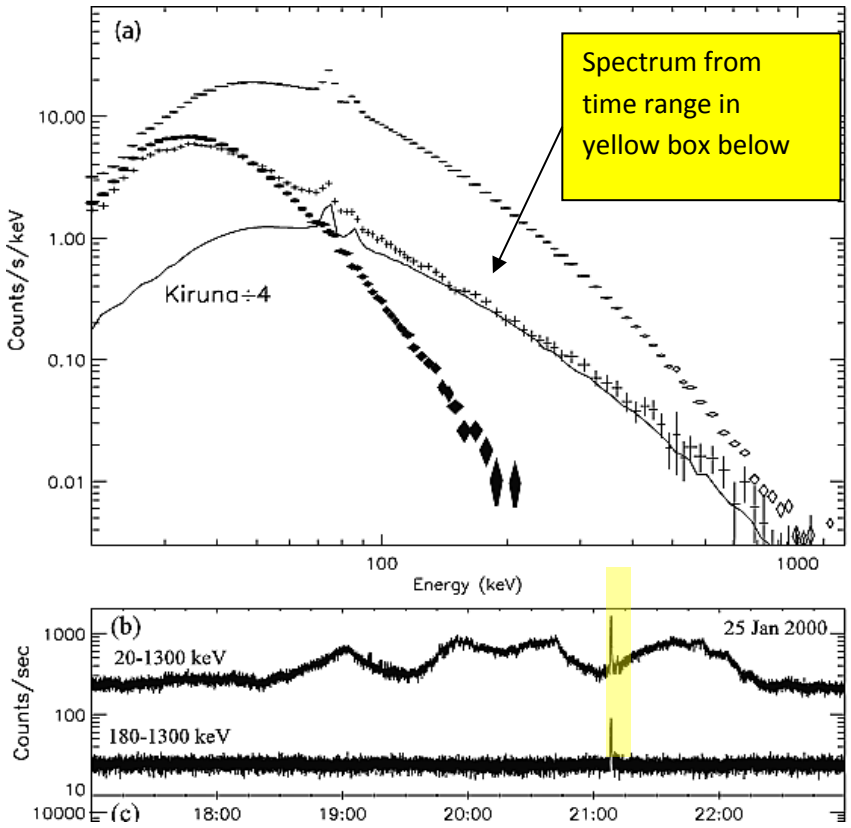

Figure 1.33: Filled diamonds are a typical soft precipitation spectrum. This spectrum was recorded during the time range indicated in the bottom panel on Jan. 25 excluding the time around the spike at 21:10. The Spike Spectrum is shown as + symbols with the Kiruna spectrum scaled to match in flux. The top spectrum (open diamonds) is the event B2a, bright, and long duration, but more steeply falling with energy.

2 The MINIS Balloon Experiment

2.1 Introduction

The MINIS campaign was designed to complement existing balloon and spacecraft measurements of REP by helping to separate spatial and temporal variations in the precipitation, establishing a scale size for the precipitation to refine estimates of instantaneous loss rate of relativistic electrons due to Duskside REP, and measure conjugacy of precipitation in the northern and southern hemispheres. MINIS also hoped to observe relativistic electron microbursts, look for electric and magnetic field variations that might be associated with REP and to take advantage of additional space based instrumentation that was not available during MAXIS and the Kiruna flight such as particle measurements on several GPS satellites (only one GPS particle instrument was available for MAXIS) and imaging of the plasmasphere by IMAGE.

In order to achieve the goals of MINIS, four identical payloads were successively launched from the South African Antarctic station, SANAE IV. Each of these payloads carried a 3”x3” NaI scintillator, a 3-axis DC measurement of E and B, and a single axis measurement of VLF (~1-50 kHz) oscillations in E and B. There were also two payloads launched from Ft. Churchill, Canada, which had a chance of making magnetically conjugate observations. These northern hemisphere payloads were similar to the southern but had only a DC B-field measurement and no electric field instrument.

Figure 2.1:A photo of a MINIS payload being transferred to the flight line. The electric field booms are clearly visible as well as the ground planes surrounding the payload.

2.2 Instrumentation

2.2.1 NaI Scintillator

The principal science instrument aboard the MINIS payloads was a 3” diameter by 3” height cylinder of Sodium Iodide (Tl) used to measure bremsstrahlung X-rays produced by precipitating relativistic electrons in the tenuous atmosphere above the payload. When an X-ray interacts with the NaI crystal, a pulse of light whose brightness is proportional to the energy deposited by the X-ray is produced. The scintillator was optically coupled to a photocathode sensitive to the characteristic wavelength of light produced by the crystal (~540 nm in this case). The photocathode emits a number of electrons proportional to the light pulse. These are then accelerated through a series of dynodes in a photomultiplier tube (PMT). The end result of which is a current pulse proportional to the incident photon energy. The NaI crystal and PMT used on MINIS are shown in their light-tight mounting tube and a schematic diagram here fig 2.2.

Although NaI provides reduced energy resolution when compared with the two previous principal missions concerning ~MeV precipitating electrons (which used liquid N2 cooled Germanium for spectroscopy), those studies showed that the spectrum from precipitating electrons was sufficiently smooth that it did not require such high energy resolution. A spectrum from the most intense event observed by MAXIS is shown in Figure 1.33, no fine structure is observable.

The MINIS spectral data was ultimately limited in energy resolution not by the type of detector but by the telemetry limitations of the payload. In addition to its sufficient energy resolution, NaI is fast enough to accommodate a significant counting rate, has better stopping power compared to Ge especially at the highest energies (>1 MeV for the configurations used) and is relatively

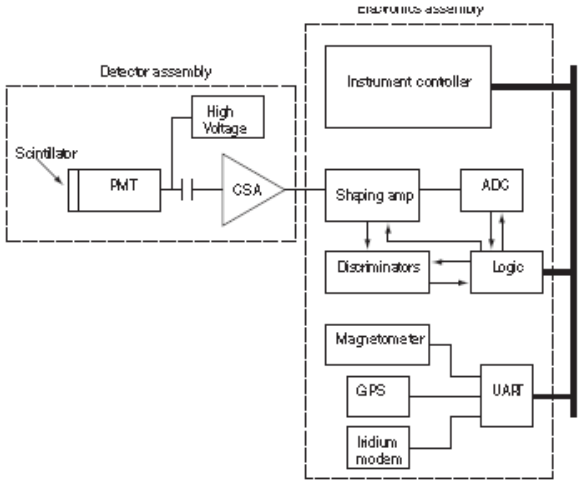

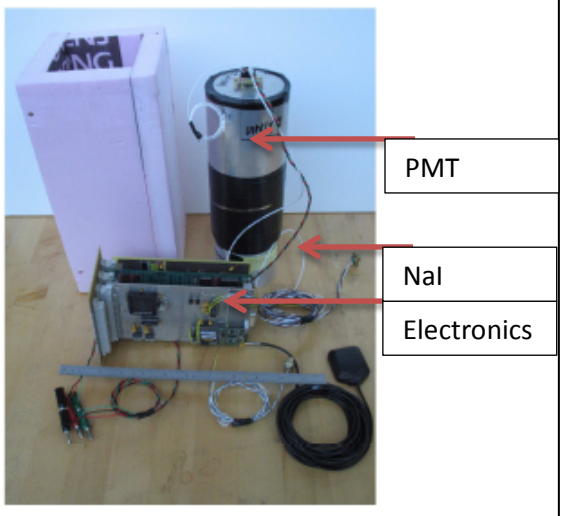

Figure 2.2: A schematic of the scintillator, PMT and electronics, as well as a photo of the assembly. In the picture, the NaI is facing down, as otherwise the assembly is top-heavy. The foam box shown insulates the NaI from damage from thermal shock with rapid temperature transitions.

inexpensive to fly. It is hydroscopic, has a simple gain change with temperature and energy as well as a gain change from the PMT with temperature, and should be handled with care for vibration, shock, and rapid temperature changes which can damage the crystal. For a mission involving multiple small hand launched payloads it was also important to choose a detector material that did not require a cryogen support system as Ge-based detectors use as these weigh more than the entirety of the MINIS payloads.

The spectrometer covered the energy range from 20 keV to 10 MeV. PMT pulses were shaped by an associated analog electronics board, then digitized using 12 bits of energy resolution spread linearly across the energy range. The instrument board then issued an interrupt to the flight computer which recorded the time of this interrupt at 20 Hz (50 ms) resolution. Counts were then recorded in the data stream in two separate manners. Every 8 seconds a summed spectrum from 20 keV to 10 MeV was recorded in 208 channels which were sized pseudo-logarithmically across the energy range. At a significantly higher cadence (20 Hz) the instrument also recorded 4 broad energy channels from approximately 20-175 keV, 175-540 keV, 540-825 keV, and 825 keV to 1.5 MeV. These energy ranges were chosen to complement the existing observed ranges of electron microbursts at time resolution comparable to previous observations.

2.2.2 Electric Field Instrument

MINIS employed three double Langmuir probes to measure the vector electric field at the payload. The two horizontal measurements were sampled at 1 Hz and the vertical pair was measured at 4 Hz. The local conductivity was measured every 10 minutes by briefly charging the spheres and observing their relaxation. The double Langmuir probe technique involves measuring the potential difference between two spheres separated by suitably long booms of very high impedance. For MINIS the spheres were 15cm in diameter and separated from the payload center by 2.0 m (horizontal) for a 4.0 m total separation. The vertical pair of spheres was rigidly separated by a 1.0 m boom which was threaded over the payload loadline (the rope connecting the balloon and the payload). The potential of each sphere is measured relative to a common payload ground and the electric field is simply the potential difference divided by the separation of the spheres. In most cases the vertical electric field is much larger than the horizontal electric field. If the gondola is not perfectly balanced and there is a vertical separation in the probes, the vertical field significantly contaminates measurement of the horizontal field. To resolve this issue the entire payload is rotated by putting a motor in line with the load line. The resulting measurement is of an offset oscillatory signal. The offset is from the vertical field and can be subtracted, the oscillation amplitude is the horizontal field strength and the phase indicates direction in the horizontal plane. The MINIS rotation rate was ~2 rpm, but it varied throughout flight and between payloads. The first order determination of azimuthal orientation was done by comparing the local magnetic field measurement described in 2.2.4 with a model field. To ensure a uniform work function and a large ground area, the spheres are coated with Aquadag, a carbon suspension which creates a black surface of uniform and relatively high work function (4.6 eV). The payload is surrounded by 4 large area planes, similarly Aquadagged, these served to establish payload measured “ground” for the potential measurements. The black planes strongly influenced payload thermal design. They were backed with a low emissivity aluminum surface and were held off from the main payload by 1” standoffs (also important for electrical purposes).

In addition to the DC electric field measurement described above, MINIS also split the signal from one horizontal and one vertical pair and passed this through a series of VLF (Very Low Frequency) band-pass filters centered at 1 kHz, 5 kHz, and 25 kHz. The width of the band-passes was roughly ½ the central frequency. Horizontal and vertical sensitivities were set on the ground for expected relevant signals from whistler-mode waves that penetrated to balloon altitudes, but no power was ever detected in these channels.

2.2.3 Search Coil Magnetometer

A small single axis search coil was also flown. The output was passed through a preamp and then into an identical set of bandpass filters as used for the electric field measurements. The coil was aligned with the load line, i.e. sensitive to variations in the vertical field. Unlike the VLF electric field variations, which are almost impossible to test end-to-end on the ground, the search coil magnetometer was carefully calibrated in a small Helmholtz coil both with and without the filter banks looking at the output. Sensitivity was comparable to expected signals. However, once again the observations showed almost no detected wave-power in the measurement. The AC- B and E field measurements will not be discussed further.

2.2.4 DC-Magnetometer

The ~DC magnetic field was measured by a commercial magnetometer typically used for navigation (PNI Systems TCM2-50 magneto-inductive magnetometer). Although little characterization was done on the magnetometer prior to flight, the observed sensitivity was comparable to the data sheet values of ~10 nT. Further work with other copies of the magnetometer has confirmed this sensitivity (see for instance chapter 6 on BARREL). The DC magnetometer was used to orient the electric field instrument, observe large changes in the local magnetic field due to magnetospheric currents (e.g. magnetic bays), and if independent azimuthal information were available (e.g. from the sun sensor, which ultimately did not work with sufficient accuracy to be used) to look for Ultra Low Frequency (ULF) oscillations that might modulate the relativistic electron precipitation. One such mode is the field line resonance discussed earlier. The magnetometer can also provide a comparison to magnetic field models to determine the accuracy of those models during the magnetically dynamic (and therefore not always captured by the models) times surrounding geomagnetic storms. In practice, looking for small, real oscillations in the magnetometer data has proven difficult. The pendulum motion of the balloon, small changes in the rotation rate, and inaccuracies in the sun sensor have stymied extraction of ULF waves from the magnetometer data. Ground based magnetometer data available near the payloads during event times is sometimes available and shows power in the tens of mHz frequency range. This range is unfortunately close to the 30 mHz rotation rate of the payload.

2.2 Power System

MINIS was powered by large lithium chemistry primary (non-rechargeable) cell batteries to power a series of DC-DC converters that in turn powered the payload's components. For each payload, the batteries cost $6K and weighed 16 kg, constituting the largest individual weight in the payload. The battery stacks were divided into 2 dioded parallel stacks of 11 Lithium Thionol Chloride cells at 3.3 V nominal voltage per cell for a 36 V operating voltage. These stacks were

Supply Name	Voltage	Current	Notes
IRID+5	4.4 V	~1 A Highly variable	Vicor VI-220-CY is oversized at 15 Amps but handles large turn on transient of ~3A. Could be power cycled through Parallel port to optocoupler
Filters	±5 V	160 mA each	1mH inductor and Full 4 capacitor filtering
Boom	±12 V	70 mA each	Same filter as Filters but without large 150 uF capacitor
Search	±12 V	225 mA each	Same as “Boom” for isolation only
PMT/Shaper	±5 V	+100 mA -5 mA	Same as “Filters” for isolation only
Computer-Analog	±12 V	180 mA	250mA supply-unfiltered
Computer-Digital	+5 V +3.3 V	800 mA 17 mA	2A supply-unfiltered with linear regulator for GPS 3.3V supply
Relay	+12 V	120 mA	Duty cycled, only on during E-field Conductivity measurement. 425 mA supply-unfiltered
Table 2.1	The MINIS power system.		

then put in parallel with 3 stacks of 10 cells. During the first part of the flight, the payload is entirely operated off of the two stacks of 11. Once these batteries are nearly exhausted, their voltage drops to and then below that of the stacks of 10 which then contribute most of the current. This scheme was used to maximize the available battery capacity by putting the current output of the cells near their most efficient output current. The scheme also had the advantage of showing the amount of total battery capacity remaining on the payload. This is necessary because lithium primary cells have exceptionally flat discharge curves, so the telemetered battery voltage did not provide significant information on the state of charge except the readily apparent transition from the stacks of 11 to stacks of 10. This allowed for the possibility of battery management by controlling the power consumption of the payloads.

The raw battery voltage was fed into a series of 8 parallel DC-DC converters (4 of which were double ended, two at ±5 V and two at ±12 V) that supplied power to the rest of the payload. The 4 double ended supplies were heavily filtered and supplied instrument analog power. The separate supplies were supposed to ensure isolation between instruments, however significant noise did appear in the lowest energy channels of the NaI detector, dithering energy resolution and raising the threshold to >20 keV.

2.3 Housekeeping

MINIS telemetered a range of voltages and temperatures to the ground as a means of monitoring the payload state. These values and the cadences at which they were measured are included below in table 2.2. Thermistors and a sun-sensor were hoped to be used for determining azimuthal angle independent of the magnetic field; however, small oscillations of the balloon-

payload pendulum and variation in the rotation rate of the load line motor make the sunsensor data difficult to use. This analysis has not been completed. The thermistor based orientation failed to yield any useable attitude information.

The payloads also sent, at a 16 s cadence, GPS latitude, longitude, altitude and time from a Trimble Lassen SQ GPS receiver. Latency on the position information was considered unimportant and was not well characterized (the payloads do not move quickly after all), but in order to establish accurate inter-payload timing, the GPS time relative to the payload computer clock had to be well characterized. Rather than using the pulse per second output of the GPS receiver, MINIS employed the simpler technique of querying the GPS, waiting a fixed number of computer cycles, which amounted to ~40 ms, and accepting the GPS time as reported. Thus there is a possible error to inter-payload timing of ±20 ms plus any drift that occurs in the computer clock over the 16 seconds. Postflight analysis of the computer clock drift found drifts to be smaller than the 20 ms latency error. The highest time resolution data has already been discussed, the 20 Hz (50 ms) X-ray countrate, so a possible shift of approximately half of a data point is possible in this data set. Most of the analysis in this work will focus on 1 second accumulations of these X-ray countrates, for which a relative drift in payload clocks is neglected. On the ground verification of inter-payload timing was verified to the accuracy of the fastest data product by passing a radioactive source in front of a very narrow window in a lead shield that looked out on multiple running payloads with their NaI detectors recording at 20Hz. The timing scheme described above always returned synchronous pulses in a single time bin. Although the environment was not controlled for in this test, the in-flight clock drifts that were established by the 16 second GPS information combined with the accuracy on the ground give us a maximum 20 Hz error of 1 time bin.

2.4 Data Acquisition

2.4.1 Flight Computer

MINIS utilized a PC104 stack 3 3MHZ 486 based PC running a DOS equivalent OS. The CPU handled gathering, buffering and framing the data for telemetering to the ground station. In addition to the main computer board, a VGA graphics card for screen output and an additional serial interface card were included on the stack. The VGA cards were not removed before flight, but were used only on the ground monitoring of the flight software. The additional serial card was required because three flight systems required a serial interface (GPS, Magnetometer, and Iridium Telemetry) and only two such ports are available on the main CPU board. The CPU stack was directly connected via the PC104 bus to a custom built interface board which connected to the scintillator board, E-field instrument, bandpass filters for both E and B, voltage monitors, temperature monitors, a crystal based oscillator for improved payload clock, and facilitation of the GPS.

Flight software was written primarily in C and compiled in a small memory module architecture to maintain speed. This limited the size available for the onboard data storage to roughly 540 frames. Each frame of 256 bytes holds 1 second of data giving a 9 minute buffer. While most data was collected at a fixed point time within each second (i.e. the potential on number one of the six E-field spheres was always measured 0.13 seconds, controlled by the interface board oscillator, into the frames worth of data), the scintillator data was given priority and operated on an interrupt based interface.

Housekeeping NAME	Period of recording each in (s)	Notes
Frame Counter	1	Low 15 bits = frame counter
Time	1	Tick Counter running at 100 Hz. This is not GPS time, oscillator time from Interface Board
4 Sun Sensors	1	1 second each
4 Thermistors	1	1 second each (for orientation)
Thermistor	1	10 mV per degree K. (shielded thermistor for atmsosphere)
GPS X	16	LAT IN RADIANS (+North; -South). See below.
GPS Y	16	LONG IN RADIANS.
GPS Z	16	ALTITUDE IN METERS. MSL.
GPS TIME	16	UTC time of week in seconds.
computer time	16	UTC in seconds
EF Therm , Batt+28	32	Thermistor and voltage multiplexed
5VA, 3.3VGPS	32	Voltages
Irid5V, FILTER5V	32	Voltages
Boom+5,Boom-12V	32	Voltages
SC+12,SC-12	32	Voltages
PMT+5,PMT-5	32	Voltages
PMT RATE CNTR1	16	Assesses state of health for scintillator+ gives ULD-info
PMT RATE CNTR2	16	Assesses state of health for scintillator
PMT RATE CNTR3	16	Assesses state of health for scintillator
2 Thermistors	32	10 mV per degree K.
2 Thermistors	32	10 mV per degree K.
Table 2.2: MINIS Housekeeping data		

This gave accurate time tags to incoming photons which were promptly binned into both the 8 second accumulation spectrum, and the 20 Hz 4-channel lightcurves. However, this also resulted in paralyzeable system, as the CPU would slow in response to very high count rates from the scintillator electronics. Expected count rates based on the MAXIS data set were sufficiently low, such that we did not anticipate the flight computer being paralyzed. However MINIS observed higher counting rates during peak electron precipitation times and during a large Solar Energetic Particle event than the system was capable of handling efficiently. While X-ray data was almost always still reliable, other data may have been corrupted. The interrupt based system also had some implications for the telemetering of the data buffer, described below in the telemetry section.

2.4.2 Telemetry

The MINIS data set had a significant number of data gaps, some occurring during unfortunate times. MINIS used an L-band Iridium modem for telemetry. The same model, Motorola 9522 was used on both the flight and ground sides. For the flight side, the modem was operated in an autoanswer mode, with calls placed to it from a UC Berkeley ground station. The flight modem was the largest single power user taking ~5 W when in an active call, but only using 300 mW when in standby mode. This meant payload power use could be modulated by ~30% by a ground based decision to call the payload. However at most times, including all science data used for this dissertation, the ground station would call the payload as quickly as possible after it determined the call was dropped (a 15 s data silence). The payload was designed to reset its Iridium modem if it had not received a 4 byte handshake within the previous 5 minutes. After receiving a call, the flight computer would attempt to empty the data stored in the onboard buffer at a rate greater than the data generation rate (256B/s). The Iridium network's nominal maximum data rate of 300B/s was occasionally exceeded; however, call stability tends to decrease as the attempted data rate increases. Flight software was a relatively simple loop that responded to interrupts to gather x-ray data and determine timing. Every 13 times through the flight software's primary operation loop software sent a byte to the modem. For low and moderate X-ray counting rates this meant the flight computer would attempt send close to 300 B/s to the Iridium. This would mean 44 B/s of excess (transmission rate) – (data generation rate). This further implies that when the data buffer was nearly full the excess transmission rate would empty the buffer within ~200 s and the flight computer would then only transmit data at the data generation rate (256 B/s). During times of high X-ray count rate when the computer would slow, the maximum data transmission rate would also slow. Although a slower transmission rate generally leads to more stable connections in ground based testing, this does not appear to be the case in flight,

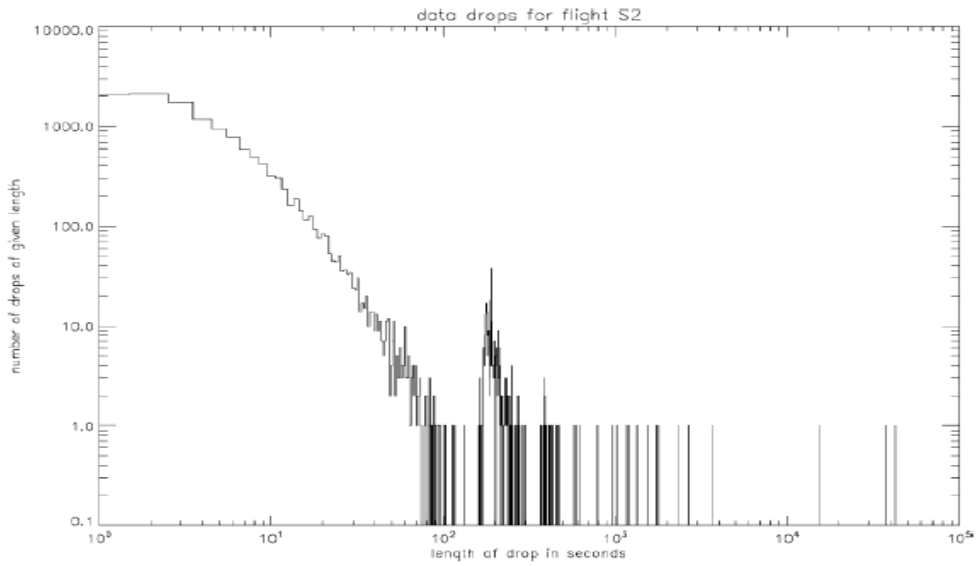

Figure 2.3: length of data drops experienced on flight S2. The second peak at ~200seconds is related to the size of the on-board buffer. The drops of thousands of seconds are not well understood.

perhaps because ground testing of transmission rates did not rely on bogging the computer down, but by changing the number of times through the primary loop (the 13 used in flight was chosen as slightly faster than the ground based optimum). The end result is that the MINIS data set has a significant number of data gaps.

The Iridium modem also seemed susceptible to longer outages, the source of which has not been determined. This included some dropouts with a diurnal cycle which may have biased observations to particular local times later in the S3 flight. A plot of data dropout length for payload S2 is included here as Figure 2.3. As can be seen in the following chapter there are unfortunate long data gaps later in flight 3 and small data gaps around the electron precipitation during the magnetic storm of Jan. 21st.

2.4.3 Ground Support Equipment

The MINIS ground station software was written as a Labview Graphical User Interface and was based extensively on the MAXIS ground station with the addition of an interface to the Iridium modem. Four separate computers were used, each with a dedicated Iridium modem, but all sharing a common keyboard, mouse and monitor. The software was designed to call the payload continuously, unless power saving on the payload was desired.

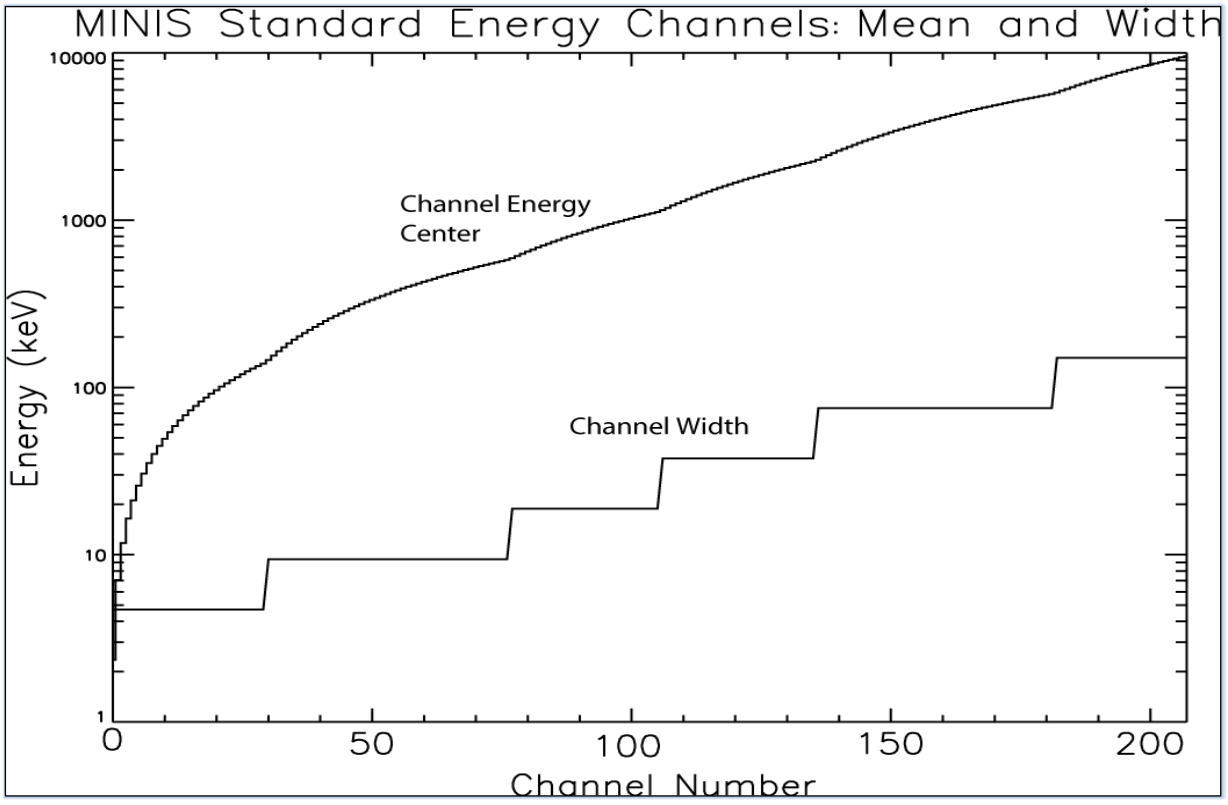

Figure 2.4: The MINIS standard energy channels cover 0-10MeV with 208 quasi-pseudo-loq bins, starting at 4.7keV per channel and ending in 150keV bins.

2.5 NaI Calibration

2.5.1 Energy resolution

The final MINIS spectrometer energy resolution was determined by telemetry constraints. Since the primary science objective was based on the inversion of smooth electron bremsstrahlung spectrum, line quality resolution was not necessary.

A plot of a typical energy vs. channel number is included as Figure 2.4. However, additional energy bins were placed around the typical location of the 511 keV line as a means of calibrating the spectrometer gain post flight. Although the spectrometer gain was well characterized on the ground as a function of temperature, post flight we did not have confidence in a sufficient thermal coupling being established between housekeeping thermistors and the NaI crystal, so a single parameter gain solution was generated by tracking the 511 line. This ensures the highest accuracy in energy determination near 511 keV. Although the energy spectrum was read out to ~10 MeV in case of unusual high energy events, energy resolution was poor above several MeV, and the gain solution probably inaccurate by more than 10% at the highest energies as is sometimes evident in the background subtraction at very high energies (5-10 MeV). There additionally may be offset and gain errors at the low end of the spectrum which may contribute to poor model fits at typically < 100 keV in the spectrum. A plot of each payload's energy/channel as a function of time is included in Fig. 2.5.

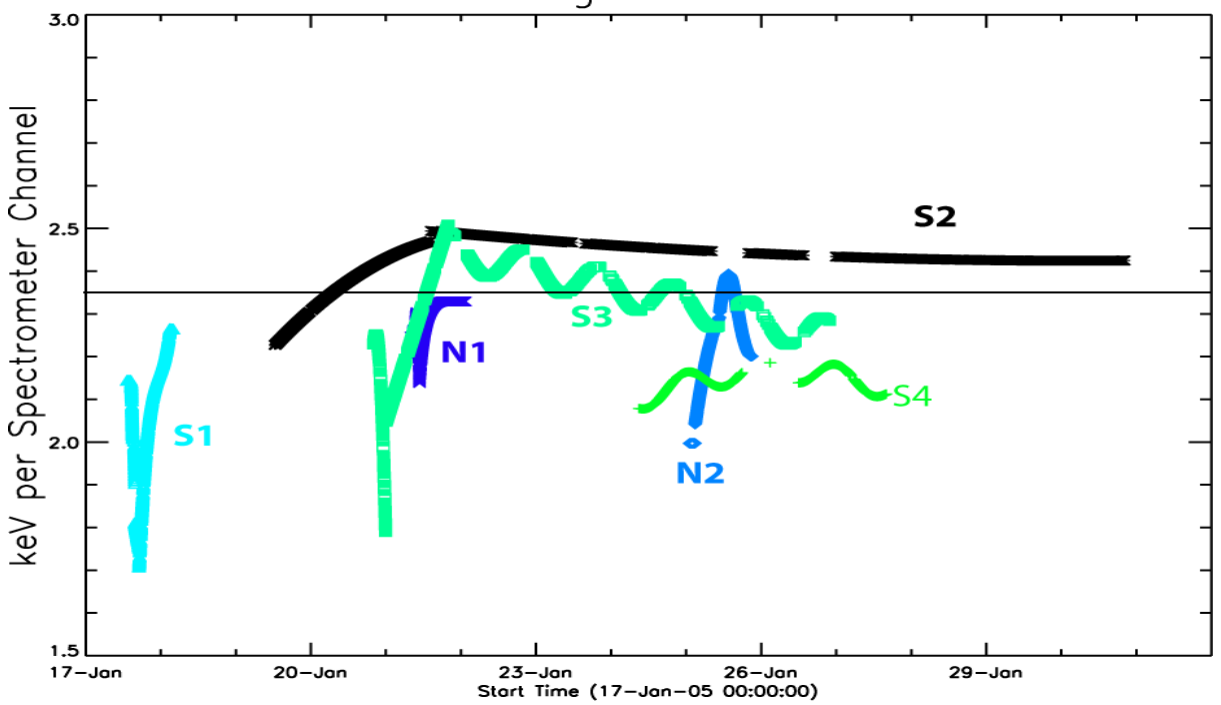

Figure 2.5: shows the gain solution used for the MINIS spectrometer throughout the course of each of the flights. This was determined by fitting the 511keV line. The average value used for processing spectral products through the detector response matrix is 2.35keV/channel and is shown as the horizontal line

An important note on the binning of the 4 light curves is that it is also done in channel space in flight, so the real channel energies are susceptible to gain changes. These changes are expected to be slow enough that they can be ignored for most analysis. However, very high time resolution inference of the input electrons to the top of the atmosphere needs to take energy channel changes into account, in particular when subtracting baseline count rates for background removal. In 12 bit channel space for reference these boundaries are 0-74, 75-229, 230-349 and 350-619 keV.

2.5.2 Gain Calibration

On the ground gain calibration was performed using several line sources at limited temperatures. The calibration was performed in 4096 channel space and not in the final 208 telemetered channels. The gain calibration was performed by Dr. Michael McCarthy at University of Washington. An example of one such calibration spectrum is included here in Figure 2.6. The figure shows the results of fitting lines of known energy and measured channel number to parameterized Gaussian distributions. Plotted are the ratio of peak channel/energy normalized by the ratio for the Cs-137 line at 662keV. Ratios > 1 mean the system gives a slightly larger output per unit energy than at 662 keV. The figure shows that a low energy channel is a little bit wider than a high energy channel. The multiple sources of gain variation probably contribute to something other than the simple linear gain solution used in flight, but calibration of the system end to end on the ground showed offsets that are negligible for the primary science discussed here, and nonlinear gain variation that were estimated at ~5% for the observations that are discussed as part of this thesis.

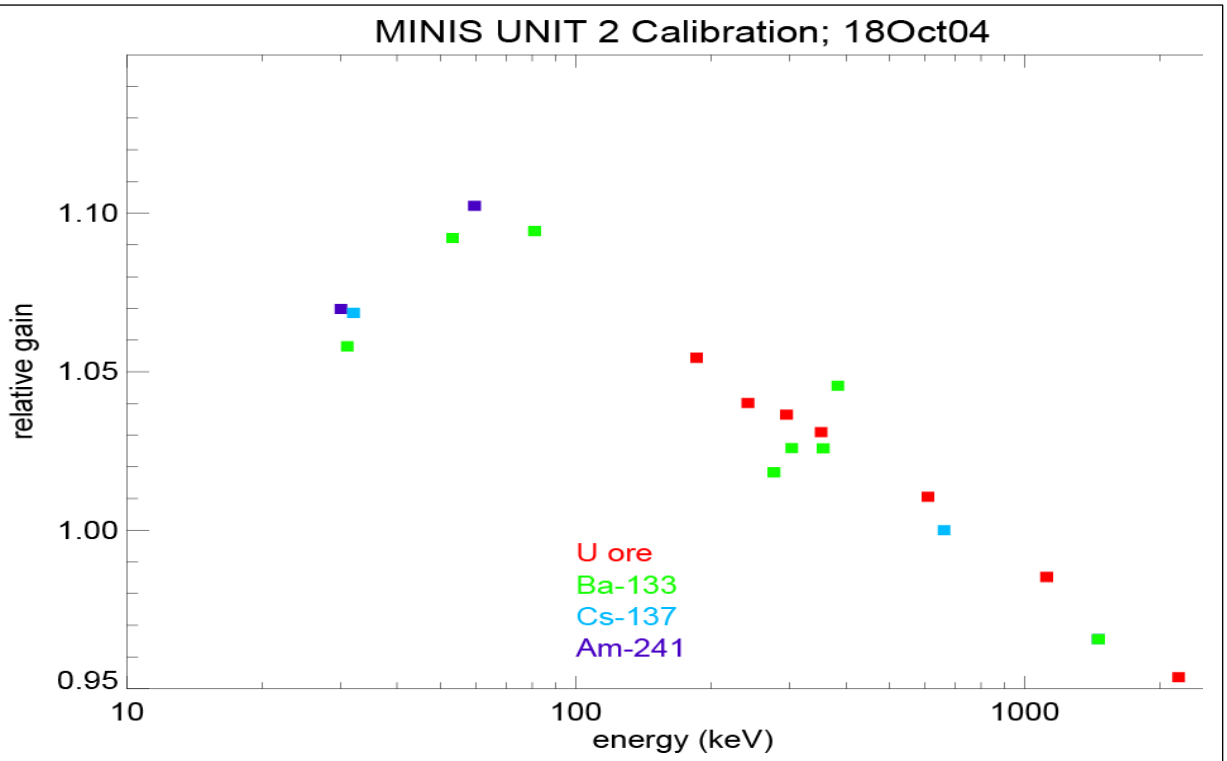

Figure 2.6: Showing the relative gain with energy found for one of the MINIS scintillators.

2.5.3 Instrument Deadtime correction

A simple model is used for estimating the effect of instrument deadtime on the count spectras is used throughout the data analysis. Using 8 μs of non-paralyzeable deadtime in the following formula:

$$N \approx \frac{N_m}{1 - N_m \tau / T}$$

Where N is the actual number of events, N_m, is the measured number of events, τ is 8 μs and T is the spectrum accumulation time which is 8 seconds for the analysis here. For the brightest events seen by MINIS this can be up to a 30% correction in an 8 second spectrum, but for the primary event periods from January 21st that are discussed in the following chapters the average correction is closer to 5%

2.5.4 Instrument and Atmospheric Response Matrices

To determine the precipitating electron spectrum we follow a method similar to that discussed in Milan '02 and Smith 92, involving the processing of a wide range of parameterized input electron spectra through a series of steps. The continuum electron distribution is calculated, followed by a bremsstrahlung cross section calculation resulting in an X-ray distribution which is then folded through an atmosphere instrument response matrix that was generated from a GEANT Monte Carlo model. The bremsstrahlung generation is assumed to take place in a thin layer around 70km. Although low energy electrons will stop higher in the atmosphere (and conversely very high energy electrons ~2 MeV will penetrate deeper), the bulk of the counts that MINIS sees during these event times are from electrons that stop in this altitude range. A more thorough effort in determining the overall height profile of electron stopping depth in the atmosphere has been taken by Kokorowski [2008], which confirms these assumptions for energies of interest. Further, small changes of 1-2 km in the initiation height were tested and shown to have no measurable effect on the final result. Thus the atmospheric response matrix begins at 70 km for the bulk effort which use input photons as described below. This may contribute to errors in the model at low energies where atmospheric absorption will be more important, and in low statistics model runs that start with electrons at the top of the atmosphere this

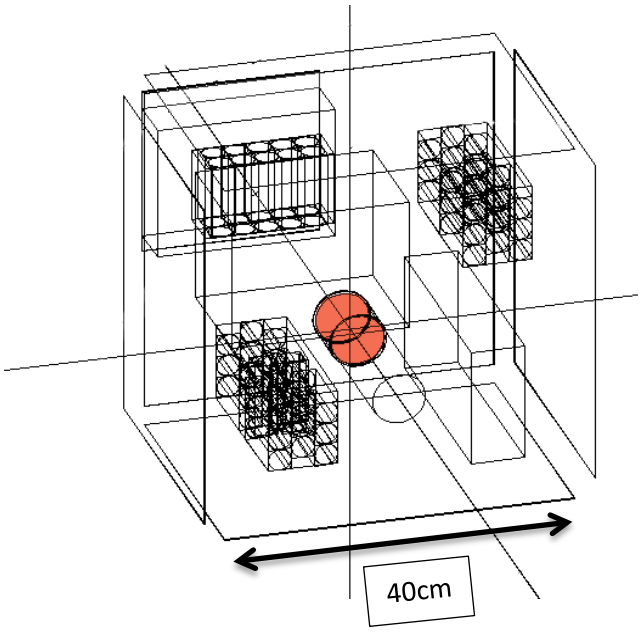

Figure 2.7. A view, through the bottom of the payload, of the materials and geometry used for the Monte Carlo model that relates input photons at the top of the atmosphere and converts them to counts in the detector. The NaI volume is shown in red. The batteries, electronics boxes , topplate and ground planes are also evident.

does indeed show up as excess counts at low energy without changing the shape at high energy substantially.

The generation of this response matrix is accomplished by using the GEANT 3 Monte Carlo code. GEANT(GEometry And Tracking) was developed principally at CERN as a particle tracking and material interaction code. It described in great detail by Apostolakis, [1993]. With the addition of a low energy compton scatter model developed at Los Alamos [Kippen, 2004], GEANT includes all relevant cross sections for modeling the MINIS response. To determine how an X-ray at 70 km transits to the payload at 32 km. A mass model with all relevant compositions and densities was created. In total the model has 79 components, mostly in the higher density materials immediately surrounding the detector.

The atmosphere is modeled as ten layers of exponential density, each 4 km thick above the payload and a dense layer below the payload to include photons that backscatter up to the balloon. The atmospheric density is based on the MSIS-E-90 Atmosphere Model for January at 70° South latitude [available from: http://ccmc.gsfc.nasa.gov/modelweb/]. A small adjustment

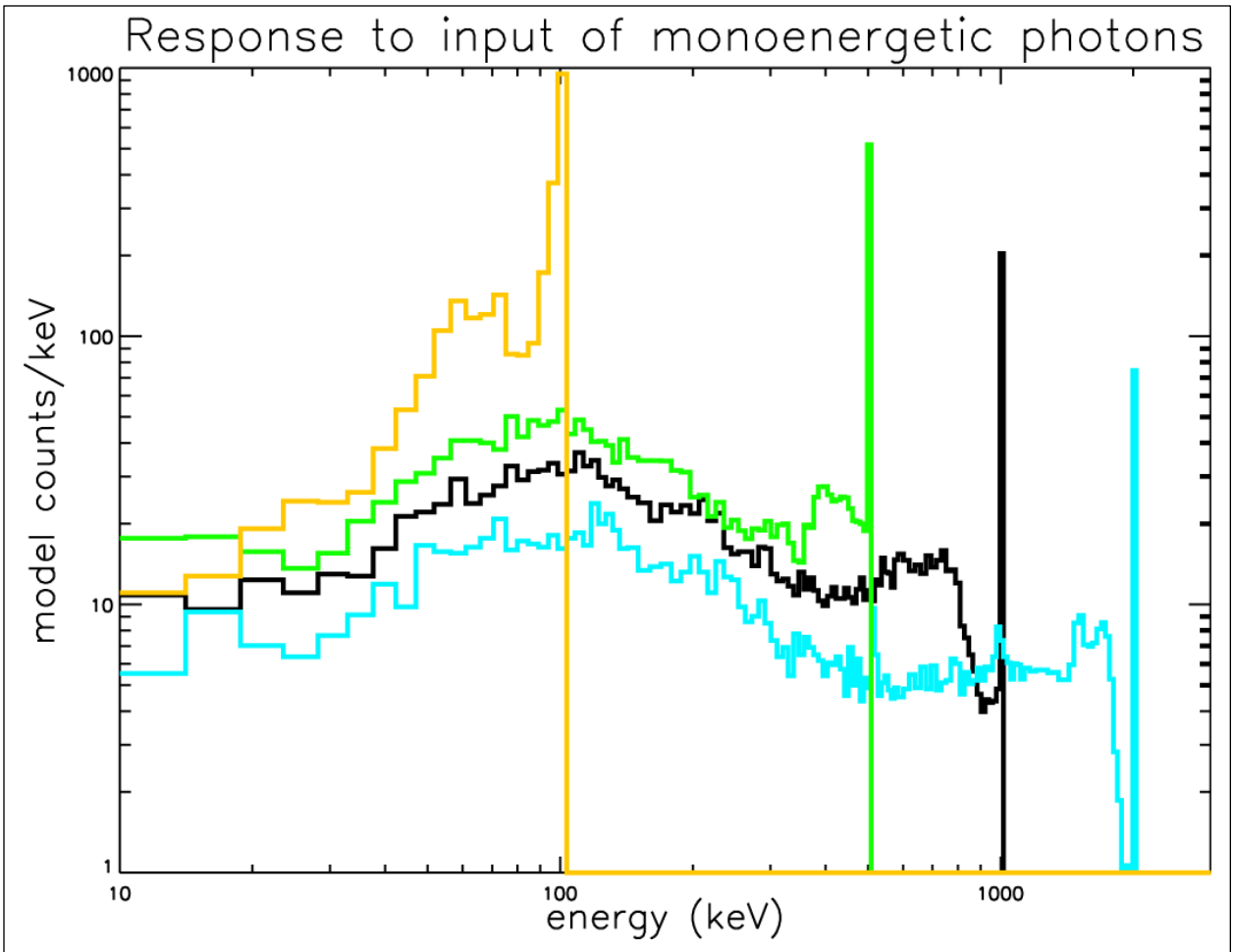

Figure 2.8: The spectrum as seen by MINIS for the input of monoenergetic **photons** at the top of the atmosphere. It is important to note that even a distribution of monoenergetic electrons do not create monoenergetic photons at the top of the atmosphere. Input energies of 100 keV, 500 keV, 1 MeV and 2 MeV are shown.

was made for the altitude difference between payload S2 and S3 by increasing the density and thickness of the bottom layer for S3 which was ~1km deeper in the atmosphere. A wire-frame representation of the payload mass model is shown here as Fig. 2.7 with the scintillator crystal (where energy deposits are ultimately recorded) highlighted in red.

Input X-rays are distributed uniformly across energy and isotropically over initial direction. For response matrices of different angular distribution, the photons were distributed isotropically between a minimum and maximum angle. For generating the response matrix, energies are evenly distributed between 1 keV and 10 MeV in 1 keV steps. When energy is deposited in the NaI crystal, we record the initial photon energy and the NaI deposited energy to generate a matrix relating, on average, a bremsstrahlung photon to a detector energy count. Figure 2.8 shows the systems response to mono-energetic photons at 70 km for 4 energies, 100keV, 500keV, 1MeV and 2MeV. Each input energy corresponds to a horizontal line in the overall response matrix. An example of the generated matrix where color scale refers to number of recorded counts at energy X per input photon at energy Y is shown in Figure 2.9. The response matrix is shown in channel space, as opposed to energy. A plot of the MINIS standard energy channels was shown earlier this chapter in Fig. 2.4. For instance, the vertical line that occurs in the response matrix around X=78 is a count of 511 keV recorded in the detector.

Because MINIS spectra were recorded out to 10 MeV we use a square matrix with 10 MeV as

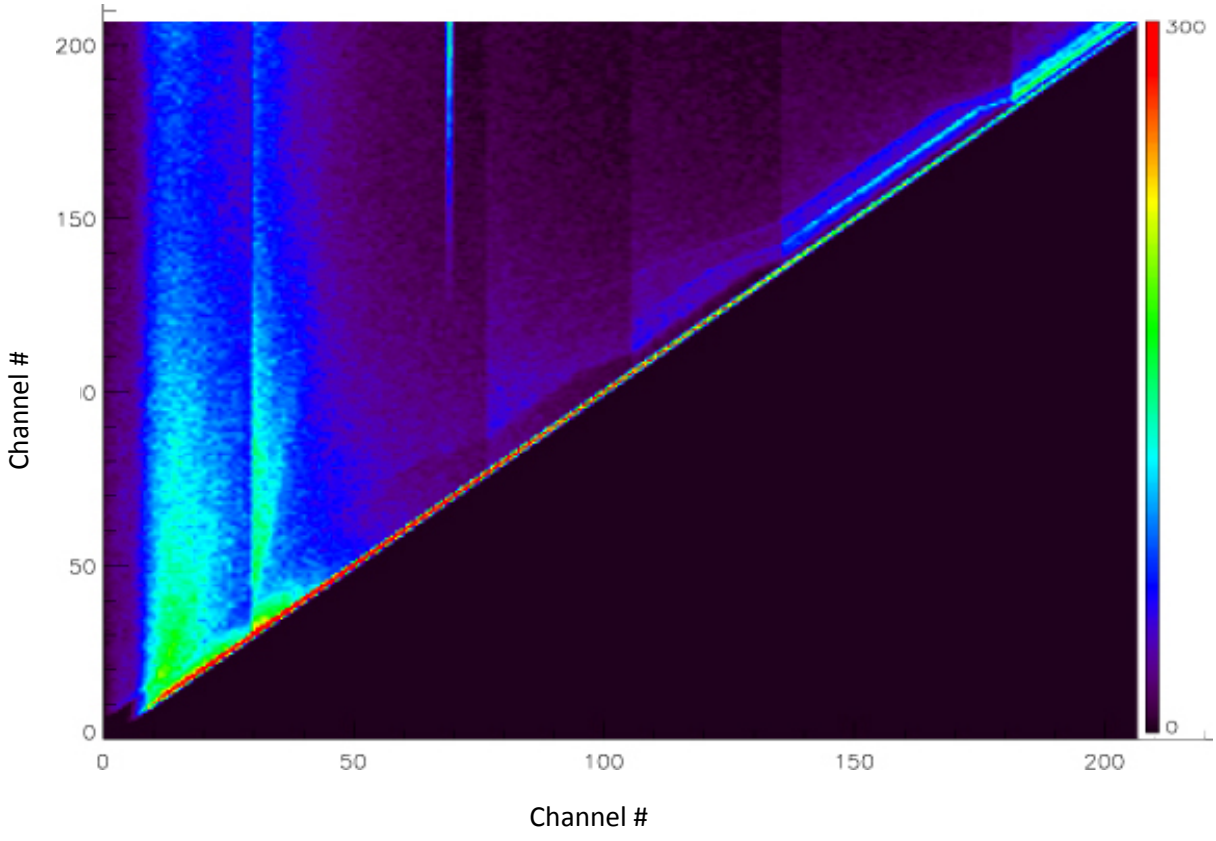

Figure 2.9: An example of a MINIS response matrix relating input photon energy(y) to measured count energy (x). The axes are marked in MINIS channel space as described in the previous chapter (pseudolog from 20 kev to 10 MeV).

the maximum energy. While photons of initial energy > 10MeV can still contribute to counts in the energy range of interest around 1 MeV and below, flux at these high energies is assumed to be too low for significant contribution and is disregarded. For this reason use of this response matrix should not be made for interpretation of the highest energy part of the MINIS spectrum, ~ several MeV.

2.5.5 Detector Sensitivity to precipitating electrons

Based on the MAXIS experience, typical distributions of precipitating electrons result in X-ray spectra with e-folding energies in the several hundreds of keV to ~MeV, consistent with the precipitation of monoenergetic electrons of several MeV. The relation between monoenergetic and exponential input electron distributions is discussed in more detail in chapter 4. The most important counts in contributing to accurate separation of possible spectral parameters are the highest energy counts above background. An example from Millan 2.10 shows the almost identical spectra that two candidate electron distributions would have created in the MAXIS detector, the distinguishing feature only occurs >1 MeV. We chose NaI for MINIS in part to increase the effective area (at comparable detector volume) for counts in this energy range. The same two model spectra as would be seen by MINIS are shown in Figure 2.11. Again the spectra still only begin to separate around 900 keV, but the exponential spectrum in particular has fallen by a relatively smaller amount from the peak. Increased statistics are often available in the data spectra as will be shown in the next chapter. Increased sensitivity at high energies also places limits on the previously discussed relativistic electron microbursts which have not been observed

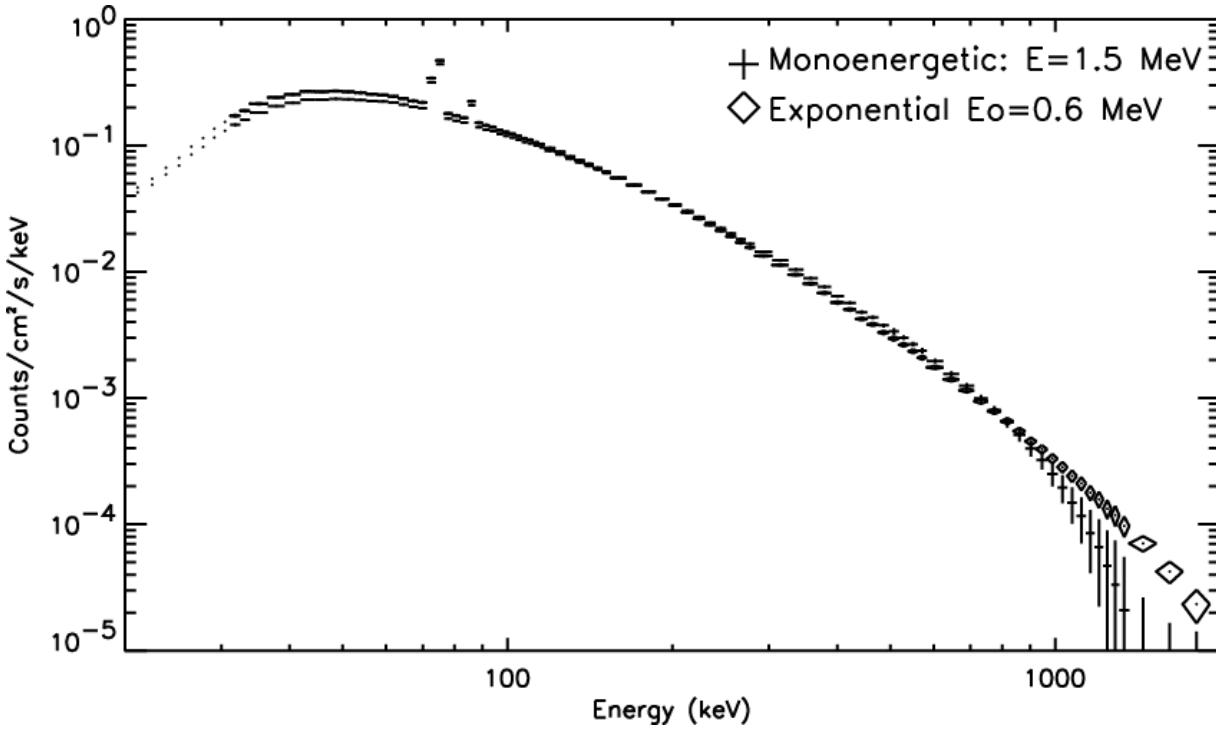

Figure 2.10: Distinguishing the spectral shape of two different input electrons spectra relies heavily on counts near the monoenergetic energy [or equivalently at several e-foldings). Thus sensitivity at >1 MeV is strongly desired for identifying spectral shape.

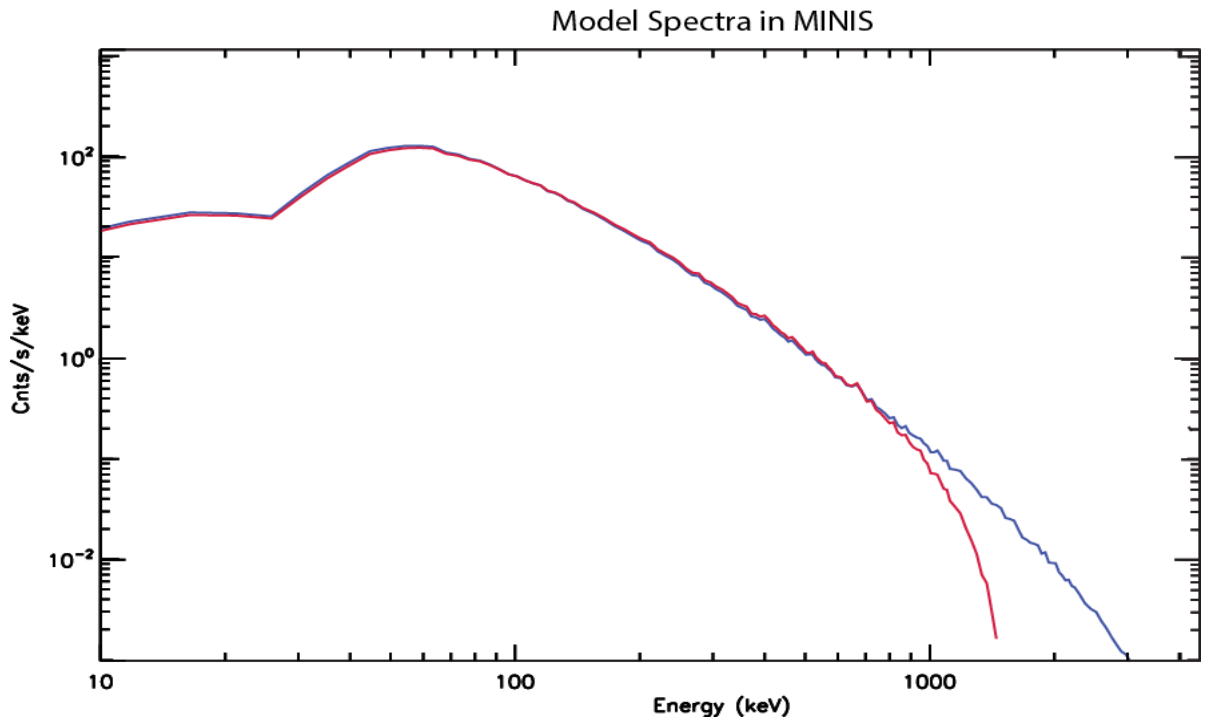

Figure 2.11: The same input electron spectra as shown in the previous figure but now as seen by MINIS NaI spectrometer.

by balloon payloads.

Although determination of electron spectra is primarily accomplished by forward fitting parameterized electron spectra through an atmosphere-instrument response matrix (generated by Monte-Carlo methods) described in the previous section, it is useful to have as a reference (and a relatively simple physical picture to check of the more complex method) a simple physics model for a sky filling precipitation (1D) as is likely for duskside relativistic electron precipitation [Foat, 1998], or for a quasi-point source of precipitation on the sky with r^2 attenuation (which may be comparable to a microburst) [Blake, 1996].

If we consider a monoenergetic beam of electrons with normalized energy T_0 where T_0=1 corresponds to electron of 511 keV kinetic energy, then the efficiency [energy in bremsstrahlung/energy in electron input] of bremsstrahlung production is given by Koch and Motz [1959]

$$\epsilon_\gamma = 5 \times 10^{-4} Z T_o$$

Where Z is the average atomic number of the bremsstrahlung producing target, in this case the atmosphere above the payload. Following a formula from Markowicz and Van Grieken [1984], a weighted Z for the region of interest is ~7.5 (close to nitrogen as expected). This efficiency allows us to relate the energy input at the top of the atmosphere to the energy that we see in the detector.

$$[Detected\ photon\ Energy] = \epsilon_\gamma * [Input\ Electron\ Energy]$$

$$\frac{\int E_\gamma J_\gamma(E)\, dE}{A\epsilon_d} = \epsilon_\gamma \int E_e J_e dE$$

Which for this discussion will be limited to monoenergetic input electrons, thus:

$$\frac{\int E_\gamma J_\gamma(E)\, dE}{A\epsilon_d} = \epsilon_\gamma E_e J_e$$

Where $A\epsilon_d$ are the detector area and efficiency, J_γ is recorded detector photon spectrum in cts/s/keV, E is energy in keV and the right hand side has electron equivalents with J already in /cm^2/s. As will repeatedly be seen throughout chapter 4, the detected photon spectrum from a monoenergetic input electron source falls off quickly for photons- just below the input electron energy. As an example, we can choose that energy as E_e for one of the MINIS spectra shown in figure 2.12 and calculate J_e assuming 100% detection efficiency, i.e. $A\epsilon_d$=A=45.6 cm^2. From the spectrum E_e~3.5MeV

$$\int_0^{E_e} E_\gamma J_\gamma(E) dE = 1.02 \times 10^6 \ \ (\frac{keV}{s})$$

$$\epsilon_\gamma = .025$$

$$E_e J_e = 8.7 \times 10^5 \ \ (\frac{keV}{cm^2 s})$$

$$J_e = 2.5 \times 10^2 \ \ \left(\frac{e^-}{cm^2 s}\right) (at\ 3500keV\ each)$$

If we then compare this result to the best-fit Monte Carlo result discussed later which found $J_e = 9.8 \times 10^2$ /cm^2/s. we conclude that ϵ_d~25%. This of course includes the inefficiencies of atmospheric absorption and backscatter as well as X-rays which do not leave their full energy in the NaI crystal. Koch and Motz [1959] note as well that their efficiency formula has been reported at up to 40% lower, which would imply ϵ_d~42%.

If we take the same input electrons and the 25% detector efficiency and put them into a small patch on the sky, as may be the case for relativistic microbursts [Blake, 1996], with 10 km diameter and concentrate it to a point source of downward isotropic electron precipitation directly over the payload then:

$$J_e = 7.6 \times 10^{14} \ \ (e^-\ at\ 3500keV/s)$$

$$E_e J_e = 2.7 \times 10^{18} \ \ (\ keV/s)$$

$$\epsilon_\gamma = .025$$

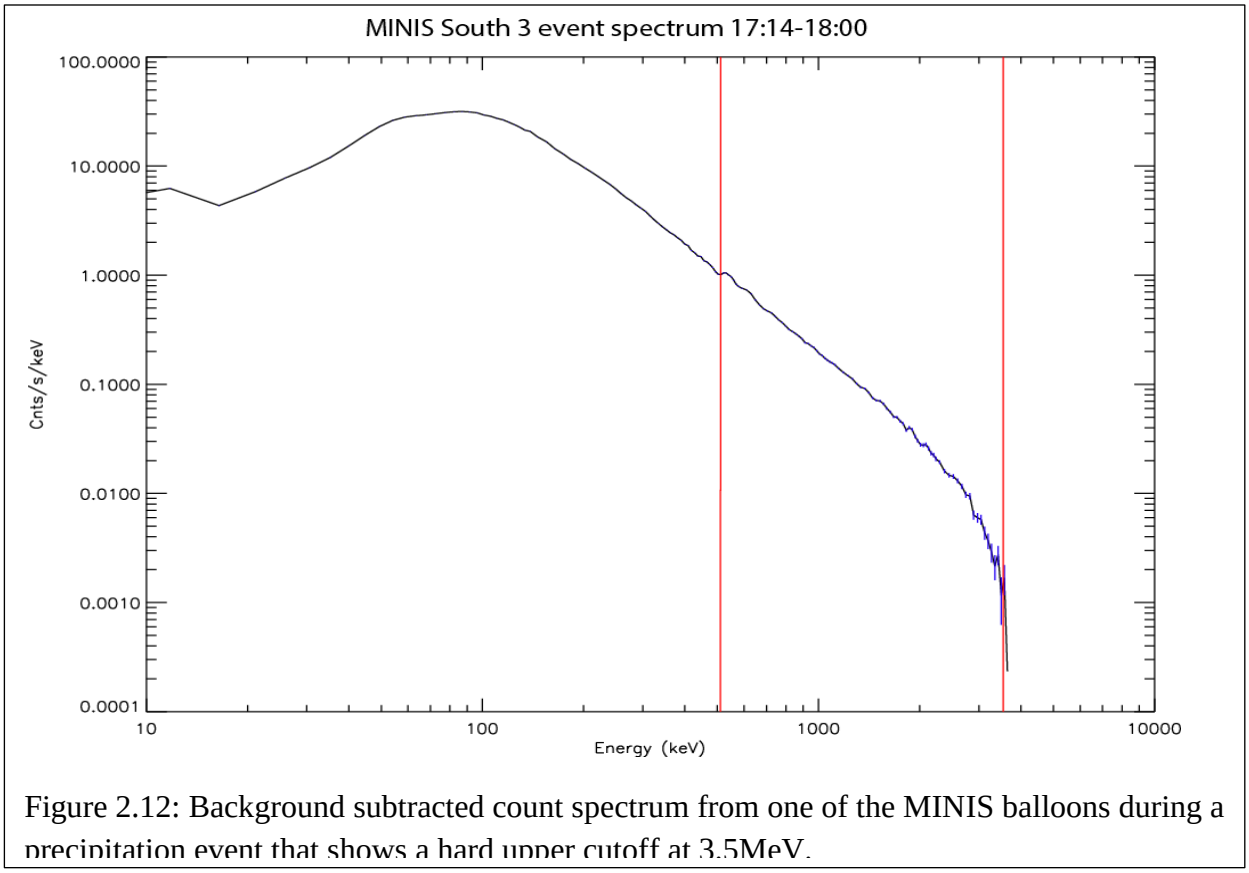

Figure 2.12: Background subtracted count spectrum from one of the MINIS balloons during a precipitation event that shows a hard upper cutoff at 3.5MeV.

$$\int_0^{E_e} E_\gamma J_\gamma(E)dE = \frac{A\epsilon_d}{2\pi r^2}\epsilon_\gamma E_e J_e = 1\times 10^4 \ \ (keV/s) seen\ in\ the\ detector$$

Which is simply the effect of the ratio of microburst area to area at the observation altitude ~35 km away. Thus MINIS and similar balloons are at least 2 orders less effective at seeing relativistic microbursts than they are at seeing sky filling precipitation. Still one can ask the question: If the above microburst were to last 1s, how would this show up in the MINIS 3rd energy channel? We have here used the same spectral shape for a microburst as we had for this much longer integrated event so that we could scale to the lightcurve channels. Making the channel are only 30 cts/s, so the microburst would not be visible in this channel. scaling shows a rate of 1.6 cts/s in the 540-820 keV lightcurve. Typical background rates in this

Chan	Energies (kev)	µBurst cts/s	background rate (cts/s)	Standard Deviation in bkgnd (cts/s)	SNR
1	0-175	37	450	25.7	1.44
2	175-540	14	200	14.5	.965
3	540-825	1.6	30	5.5	.29
4	825-1500	-	35	5.8	-

Table 2.3 Response in lightcurve channels for a microburst like structure. All cts/s are for 1 second bins.

Because the background is typically harder in spectrum than the bremsstrahlung spectrum, perhaps the lower channels are more effective at seeing microbursts? Indeed channel 2 from 175 keV to 540 keV shows ~14 cts/s on a background of 200, while channel 1 is 37 cts/s on a typical background of 450 cts/s. These results are summarized in Table 2.3.

While microbursts seen by SAMPEX are much softer than the above input spectrum, they are often much brighter. Published reports show >1MeV observations of J ~10^5 $e^-/cm^2/s$. If we assume that ϵ_d~25% is not significantly energy dependent (simulation comparison shows only 5% change) we can remake the above table for 1MeV electrons input at these higher flux rates. The bremsstrahlung efficiency will decrease to $\epsilon_\gamma = 0.007$. I will also scale off of a modeled spectrum of 1 MeV input electrons. We would then find:

$$\int_0^{E_e} E_\gamma J_\gamma(E) dE = \frac{A\epsilon_d}{2\pi r^2}\epsilon_\gamma E_e J_e = 8.3 \times 10^4 \ \ (keV/s) seen\ in\ the\ detector$$

Which is 8.3 times higher than the previous calculation, however, because the spectral shape has changed, the results aren't simply 8.3 times the previous. In particular, the lowest two energy channels show the burst clearly, but identifying the microburst as one containing MeV electrons, and not just a bright lower energy burst, would involve careful comparison of the ratio of counts in the first two channels. Another difficulty is that statistics are actually somewhat worse than those shown because a typical burst lasts for less than 1s. Further work on the spectral shape of SAMPEX [Comess, 2012] observed microbursts is being done and significant numbers of electrons <1 MeV are also being precipitated, with e-folding energies up to 300 keV. These lower energy electrons will also influence the ratio of counts in the first two energy channels and thus make microburst spectral determination increasingly difficult. The above assumption of 10 km diameter burst size, as well as the distance of the payload away from the burst will also strongly influence how MINIS-like payloads observe these phenomena.

Chan	Energies (kev)	uBurst cts/s	background rate (cts/s)	Standard Deviation in bkgnd (cts/s)	SNR
1	0-175	660	450	25.7	25.7
2	175-540	97	200	14.5	6.7
3	540-825	3.3	30	5.5	0.6
4	825-1500	-	35	5.8	-

Table 2.4 The channel response for MINIS to a modeled microburst at 1 MeV monoenergetic input electrons with intensity based on a review of peak SAMPEX fluxes.

.

3 MINIS Flight Summary

The MINIS balloon campaign consisted of four southern payloads launched from SANAE, Antarctica sequentially from Jan. 17-Jan. 24, 2005, and two northern payloads launched from Ft. Churchill, Canada on Jan. 21 and Jan. 24. Flight tracks for the four southern payloads (referred to as S1, S2… by launch order) are shown in Figure 3.3, and for the northern payloads (N1, N2) in Figure 3.1. A summary plot of the 6 payloads countrate in the low energy X-ray lightcurve (120 keV-260 keV) is shown here in Figure 3.4.

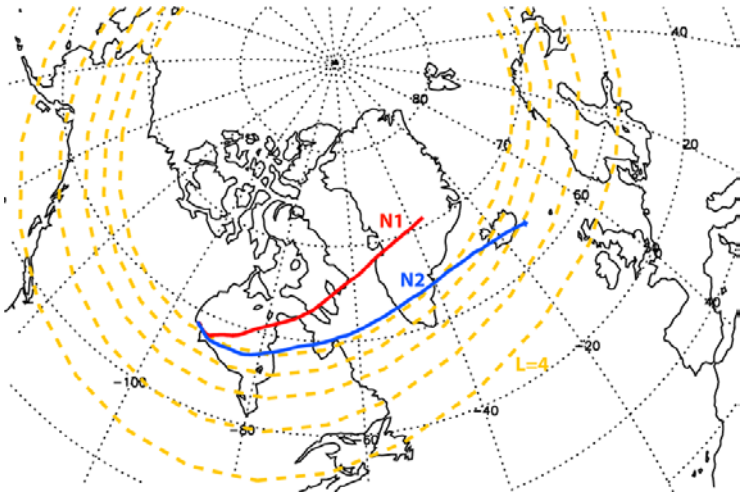

Figure 3.1: Map of the N1 and N2 payload trajectories after launch from Ft. Churchill, Canada. Dashed lines indicate IGRF L-shells: L=4,5,…8 (4 is the lowest latitude pictured)

Figure 3.2 One of the MINIS balloons being hand-launched from SANAE, Antarctica

Truly conjugate ($\Delta L < 0.5$) observations were never made because the northern payloads drifted to significantly higher L-shells than the southern payloads. However, observations in both hemispheres were available on Jan. 21 during the Storm Sudden Commencement (SSC) phase of a moderate geomagnetic storm and high energy electron precipitation was observed in both the north and the two southern payloads. This would indicate either a very large range in L shells showing precipitation (3.5 to 10 IGRF as evident on the included map) or the two areas of precipitation may be unrelated. Figure 3.4 shows time ranges when multipoint observations of precipitation were possible. In total MINIS returned observations from ~550 hours of flight with a data throughput of ~350 hours.

The payload tracks for each of the

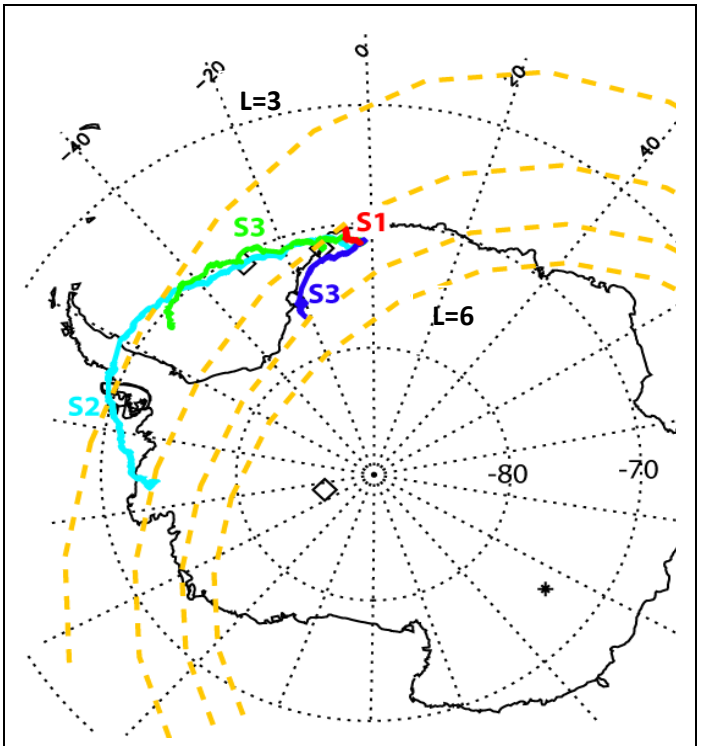

Figure: 3.3: The 4 southern MINIS flights launched from SANAE, Antarctica.

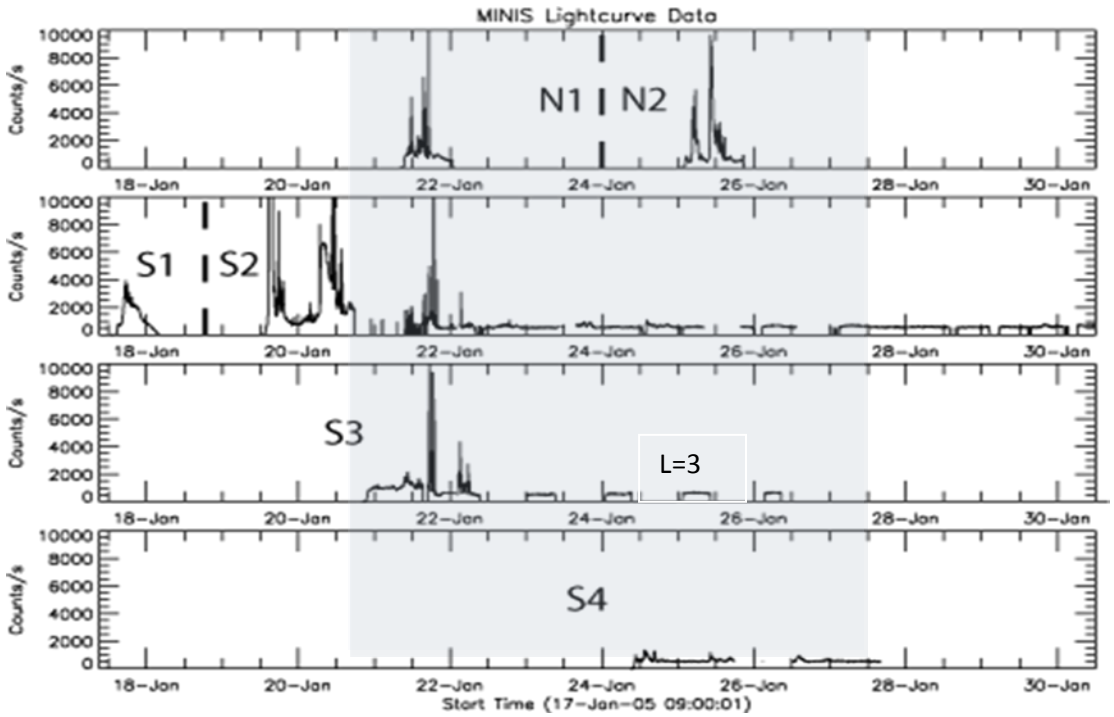

Figure 3.4: The 120keV-260keV channel for all six MINIS payloads. The format is the same as Figure 3.5 The focus is on the time on January 21 when N1, S2 and S3 were all recording precipitation.

MINIS payloads in L-shell are shown in Figure 3.5. The multiple color traces indicate choice of magnetic field model used to determine the geomagnetic coordinate from the payload position (from the payload GPS). The highlighted area is the time frame of interest associated with a magnetic storm described in the next section. The choice of magnetic field model makes some difference in assigning L-shell to a payload, but for the southern payloads at relatively low latitudes, the difference is minor ($\Delta L=0.3$), while for the N1 payload the difference is very large, and is not even defined for the realistic magnetic field models that incorporate solar wind, and ground based magnetometer data [e.g. Tsyganenko, 2004]. Even these more realistic field models are probably in gross error at some times due to the extreme nature of the geomagnetic compressions that occurred during this campaign. Similar events and related errors in L-shell mapping are described in more detail in Reeves [1996].

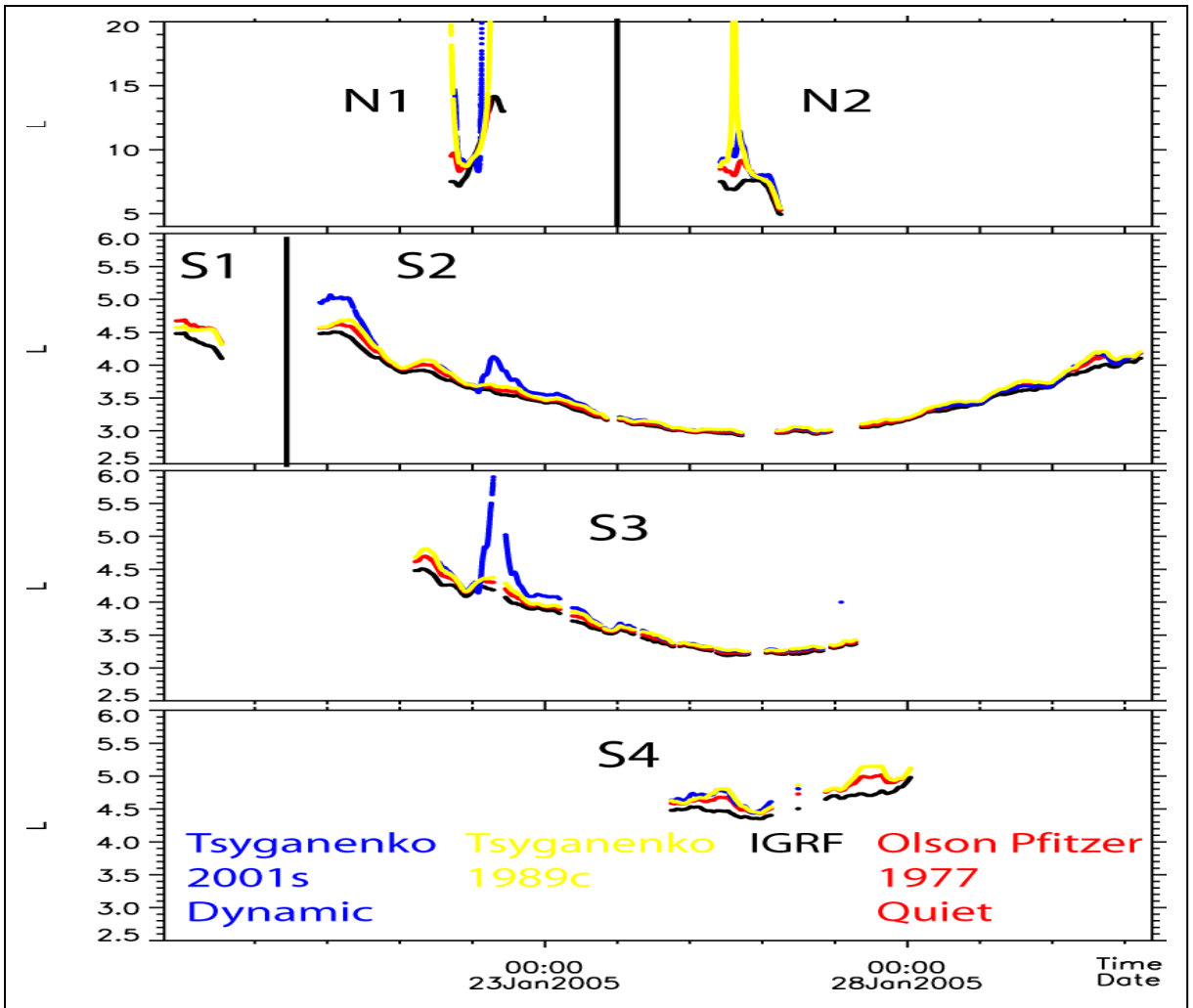

Figure 3.5: Shows the position in L-shell of the MINIS payloads in 4 different magnetic field models. N1 and N2 as well as S1 and S2 are combined into the top two panels to save space as they did not overlap. The models disagree most substantially (and are also probably most incorrect) during the SSC and main phase of the geomagnetic storm on Jan. 21st.

3.2 Geomagnetic activity

The MINIS campaign encompassed a remarkable period in geomagnetic activity, so much so, as we will see, that some data are difficult to place in a larger context. Almost immediately after launch of the second southern payload (S2), a large solar flare occurred (X7.1 in the GOES classification system) the MINIS observed spectrum is shown in Fig. 3.6 an associated Coronal Mass Ejection (CME) streamed towards the magnetosphere and Solar Energetic Particles (SEPs) soon began hitting the top of the atmosphere. The impact of the SEPs on the MINIS S2 payload were dramatic, causing bitflips from penetrating particles, rolling over light curve counters, and eventually resetting the flight computer. Following this event spectral performance was degraded, probably due to a stuck bit in the interface between the flight computer and the pulse height analyzer in the detector electronics. The SEPs also generated atmospheric spallation lines that were detected by the MINIS spectrometers. A spectrum of lines as observed by MINIS S1 is included here in Fig. 3.7. The highlighted lines are at features previously identified by other works on SEP generated atmospheric lines [Share, 2002]. They are from left to right; 511, 735, 1630, 2313, 2780, 3378, 3911, and 4422 keV, but additional features are present at higher energies which have not been identified.

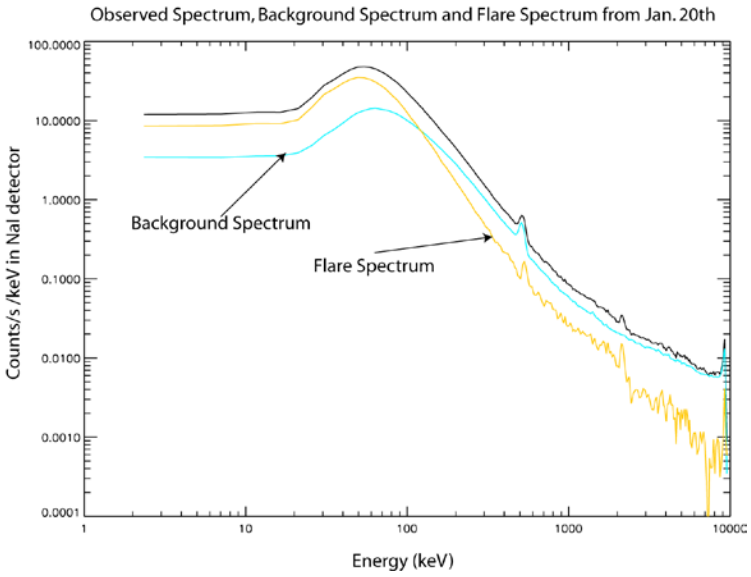

Figure 3.6: MINIS-S2 observed the X7.1 flare on January 20th. This data was taken before the associated SEP degraded the S2 energy response

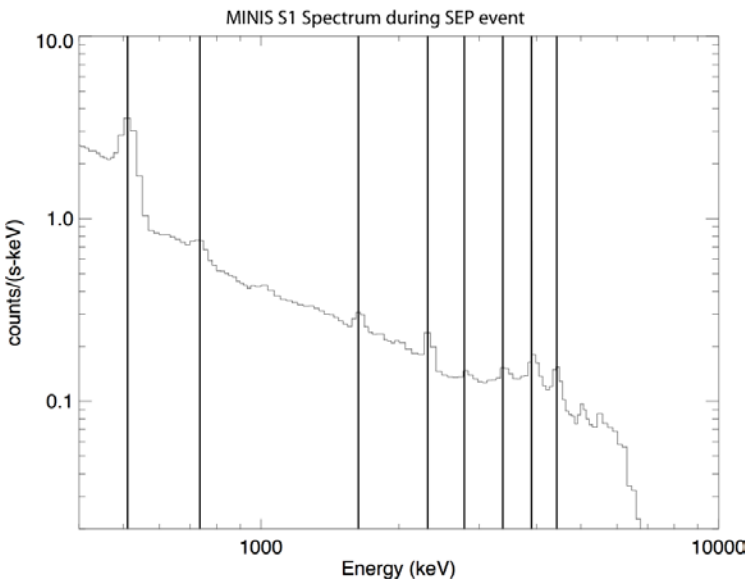

Figure 3.7. In addition to showing MINIS observations of the SEP generated spectral lines, the above plot shows typical resolution around the 511 keV line (far left).

The CME associated with the X7.1 flare impacted the bowshock approximately two days later. Many of these remarkable events are captured in

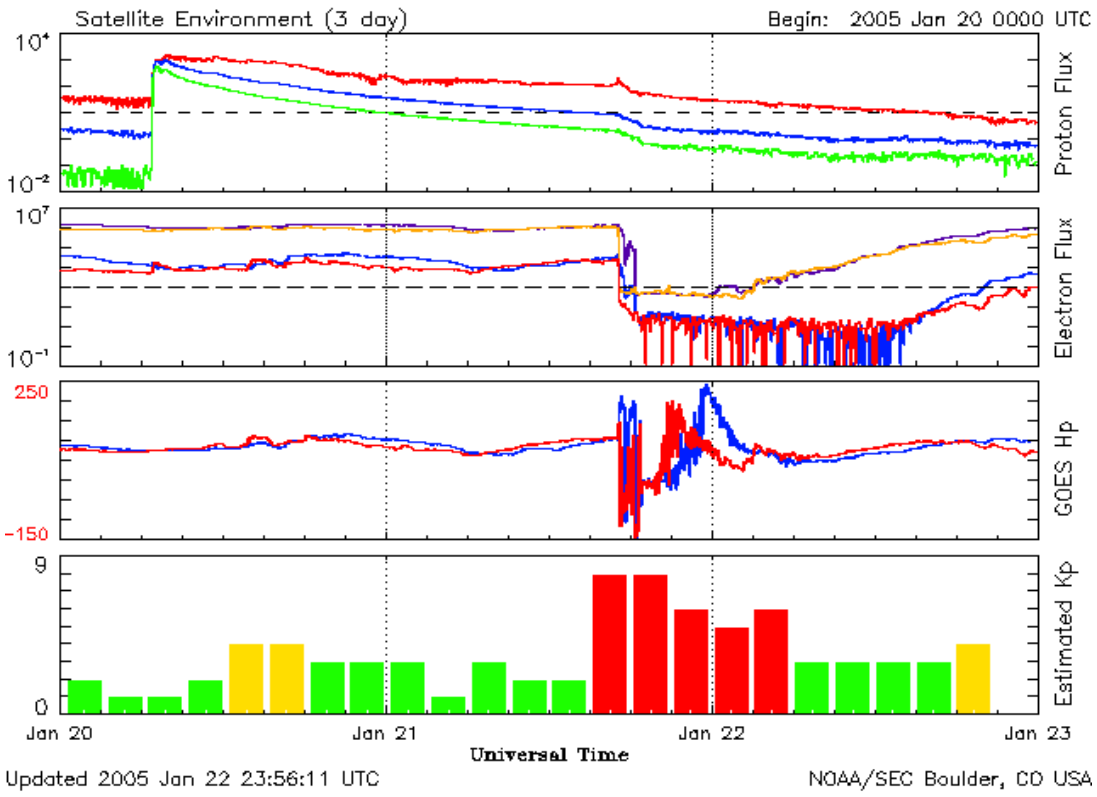

Figure 3.8: The 3-day Satellite Environment Monitor plot from http://www.swpc.noaa.gov/ftpmenu/ warehouse/2005/2005_plots.html captures the decay of the SEP event on the 20th [top], the dropout of electron flux at GOES and transition to measuring magnetosheath magnetic fields as the magnetosphere is compressed by the shock [middle pair], and the geomagnetic disturbance as captured by the Kp index.

the 3-day Space Environment Monitor product from NOAA Fig. 3.8. Data from the ACE spacecraft showing the velocity and density profile of the shock upstream of the magnetosphere is presented in Figure 3.9 for the month of January, and Figure 3.10 for the immediate time range around shock arrival. The shock arrival on January 21 initiated a moderate (-99 Dst) geomagnetic storm, which included a strong +16 DsT storm sudden commencement (SSC) pulse associated with magnetospheric compression by the increased solar wind dynamic pressure. The solar wind velocity and density are combined to arrive at the solar wind dynamic pressure using:

$$P_{dyn} = (1.6726 \cdot 10^{-6}) \cdot n \cdot v_{sw}^2$$

Where n is the proton number density per cm^3, and v_{sw} is the GSE-X component of the solar wind velocity in km/s, P_{dyn} is in nPa. P_{dyn} is shown in the bottom panels of Fig. [ACElong] and [ACEsh], which shows two clear impulsive events at 17:12UT and 18:45 (the data has been time shifted based on the measured solar wind velocity and its expected arrival time at earth). On each plot with the time range of 16:00-20:00 on Jan. 21st the two vertical red lines indicate the time of significant compression of the magnetosphere as measured by ground based magnetometers.

The dynamic pressure is the key factor in determining the bow shock nose location and the magnetopause standoff distance. Figure 3.11 shows a modeled picture [Shue, 1998] of the equatorial latitude magnetopause at several points in this time range. The GOES satellites are shown at their 17:10 position. MINIS payloads are pictured at the equatorial L-shell their position maps to at 17:10

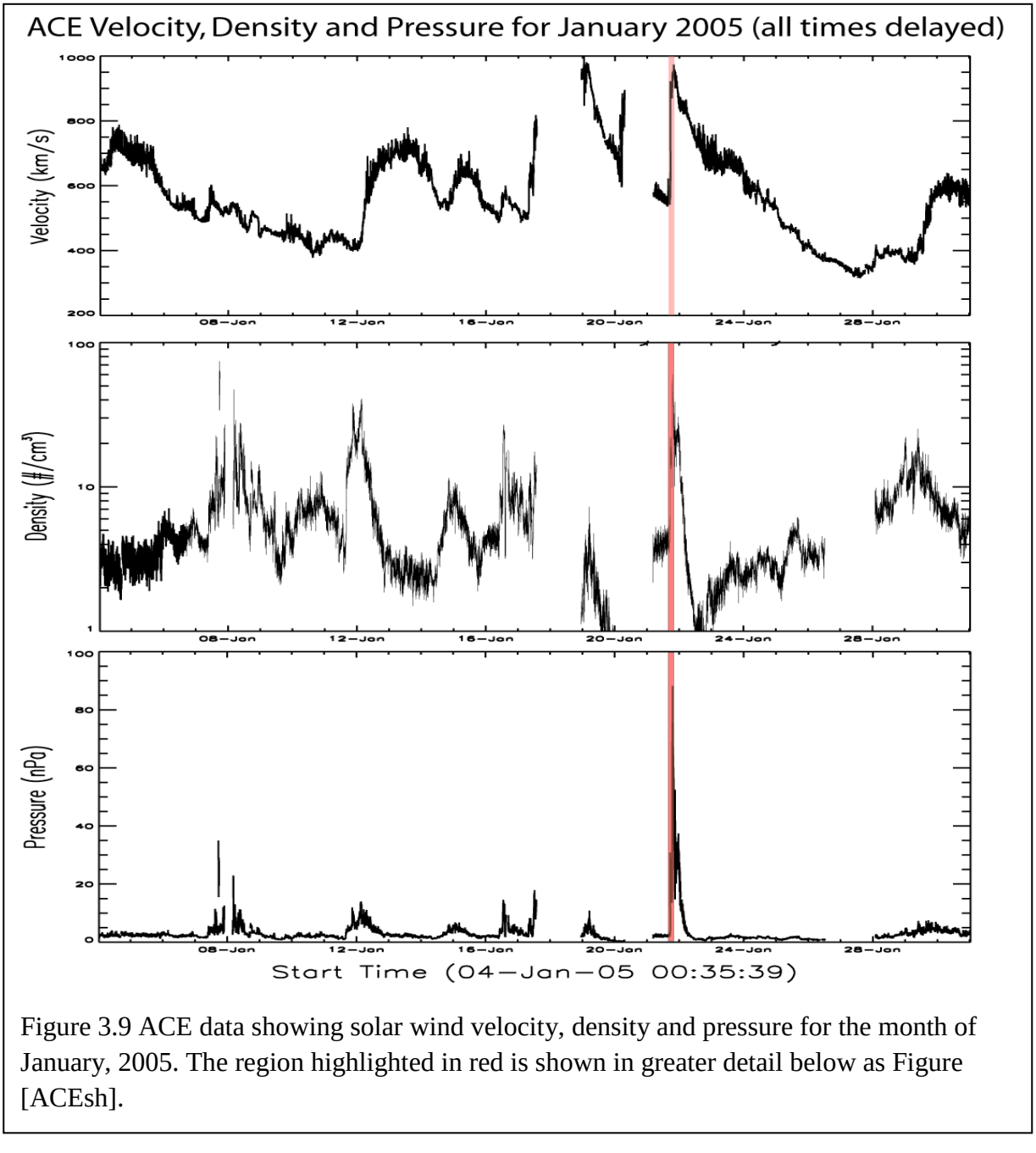

Figure 3.9 ACE data showing solar wind velocity, density and pressure for the month of January, 2005. The region highlighted in red is shown in greater detail below as Figure [ACEsh].

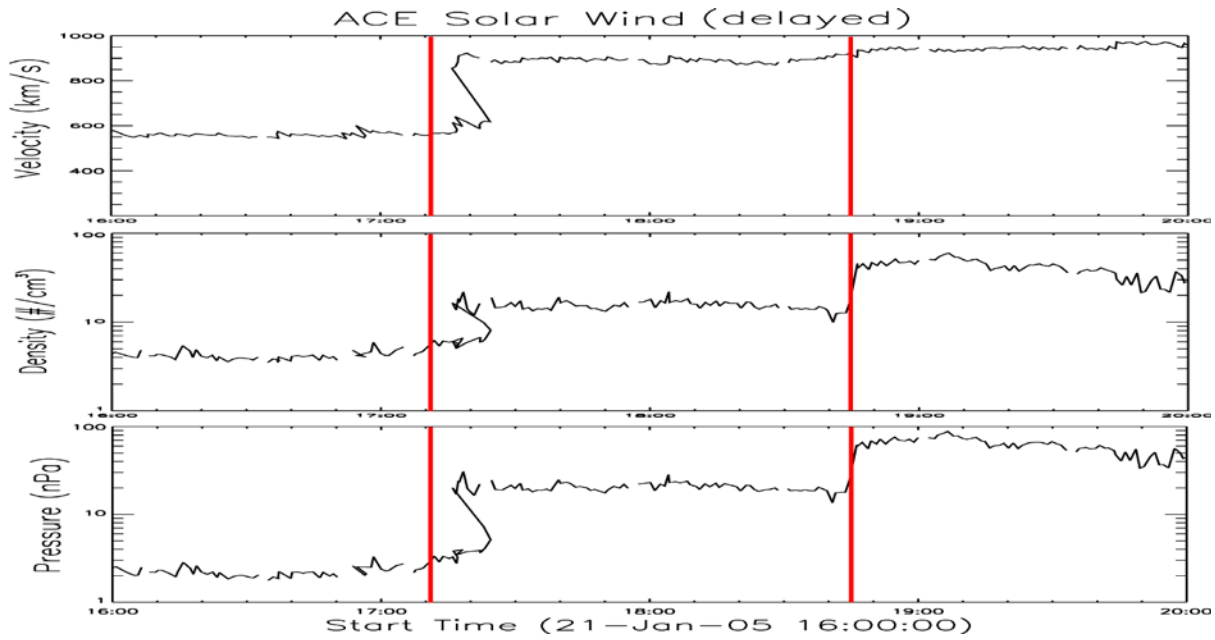

Figure 3.10. A close up of solar wind parameters during the time range on Jan. 21, 2005 when substantial magnetospheric compression occurred. Times in this plot are delayed to X=0 (Earth Center) by the measured velocity, which accounts for the multivalued functions at the initial jump in velocity.

The ACE spacecraft is located upstream of the magnetosphere by ~1.5 million km, so the data for the shock is delayed to Earth's position by using the measured velocity. This accounts for the non-physical jump at the start of the first shock. The higher speed solar wind has overtaken the previously measured slower moving solar wind. This interpenetration is clearly unphysical. No similar difficulty is encountered by propagating the second shock to Earth, as this shock is caused only by a sharp increase in the density of the solar wind.

There is some debate over what actually happens in the piling up of shock fronts as they approach the magnetosphere. By comparing multiple spacecraft making plasma measurements in the solar wind, Weimer et al. [2003, revised], has

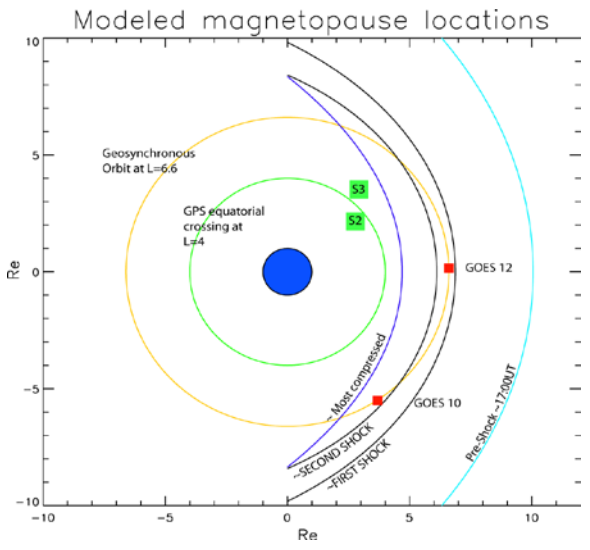

Figure 3.11: Showing the range of possible magnetopause locations following the shock arrival on Jan. 21st. The "most compressed" magnetopause is taken at the time of southward magnetic field following the second shock.

developed a method of delaying shock fronts to a modeled bow shock location. The bow shock location is given by Farris and Russel [1994], and using the magnetic field data found in Fig. 3.12 for the time range in question, the BSN is plotted in Figure 3.13.

Even in this more rigorous method, it is unclear what happens to the actual profile of the shock. One solution is to average over all points of the solar wind that will reach the bow shock in a given minute. This is the method of the Omniweb data archive maintained at http://omniweb.gsfc.nasa.gov/ which gives the results shown here. This method gives a more accurate agreement with the onset timing of precipitation seen by MINIS and the sym-H index. However, the actual value of the pressure and magnetic field to use for input into magnetopause standoff locations is still unclear. For this reason I have shown the limits of the magnetopause compression at each time range. GOES magnetometer data shows a patchy magnetopause that is in rough agreement with the depicted traces.

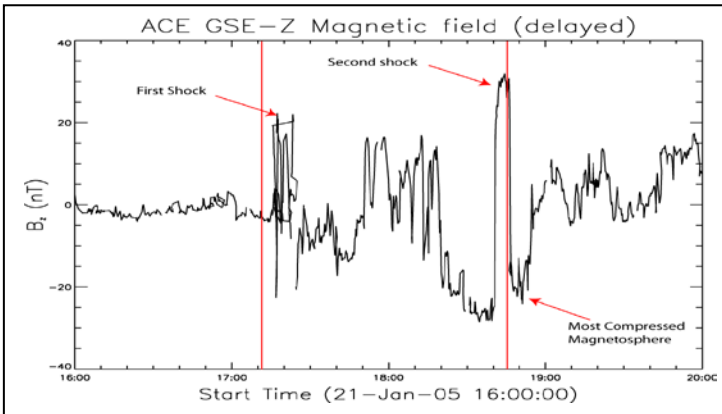

Figure 3.12 Showing the choice of solar wind magnetic fields used in determining the magnetopause location.

Notice that the second shock manages to compress the magnetosphere to the point where geosynchronous orbit is outside the magnetopause. This severe compression explains the dropout seen in energetic electrons by the GOES spacecraft during this timeframe. Plots of GOES > 2 MeV electrons for both GOES-10 and 12 are included here in Figure 3.14. The slower decay of electrons at GOES-10 is consistent with its location (initially) further inside the magnetosphere. The GOES positions at the two times are indicated in the magnetopause model. The highly compressed nature of the magnetosphere implies that magnetic field models

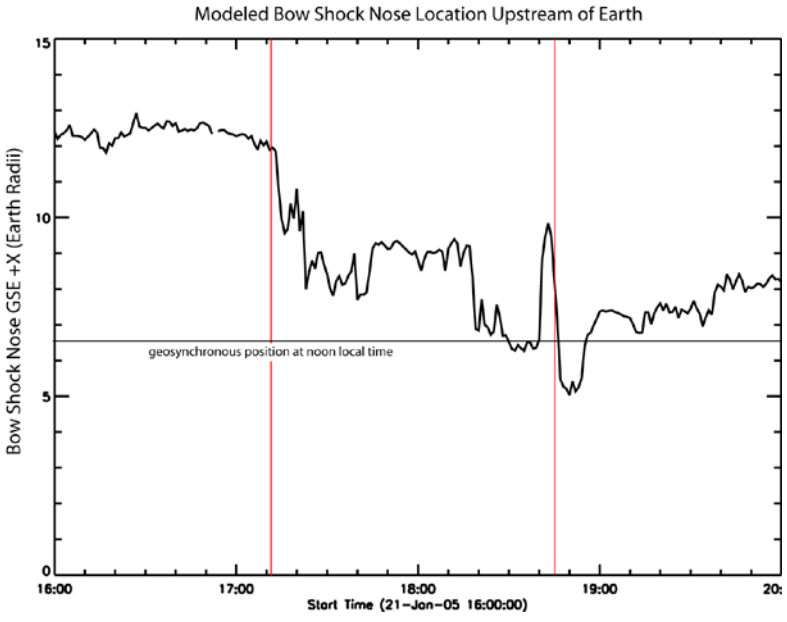

Figure 3.13: The location of a model bow shock upstream of the Earth. Geosynchronous altitude is shown for reference, a GEO satellite will only be at this +X position at noon local time.

will have their greatest inaccuracies at this time [Reeves et al, 1996], and that the northern MINIS payload is likely on a field line that is or rapidly becomes connected to the IMF through the magnetopause.

Another way to look at the compression pulse and how it affects the organization of the radiation belts is through the use of ground based magnetometers. The Dst index was described earlier in chapter 1, and is plotted here as Figure 3.16 for the magnetic storm in question. For increased time resolution we will also use Sym-H. Sym-H is a measure of the horizontal (thus H) equatorial magnetic field. The Sym refers to the separation of the variation in the field measured at various longitudes into a symmetric and anti-symmetric (usually a day-night) component. Sym-H is calculated at a higher time resolution (1 min) than Dst (1 hour), and thus it can capture some of the dynamics of the magnetospheric compression caused by these two shocks. Panel 4 of Figure 3.19 shows the Sym-H index for the time range 17:00 to 20:00 UT on Jan. 21, and it is plotted in more detail in Figure 3.17. The two impulsive events are clearly visible as sharp rises in the index at 17:12 and 18:45. The jumps take < 1 min to occur, indicating a change which is clearly in violation of the third adiabatic invariant for

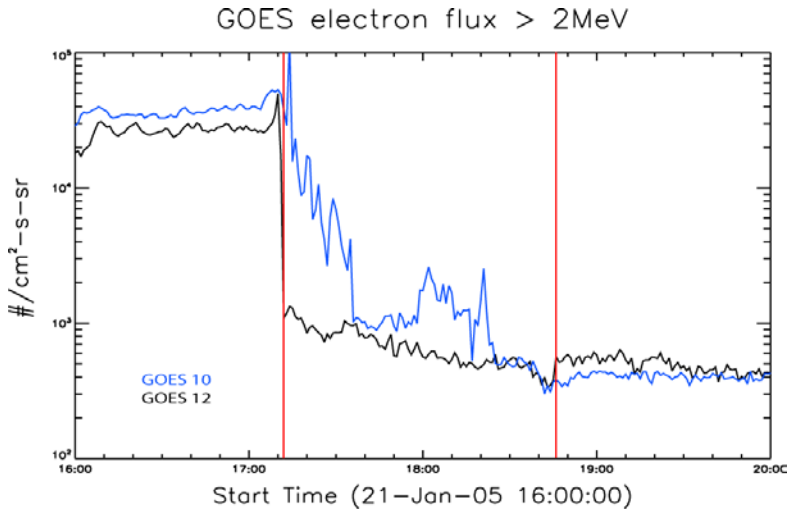

Figure 3.14 The GOES >2MeV electron instruments showing the rapid dropout of measured flux as the magnetopause is compressed. This is not evidence of actual losses occurring.

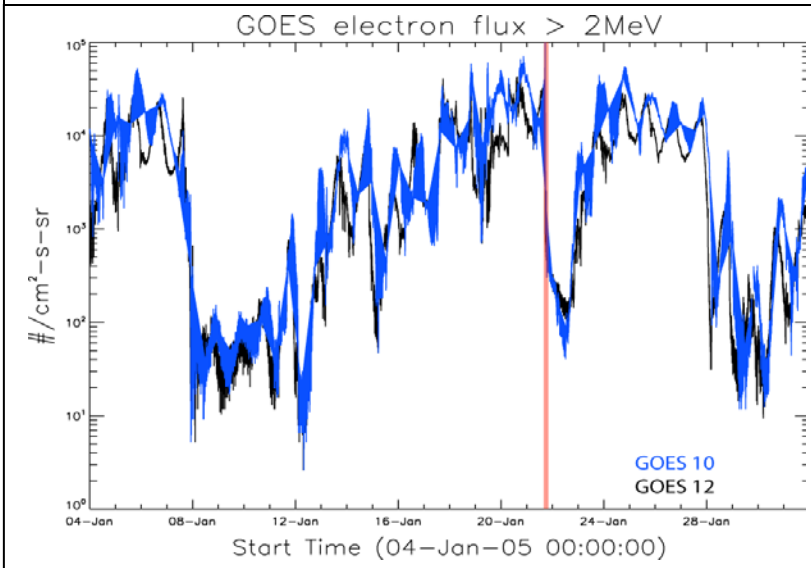

Figure 3.15: The GOES spacecraft at geosynchronous altitude measures >2MeV electrons during January 2005. The time of MINIS observed precipitation is highlighted in red. Much of the initial dropout is more a result of the spacecraft moving outside the magnetopause, and electrons moving inward radially for a short period of time (adiabatically) than by real losses. This is evidenced by the rapid recovery of flux as the magnetic field recovers. This is in contrast to the flux dropout that occurred around Jan. 7th. Where flux remains low even after the magnetic field is restored.

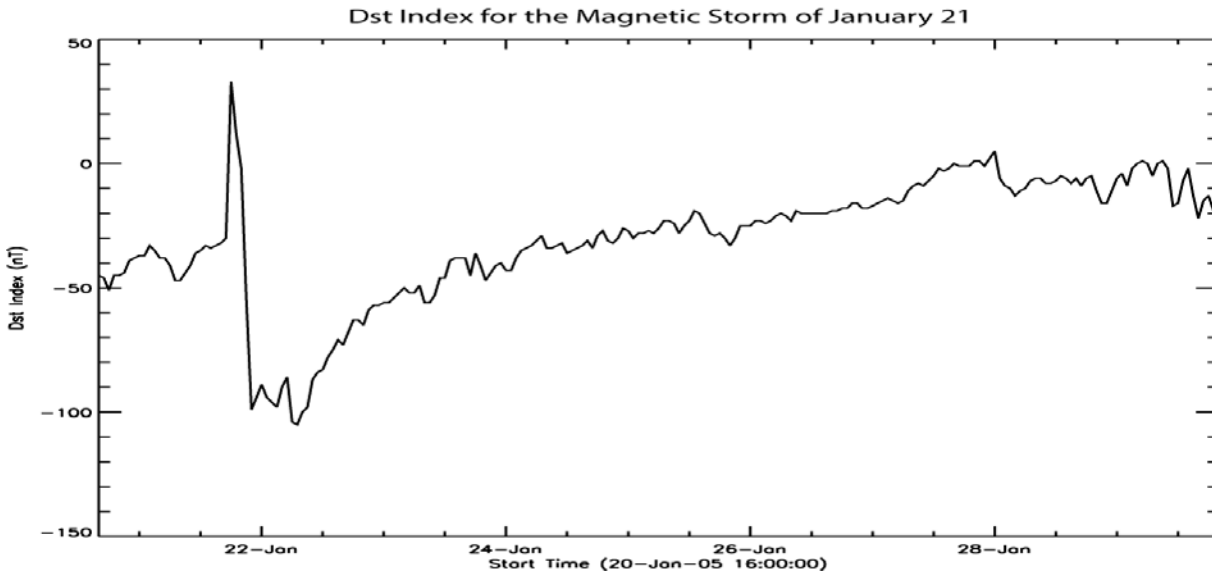

Figure 3.16: The magnetic storm of January 21st 2005 began with a very large SSC but was a relatively modest storm, with Dst decreasing only ~50nT below pre-storm levels Dst is an hourly index.

electrons of ~1 MeV which have drift times on the order of 10 minutes at L shells comparable to the MINIS balloons and these geosynchronous satellites.

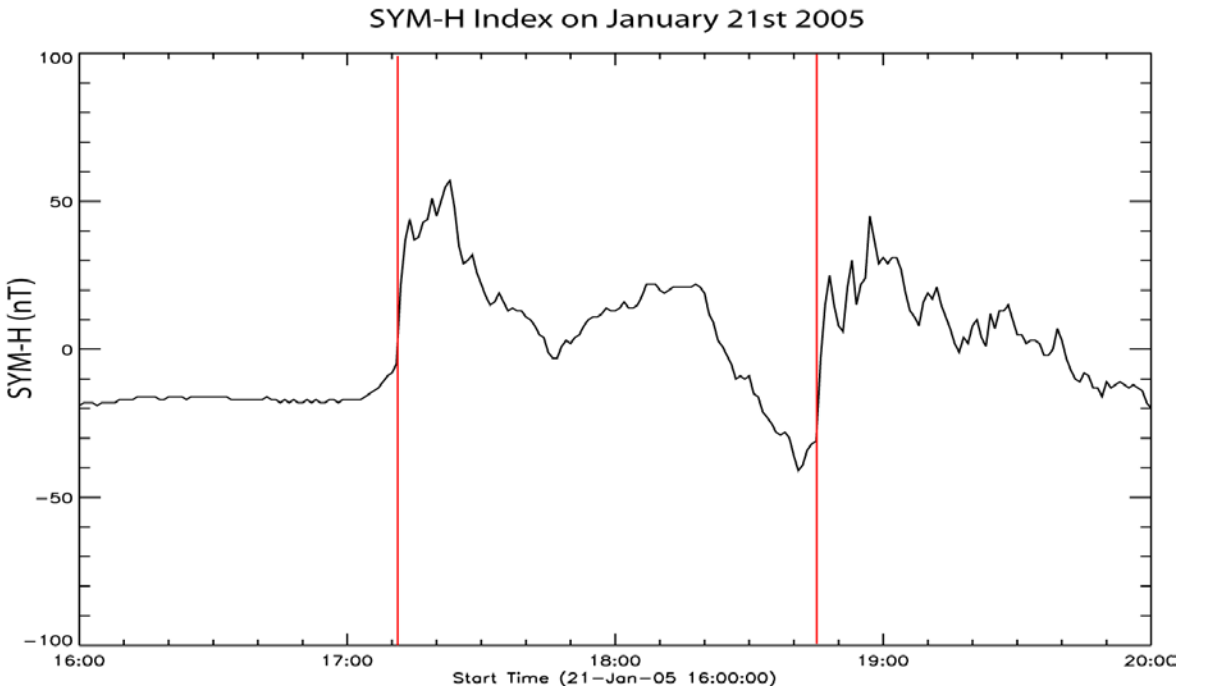

Figure 3.17: A more detailed look at the sym-H index during the Storm Sudden Commencement. .

3.3 The Trapping Boundary

The trapping boundary has been defined in several different ways, but the two most common involve using spacecraft which cut across L-shells and using magnetic field models to calculate drift shells. The latter technique will not produce useful results for this data set because the time period is defined by such large shocks that even the dynamic field models fail to capture changes in the radiation belt structure and because that definition favors equatorially mirroring particles with larger gyroradii, while this data set deals more directly with the nearly field aligned population. If we choose to define the trapping boundary as the point where GPS measured electron flux drops by 100x from its peak the result ends up looking like Figure 3.18. This definition is similar to the definition used by Millan who found that those precipitation events referred to as 'MeV events' occurred on the duskside near the trapping boundary when that trapping boundary was moving towards lower L-shells.

Although the trapping boundary defined this way may be more relevant to the MINIS observations, the inward motion of the trapping boundary which appears so dramatic in the

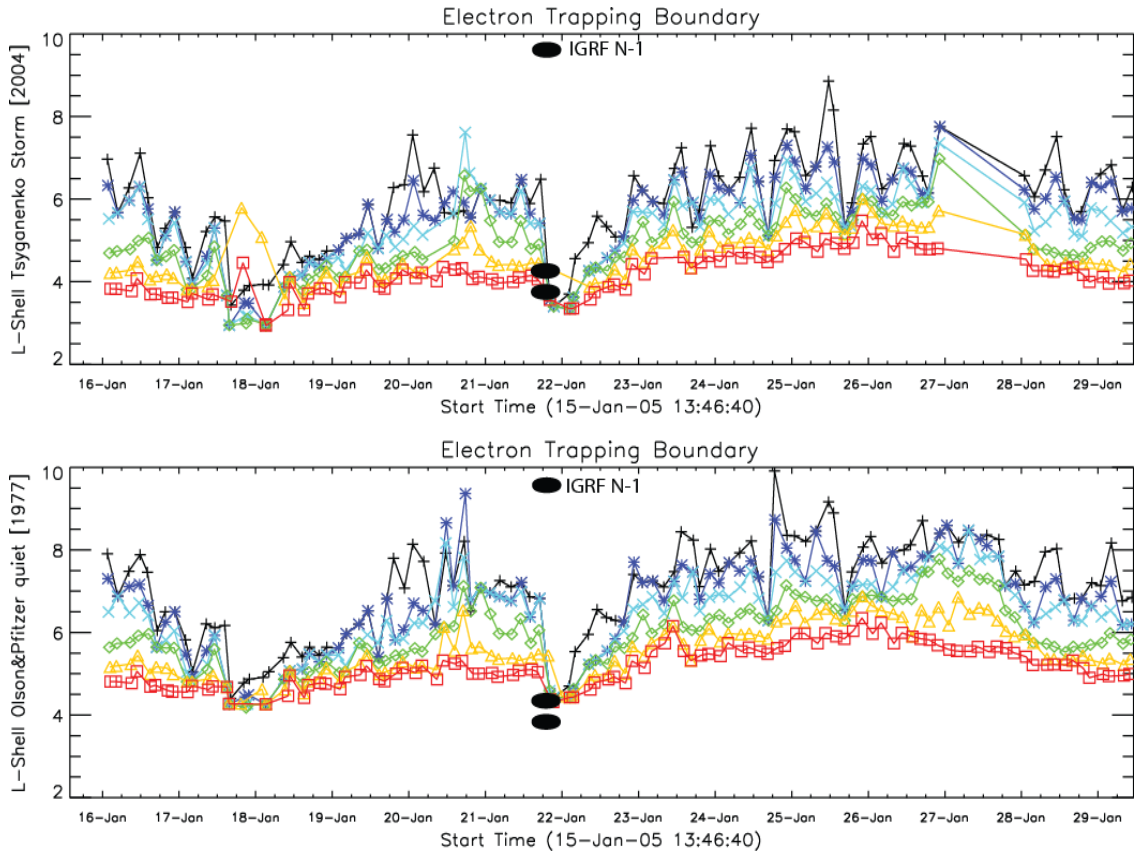

Figure 3.18: The electron trapping boundary at 6 different energies and using two different magnetic field models to determine L-shell. The black dots indicate the approximate locations of the MINIS payloads at the time. The time resolution of GPS satellites at L=4 is not sufficient to catch the SSC. The topmost curve starts at 100keV, edges following that are 190, 350, 650, 1220,2290, and greater than 4280 keV.

Figure is largely an adiabatic effect. GPS orbits cross L-shells approximately every three hours, so the SSC time frame where MINIS observations occur gets missed, and L=4 is not measured at the same time as e.g. L=6.

3.4 X-ray and Field Data

A summary plot of the low energy (< 180 keV) countrate of all 6 MINIS payloads is included earlier in figure 3.4. Besides the activity on January 21st associated with the storm sudden commencement, the MINIS payloads did not see significant high energy precipitation, but some additional low energy precipitation is evident. The focus of this effort will lie in the time range shown in Figure 3.19, which occurs during the SSC. This figure shows all four energy channels recorded by three of the MINIS payloads as well as Sym-H during this time range. The SSC begins with the first sharp rise in Sym-H.

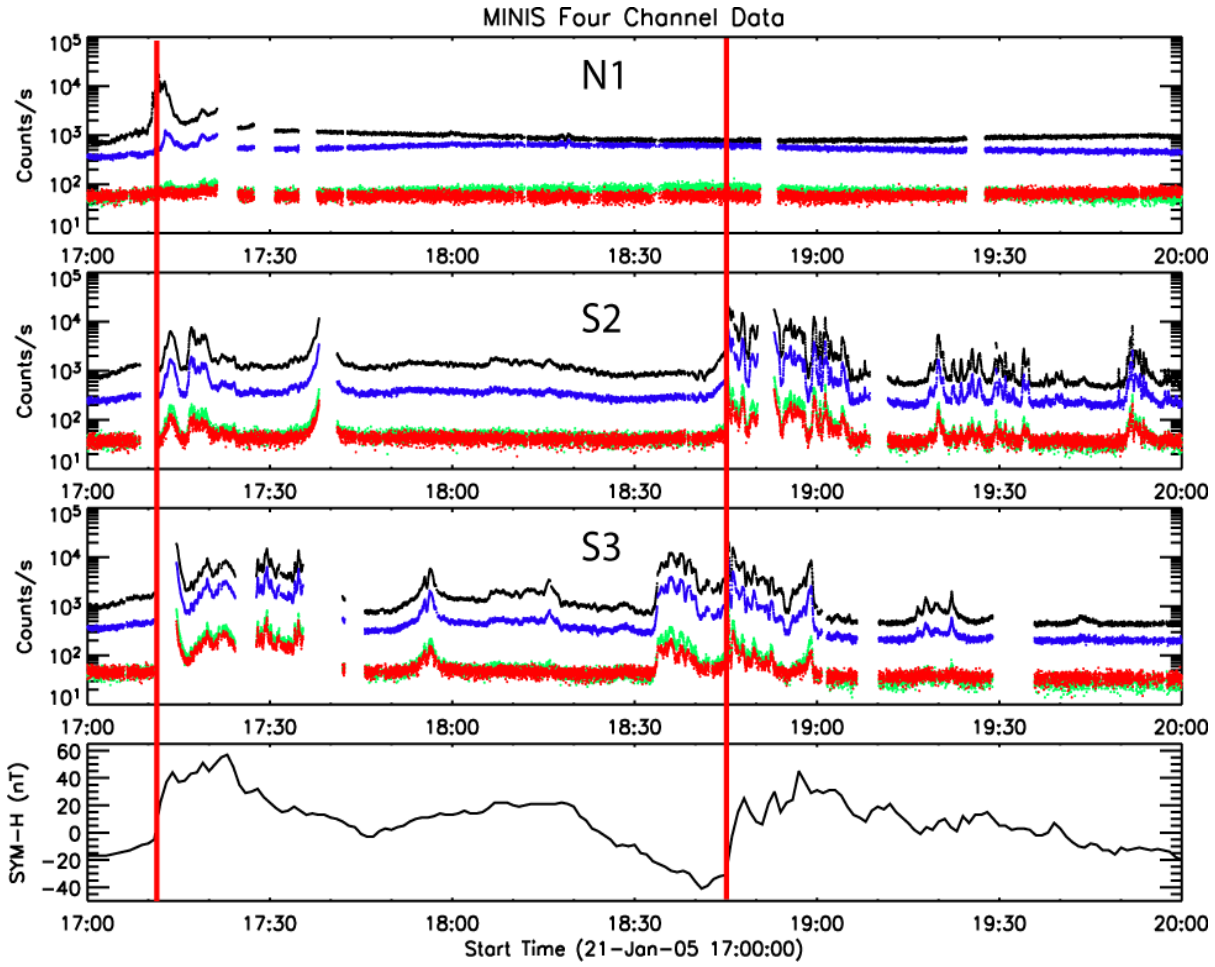

Figure 3.19. Showing the 1 s X-ray countrate observed by the three MINIS payloads on Jan. 21st during the time of the SSC. From top to bottom panels: N1, S2,S3 Vertical dashed lines indicate the times of the sudden impulses in Sym-H. This occurs during a data gap for the first impulse, for the second impulse data coverage is good. A blow up of this time range showing the almost simultaneous rise in countrate is included in Fig. [5.10, in chapter 5]

3.4.1 Background Selection

Because the events of interest occur during very active times, background selection is non-trivial. The time range immediately prior to the event is often chosen because the balloon moves very slowly in geographic coordinates, so the source of background should be relatively constant through the event interval. As previously discussed, cosmic rays -and to a lesser extent the decaying flux of SEPs- are the likely sources of most background counts observed in the payload and both of these sources will be modulated by the earth's magnetic field. As the Earth's magnetosphere field is compressed during the SSC, ground based magnetometers see an increase in the local field.

To confirm that the time range prior to the event period, but after the decay in SEPs from the previous day (see Figure 3.22 showing a series of ground based neutron monitors), is an acceptable time frame, we plot the magnitude of the z-component of the magnetic field and the angle of declination ($\arctan(B_{horizontal}/B_{vetical})$) as measured by the S2 and S3 payloads (Figure 3.20). Very little change in the local field is evident and we assume that any changes in the background flux due to this variation are small. Some changes in Bz are evident, but not coincident with shock arrivals, or sudden precipitation changes. The large envelope in the declination is due to the offsets and differential gain in the magnetometer combined with some

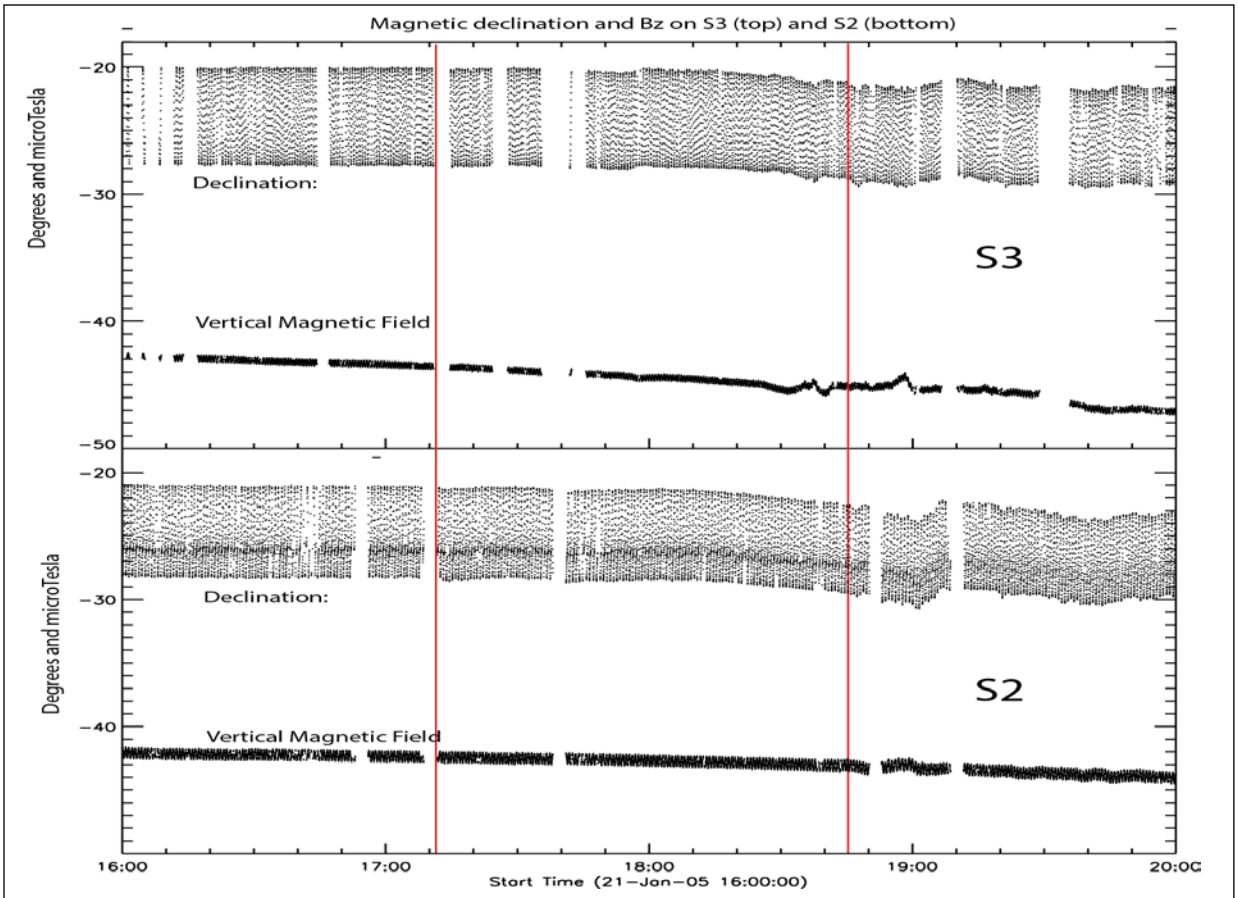

Figure 3.20: This figure shows the declination angle and the vertical magnetic field for the S2 and S3 payloads during the timeframe of the SSC.

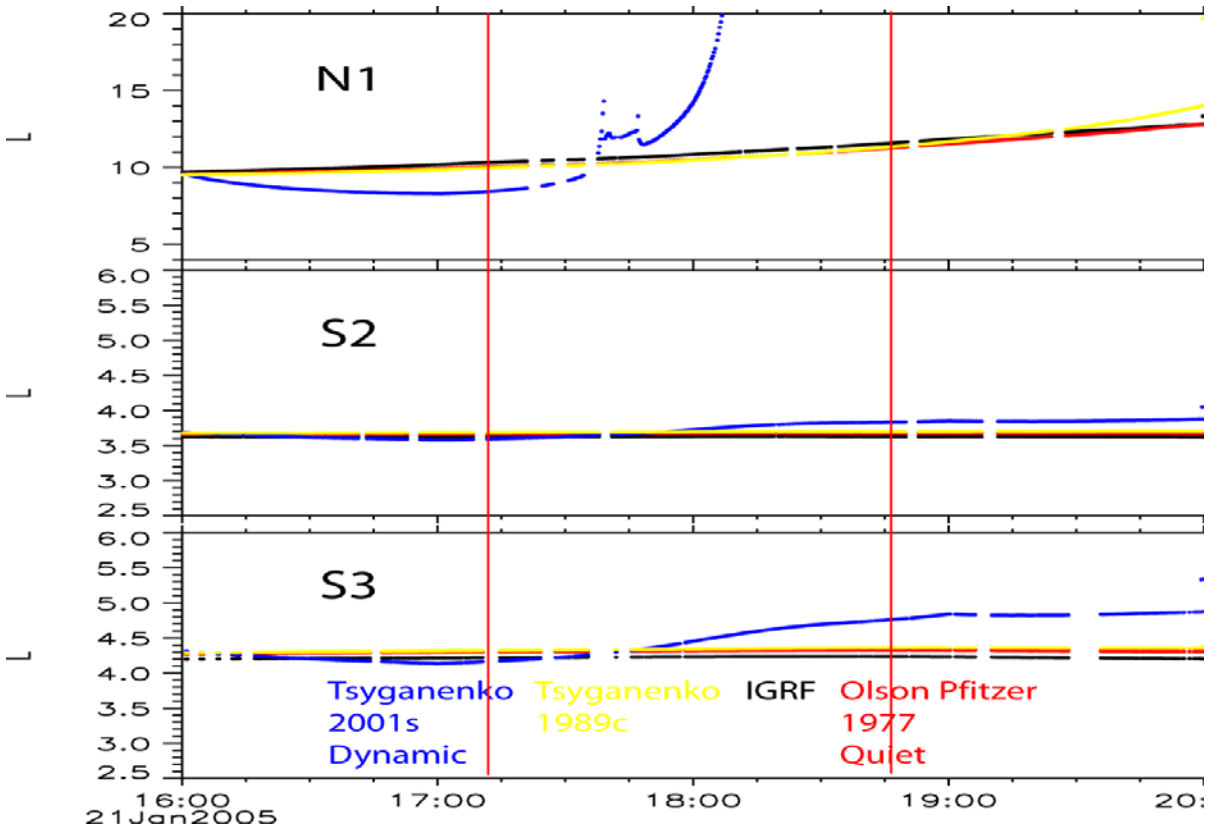

Figure 3.21: A closer look at the MINIS observation L-shells during the time of precipitation observations.

pendulum motion. Although difficult to see because of the envelope, there is some effect on the declination angle during the precipitation that occurs after the second shock arrival. Magnetic field models are also not doing an adequate job of capturing the large scale reorganization of the magnetosphere that is evident in the magnetic field and electron flux seen at GOES on these time scales 3.21, so we cannot use them as a way to determine the magnetic cutoff for cosmic rays and scale background from that determination.

The background will also vary because of changes in the solar wind's influence on cosmic rays. On long time scales cosmic ray flux moves out of phase with solar activity a behavior familiar to many and known as the Forbush effect (Forbush, 1956). This is because a more intense solar wind, in terms of magnetic field, density, and velocity reduces the ability of cosmic rays to reach earth. The effect is not as well quantified on short time scales, but included here as Fig. 3.22 is a plot showing Neutron Monitor (NM) counts from McMurdo, Antarctica and South Pole Station for the time range of the Storm Sudden Commencement. The high values just prior to these plots are the decay of the SEP induced Ground Level Event from Jan. 19, the largest GLE in nearly 50 years.

As a final verification of the choice of background selection we note that the background subtracted spectrum should contain only a small remnant of the 511 keV electron-positron annihilation line. This is probably appropriate because the dominant source of this line will be cosmic ray generated. Several background scaling methods were tested, including scaling to the

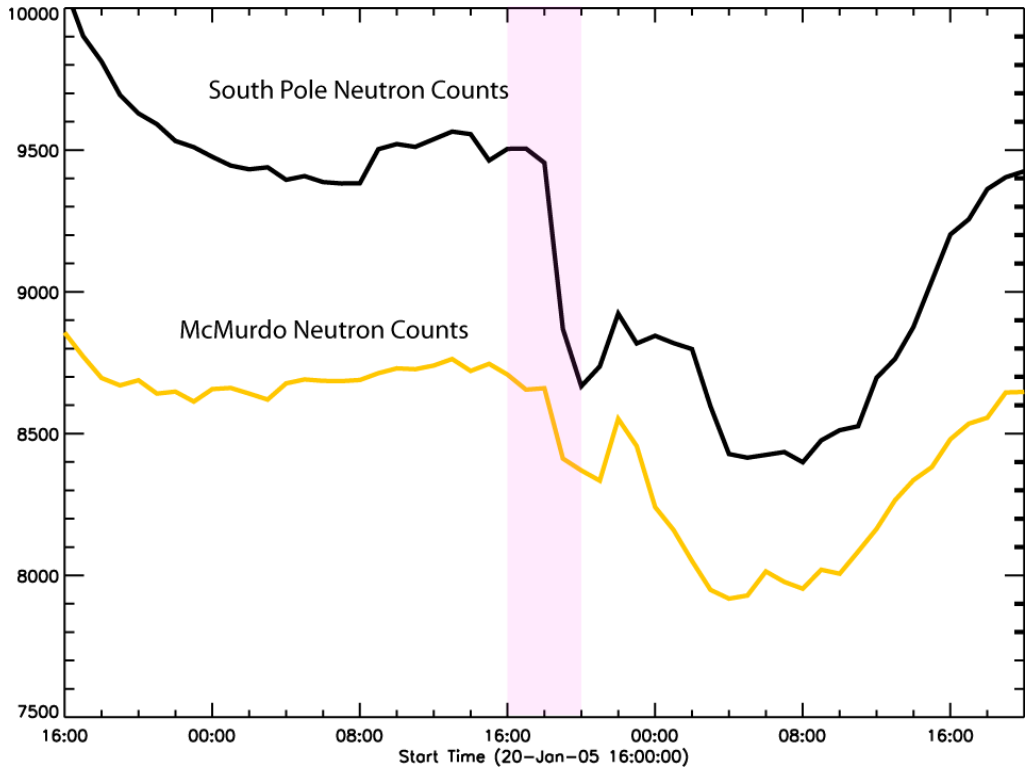

Figure 3.22: Neutron monitor counts from McMurdo and South Pole, Antarcitca. These detectors usually represent low rigidity Cosmic Ray flux at the Earth, but also show the decay of the large Ground Level Event (left side of plot) cause by solar energetic particles. The highlighted region is 16 UT to 20 UT on Jan. 21st

upper level discriminator (ULD) rate. This proved less successful than scaling by the counts above ~3 MeV. While the two methods are similar, the latter seems to give more accurate results across a wider range in gain. For confirmation of the background subtraction scaling we can look at the results of the Monte-Carlo model described in chapter 2 to make sure that pair production generated by the event itself does not contribute to a significant 511 kev line. A close up of the region around 511 keV is shown in Figure 3.23 for data from an event, after background subtraction, and modeled with an appropriate input electron spectrum.

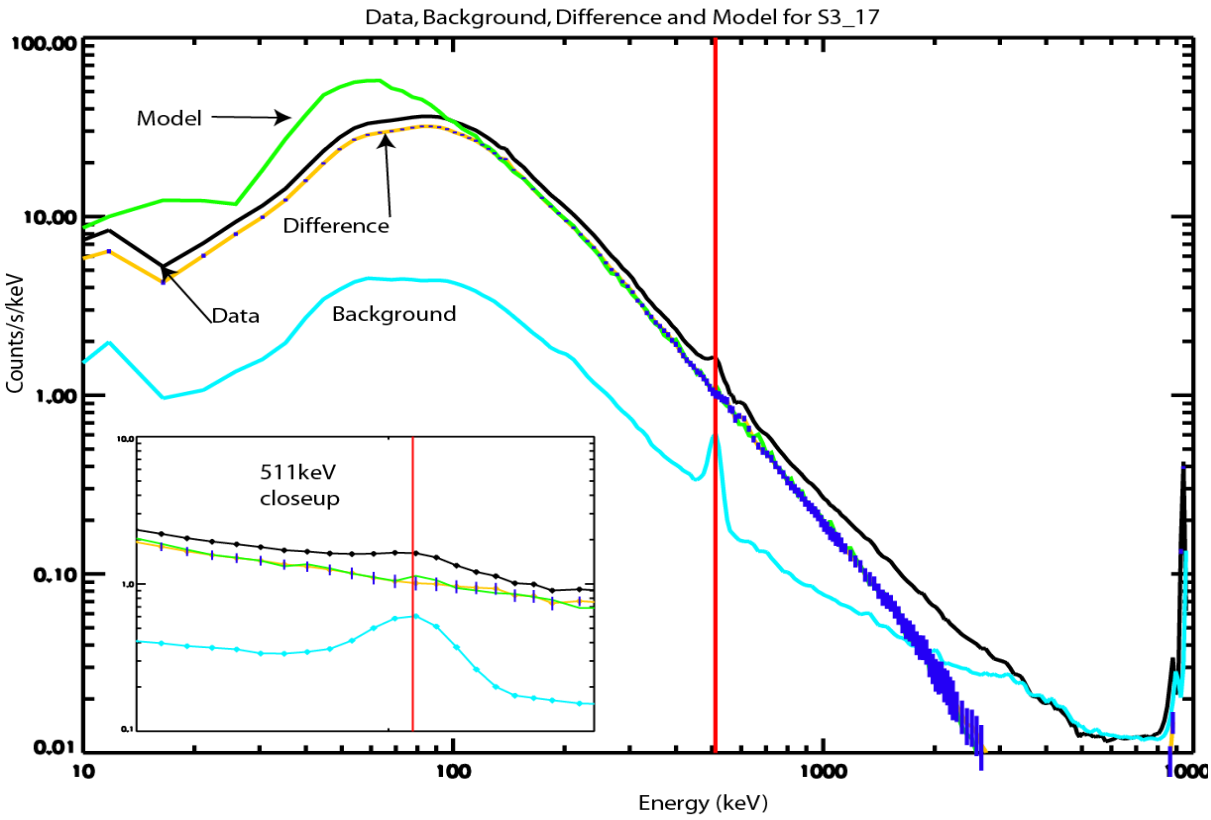

Figure 3.23: Showing the data for event S3_17. The background has been scaled to 125% to accurately subtract counts above 3 MeV. The 511 keV close-up shows only a slight over subtraction of the 511 line as compared to the model which best fits the spectrum from 100 keV to 3 MeV (in this case a Flat spectrum with a high energy cutoff at 4.6 MeV.

4 Modeling the spectral shape of High Energy Precipitation Events

The input electron distribution is chosen from 3 candidate distribution functions. These electron distributions produce the bremsstrahlung spectrum at the top of the atmosphere which is then folded through the response matrix described in chapter 2. Because bremsstrahlung is a relatively inefficient process and most of the electrons lose their energy by scattering in the atmosphere, we calculate (numerically in practice, but described below) the equilibrium distribution of electrons. These are the bremsstrahlung producing electrons. The precipitating distribution F(E) is used to calculate the density of the bremsstrahlung producing distribution of electrons N(E) obtained here from a continuity argument :

$$\frac{dN}{dt} = F(E) - \frac{d}{dE}(N(E)\frac{dE}{dt})$$

We assume that the transit time of electrons through the region of bremsstrahlung production is small compared to the time over which we are able to determine the spectrum (more on this in chapter 5). This allows us to neglect the left hand side in the above equation, i.e we. assume an equilibrium is reached faster than changes in F(E).

$$N(E) = [\frac{dE}{dt}]^{-1} \int F(E)dE$$

We find $\frac{dE}{dt}$ from the Bethe expression for soft collisions of electrons.

$$\frac{dE}{dt} = v\frac{dE}{dx} = c4\pi NZ\frac{z^2e^4}{mc^2\beta}\{\ln(B_q) - \beta^2\}$$

$$Where:\ \ B_q = \frac{\sqrt{2}\gamma\beta\sqrt{\gamma-1}mc^2}{h\langle v\rangle} \qquad after\ Jackson\ [1999]$$

and $h\langle v\rangle$ is the average ionization potential of the atmosphere

Once we have obtained the equilibrium distribution of bremsstrahlung producing electrons we produce the X-ray spectrum by folding the equilibrium electron distribution through a bremsstrahlung generation cross section using appropriate energy range formulas from Koch and Motz [1959]. These cross sections may have errors up to ±20% but this will only affect the absolute value of the derived electron fluxes, and not the spectral shape of the electrons [Johns and Lin, 1991].The three precipitating electron distributions that this effort uses to fit the data are referred to as flat, exponential and monoenergetic.

$$Flat:\ \ F(E) = \begin{cases} A, & E < E_{max} \\ 0, & E \geq E_{max} \end{cases}$$

$$Monoenergetic\ or\ ME:\ \ F(E) = A\delta(E - E_m)$$

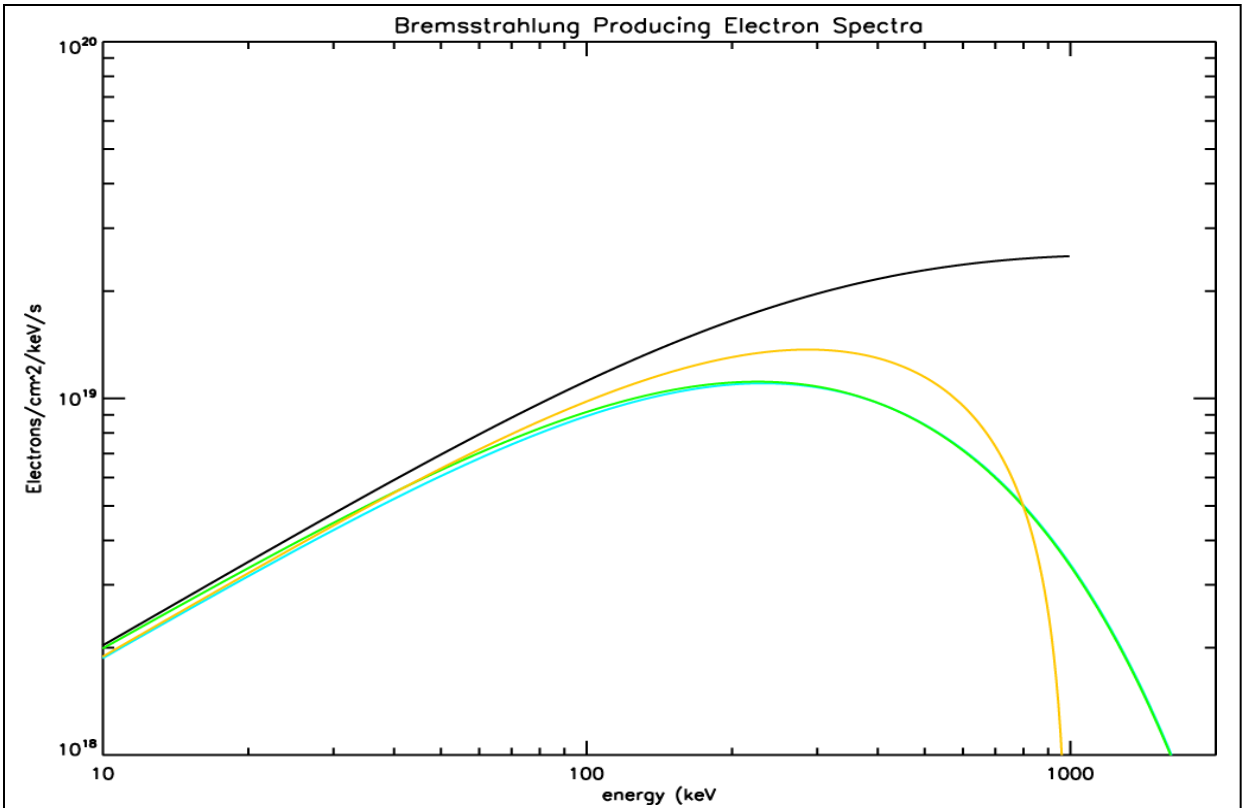

Figure 4.1: The equilibrium distributions calculated for 1 MeV monoenergetic electrons (black), a 500keV e-folding (green), and a Flat distribution with E_{max}=1 MeV (yellow)

$$Exponential: \quad F(E) = Ae^{-E/E_0}$$

Although the three spectral shapes we use for forward fitting are radically different in electrons, the combined effect of the continuity equation and the bremsstrahlung generation dramatically reduce these differences. Three example equilibrium distributions (N(E)) are shown in 4.1. Already in the bremsstrahlung producing distribution the sharp differences between the precipitating electron distributions are starting to be lost. By the time one gets to the bremsstrahlung spectrum itself the difference is even harder to recognize. Three example photon spectra that go into the various response matrices are shown here in Figure 4.2. The atmosphere and instrument responses blur these distinctions even further and only at the highest energies are they really distinct.

Again, the top spectra are scaled to match flux in 300 keV to 3 MeV, although this slightly favors the flat and monoenergetic spectra across their valid range because they have no photons between 2.5 and 3 MeV. Visual inspection shows this is a very minor effect. The similarity of the spectra up to at least the e-folding energy again demonstrates the need for significant counts at high energies to distinguish the spectral shape.

The unscaled (or alternately consideration of the scale factors) also give an indication of how the choice of spectral shape influences the number of electrons that most accurately supports the data. Electron losses in the literature are often listed as a $e^-/cm^2/s$ above a given energy. Thus, it

can be misleading to report only one type of spectral shape. For instance, as seen below in table 4.2 of the best fit parameters for various events showing duskside REP, we see a time period from 17:2-18:45 on S2 where an e-folding of 700 keV, a monoenergetic 2.2 MeV, and a Flat 2.8 MeV all fit the data comparably. In the exponential case there are 2600 precipitating $e^-/cm^2/s$, above 500 keV (an energy threshold that is often used to define REP). In the ME case, the scale factor appears smaller, only 920 $e^-/cm^2/s$.

For comparison to some satellite data sets, 1 MeV or 2 MeV are more useful thresholds. If we use the >2 MeV threshold, the exponential is reduced to 300 $e^-/cm^2/s$. Although this note may seem obvious, it is important to remember as it often leads to miscommunication with the larger community making *in-situ* electron measurements. Indeed the MAXIS loss calculations are dominated by a single long event that was very bright (and long) when reported as >500 keV, but was in fact the softest of all the "MeV Events" with a best-fit e-folding of 300 keV. That event is substantially less significant when its >2 MeV loss rate is compared to the radiation belt content. In fact the entire MAXIS loss rate calculation becomes less significant when the softness of this spectrum is considered, so it should be carefully specified how scale factors and energy thresholds are reported.

There is of course some pattern to the relation between a given ME and an exponential distribution. On average the best fit E_m is 3.12 times larger than the best fit E_0. Millan [2002] fit a power law to the observed x-ray spectra between 100 and 180 keV for each event as a way of

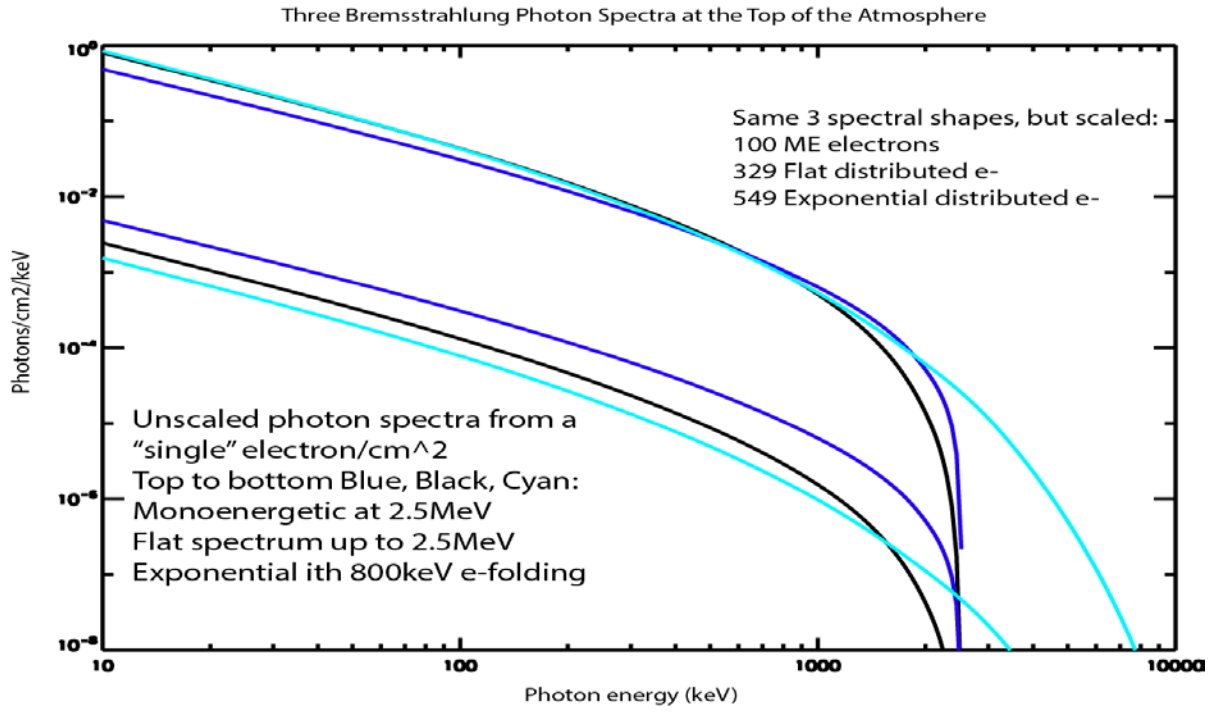

Figure 4.2: The bottom three traces are unscaled photn spectra at the top of the atmoshpere (before the response matrix) from 3 different input electron distributions. Bue = ME with E_m Black=Flat with E_{max} at 2.5 MeV, and Cyan=Exponential with E_0=800 keV. The same three spectra scaled to match the bremsstrahlung x-rays between 300 keV and 3 MeV are plotted on the upper portion, with scale factors shown in the top right.

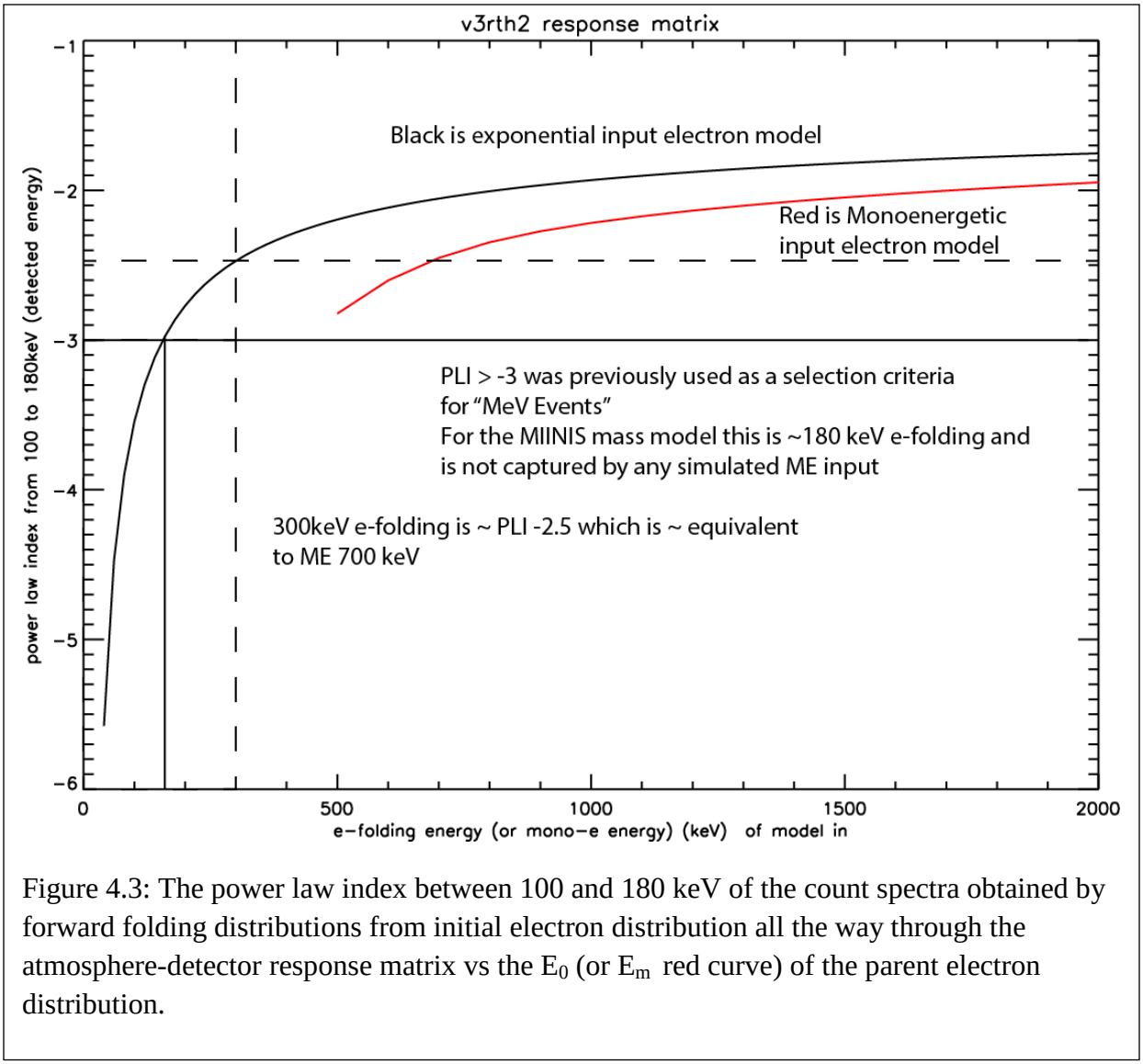

Figure 4.3: The power law index between 100 and 180 keV of the count spectra obtained by forward folding distributions from initial electron distribution all the way through the atmosphere-detector response matrix vs the E_0 (or E_m red curve) of the parent electron distribution.

classifying "MeV Events" from lower energy events. Even a 300 keV e-folding will fall on the harder side of such a classification scheme as can be seen here for model input data into the MINIS response matrix when it is fit to the same energy range 4.3. MINIS saw very few soft events during flight, so such a fitting scheme has not been used to separate out MINIS events. For looking at higher energy events it may prove useful in longer future missions to adjust the energy range over which the power law is fit so that such an index can be used to estimate high time resolution losses at higher energies than a few hundred keV where the current fit is most sensitive.

4.2 Variations in the atmosphere-detector response and input electron spatial and pitch angle distribution

In order to more descriptively capture the precipitating electrons several variants of the atmosphere-detector response matrix were explored and in each case the resulting response matrix was used to attempt to fit the observed x-ray data to determine if a more accurate model fit could be achieved. Variations in pitch angle distribution of the input electrons, distribution of

the precipitation region on the sky, and various levels of detector shielding were used. While a sky filling isotropic spectrum is used for most of the MINIS data, the ability to distinguish variables such as pitch angle, distribution on the sky and the low energy response will be useful in the future when smaller yet more thoroughly observed precipitation is studied.

In total more than 40 detector response matrices were created (some with excellent statistics and some with poor statistics depending on initial results) with a wide range of input angular distributions, spatial distributions, a few modifications of the physics allowed by GEANT to check for consistency, limits on the mass model, refinements in the atmospheric and payload mass model, as well as a few models using input electrons directly into the top of the atmosphere.

Many models were run keeping track of the initial photon location and direction so that the response could be rebinned to particular angular distributions and particular spatial distributions. This flexibility also can be used to show properties of where counts showing up in the detector originated from and with what angular distribution the bulk of the detected X-rays originated from. An example of the radial distance for photons which end up depositing some fraction of their input energy is shown in Figure 4.4. The number of counts divided by the area over which they were launched as a function of launch radius (in km) of any photon that produces a count in the detector is shown as the top curve, the lower curve is from those photons which end up

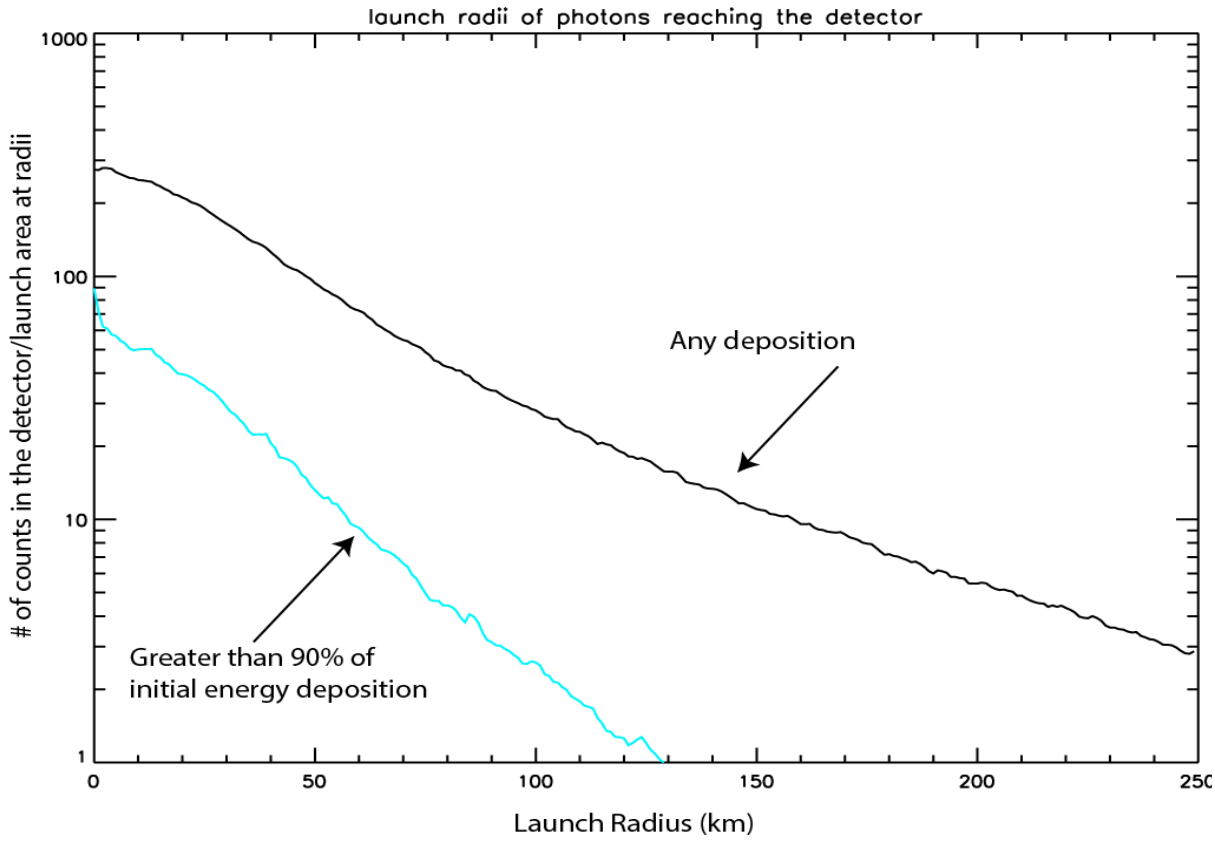

Figure 4.4: This figure shows the number of detector events found in the model as a function of their initial radius in the simulation. The # of counts has been corrected for the increased area as a function of radius. The lower curve represents only those counts where most of the initial energy in the photon was deposited in the detector.

depositing more than 90% of their initial energy in the detector. Importantly, the model shows the detector is still sensitive to photons initiated out at 250 km, simulating smaller launch areas can influence the scaling, so the assumption of 'sky-filling' precipitation is important to consider and it includes a large area.

4.2.1 Low energy response

The forward folded spectrum does a good job of matching the observed X-ray count rate at energies above ~200 keV, as well as sometimes down to 100 keV, but clearly overestimates the counts at lower energies. It is not simply a matter of reducing the number of low energy electrons input into the model because most of the counts at these low energies are the result of high energy electrons that have generated a lower energy count through collision, Compton scatter in the atmosphere, incomplete collection in the crystal, or from a partial energy deposit occurring elsewhere in the payload. For instance a mono-energetic input electron spectrum at 1.5 MeV is the best fit for event S31845, but the result of the forward folding still has far too many counts at 100 keV.

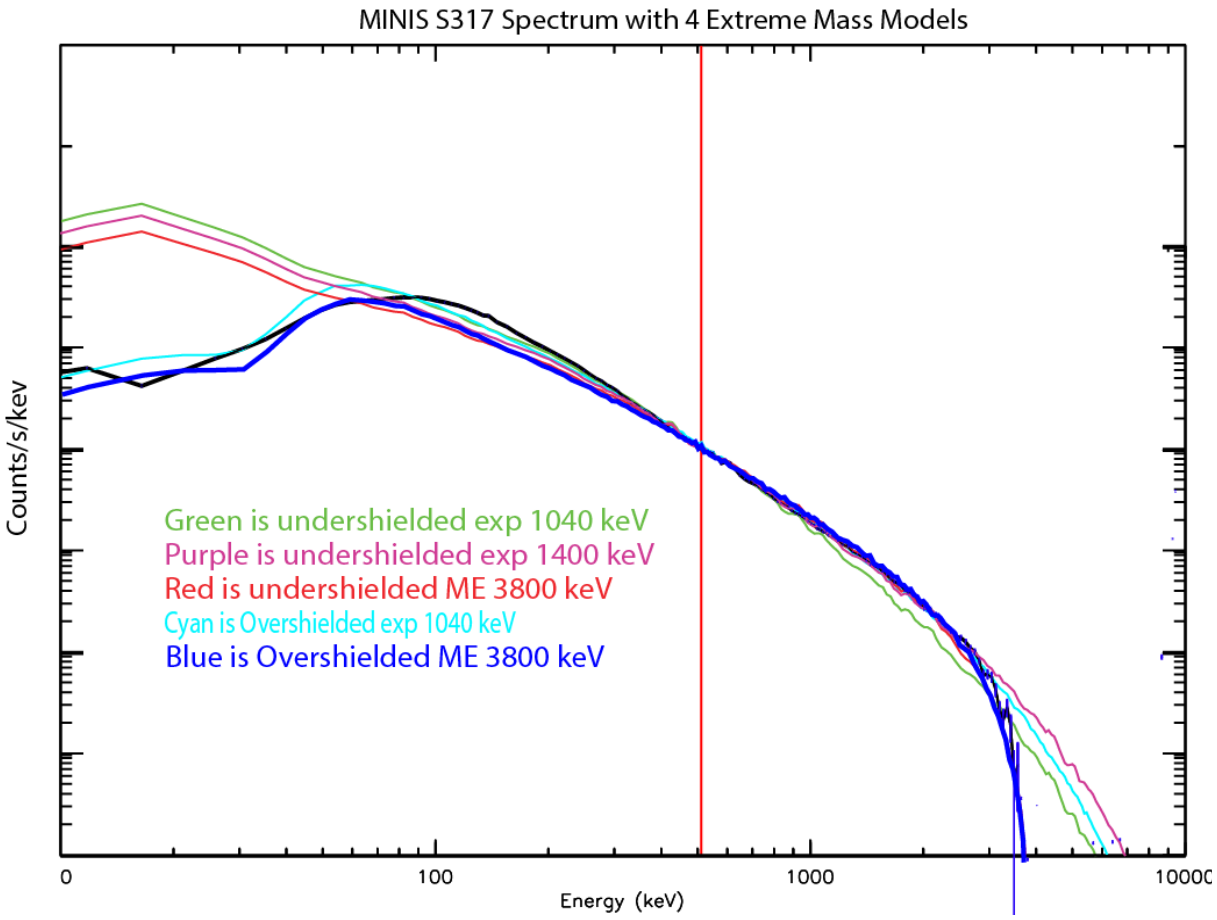

Figure 4.5: Two response matrixes are shown with 3 different spectral shapes input (over shielded exp 1400 keV is not shown), black is the data from the S3 payload during the 17:10 time frame. The models are called out in the figure and are listed in order by their intensity at 20 keV.

In order to investigate why this may be, several additional GEANT mass models were constructed, a few in which the amount of absorbent material above the detector was dramatically increased (excess atmosphere and/or aluminum were used), and another where the detector crystal exists within a vacuum. Although these situations are clearly non-physical the actual mass model is clearly somewhere in between these two extremes. The results of using these models are included here for event S317 with several spectral variants in Figure 4.5. Imposing an energy offset on the spectral data (accomplished in energy space by subtracting a 25 keV baseline from the channel boundaries of the data spectrum) improves the fit of the models down to ~60 keV especially when combined with the over shielding models, but we have no calibration data that indicates the need for this correction, and the over shielding models are substantially unphysical.

As can be seen in the figure, under shielded models don't roll over at low energies, while the over shielded models can do quite well except for a lack of counts from ~80 keV to 300 keV. The shown over shielding model included ~10 grams/cm^2 excess atmosphere over the expected real value and 'an extra gram/cm^2 of aluminum over the known value. The most significant possibility similar to this over shielding situation would be the case of significant precipitation

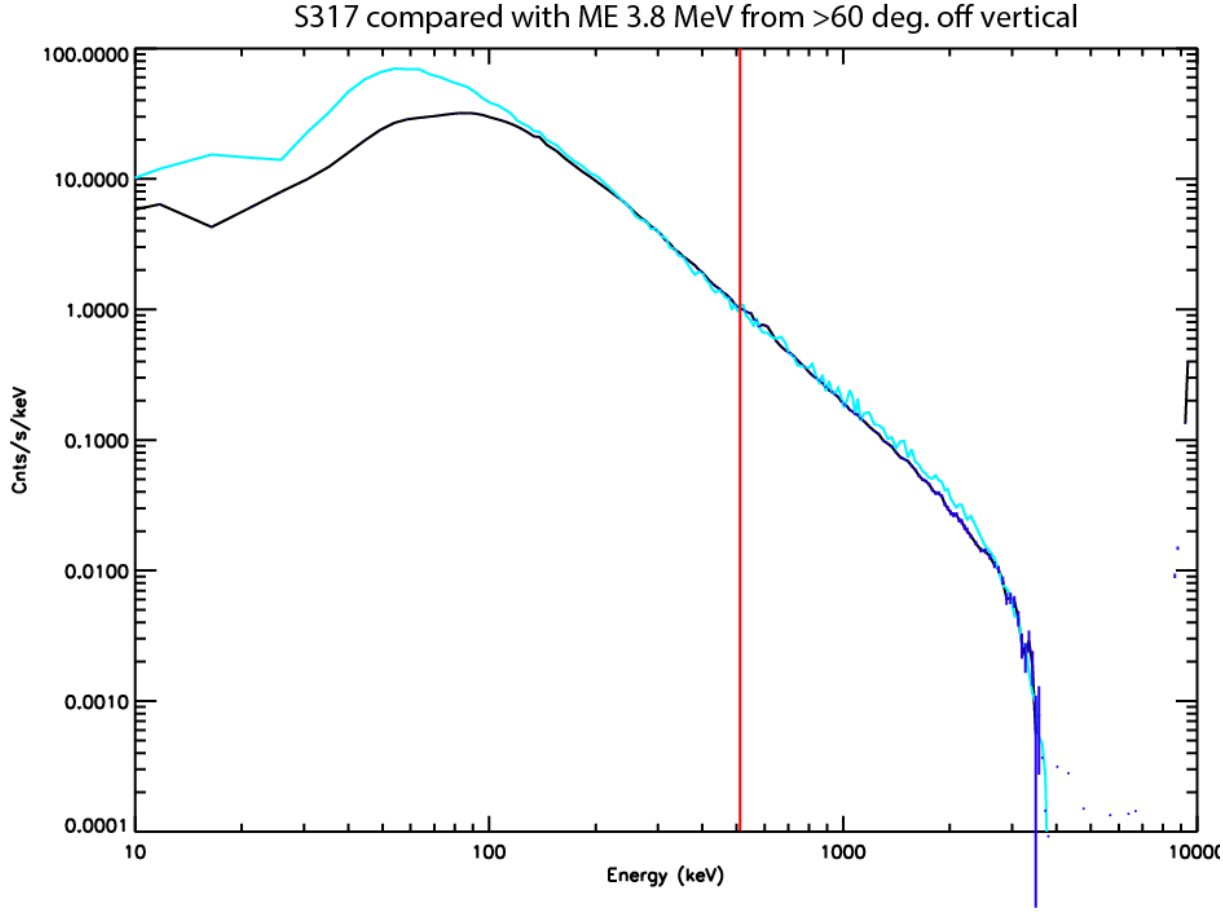

Figure 4.6: The S317 compared with a forward folded distribution of 3.8 MeV precipitating electrons. The mass model used only includes photons launched from >60 deg. off vertical, i.e. ~80 km off on the horizon.

well out on the horizon so that the majority of photons had a longer path length through the atmosphere and the payload top plate.

The over shielding values are roughly a factor of two over the expected thicknesses and thus most precipitation would be coming from > 60 degrees off axis from the vertical. While this is a possibility some second lower energy source would have to be included to make up for the 80-300 keV range. Multiple source distributions were not modeled for any of the event spectra although this may prove useful in the future. Additionally, since payloads S2 and S3 see precipitation simultaneously across > 600 km separation it would take a very peculiar spatial distribution for both payloads to only be seeing the precipitation on the horizon. Since we can limit the most thorough mass model to photons launched from > 60 degrees off vertical we can test this model as well. Such a response matrix produces spectra as in Figure 4.6. Again we are comparing to event S317 and the low energy excess has not been corrected, as one would expect the required number of electrons has increased substantially.

4.2.2 Pitch angle variations

The response matrix also allows us to examine the effect that the initial pitch angle of the electron (and thus parent photon) might have on the observed spectrum. Initial results all used an isotropic input photon spectrum. The photon spectrum "pitch angle" distribution is related to the parent electron spectrum because the electrons of interest have such high energies that bremsstrahlung will be beamed forward. The mean angle of emission is on the order of $1/\gamma$ [Jackson, 1999] and the on axis radiation fraction is proportional to the energy of the electron to at least a 3.2 power [Koch and Motz, 1959]. The forwarded folded spectra (as appears in the model detector) of a pair of electron distributions is shown here in Figure 4.7. The three different response matrices differ only in the input pitch angle distribution used in the Monte-Carlo model. "Downward isotropic "spreads photons isotropically between 0° and 85° off of nadir. The "beamed" distribution is isotropic between nadir and 5° off axis, and the "mirroring" distribution which attempts to simulate particles that are barely encountering the atmosphere is isotropic between 75° and 89° away from nadir.

For the top section of the plot, the total number of input electrons has been held constant (in fact 1 precipitating electron per cm^2), while the lower group of spectra have been scaled so the resultant X-ray spectra have a common intensity in the 300 keV to 3MeV range. This range is chosen throughout as the default energy range for comparison because it ensures the scaling of spectra occurs above the errors in the low energy response and below the poor background subtraction at high energies. Each of the spectra in the subsequent section was also fit with a scaling where the low and high energy boundaries (the equivalent of the 300 keV and 3 MeV standard) was determined by where the count rate in the background subtracted spectra was comparable to the error in the count rate. For very brief integrations within events this ends up influencing the range of acceptable fits, but affects the characteristic energy of the best fit E_0 by only tens of keV in practice. Flat and ME distributions are not affected because the change in $E_{m(ax)}$ is smaller than the simulation resolution.

The two display methods in Figure 4.7 highlight two distinct differences in the effect of the pitch angle distribution on the detected spectrum. First let us consider the scaled lower section. Although the beamed downward spectrum is often the best fit to the data, particularly at the low energy, there is little physical justification for such a distribution, and because the low energy

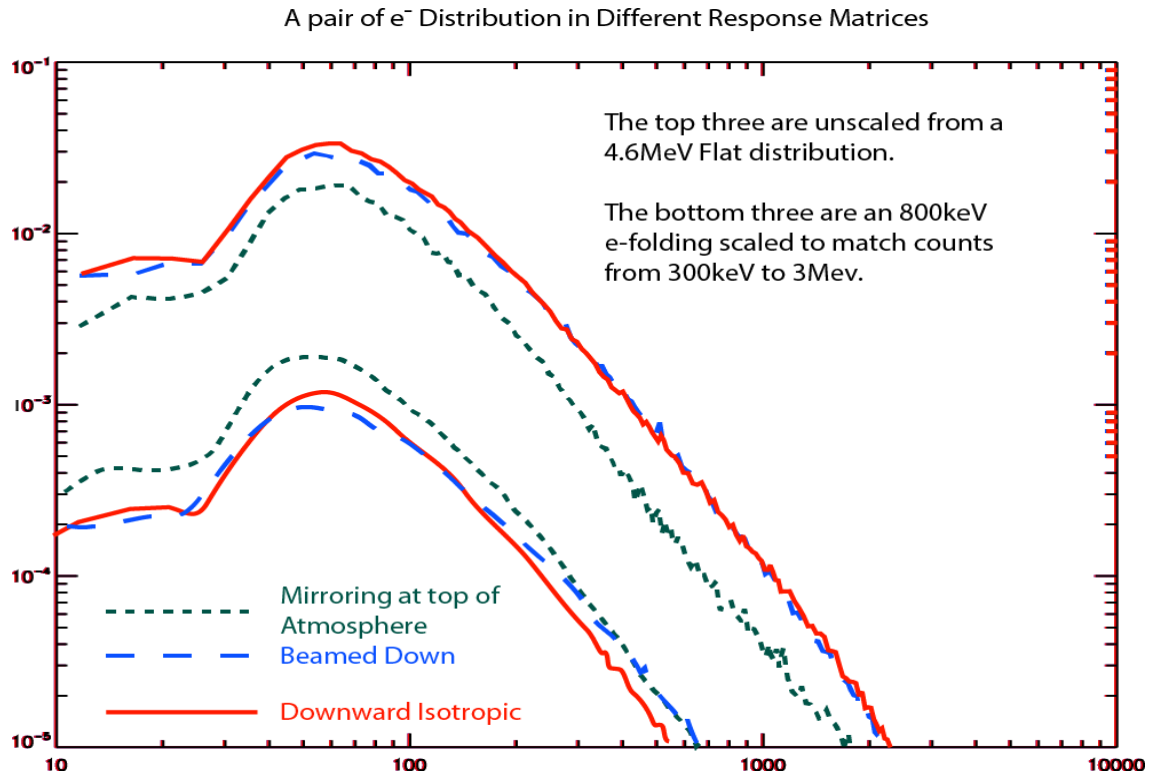

Figure 4.7: The effect of using a response matrix with three different input pitch angle distributions are shown as they will modify a pair of different input electron spectra. The upper group of spectra is from a flat "single" electron distributed up to 4.6 MeV, the lower group of spectra is from an 800 keV e-folding. In the lower case, the three spectra have been scaled to match flux from 300 keV to 3 MeV.

part of the spectrum has proven difficult to accurately model it is hard to determine pitch angle from the observed differences in the measured spectrum. It should be noted however that the mirroring distribution makes the low energy problem even worse. Other arguments can be made that emphasize the likelihood of downward isotropic or weak pitch angle scattering based on the timing of spectral changes, connections to spacecraft observations, and/or interpayload timing but at this time direct spectral determination of the pitch angle distribution cannot be made.

Although choosing a higher e-folding energy brings down the low energy excess somewhat (alternatively stated: the mirroring electrons give a softer spectrum), the change in slope is not dramatic enough to compensate. The best fit e-folding when processed through the mirroring response matrix is typically 5% higher than when processed through the downward isotropic response matrix.

A more direct modeling effort with large numbers of electrons launched at significantly higher altitude, perhaps including effects of magnetic field which will bias the direction of bremsstrahlung emission, especially for mirroring distributions, and better calibration of future detector gain and offset in flight-like scenarios will be needed to resolve pitch angle distribution's effect on the observed spectrum.

A second difference the pitch angle distribution has on the observed spectrum is clear from the upper portion of the plot. For these three spectra a common input intensity was used. If the precipitation MINIS observes is from electrons mirroring at the top of the atmosphere, then the number of electrons required to produce the observed intensities is almost an order of magnitude higher than if downward isotropic distributions are used..

4.2.3 Forward Folding Model Results

The following pages show the MINIS observations broken into event time ranges and then compared to the forward fit models that have just been described. The S3 payload is divided into 13 time ranges which are either isolated in time or changes in spectral hardness are notable. The S2 and N1 payloads which had spectral degradation during event time periods (as can be seen below) are divided into fewer time ranges because the error in fitting the spectrum is otherwise to large. In each case the best fit monoenergetic is shown in green, the best exponential fit is in red and the best flat fit is in cyan. Each spectra is plotted on the same horizontal scale, but not necessarily the same vertical scale. The 511 keV line is shown as a red vertical line throughout. Table 4.1 which summarizes this data as well as intensity of the fit electron distribution is included after the spectra. Time periods are specified in the chart titles. The presentation order is chronological by time period of the spectrum accumulation start time.

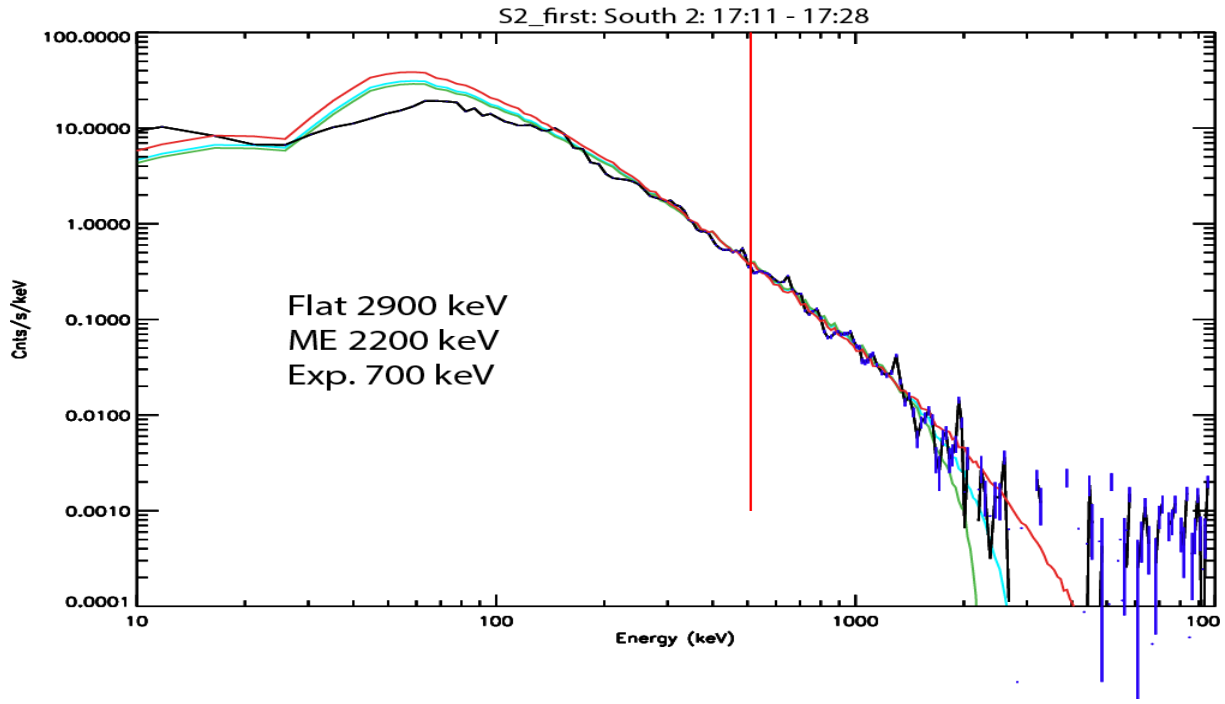

Forward folding model results are presented on the following pages in figures similar to this one. In each case the time range and payload ID are shown in the title and the best fit spectral parameters are shown in the plot area. The black curve with blue error bars is the data, while the red(exponential), cyan (flat) and green (monoenergetic) curves are the model fits.

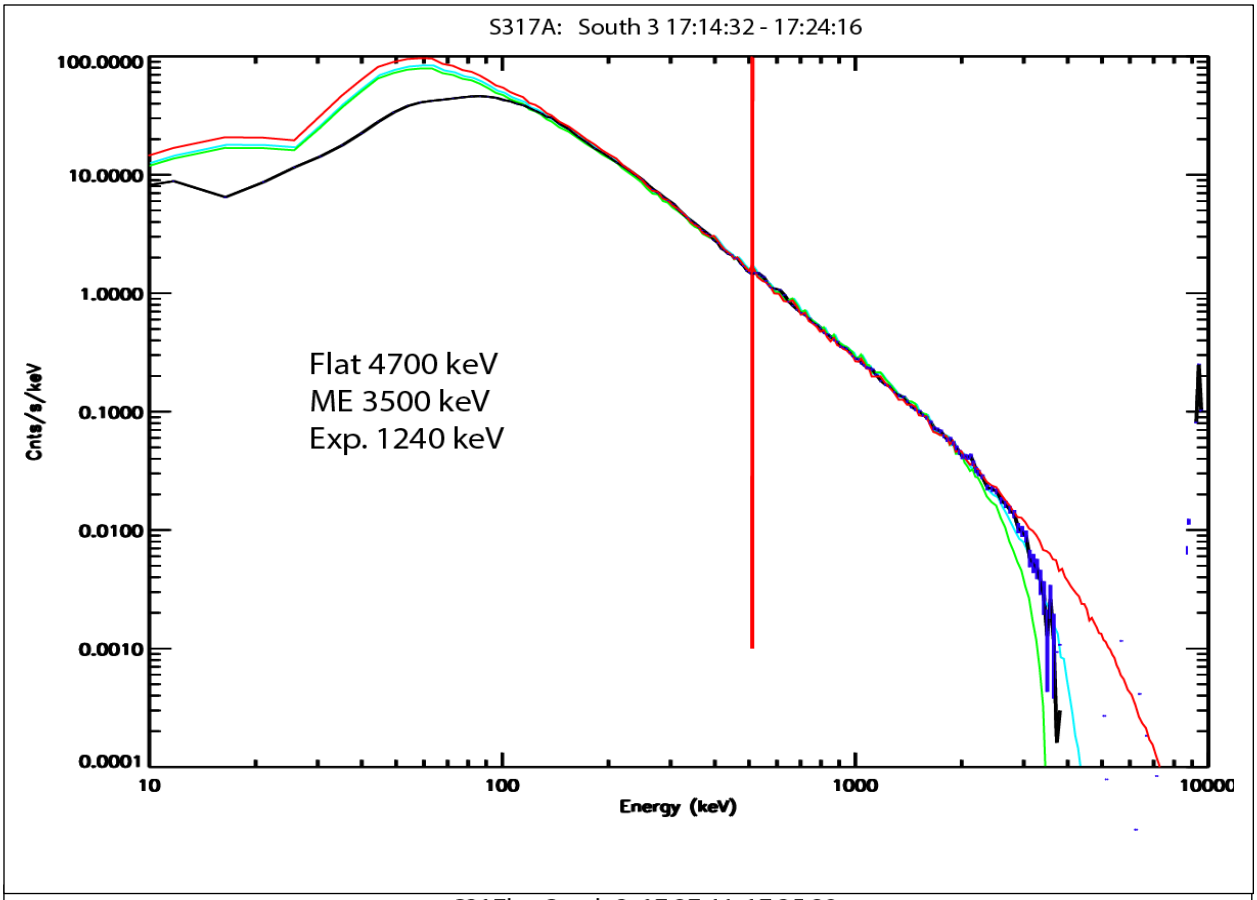
S317A: South 3 17:14:32 - 17:24:16
Flat 4700 keV
ME 3500 keV
Exp. 1240 keV
Cnts/s/keV
Energy (keV)
100.0000
10.0000
1.0000
0.1000
0.0100
0.0010
0.0001
10
100
1000
10000

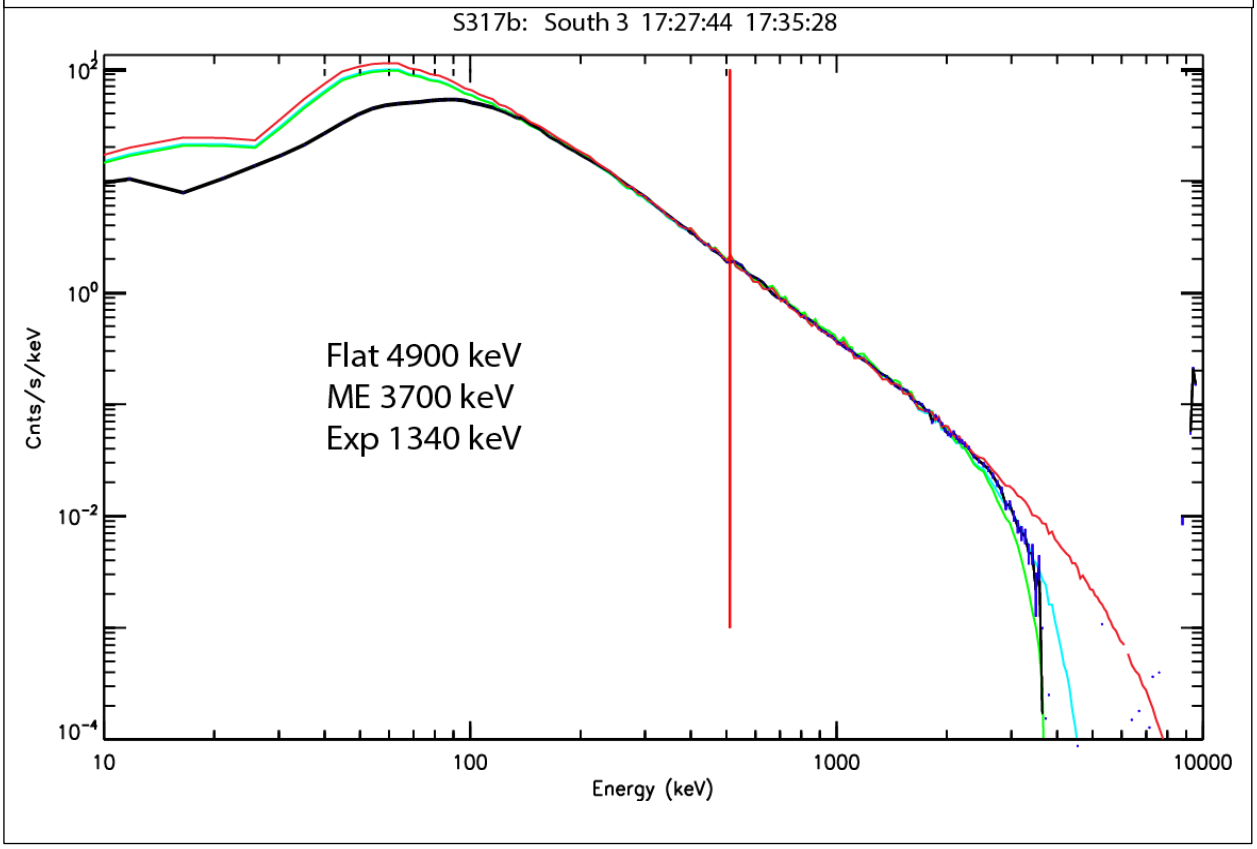
S317b: South 3 17:27:44 17:35:28
Flat 4900 keV
ME 3700 keV
Exp 1340 keV
Cnts/s/keV
Energy (keV)
10
100
1000
10000

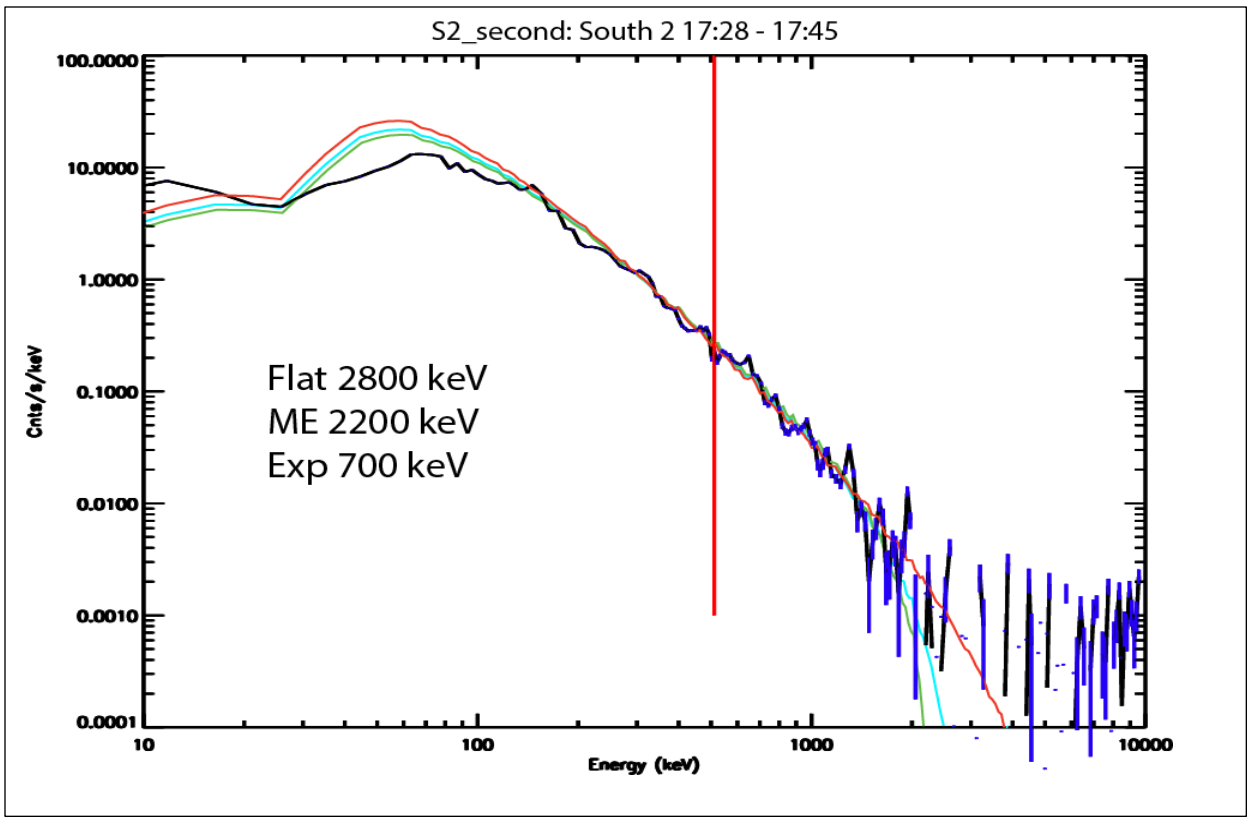
S2_second: South 2 17:28 - 17:45
Flat 2800 keV
ME 2200 keV
Exp 700 keV
Cnts/s/keV
Energy (keV)
100.0000
10.0000
1.0000
0.1000
0.0100
0.0010
0.0001
10
100
1000
10000

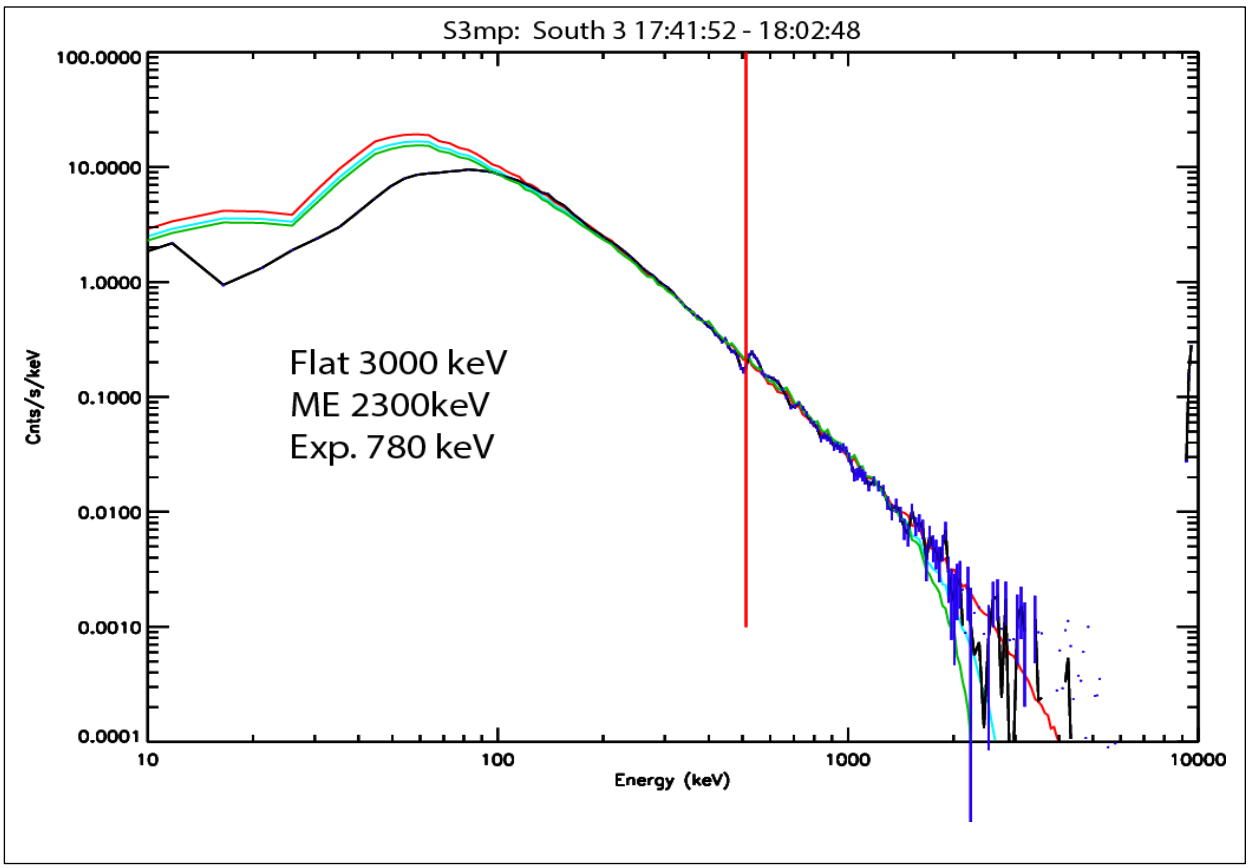
S3mp: South 3 17:41:52 - 18:02:48
Flat 3000 keV
ME 2300keV
Exp. 780 keV
Cnts/s/keV
Energy (keV)
100.0000
10.0000
1.0000
0.1000
0.0100
0.0010
0.0001
10
100
1000
10000

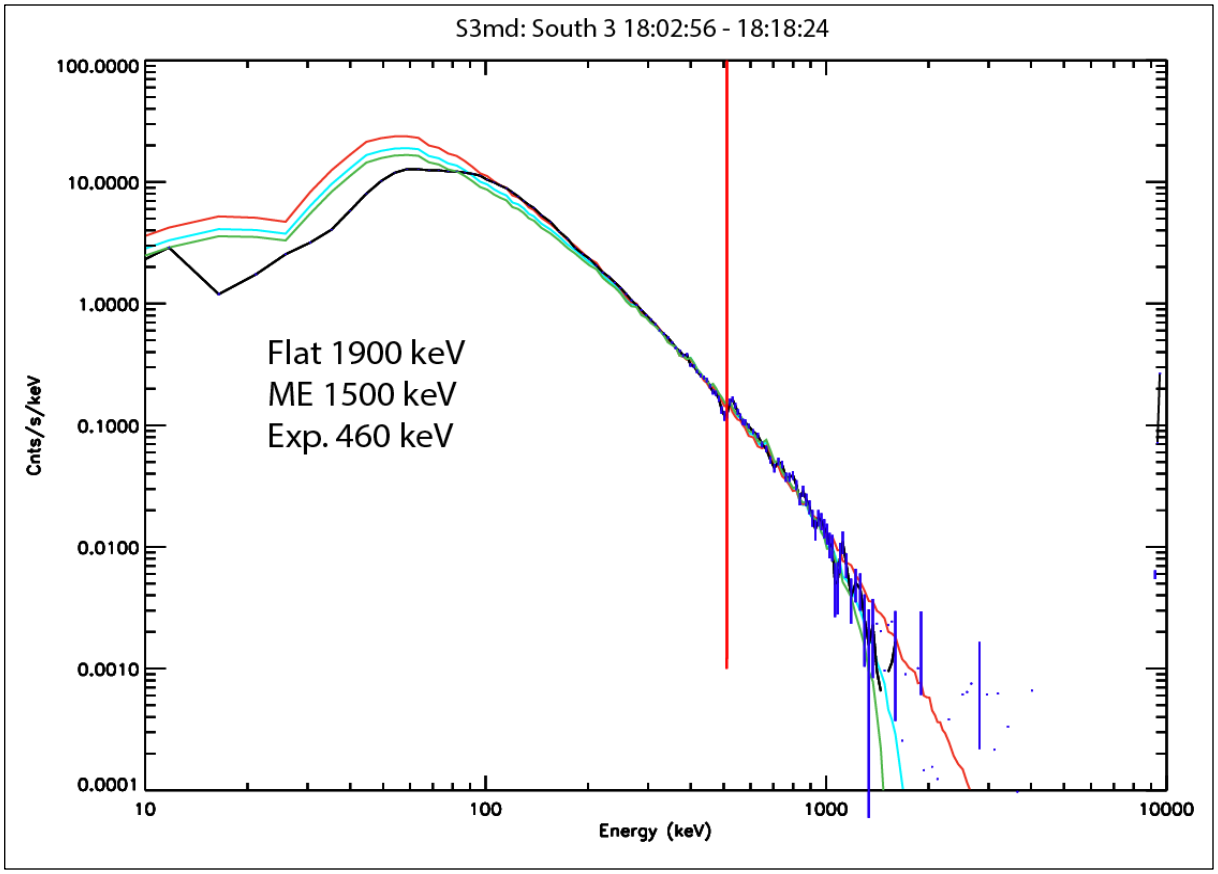
S3md: South 3 18:02:56 - 18:18:24
Flat 1900 keV
ME 1500 keV
Exp. 460 keV
Cnts/s/keV
Energy (keV)
100.0000
10.0000
1.0000
0.1000
0.0100
0.0010
0.0001
10
100
1000
10000

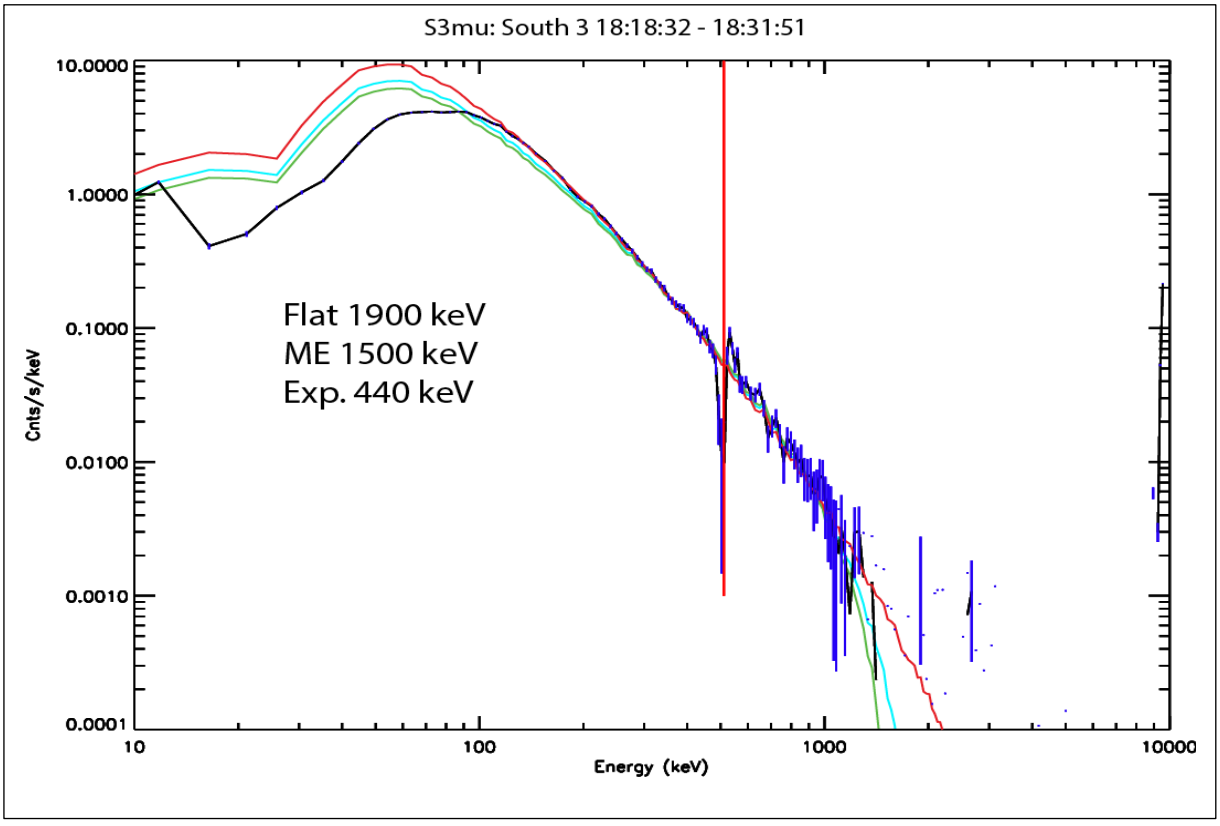
S3mu: South 3 18:18:32 - 18:31:51
Flat 1900 keV
ME 1500 keV
Exp. 440 keV
Cnts/s/keV
Energy (keV)
10.0000
1.0000
0.1000
0.0100
0.0010
0.0001
10
100
1000
10000

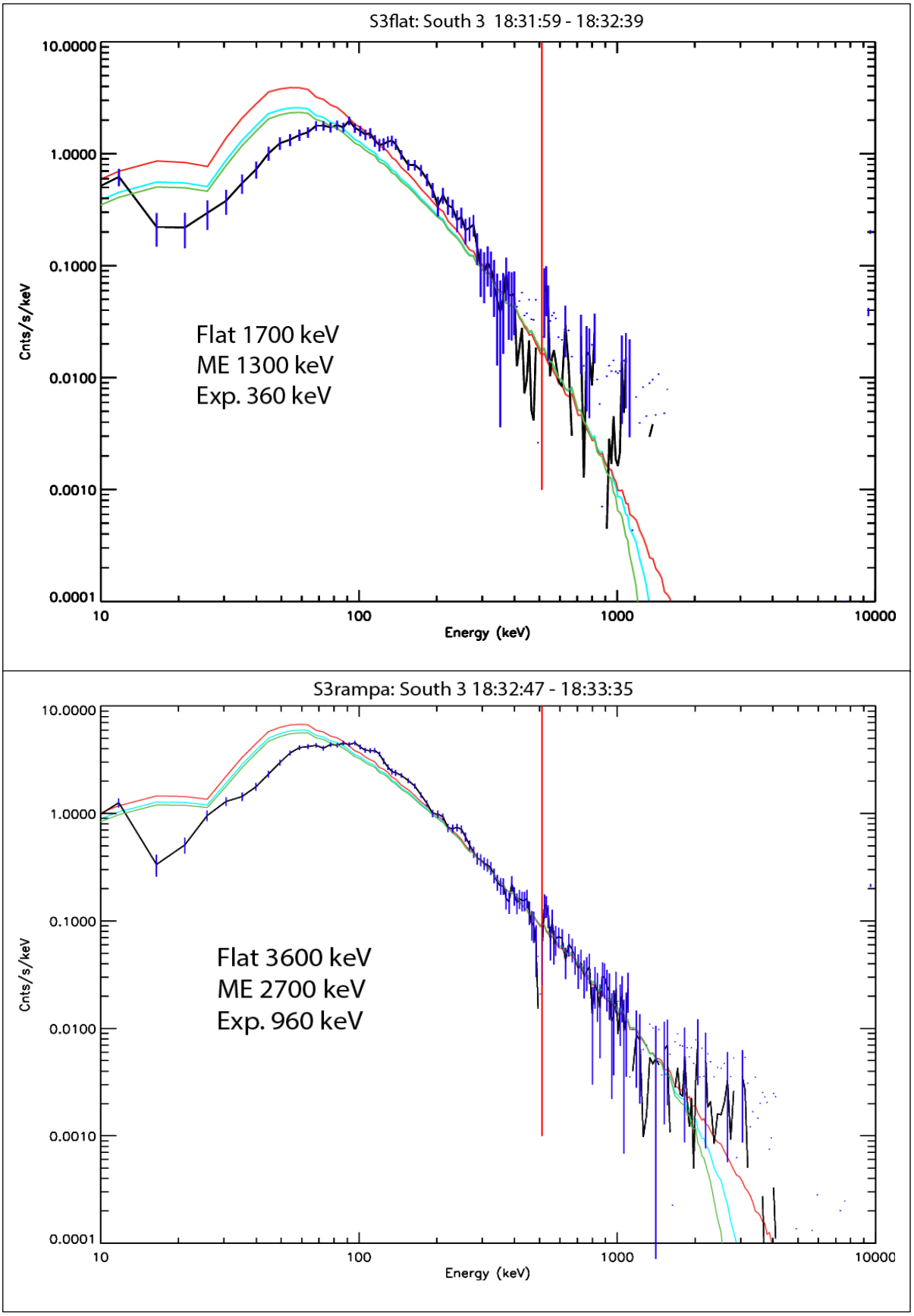
S3flat: South 3 18:31:59 - 18:32:39
Flat 1700 keV
ME 1300 keV
Exp. 360 keV
Cnts/s/keV
Energy (keV)
S3rampa: South 3 18:32:47 - 18:33:35
Flat 3600 keV
ME 2700 keV
Exp. 960 keV
Cnts/s/keV
Energy (keV)

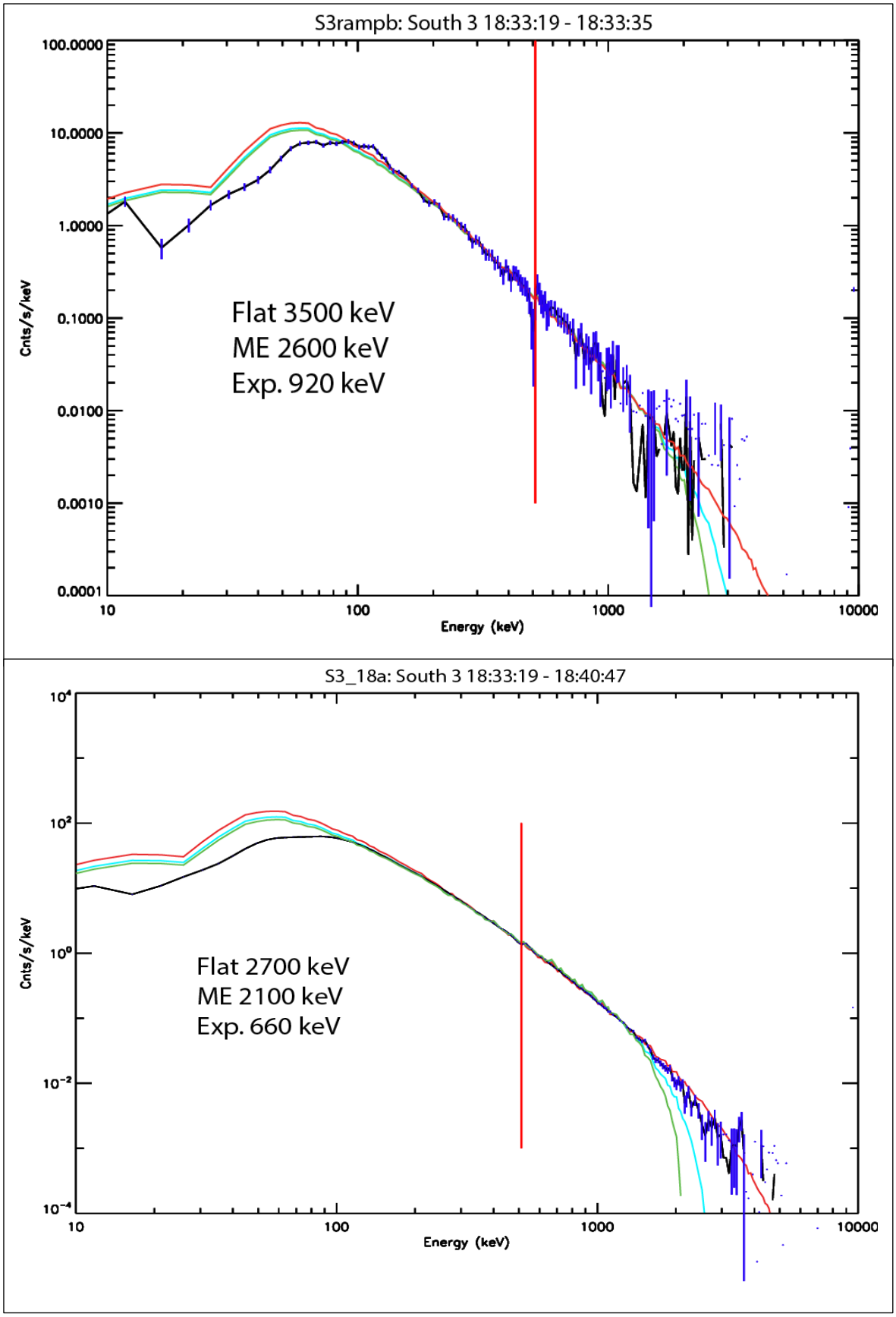
S3rampb: South 3 18:33:19 - 18:33:35
Flat 3500 keV
ME 2600 keV
Exp. 920 keV
Cnts/s/keV
Energy (keV)
S3_18a: South 3 18:33:19 - 18:40:47
Flat 2700 keV
ME 2100 keV
Exp. 660 keV
Cnts/s/keV
Energy (keV)

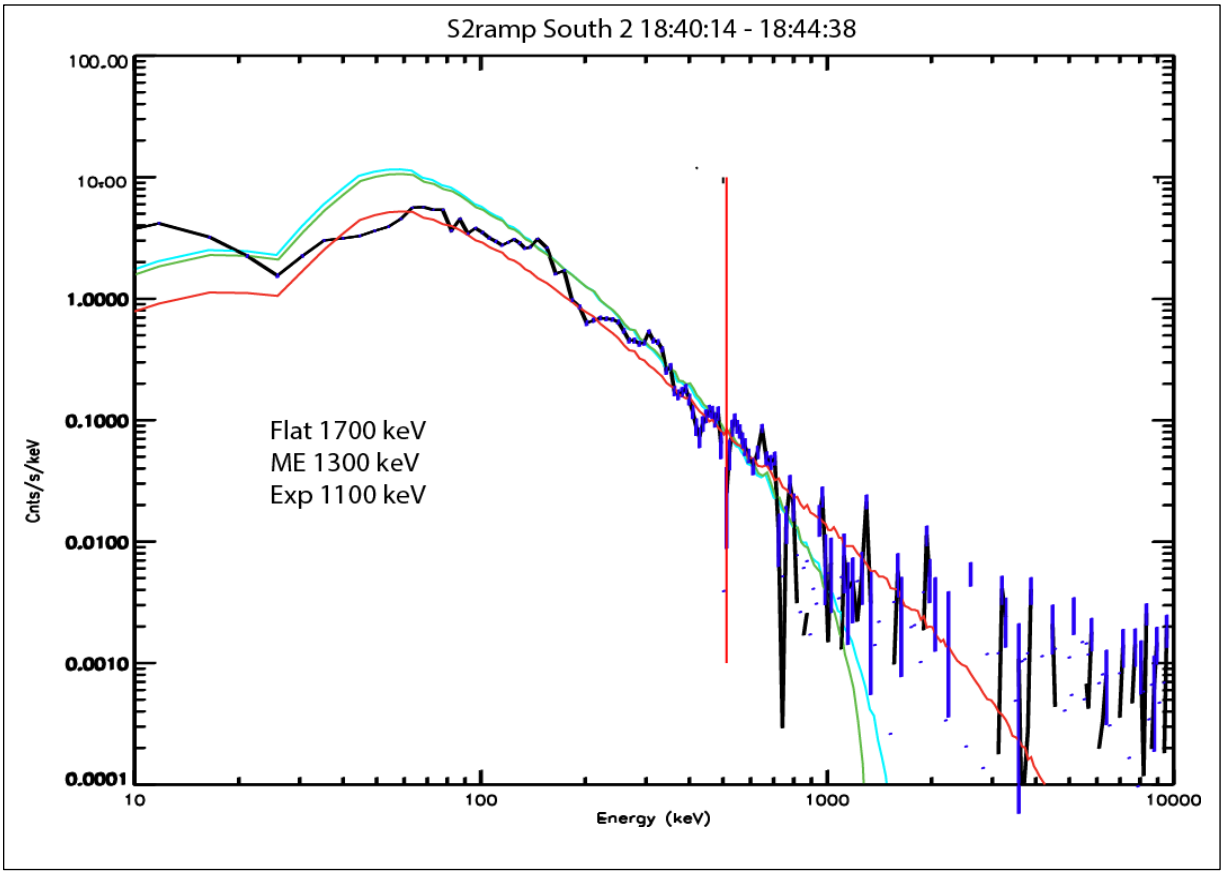
S2ramp South 2 18:40:14 - 18:44:38
100.00
10.00
1.0000
0.1000
0.0100
0.0010
0.0001
Cnts/s/keV
Flat 1700 keV
ME 1300 keV
Exp 1100 keV
10
100
1000
10000
Energy (keV)

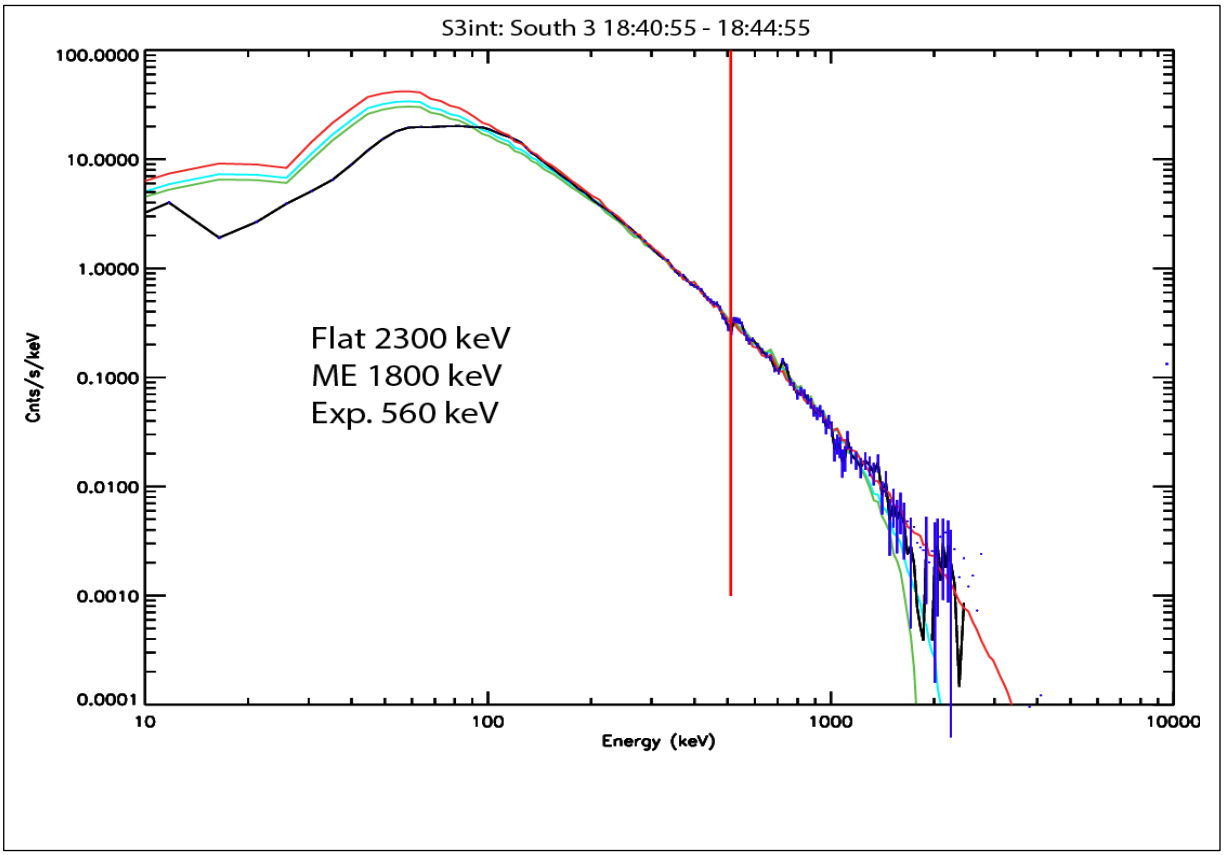
S3int: South 3 18:40:55 - 18:44:55
100.0000
10.0000
1.0000
0.1000
0.0100
0.0010
0.0001
Cnts/s/keV
Flat 2300 keV
ME 1800 keV
Exp. 560 keV
10
100
1000
10000
Energy (keV)

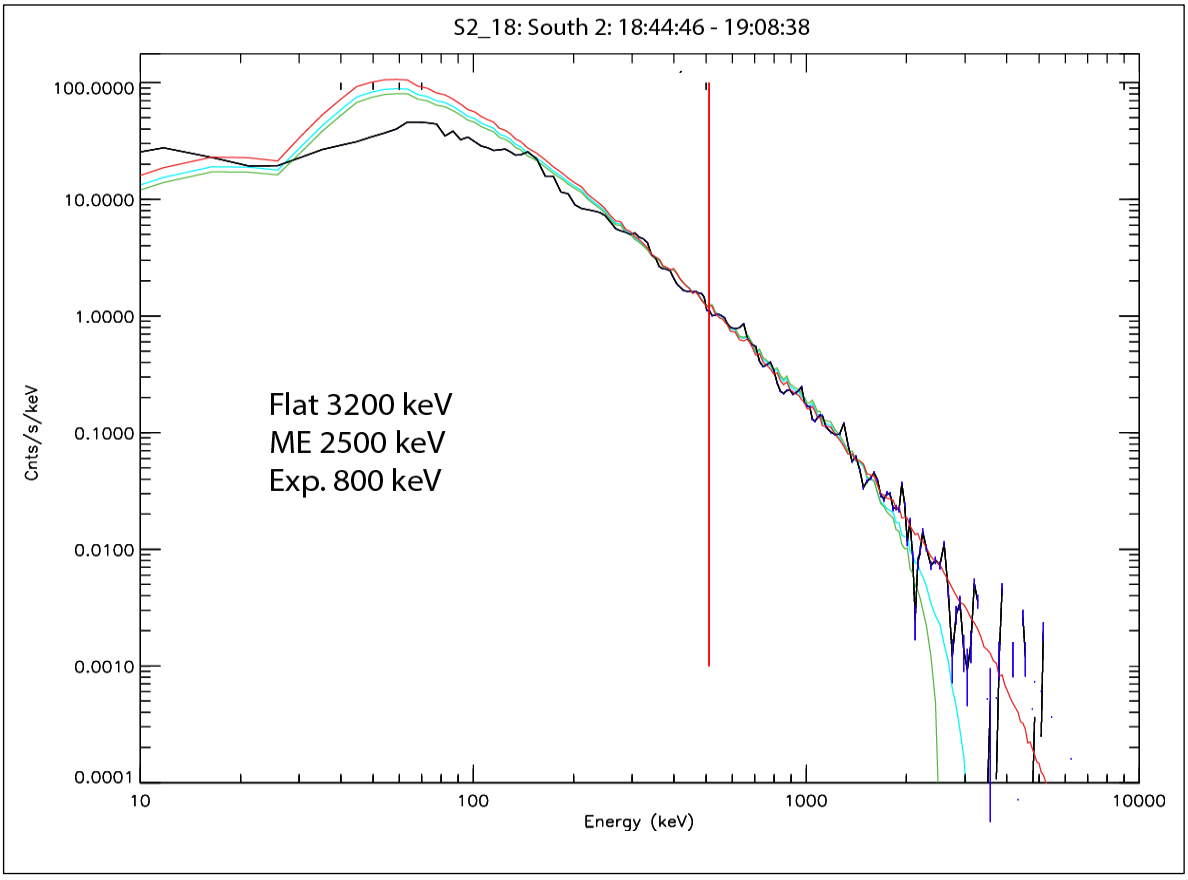
S2_18: South 2: 18:44:46 - 19:08:38
100.0000
10.0000
1.0000
0.1000
0.0100
0.0010
0.0001
Cnts/s/keV
Flat 3200 keV
ME 2500 keV
Exp. 800 keV
10
100
1000
10000
Energy (keV)

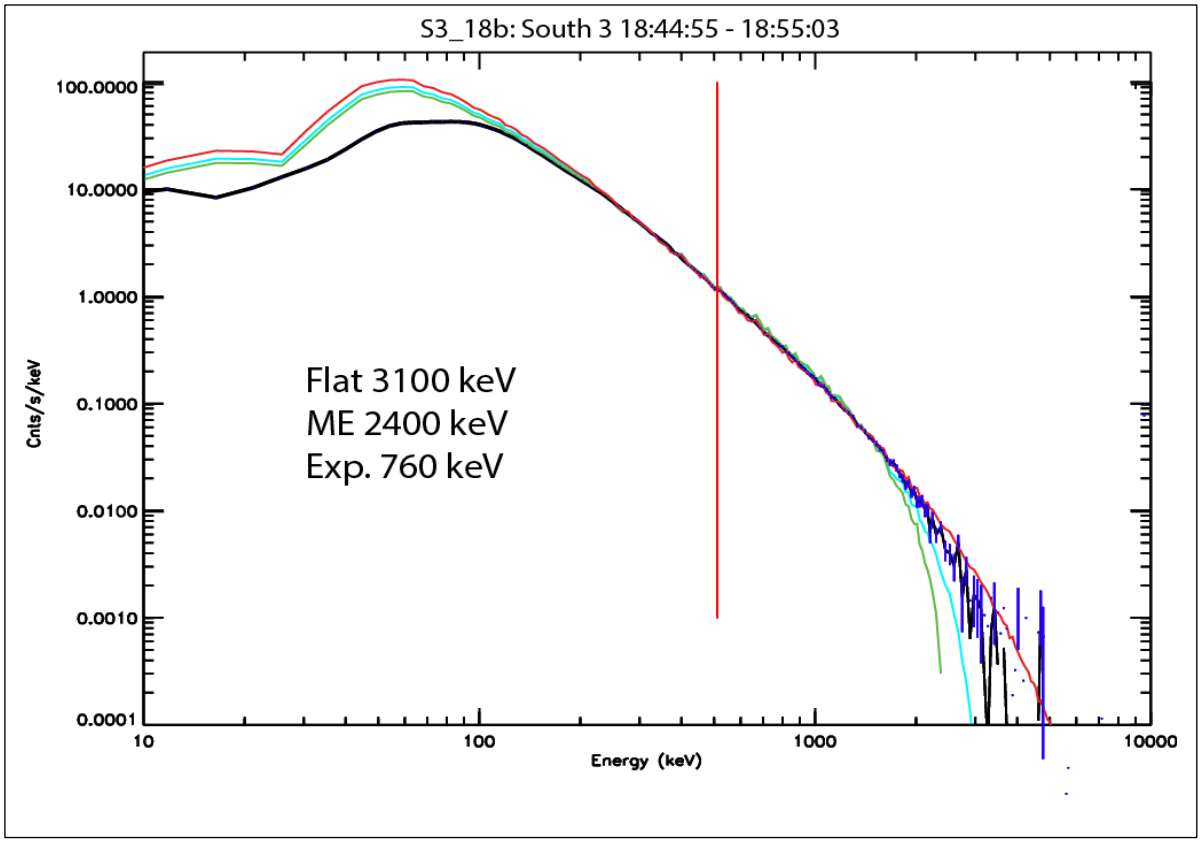
S3_18b: South 3 18:44:55 - 18:55:03
100.0000
10.0000
1.0000
0.1000
0.0100
0.0010
0.0001
Cnts/s/keV
Flat 3100 keV
ME 2400 keV
Exp. 760 keV
10
100
1000
10000
Energy (keV)

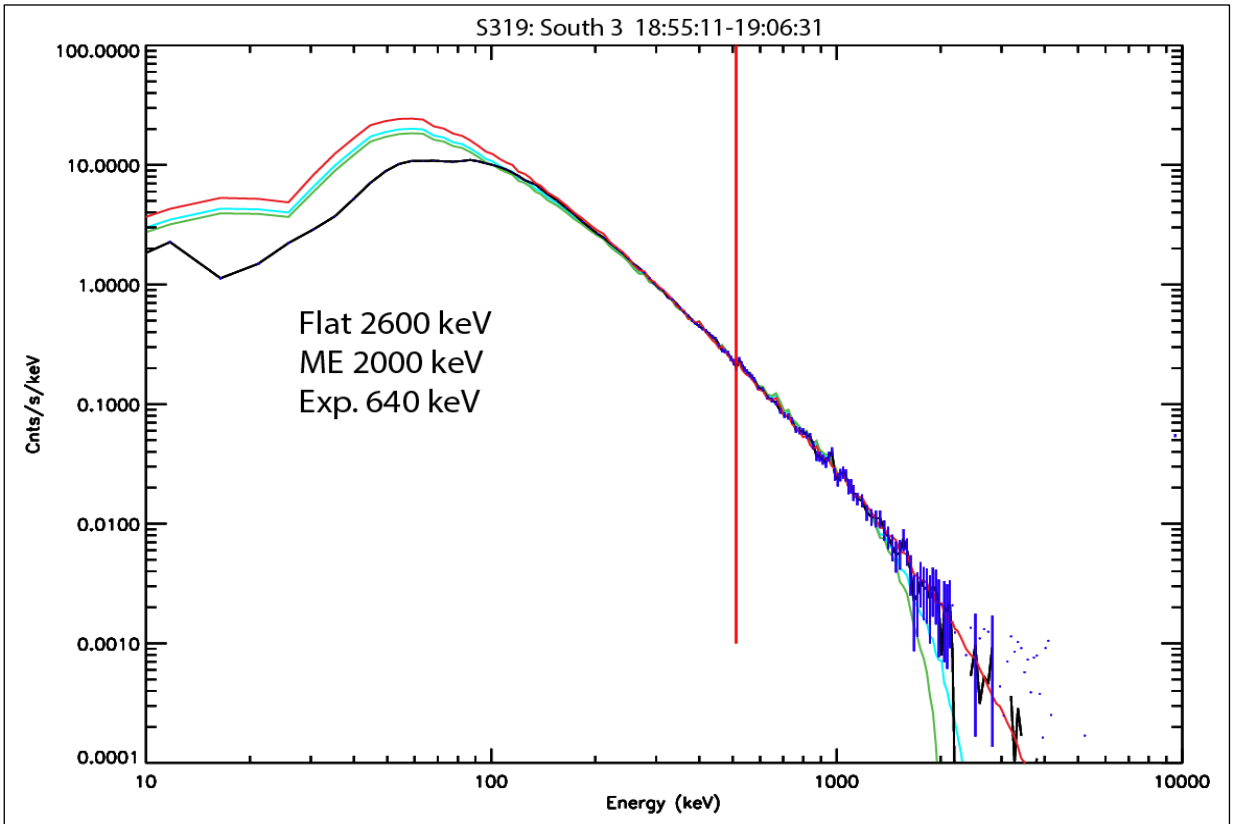
S319: South 3 18:55:11-19:06:31
100.0000
10.0000
1.0000
0.1000
0.0100
0.0010
0.0001
Cnts/s/keV
Flat 2600 keV
ME 2000 keV
Exp. 640 keV
10
100
1000
10000
Energy (keV)

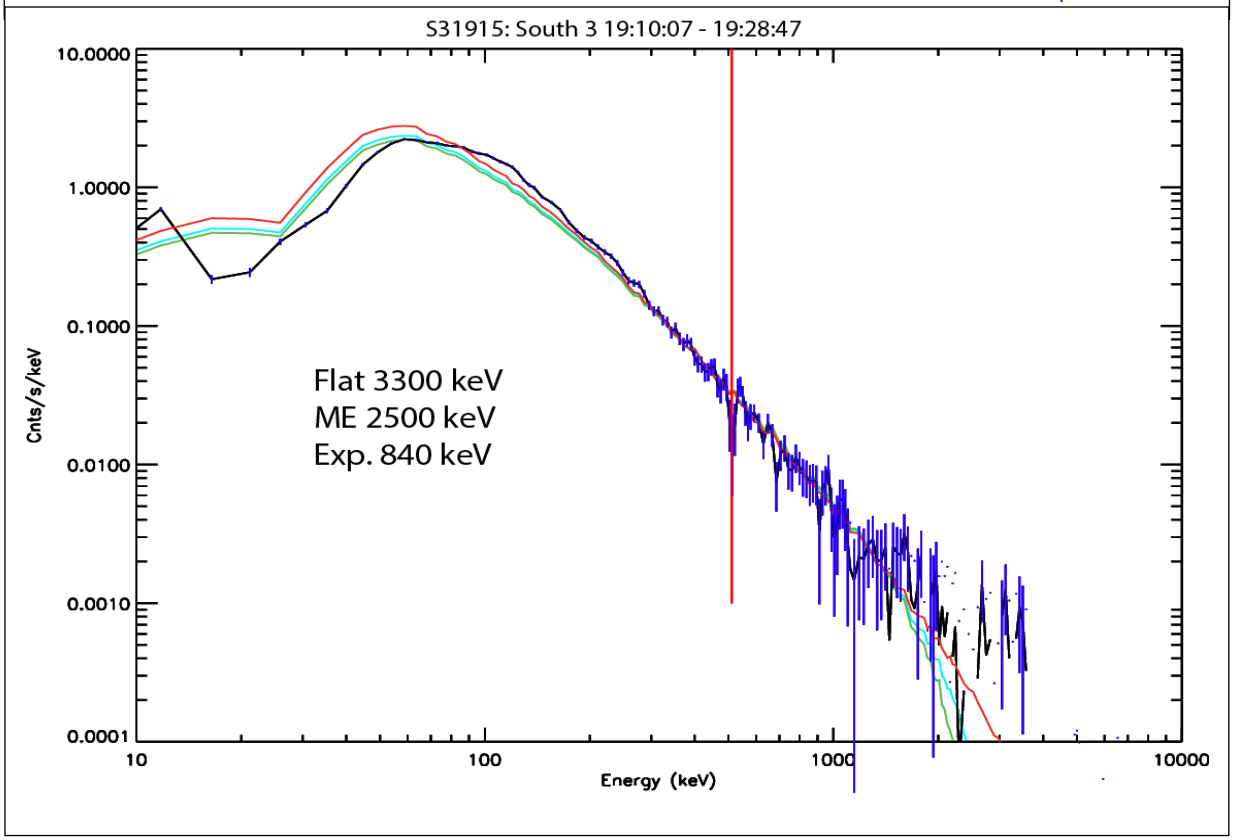
S31915: South 3 19:10:07 - 19:28:47
10.0000
1.0000
0.1000
0.0100
0.0010
0.0001
Cnts/s/keV
Flat 3300 keV
ME 2500 keV
Exp. 840 keV
10
100
1000
10000
Energy (keV)

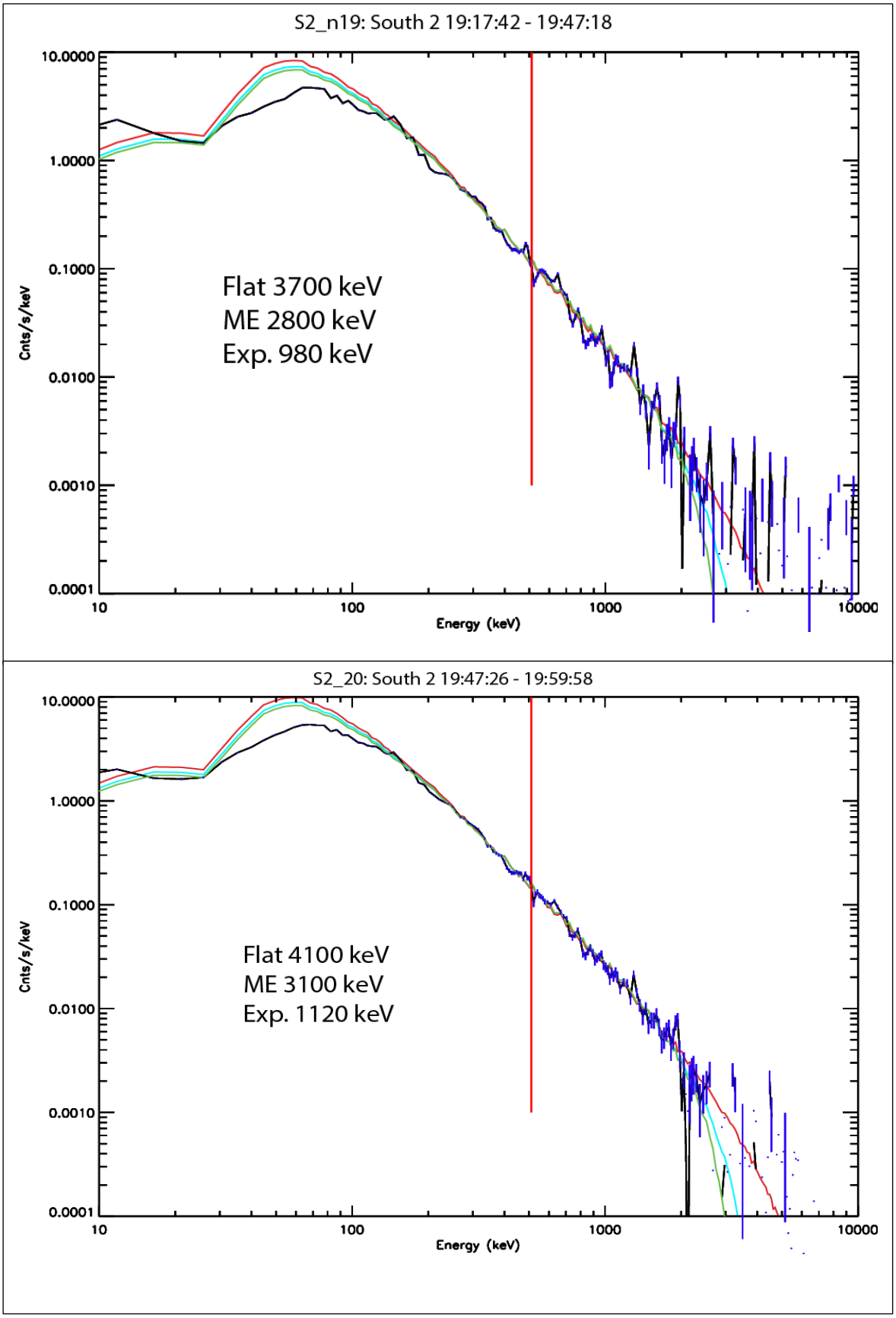
S2_n19: South 2 19:17:42 - 19:47:18
Flat 3700 keV
ME 2800 keV
Exp. 980 keV
Cnts/s/keV
Energy (keV)
10.0000
1.0000
0.1000
0.0100
0.0010
0.0001
10
100
1000
10000
S2_20: South 2 19:47:26 - 19:59:58
Flat 4100 keV
ME 3100 keV
Exp. 1120 keV
Cnts/s/keV
Energy (keV)

specname	best fit exp	gt500 electrons	best fit flat	electrons	best fit ME	electrons	tstart	tend	duration	seconds	exponential local> 500 keV loss
s2_first	700	2895	2900	1824	2200	1025	17:11	17:28	0:17:04	1024.00	1.2E+20
s317a	1240	4205	4700	2409	3500	1421	17:14:32	17:24:16	0:09:44	584.00	9.8E+19
s317b	1340	4652	4900	2797	3700	1599	17:27:44	17:35:28	0:07:44	464.00	8.6E+19
s2_second	700	1949	2800	1341	2200	693	17:28	17:45	0:16:16	976.00	7.6E+19
s3mp	780	1328	3000	934	2300	511	17:41:52	18:02:48	0:20:56	1256.00	6.7E+19
s3md	460	2430	1900	2163	1500	1078	18:02:56	18:18:24	0:15:28	928.00	9.0E+19
s3mu	440	983	1900	822	1500	409	18:18:32	18:31:51	0:13:19	799.00	3.1E+19
flat	360	408	1700	332	1300	178	18:31:59	18:32:39	0:00:40	40.00	6.5E+17
rampa	960	382	3600	252	2700	147	18:32:47	18:33:35	0:00:48	48.00	7.3E+17
rampb	920	753	3500	495	2600	293	18:33:19	18:33:35	0:00:16	16.00	4.8E+17
s3_18a	660	12085	2700	8190	2100	4313	18:33:19	18:40:47	0:07:28	448.00	2.2E+20
s2_rampe	360	1910	1700	1556	1300	836	18:40:14	18:44:38	0:04:24	264.00	2.0E+19
s3int	560	3738	2300	2833	1800	1463	18:40:55	18:44:55	0:04:00	240.00	3.6E+19
s2_18	800	7080	3200	4467	2500	2340	18:44:46	19:08:38	0:23:52	1432.00	4.1E+20
s3_18b	760	7749	3100	4810	2400	2574	18:44:55	18:55:03	0:10:08	608.00	1.9E+20
s319	640	1978	2600	1396	2000	754	18:55:11	19:06:31	0:11:20	680.00	5.4E+19
s31915	840	177	3300	113	2500	64	19:10:07	19:28:47	0:18:40	1120.00	7.9E+18
s2_19	980	461	3700	298	2800	169	19:17:42	19:47:18	0:29:36	1776.00	3.3E+19
s2_20	1120	478	4100	311	3100	381	19:47:26	19:59:58	0:12:32	752.00	1.4E+19

Table 4.1 Shows the best fit numbers for all the spectra shown in the Forward Folding Results section 4.1.3 for each of the three parent electron distributions.

4.3 Spectral comparison to previous DREP

MAXIS found ambiguity in modeling the electron precipitation spectrum, largely because of insufficient counts at high energies for most of the events observed. This ambiguity resulted in most events being comparably well modeled by both exponential distributions of precipitating electrons and mono energetic sources (flat spectra were also successful in modeling MAXIS events) MAXIS saw a total of 9 events, and several were weak enough (or brief enough) that counting statistics dominated the errors. In the brighter events, an estimated error of 20% in the assumed bremsstrahlung cross section dominates. In the case of MINIS, mono-energetic, exponential and flat spectra (as well as cut-off- power-law spectra, but these showed no success in the forward fits.) were considered for each of the precipitation periods and payloads. In each of the longer events on S3 there is some clarity in the choice of spectrum, but that choice is not the same for each event. This increased certainty is the result of the good counting statistics that MINIS NaI detector was able to achieve at the high energy end of the event counting spectrum. Table 4.2 and 4.3 compare the best fit modeled parameters for each of the event periods to the MAXIS data and a comparable set of data for MINIS.

MINIS S2 and N1 suffered from significant spectral degradation. In the case of MINIS s2 that occurred during unexpected radiation damage to the payload during a very large solar energetic Particle event. The cause of the degradation on N1 is unknown although the damage appears similar. For events on S3 where the statistics are good, it is usually possible to rule out either exponential or monoenergetic. Flat distributions, falling between the two other possibilities, are often difficult to rule out. For determining the loss rate in given energy bands such as >500 keV I

Event	Best Fit	Acceptable Fit	>500keV rate from best fit. (e^-/s)	Duration (min)	Total electrons lost in field of view
B2a	E:330	E:325-340	8.70E+17	145	7.57E+21
B2b	E:550	E:490-580	2.20E+17	60	7.92E+20
C2b	F:10000	E:>3000, M:>2400, F:>5000	1.40E+16	15	1.26E+19
C2e_i	E:325	E:350-550,M:900-1000,F:1000-1600	8.00E+16	5	2.40E+19
C2e_ii	E:315	E280-E340	9.70E+16	40	2.33E+20
D1b_i	F:1300	E:360-400, F:1250-1350	2.90E+17	40	6.96E+20
D1b_iii	E:170	E:145-180	9.90E+16	25	1.49E+20
D2a_sp	F:5000	E:900-3000+, M:1500-2600+,F:>2100	2.10E+16	5	6.30E+18
D2b	F:1600	E:390-700,M:900-1600,F:1200-2200	5.50E+16	10	3.30E+19

Table 4.2 Summary of the MAXIS spectral fits.

Event	Best Fit	Acceptable Fit	>500keV rate from best fit. (e^-/s)	Duration (min)	Total electrons lost in field of view
S2_1711	F:2900	E:800-850	5.11E+16	26	1.95E+20
S3_1714	F:4800	E:1500-1750	8.72E+16	45.5	3.73E+20
S3_1833	E:660	F:2600-2900	3.46E+17	7.5	2.17E+20
S3_1844	E:760	F:3100-3400	2.4E+17	11	1.88E+20
S2_1844	E:800	F:3100-3400	2.30E+17	24	4.53E+20
N1_1710	E:1020	F:3900-4100	2.46E+19	11	2.64E+19
N2_25	E:280	F:1200-1300	1.47E+21	150	1.47E+21

Table 4.3 Shows longer integrations of the MINIS data for comparison with MAXIS spectra. Acceptable fit is always given as the exponential range unless exponential is the best fit. This is to allow for integration of the precipitating spectrum into various energy ranges (including the calculated >500keV rate and electrons lost column).

will use the best fit exponential, even if it is not the best fit. For calculations of drift timing, and energy time dispersion, I will use the mono-energetic fits.

Weighted by electrons lost the MINIS observations are harder spectra than the MAXIS observations. Although the hardest spectrum is from MAXIS C2b, this event was relatively low intensity and didn't lose many electrons. The MINIS spectra are definitely harder than the trapped electron spectra at the time see Figure 4.8 which indicates a scattering mechanism that is relatively more efficient at higher energies. This is consistent with scattering by EMIC waves, although EMIC waves have some difficulty explaining other aspects of the MINIS data. The relative hardness of the MINIS spectra make one ask the question what energy the loss rate observed by MINIS becomes significant relative to the trapped population, losses observed elsewhere, and losses observed by MAXIS. This question is explored in the following chapter.

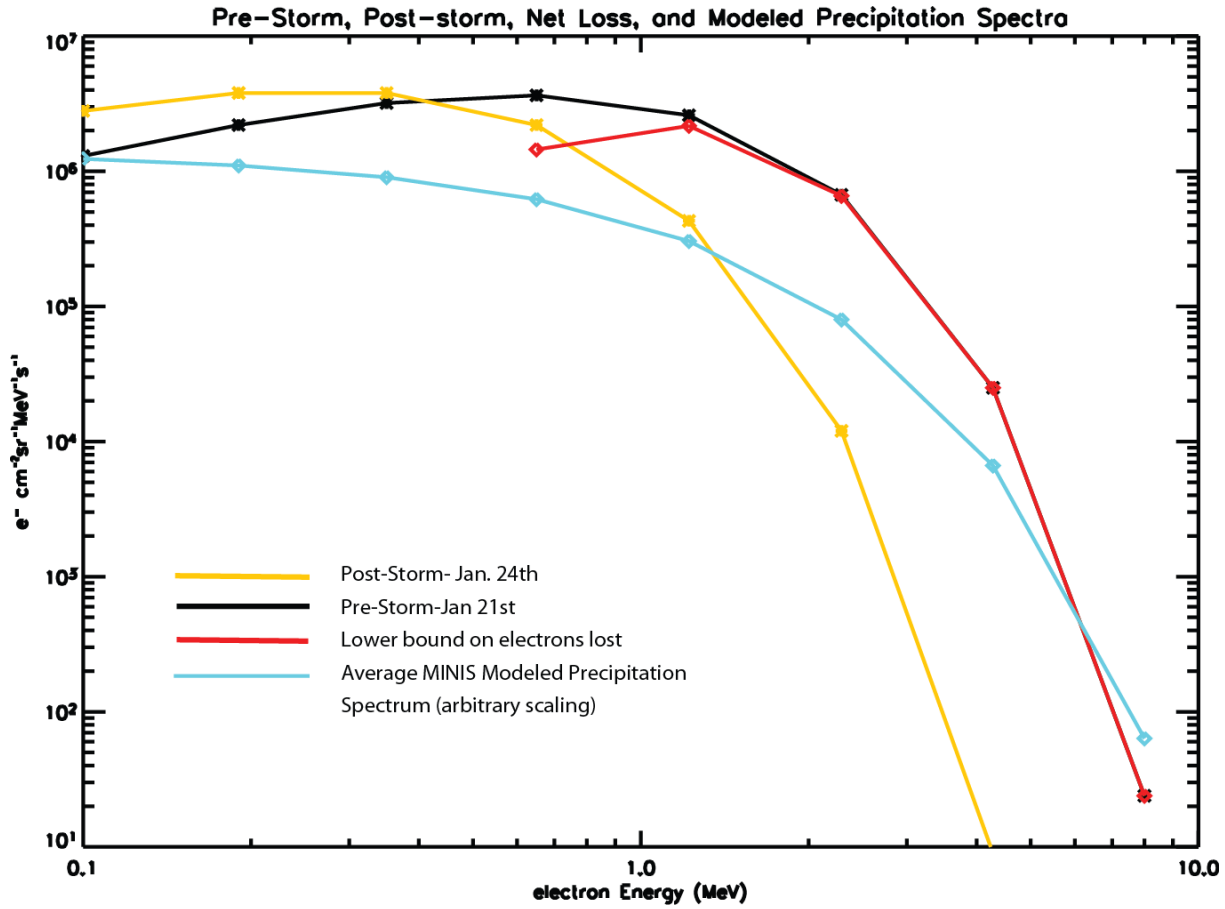

Figure 4.8 The electron spectrum observed by GPS satellites in the L-range around MINIS S3 pre-storm, post storm and the difference (red) show that all three are softer spectra than the losses observed by MINIS (800 keV e-folding shown)

5 Electron Losses from Duskside Relativistic Electron Precipitation

5.2 Loss Rates

5.2.1 Instantaneous local loss rate

The instantaneous local loss rate is simply the result of the previous chapter's forward fitting simulations, but these numbers are ultimately not very important unless weighed against the content of the radiation belts, the changes in radiation belt content, and losses observed by others. Moving beyond the local loss rate is a question of the spatial scale of the precipitation region as well as the duration of the precipitation. The simulation results provided in the previous chapter are for sky-filling, downward-isotropic response matrix calculations. Although this is useful as a direct comparison to previous work, expanding beyond these can provide insight into the spatial properties of the precipitation region and thus provide better quantification of the instantaneous losses.

The instantaneous loss rate calculation (including non-local losses) depends on the relative areas between the FOV of the detector and the area of the region where the electrons are precipitating. If one can correctly gauge the area of precipitation then the number of electrons lost is simply the observed intensity times the duration times the area. MINIS observations of the intensity are shown for the grossly integrated events in the table at the end of the previous chapter. This chapter will look at scale size, attempt to understand the drifting nature of the precipitation, and look at relevance to the radiation belts.

5.2.2 Average loss rate

One way to determine the significance of precipitation observations is to take the average loss rate over the course of the campaign and the region over which the campaign observed. MAXIS found a significant average loss rate of 360 $e^-/cm^2/s$ across the entire region between 58° and 68° magnetic latitude corresponding to an area of $2x10^{17}cm^2$. By comparing this to the number of electrons trapped in this region, Milan [2002] was able to determine a time scale for loss of the entire outer electron radiation belt of 8 days. The MINIS data arrives at substantially lower number for its average rate, even though the intensity of MINIS events was locally often larger than MAXIS. The importance of MAXIS event B2a, which lasted far longer than any event seen by MINIS (or any other MAXIS event), and was bright but soft cannot be overstated to the average loss rate calculations. That event accounted for 80% of the MAXIS electron loss calculation. Had MINIS seen such an event the two campaigns would have seen similar average loss rates.

The closest event MINIS saw to the MAXIS event had a similarly soft spectrum (E_0 = 280 keV) and was found on flight N2 on January 25th. That event, like the MAXIS event, occurred during relatively quiet magnetic conditions. MINIS saw a total of $3.03x10^{21}$ electrons over the course of 350 hours when we were successfully returning data. This averages out to ~60 >500 keV electrons per cm^2/s. Half of these electrons come from the single event, on the N2 payload, which had a soft spectrum of~280 keV e-folding. This event lasted two and half hours at relatively high intensity, but because of the softness of the spectrum, its importance rapidly diminishes at higher energies. That event is also not likely related directly to precipitation from the radiation belts. The event was located at midnight local time (because it lasted so long, it goes from about 2300 to 0100 local time over the course of the precipitation). The event occurred at L-shells >10 and it is softer than the GPS measured trapped spectrum.

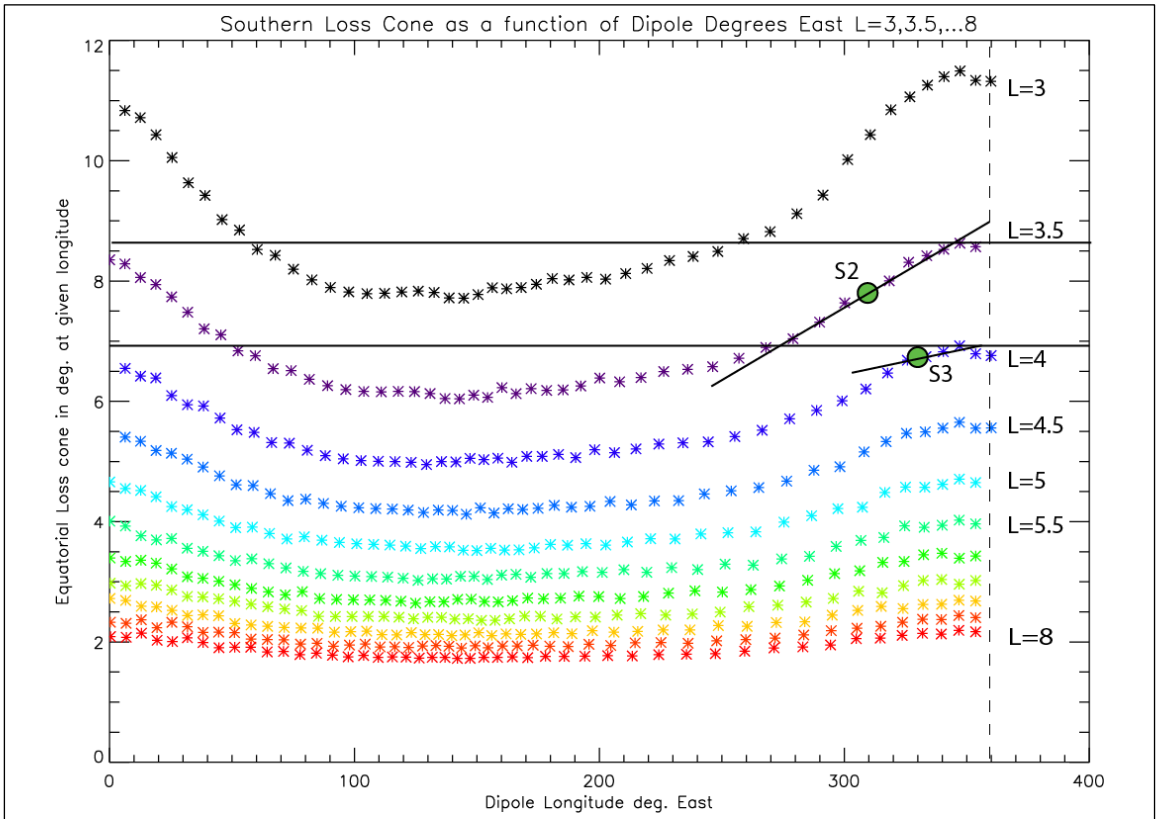

Figure 5.1: The size of the bounce loss cone in equatorial pitch angle as a function of magnetic longitude for 11 L shells. This figure is the result of modeling using the Tsyganenko-89 model. The drift loss cone is the region where particles on an L-shell are above the local loss cone but will drift (to the right) until they encounter the top of the atmosphere.

All of these descriptions point towards losses that occur as part of an injection from the tail. Clilverd [2008] showed that injections from the tail often precipitate 50-90% of the injected electrons. Although tail injections are generally lower energy electrons than those seen by N2 they are still often seen by POES in the >300 keV channel. If we choose to ignore this event for considering Dusk Side Loss from the inner magnetosphere the MINIS precipitation average is ~30 electrons >500 keV per cm^2/s. At such a low rate the losses are not significant for the general >500 keV electron population. Although GPS satellites see substantial losses during this time frame, MINIS does not see them.

If the electrons were not seen by MINIS, where were they lost? They either precipitated in the atmosphere and MINIS did not see them or they were lost out the magnetopause by the large compression. At first glance it is tempting to say that the electrons were simply missed by MINIS, but the location of the MINIS balloons at the extreme eastern end of the drift loss cone implies that they should have seen evidence of significant losses that occurred over more than 280 degrees of magnetic longitude [driftloss]. While the MINIS events may have been partially drifted events, as described in section 5.2, and the loss rate may be substantially higher than the forward folding results from downward isotropic photons show, they are still unable to account for the loss of relativistic electrons from the belts in an average loss rate sense. Instead of

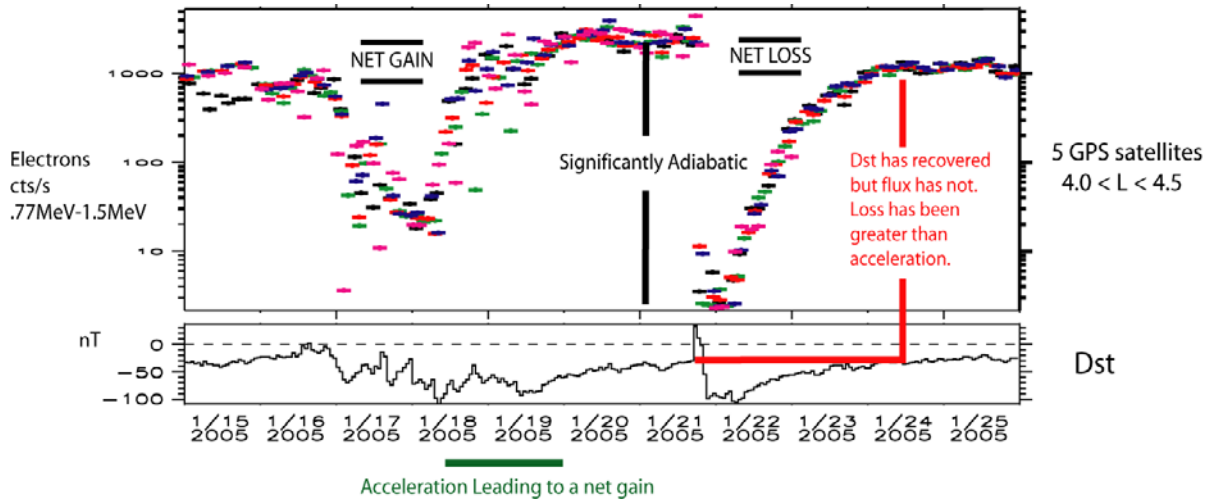

Figure 5.2: The GPS net loss around L=4 is shown in the time region marked in red. Dst has fully recovered and the electron flux is stable for ~1 day. This is a lower bound on the loss of electrons since acceleration is happening concurrently.

averaging over the 350 hours of data returned by MINIS, let us instead average over the time period that it took for the GPS flux to recover around L=4 ~72 hours (see figure5.2). We get an average loss rate of 150 electrons >500 keV per cm^2/s. This rate, if it were occurring everywhere on the dusk side near L=4 would account for ~7% of the actual number of electrons lost. Here I am comparing to GPS observations of > 650 keV electrons since the spectral resolution of the GPS satellites is rather poor. This higher baseline energy should actually favor MINIS as compared to using > 500 keV because MINIS spectra are harder than the lost spectrum.

In any case, it seems likely that most electrons were lost to the magnetopause. Although this result seems dissatisfying it can ultimately be an essential piece of information. Magnetopause losses are virtually impossible to measure. No reported direct measurements exist in the literature and the importance of magnetopause losses is largely confined to the realm of simulation. Having a null result in the precipitation regime (including using the drift loss cone as a catch-all) in conjunction with substantial losses observed by satellites is in itself a valuable measurement.

5.2.3 Comparison to LEO Satellite measurements

Unfortunately, very few satellites made good observations of precipitation during the MINIS observation time period. Because the precipitation was concentrated around the two shock times, it is relatively easy for a polar orbiting satellite like SAMPEX to miss the precipitation while the satellite is at low or extremely high latitudes. The POES satellites did make some observation of precipitation from LEO but because the magnetosphere is reacting strongly to the shocks, it is difficult to directly relate the precipitation seen by POES to the balloon observations. Precipitating electrons > 300 keV from the most closely orbiting POES satellite, N16, are shown in Figure 5.3. For ease of use the MINIS lightcurves from that time frame are also reprinted.

Although precipitation around 18:15 appears weak in the lightcurves, the counts are well above background, and MINIS S2 and S3 do observe electrons at the same time as some POES 16 observation. S2 is at lightly lower L-shells and is slightly below the peak in POES precipitation

but within a ¼ hour of the right local time at the event onset. POES sees ~4000 $e^-/cm^2/sr/s$ in the drift loss cone (locally mirroring detector) when it is closest to directly above S2, while the bounce loss cone measurement at that point is ~10 $e^-/cm^2/sr/s$ of electrons (not shown).

This time period on MINIS s3 is shown spectrally in the previous chapter under the figure title S3mu. It is a low statistics event and thus all three models fit the data. The cross correlation between payloads S2 and S3 is peaked at 0s for this time frame [see figure 5.4], indicating a broad precipitation region where the structure seen is primarily temporal. This region is ~1 L shell wide from L=3.5 to L=4.5 by the POES data, and from the MINIS data it is ~1.5 hours local time.

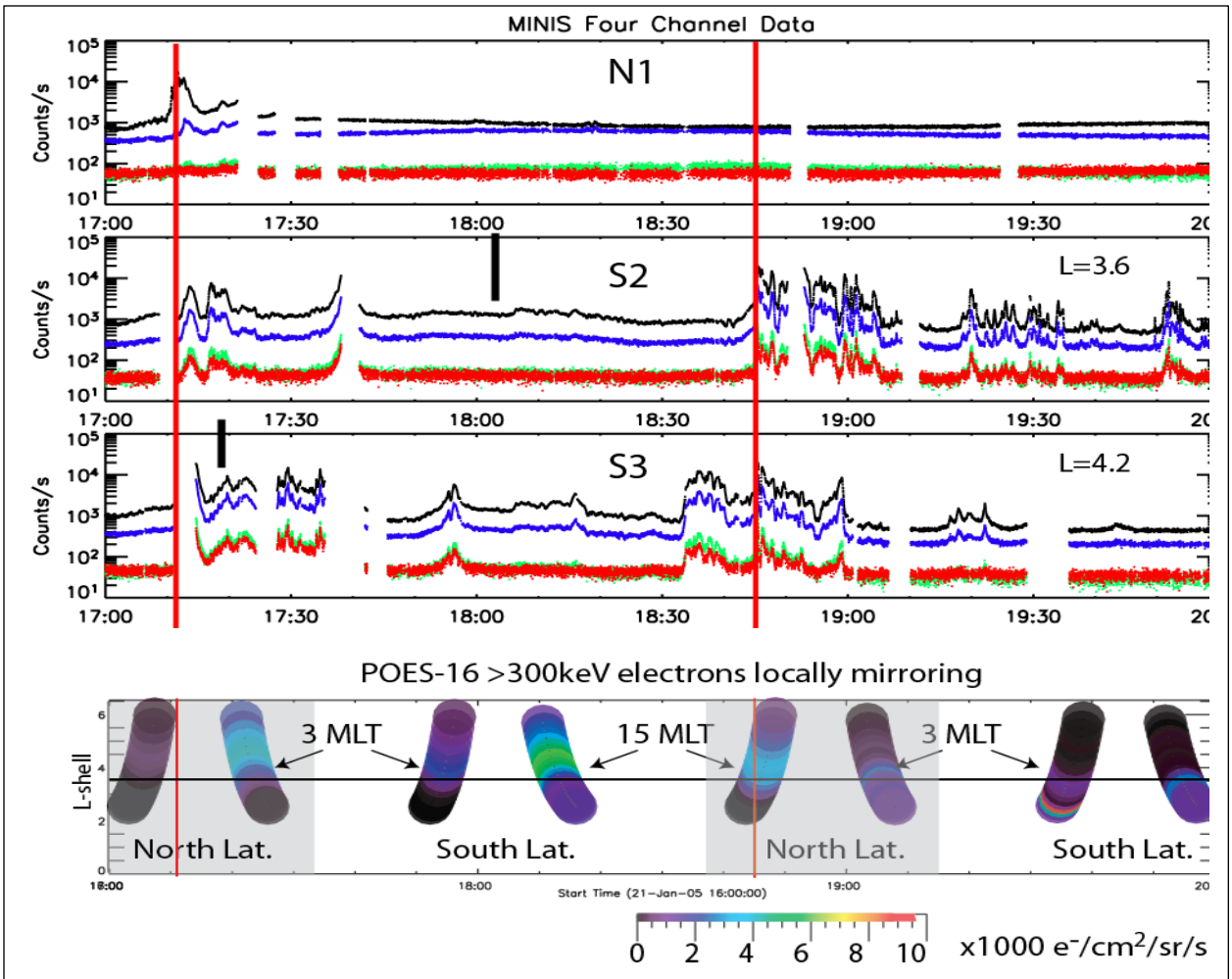

Figure 5.3: MINIS lightcurve data from the time period of most of the precipitation. POES sees precipitation across L=3.9 to 4.6 around 18:10UT. The satellite is at 15MLT and in the south, making it the closest observation we have to the MINIS balloons. The thick black lines indicate the times when the balloons were at MLT=15. The vertical red lines are as in chapter 3, the time when Sym-H jumps

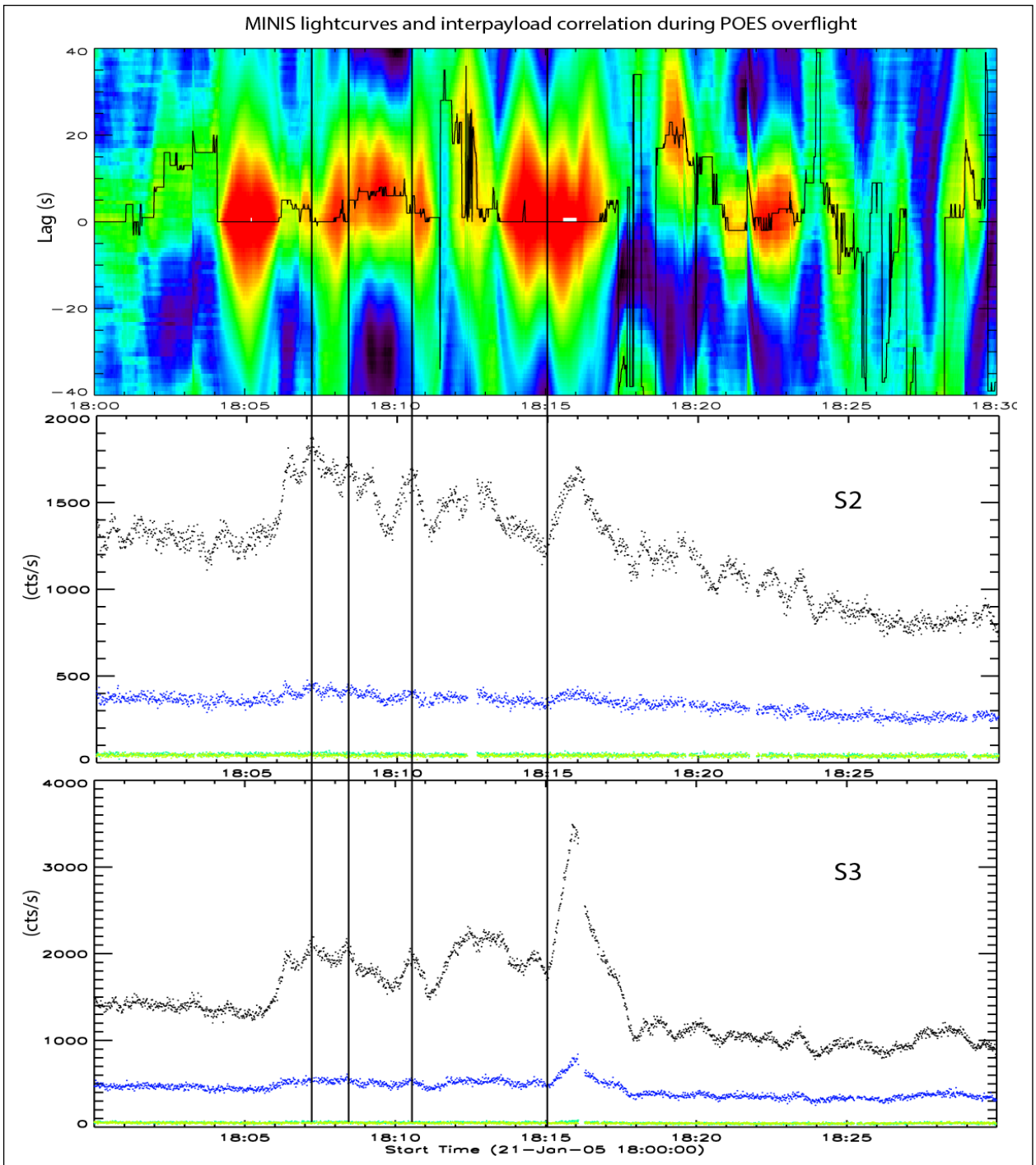

Figure 5.4: the top panel color scale shows the correlation coefficient as a function of the lag between the two payloads (vertical axis with 0 seconds lag in the middle) and time (horizontal axis). The black trace indicates the peak correlation lag as a function of time. A range of lag times up to ±40 seconds was explored and a sliding window of 120 s was used. Bright red corresponds to a correlation coefficient of 0.97 and dark blue anti-correlated at 0.62. The lower panels show the S2 and S3 lightcurves from which the top plot is derived.

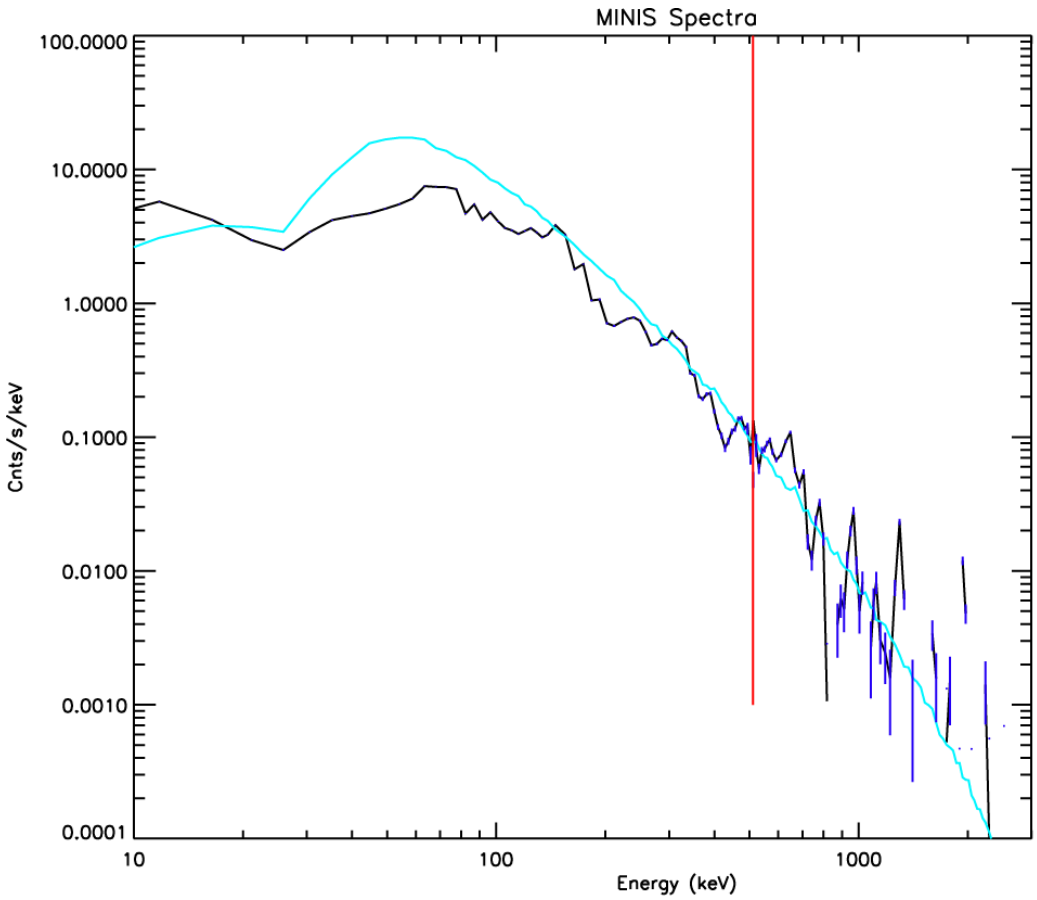

Figure 5.5: The spectrum from S2 when a POES overflight was measuring >300keV electrons *in situ*. The best fit is E0=420 keV shown in cyan.

The measured POES flux is far from isotropic, and many of the electrons that it sees in the locally mirroring channel will precipitate further east as drift loss. We can compare, or at least bound, the the *in situ* satellite vs those of the MINIS observations for the event on S2 which was extremely close to the satellite footpoint. The S2 spectrum from the time range of the POES overflight is shown here in Figure 5.5 with the best fit exponential (E_0 = 420 keV). That forward fit has a >500 keV precipitation rate of 1800 $e^-/cm^2/s$. The > 300 keV flux is algebraically computed for comparison to POES as 2850 $e^-/cm^2/s$.

The POES detectors are ±15° detectors and at the ~850 km altitude of POES the size of the local bounce loss cone is 45°. MINIS is observing the integral of everything that is in the local loss cone, while POES samples part of that range as well as the locally mirroring population. A schematic of the POES observation angles is shown here in figure 5.6. IF we take the POES >300 keV precipitating channel and multiply it by the size of the local bounce loss cone 1.84 sr, we get a precipitation rate of 18 $e^-/cm^2/s$. This is more than two orders below the MINIS observation. If we assume the electrons have a sin(α) distribution as is often measured for the bulk population near the equator when better angular resolution has been available, we would still find substantially more flux than is actually measured in the precipitating channel (~10 $e^-/cm^2/sr/s$) . If instead we fit to a $\sin^n \alpha$ distribution where we choose n such that the flux in the

precipitating and mirroring detectors match we find n = 3.1 which is identical to the value measured by Vampola [1996] at the L=4 equator. The exponent is not often a reported value at LEO. Using this distribution and integrating it over the local loss cone gives an estimate of 1200 e^- /cm^2/sr/s, as the average flux in the loss cone. When multiplied by the size of the loss cone at POES, 1.84 sr, we get ~2200 e^- /cm^2/s electrons precipitating above 300 keV. While this number is slightly lower than the MINIS observation of 2850 e^- /cm^2/s, it is important to remember that the MINIS number was arrived at using a downward isotropic pitch angle distribution. Using a $\sin^{3.1}\alpha$ distribution will substantially increase the number of electrons the forward fit requires to match the data, in fact it will likely exceed the value from assuming that distribution in the POES data. The numbers are comparable and a naive interpretation of the MINIS data falls between the expected value from using either the precipitating or locally mirroring channel.

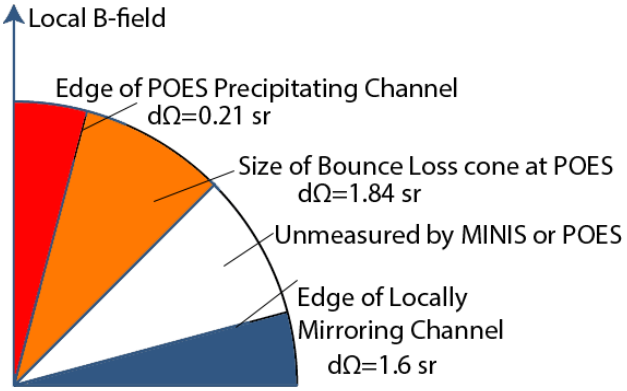

Figure 5.6: MINIS observes the sum of the orange and red regions. POES observes the red and the blue separately, and no instrument is locally measuring in the white region.

This event is barely noticeable in the lightcurves. Indeed it was not initially processed on S2 and thus it is not surprising to find that downward isotropic is not a good fit. Downward isotropic implies strong scattering, and strong scattering gives very high intensity precipitation. The next section looking at GPS data surprisingly finds again that the data is not likely downward isotropic even for those events that show up as very bright events in the MINIS data.

As a caveat, using a relatively low energy precipitating channel such as > 300 keV has difficulty in capturing losses relative to other measurements because GPS actually sees a net gain at these low energies, so the precipitation may be coming from acceleration of new particles to 300 keV like water spilling from a 'splash catcher' [O'Brien, 1964]. Although this 'losses as a byproduct of acceleration' theory was proposed for 40 keV electrons at the time, it may apply at these higher energies as well. Indeed a different O'Brien [2003] found that storms that showed the most microburst precipitation were also those where the trapped flux actually tended to increase. Losses at >300 keV combined with observation of increases in the trapped flux at those energies do put elevated limits on the source terms for those particle populations.

5.2.4 Comparisons to GPS satellite particle detectors

The change in the spectrum of energetic electrons as seen by GPS near the magnetic equator was shown in the previous chapter in figure 4.8, and a time series of GPS electron measurements in a broad channel is shown earlier in Figure 5.2]. The time series shows a far more dramatic loss than actually occurred because it captures some of the 'Dst Effect' an adiabatic reorganization of the particle population that makes a particle detector observing at fixed energy (which is not an adiabatic invariant) and position see far greater losses than are really occurring (discussed in greater detail in Chapter 1). This prevents us from looking at the number of electrons that GPS

sees as lost during the time range when the radiation belt particles are moving due to adiabatic effects. Since particle acceleration is occurring concurrently the net effect is that the change in GPS flux is a lower bound on the number of electrons lost.

5.2.4.1 Loss cone filling factors

To determine the relative amount of the GPS measured flux that is showing up in the loss cone > 500 keV and > 2 MeV we integrate the pre-storm GPS data above these energies and compare to the balloon measurements using the equation: This allows us to determine the efficiency ε of the scattering process at those energies.

$$f = \epsilon \cdot (\Delta\Omega) \cdot J_{eq} \cdot \frac{\varphi}{24} L \cdot \Delta L \cdot R_e^2$$

Where φ is the local time FOV of a single balloon, $(\Delta\Omega)$ is the size of the loss cone at the GPS satellite which at L=4 is 0.077 sr, J_{eq} is the flux at the equator, f is the rate seen at the balloon for a typical event, and ϵ is the loss cone filling factor, basically an efficiency at scattering.

> 500 keV	> 2 MeV
J=4.9x10^6 e$^-$/cm^2/sr/s f~10^{17} e$^-$/s ⇨ ϵ=2.4x10^{-4}	J=2.0x10^5 e$^-$/cm^2/sr/s f~10^{16} e$^-$/s ϵ=6x10^{-4}
Table 5.1 Summary of the loss cone filling factor calculations for 2 energy ranges.	

Loss cone filling factors are extremely low, implying again that the precipitation is not filling the loss cone or the GPS particle flux is relatively peaked near the equator such as in a $\sin^n \alpha$ distribution. If we take n ~ 3 from Vampola [1996], which used CRESS measurements, we get an increase in these efficiencies by a factor of ~250 or:

> 500 keV	> 2 MeV
⇨ ϵ=6.2x10^{-2}	ϵ=1.5x10^{-1}
Table 5.2 Summary of the loss cone filling factor calculations for 2 energy ranges assuming a peaked equatorial PAD with n=3.	

While these numbers are far more efficient, they don't change the loss rate calculations, they have effectively increased because we assumed the trapped population is peaked near 90° (as it often, but not always, is). GPS measurements of radiation belt electrons provide no pitch angle information, so it is a substantial assumption to take a 4π measurement and interpolate it down to 0.077 sr. Even assuming a peaked equatorial distribution at most we have found a relatively low percentage of the electrons that were starting out very near the loss cone are being scattered into the loss cone. But since we are considering a pitch angle distribution which starts with relatively few electrons near the loss cone, the loss rate relative to the entire population of radiation belt electrons is still small.

The strong diffusion limit is one in which particles near the loss cone see diffusion such that they are scattered more than the size of the loss cone in 1/4 bounce period:

$$D_{\alpha\alpha} \geq D_{SD} \approx {\alpha_L^2}/{2\tau_{1/4B}}$$

The efficiencies at scattering particles near the loss cone into the loss cone would be 100% for processes that are characterized as strong scattering. EMIC waves in particular reach wave amplitudes required for strong scattering at very modest levels [Thorne and Andreoli, 1980]. If EMIC waves are responsible for the MINIS observed precipitation the amplitude of those waves would be in the 10s of pT range based on these relatively low loss cone filling factors.

If the loss cone filling factors are relatively low, as is most likely the case, should we continue to assume downward isotropic pitch angle distributions when forward fitting and to determine the number of electrons lost? We have already seen for > 300 keV that the POES detectors see a weakly precipitating (but not entirely mirroring at the top of the atmosphere) pitch angle distribution during the relatively quiet time around 18:15 UT. Using a mirroring distribution increases the required number of electrons by almost an order of magnitude for the MINIS events. Using the forward fit results from a mirroring distribution brings the loss cone filling factor up to 60%-150% if we assume the GPS PAD is peaked near 90° with n=3. Obviously one of the assumptions that drove us to a mirroring distribution is an exaggeration of reality. For instance, the pitch angle distribution at the equator could be somewhat less peaked. It is also likely that the two extremes of 'downward isotropic' and 'mirroring at the top of the atmosphere' bound the actual distribution at the top of the atmosphere. Future balloon observations which will compare to far more accurate (including energy and angle resolved fluxes) equatorial measurements should consider using a response matrix setup that can adapt to a range of angular distributions at the top of the atmosphere. Since the angular distribution at the equator is such an unknown for the MINIS time frame, only the extreme cases were modeled.

5.3 Is the Precipitation Region Drifting?

One of the observation goals for MINIS was to separate out spatial and temporal variation in relativistic electron precipitation. MINIS had a better capability of understanding drift loss vs. bounce loss precipitation than previous single point measurements because the two payloads that are observing precipitation can be correlated. However, with only two points that are different enough in L-shell that the ‘downstream’ payload could easily be seeing temporal structure from electrons which are unrelated to the relevant drift loss cone it is non-trivial to determine the spatial and temporal variation. The following sections attempt to place bounds on the processes which shape in space and time the observed precipitation.

It is also true that the large shocks that strike the magnetosphere during this time frame dominate much of the time structure that we see and cross correlation of the payload lightcurves tends to grab onto these large shifts. The time frame around 18:34 UT when payload S3 sees precipitation without a substantial change in the magnetosphere while S2 sees nothing is one instructive time frame. The second time frame of interest is ~18:45 UT when both payloads see a sharp rise nearly simultaneously. A cartoon of the precipitation regions before and after this sharp rise is shown in Figure 5.7.

Figure 5.7: Since the location of the boundaries in precipitation as observed by the two payloads is unknown, rates of boundary motion as the region expands will only be upper limits and precipitation areas will only be lower limits.

Although this figure is obviously a simple schematic, one of the more important items to remember about the two point measurement is that only the existence of a precipitation boundary between the two payloads, not the location of that boundary along the distance separating the payloads, can be deduced from a simple analysis. Nor is there any information about the total extent of the precipitation except that during the times when both payloads are seeing precipitation, the region of precipitation is at least as large as the payload separation. If the payloads were substantially further apart multiple precipitation regions might be suspected, but in the MINIS case this seems unlikely.

5.3.1 The Sharp Edged Model

Looking closely at the lightcurves from MINIS data, onsets are often preceded by small ramp-ups in intensity. Is it possible that this is simply the drifting electrons coming into the field of view as they drift? If we assume that the intensity and spectral shape of an event doesn't vary substantially around onset we can attempt to see what the time series at the payload will look like in the MINIS data for that precipitation region drifting (or being driven) towards a payload. Starting with payload S3 at ~18:34, we can take the best fit spectrum from the forward fits after the rise time has passed, in this case an exponential fit with E_0=660 keV with a fixed number of

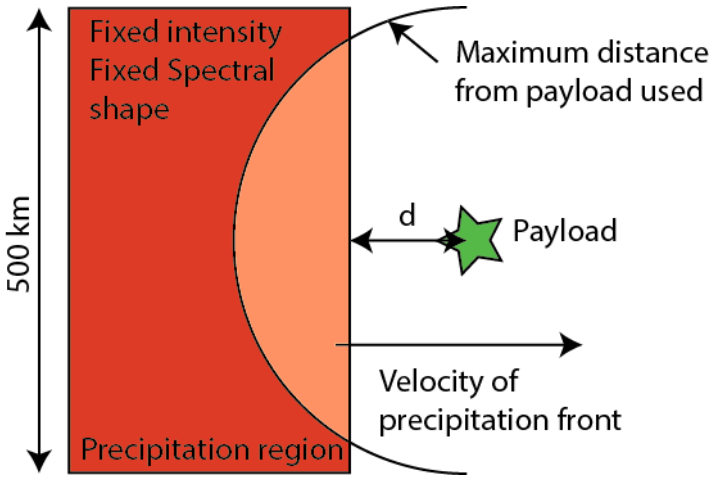

Figure 5.8: Response matrices were generated as a function of the precipitation regions distance d to the payload. For the pictured distance only the precipitation in the orange region is considered as having access to the payload.

electrons precipitating /cm^2/s, and process that through a series of response matrices that represent what a sharp edged precipitation region would give at the payload. A schematic of this process is shown here in Figure5.8.

To accomplish this, 150 separate response matrices were binned from the Monte Carlo results as a function of the distance 'd' in Figure 5.8. This series of response matrix cuts is not the same as the binning of results by radius discussed in Chapter 3 as care was taken to simulate an advancing wall. The simulation included all photon launch sites out to 250 km from the payload. By keeping the intensity in the red region constant we can vary the velocity of the precipitation front and we will see what onset would look like from such a precipitation region advancing on the payload. As described in chapter 1, the drift frequency of electrons scales with electron energy. If we transform from the large drift path to local velocities the drift velocity of the precipitation point for a 1 MeV electron at L=4 is ~22 km/s. The velocity of the equatorial guiding center is substantially higher, 170 km/s. In general for radiation belt L-shells the ratio of these velocities is ~2L. Although the term drift is used because the motion associated with the third invariant is the slowest of the three invariant motions, the drift motion appears very rapid from the balloons' point of view. The rise time from an advancing precipitation region is shown in comparison to S3 at 18:34 in Figure5.9.

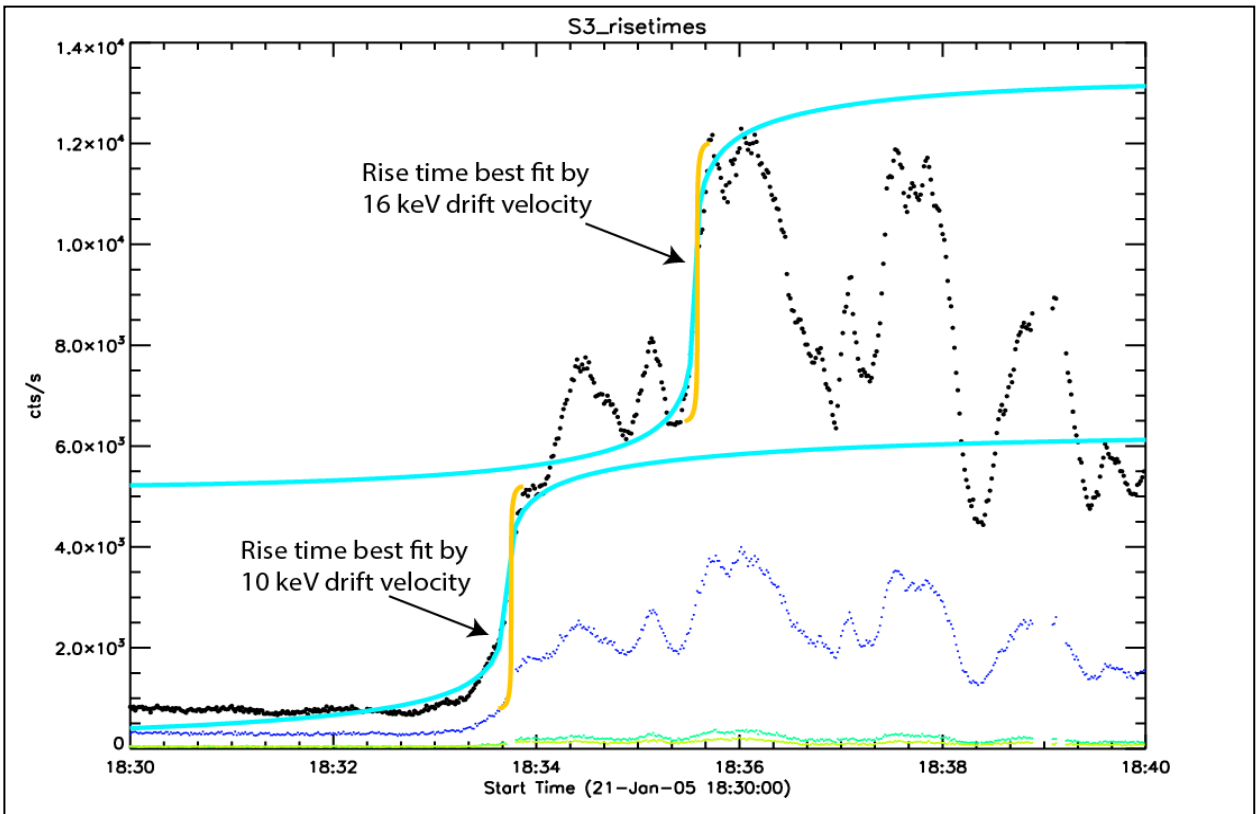

Figure 5.9: The cyan curves are the best fit drift velocities, while the yellow curves are the 22 km/s drift velocities of a 1MeV electron. The actual rise times are 60-100 times slower than the 1 MeV drift would give and even slower when compared to the expected 2 MeV electrons which result from the forward fit.

The S3 rise time in this time range is substantially slower than the rise time one would expect from the drift of a sharply defined precipitation region such as this model supposes. The best fit velocities of the advancing front are ~0.2-0.3 km/s. This would be the drift rate of the footpoint of a 10-16 keV population. Since we can actually get the spectrum of the precipitation from the general forward fit and find it is consistent with ~2 MeV electrons (twice as fast as the rise time shown in yellow), it is clear that the rise time seen in MINIS data is not due to a drifting source coming into the field of view. This leaves two possibilities, spatial gradients or inherent temporal structure.

The idea of a spatial gradient in intensity is relatively simple. In order for the ~2 MeV electrons to appear as if they approached the payload at the rate of a 10 keV electron naively requires a very gradual spatial gradient, 200 x the size of the field of view to get from zero to full intensity. This would include lots of time with weak precipitation on the horizon (the long tails seen in the cyan curves), probably not something that MINIS could see. The simulation for full intensity on the horizon is already starting out comparable to background levels. But if we focus only on the ~12 second sharp rise seen in the data around the center of the simulation (this is when the precipitation front passes over the payload, the simulation is symmetric about this point, e.g. just before 18:34) and multiply that time by the 44 km/s drift velocity of a 2 MeV electron we would estimate the region of gradual precipitation onset (approximately zero to full intensity) to be ~500 km.

This is comparable to, indeed larger than, the inter-payload separation when magnetic latitude alone is considered (200 km). We can consider the latitude separation only because longitude separation would be covered by drift. If we assume meridional gradients are comparable to latitudinal gradients it is surprising that S2 does not see at least some level of precipitation during this time period. For a drifting region of 2 MeV electrons S3 would see a delay of ~20 seconds relative to S2 during this time frame, since the event lasts far longer than that drift delay, and is seen only on the more easterly payload, it seems clear that the rise time seen at S3 is predominantly temporal and local.

5.3.2 Rapid expansions of the precipitation region

The rise time at S3 discussed above occurs when very little is happening in the magnetosphere. No shocks have arrived, no storm-time ring current has yet developed, and the rise time appears to be from a gradual temporal turn on of the precipitation rate, more so than from large spatial gradients or from a drifting region. This is not the case with the rise time at S2 and S3 during the second shock arrival at 18:45 UT. At 18:45 UT S3 is already seeing moderate levels of precipitation, the tail end of the previous section, but S2 is seeing very little. Then within 3-4 seconds the precipitation region expands to encompass both S2 and S3 5.10. S2 sees the precipitation first, so the precipitation front is moving eastward (later local times) or southward (higher L-shells). If we consider only the timing difference between the two as a drift delay, the 3.5s corresponds to a drift energy of ~11 MeV electrons. This is well higher in energy than the spectral fit predicts (~2.4 MeV fits both payloads), i.e. the timing is much faster than just a drift delay.

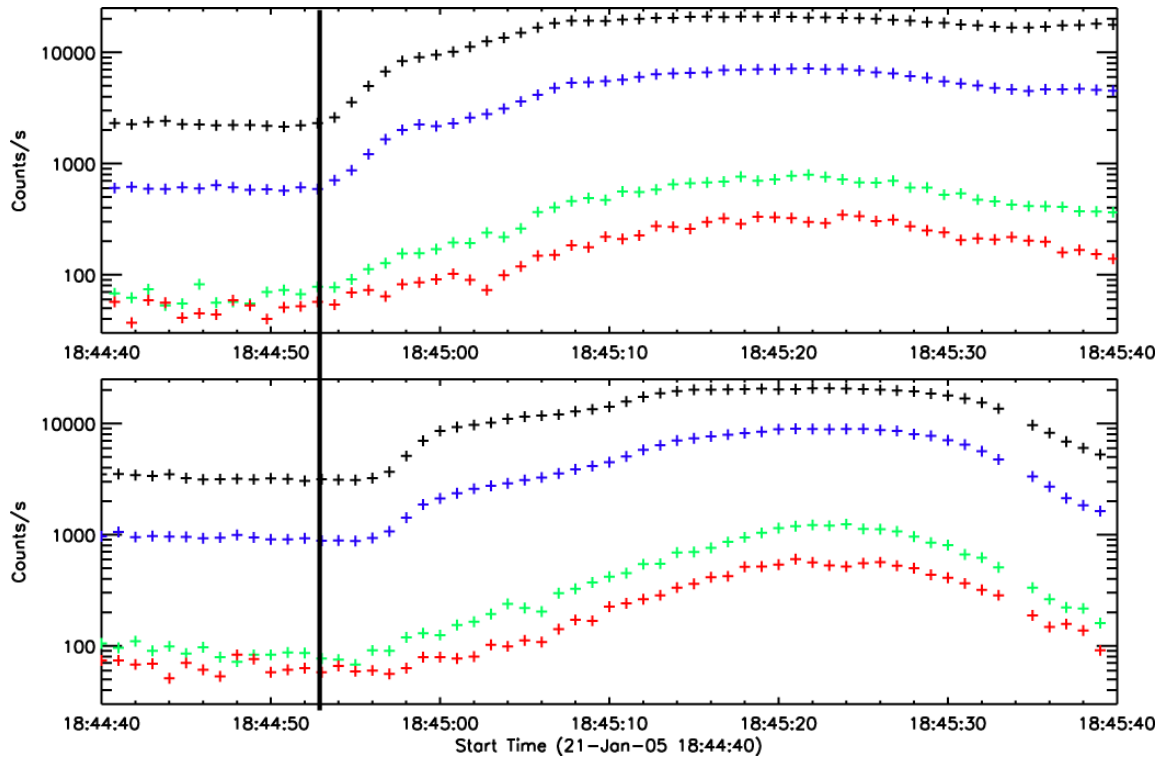

Figure 5.10: S2 (top) and S3 payload lightcurves during a rapid expansion in the precipitation region.

We can also look at the rise time in the same manner as we did in the previous section. Although a gradual temporal rise was seen there, because of the shock timing, it seems more likely here that the rise times will be related to a spatial expansion. If we model, under the same sharp edged assumptions (which may be more valid here as it seems to be a driven expansion of the front as opposed to a drift) the S2 rise time and related model fits are shown in Figure 5.11. Again the rise time is well slower than a sharp edged drifting region would imply. The rise time is consistent with a 0.23 km/s velocity. This is a lower limit on the actual velocity that the precipitation region is advancing at because the rise is potentially still due to the convolution of a spatial gradient, the gradual initiation of a precipitation mechanism and the motion of the precipitation region into the field of view. A slow turn on time could still be relevant, but is not part of the current model, slowing down the temporal rise could lead to a lower velocity from the model.

If the rise is a rapid expansion in the latitude of precipitation we can compare the velocity to other rates expected in the magnetosphere. For instance Berkey [1974] finds expansions in latitude on the order of ~1 km/s although mostly at higher latitude. Recent work on the POES data set from substorms shows a latitude expansion rate of 6 L/ hour [Clilverd, 2010] which is an order of magnitude slower than the Berkey number when computed at L=6. The MINIS expansion rate falls in between these limits, but again, the MINIS number is a lower limit based on the rise time at S2.

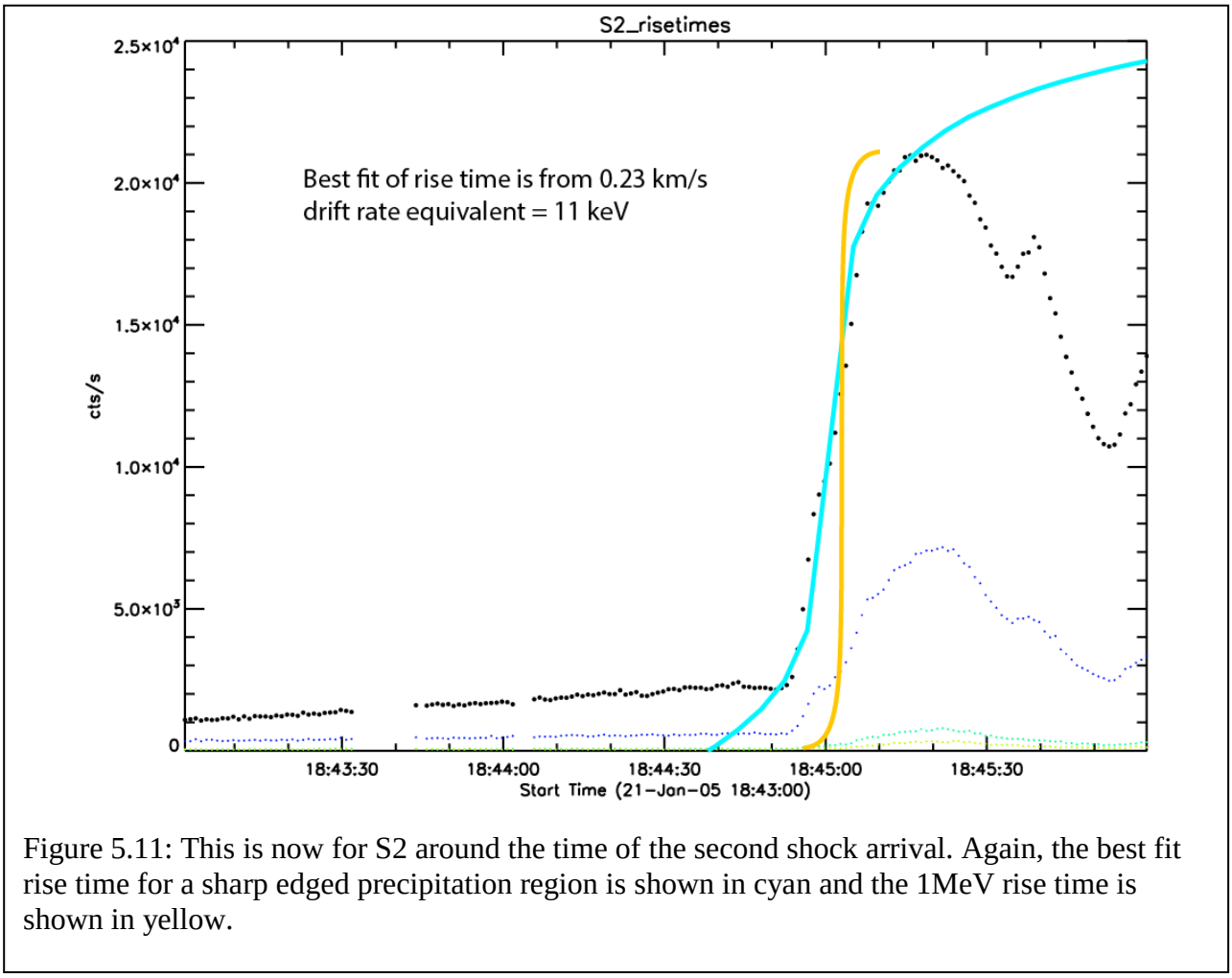

Figure 5.11: This is now for S2 around the time of the second shock arrival. Again, the best fit rise time for a sharp edged precipitation region is shown in cyan and the 1MeV rise time is shown in yellow.

MINIS can also give an upper limit on the expansion velocity based on the timing between these two payloads. The upper limit is equal to the latitude separation ~200 km divided by the delay between S2 and S3 in the onset of their precipitation rises (which is not likely due to drift). In this case the latitude expansion velocity is ~60 km/s. This is well faster than the Berkey limit, but again, since we are unsure of the initial position of the precipitation boundary, this is only an upper limit. Likely the distance covered in those few seconds is less than 200 km.

If we transform to the magnetic equator where most scattering is considered to occur we can compute the speeds connecting the two observation points. The rise time arguments give ~ 8x the velocities they did before, and the distance over time calculation gives, for a dipole field model, 7400 km equatorial separation and thus a velocity upper limit of 2100 km/s. This is comparable to the velocity of an Alfven wave acting near the equator at L=4 with a density derived from the IMAGE satellite. Although IMAGE was not in a particularly good geometry to observe the plasmasphere at the time of this precipitation 5.12, the IMAGE data can also be fed into a test particle model that returns an approximate Hydrogen equivalent ion density of 20-40/cm^3 [J. Goldstein, private comm]. If we take 30/cm^3 as our density, the Alfven velocity at L=4 is 1800 km/s with a range of 2240-1580 km/s based on the broad density range. Thus a compressive pulse, likely the transmitted wave from the shock impact, traveling through the magnetosphere appears a likely candidate for the coincident rise in precipitation at these locations.

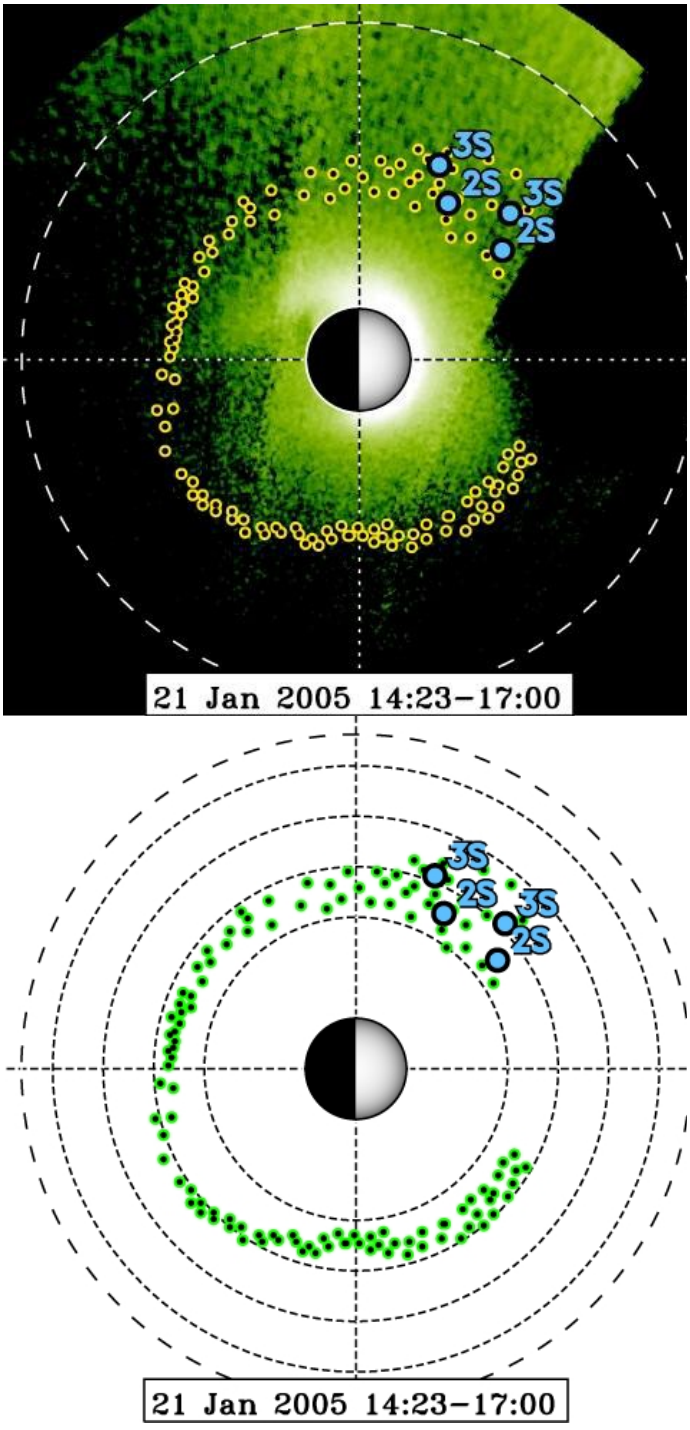

Figure 5.12: shows the position of the MINIS payloads mapped to the equator imposed on top of IMAGE plasmasphere data. The bottom plot is the plasmapause location as determined by an algorithm [Goldstein, 2004] *images courtesy J. Goldstein.*

5.3.3 Time-Energy Dispersion

We have one additional way of looking at the rise phase of the precipitation which may provide insight into the spatial scale and location of the precipitation region. If we do forward fits of the precipitation spectrum during and just after the precipitation onset we can determine the approximate relative delay between different energy electrons. MeV electrons bounce and drift faster than 500 keV electrons. Under the assumption that they are scattered at the same time and same location their arrival times at the balloon will be slightly different depending on where they were scattered. The S3 lightcurve from this time range is plotted here in figure 5.13, with regions of different spectral hardness identified as above or below the 95-105% average hardness.

If we take forward fits from the rise phase of the precipitation around 18:33 UT we get (for monoenergetic fits) a rise time spectrum consistent with ~2.6 MeV and the subsequent precipitation consistent with 2.1 MeV electrons. These spectra are taken with an 8 second gap (one spectral data product apart). If the difference in rise time arrival is due to electron drift from the scattering location then the hours of MLT upstream that the event occurred is given (with drift velocities in MLThours per second) by:

$$\Delta MLT = \frac{V_{slow}\Delta t}{1 - \frac{v_{slow}}{v_{fast}}}$$

For the event in question the ΔMLT comes out to 1.3 hours of local time. This is in contrast to section 5.2.1 which implied that the precipitation

was local based on the slow rise time and lack of precipitation at S2. Errors in this calculation are large and strongly influenced by the Δt which could be as short as 8 seconds or as much as almost 24 seconds, since the spectra are accumulated across those time ranges. If we try to estimate Δt from the lightcurves as opposed to using a spectral product, we get 18 seconds of data that is harder than what follows. Using that number we get a drift of just under 3 hours MLT or 2500 km upstream.

Looking at the same time period from the sharp-edged model (5.2.1) we concluded that the slow rise would require a large longitudinal spatial gradient > 500 km. One can make the assumption that latitudinal spatial gradients are similar to longitudinal spatial gradients. In which case S2 and S3, separated by less than 500km in latitude, should both see precipitation at this time. S2 doesn't see anything, so at the time we assumed that the shape of the turn on was temporal. Based on the time-energy dispersion we conclude that the longitudinal scale size is quite large so

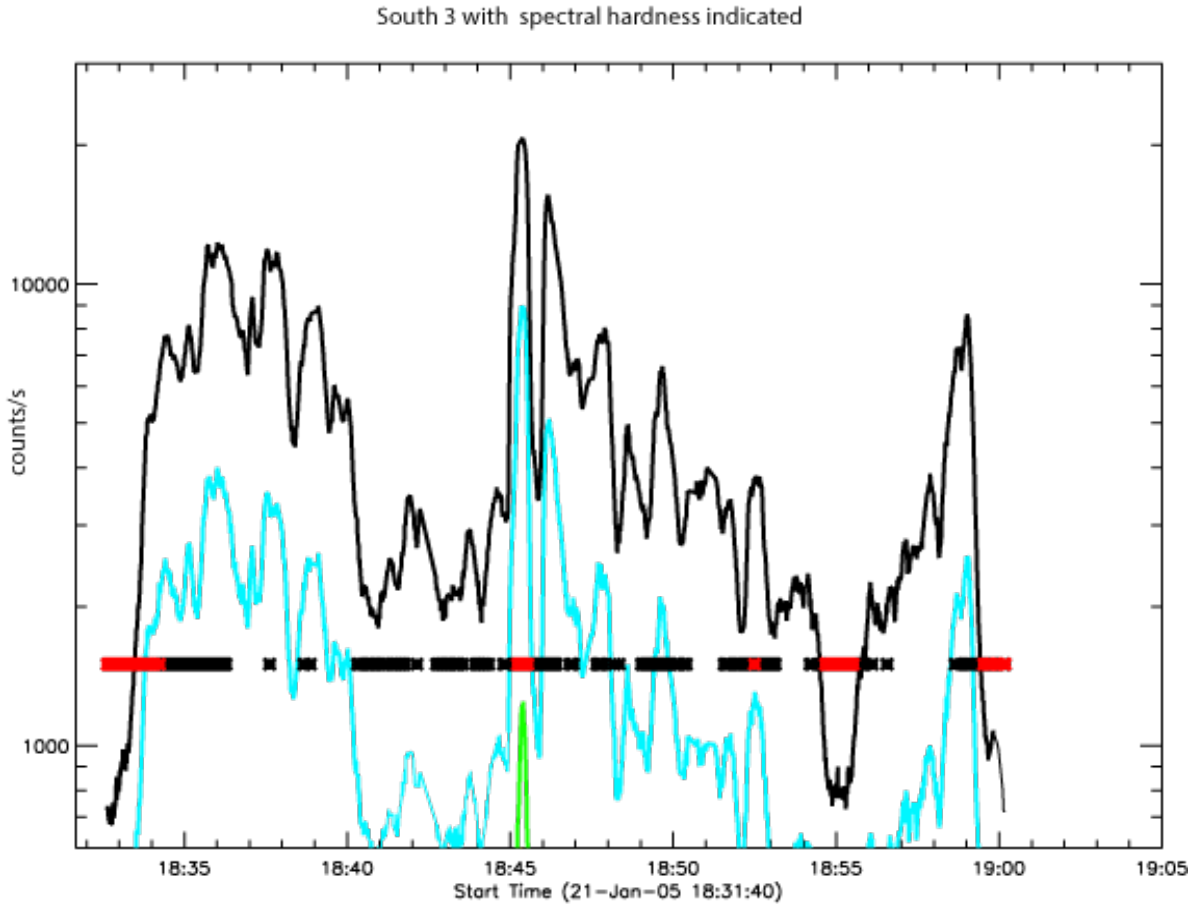

Figure 5.13: The S3 payload lightcurves: channel 1=Black, channel 2=cyan, channel 3 is briefly visible in green. Time ranges highlighted by the black stripe have the average event ratio between LC1 and LC2. The regions in red are more than 5% harder in this ratio while the regions in white are more than 5% softer. This measurement is sensitive to background estimation since the background is harder than the precipitating spectrum. Times appearing hard but with low count rates are suspect.

the assumption that latitudinal and longitudinal spatial gradients are similar seems invalid in this

case. Combining the drift dispersion result with the slow rise time of section 5.2.1 we conclude that the precipitation region does have a substantial spatial gradient in intensity.

The nature of spatial gradients in the precipitation region strongly affects how balloons and satellites observe REP. One supposition for the reason DREP has not been easily recognized in the data sets of polar orbiting satellites like SAMPEX is that the regions were so broad and with moderate gradients in latitudinal intensity that flying through them at ~10 km/s appeared as a gradual change in the countrate and thus did not stand out for easy analysis. At least for the MINIS data around 18:34 this does not appear to be the case, a rather sharp latitudinal spatial gradient must exist between S2 and S3 on the order of 100 km in the latitudinal direction. For SAMPEX this would appear as an increase in flux by orders of magnitude in only 10 seconds, a change which should be easily recognizable. A related observation is the possibility that lacking angular resolution the SAMPEX counts are often dominated by counts from electrons in the drift loss cone. If strong gradients in DREP precipitation are the norm this observation may additionally point to a lack of strong scattering in the precipitation mechanism as this would allow for DREP to be obscured even in the presence of strong spatial gradients.

The second hard peak around 18:45 UT when the shock arrival dramatically increases the size of the precipitation area does not yield to this type of data analysis. On the timescale of a spectral data product the best fit spectrum during that time period is constant and does not show dispersion. This could be the result of a drifting region at lower L-shells getting pushed over the S3 latitude. The time dispersion effect is only present at the leading drift-edge of a drifting region. After the leading edge passes, electrons of higher energy but scattered at later times will show up with the lower energy electrons that were scattered earlier. This is another example where the dramatic reorganization of the magnetosphere in response to the shock can confuse some elements of the data analysis.

5.4 Spatial scale of precipitation

Perhaps the most important observational goal of the MINIS balloon campaign was to determine the spatial scale of the precipitation region for DREP. The question of the spatial scale of precipitation strongly influences the *instantaneous* loss rate of electrons from the radiation belts. Although MAXIS was a single point measurement, its drift path and observation time allowed it to establish a substantial L-shell and local-time range where DREP can occur.

A map in magnetic local time and magnetic longitude of DREP observations by MAXIS, the Kiruna event and MINIS is shown here in figure 5.14. The large range of L and MLT that MAXIS observed over lends significance to the *average* loss rate calculation. The MINIS observations fit into the same L and MLT range, but the average loss rate observed by MINIS over the course of its flights has been shown to be relatively small, more than an order of magnitude below the MAXIS average. Meanwhile, the time period over which one can justifiably apply that average loss rate is relatively short compared to the 8 days that even the MAXIS average gives. After all, GPS electron flux at relevant L-shells exhibits strong loss in under 3 days.

If we take the MINIS observations and multiply them by the area of the precipitation region we can get the instantaneous loss rate. With two balloons aloft, despite their stationary nature, only the existence of a boundary in precipitation between the payloads can be explicitly confirmed and a minimum scale size quantified. The time series of precipitation observations shows some results drifting and others the result of rapid-L expansion of a precipitation region (or at the least it represents the effective movement of the payloads to higher L shells via compression which is not captured by the magnetic field models). The minimum scale size is pictured in figure 5.15. Its boundaries are determined by stepping along the L and MLT contours that defined the extent of each payload's FOV. The total area of the precipitation region pictured in red is 10^{15}cm^2. This means that a total of $2x10^{21}$ relativistic electrons precipitated between 17:10–17:40 and $5x10^{21}$ between 18:45–19:08.

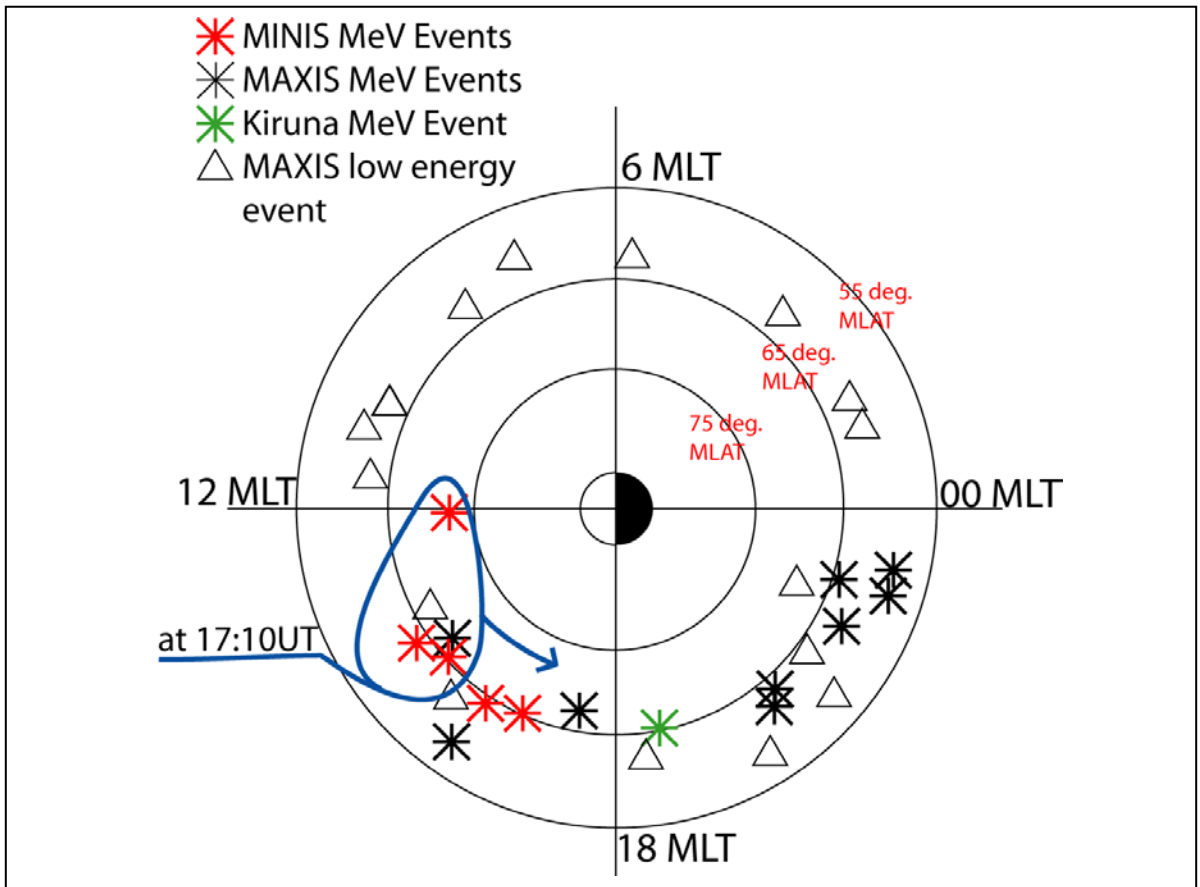

Figure 5.14: The distribution of MeV events (also called DREPs because of their location only on the duskside, as seen above, as observed by INTERBOA (green), MAXIS (black) and MINIS (red). Also shown are the more common low energy precipitation events that MAXIS observed (black triangles). The blue region is the MINIS observation at 17:10UT. The region MINIS observes moves in local time (primarily due to earth's rotation and not balloon drift) to later local times for the precipitation observed at ~18:45 UT.

If we compare the precipitation to losses of electrons initially measured on these L-shells, but we assume that similar precipitation rates are occurring across an unknown local time extent we can calculate the loss timescale for various scenarios An estimate of the pre-storm number of electrons in the radiation belts >500 keV between L=3.7 and 4.2 (using the Ts-04 model) which is the edge of the S2 and S3 FOV is $9x10^{25}$ based on the GPS electron flux. If the precipitation is constant over the L-shell extent then the loss timescale is ~$9x10^{25}/(10^{19}$ $e^-/s)$ $=9x10^6$ seconds. Since the area used in these calculations is relatively close to the area for 1 hour of MLT, then for a region of larger MLT extent, φ. the loss timescale is ~1/φ times the loss timescale from the well observed precipitation region. If the local time extent is 3 hours, the loss timescale is 33 days. This is substantially longer than the observed loss timescale but still more than twice as fast as the average loss rate from MINIS would take to drain the belts. Since MINIS made these observations for ~2 hours, the loss is still unlikely to account for the rapid depletion of radiation belt electrons even if the MINIS observations are primarily from electrons mirroring at the top of the atmosphere, which increase the required electron precipitation rate by an order of magnitude. In the most optimistic precipitation as loss scenario the local time extent of the precipitation is ~9 hours and the precipitating electrons are mirroring at the top of the atmosphere. Given those assumptions the loss timescale is 1.1days, which is still significantly longer than MINIS observed precipitation.

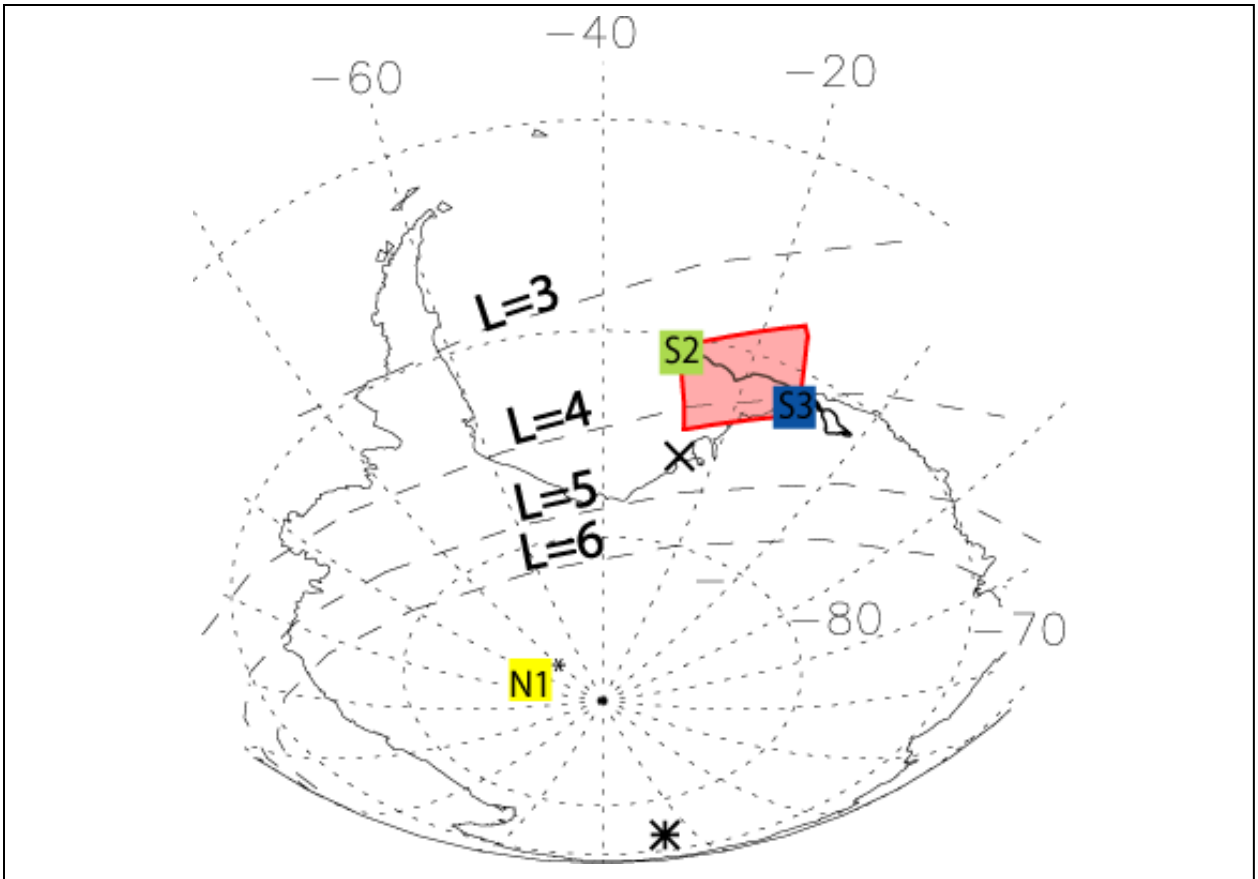

Figure [map]: Figure 5.15: The region of precipitation when both payloads are observing is shown in red. The region is defined by the L and MLT extent of the two fields of view. N1 shows the conjugate position of the Northern payload during the 17:10 UT time range.

Even choosing the extremes of spatial scale and precipitating flux from the MINIS observations it is clear that many of the electrons initially trapped in the radiation belts were not lost on the dusk side. This is despite the dusk side being the temporary location of the drift loss cone's ultimate precipitation area. It is possible that local, intense precipitation happened on the dawn side, but that precipitation would have to occur in a narrow range of longitudes such that MINIS would not have observed significant drift loss precipitation. It is far more likely that the electrons were lost to the magnetopause or at the very least redistributed away from the L-shell of the balloons. GPS orbit's minimum accessible L-shell is ~4, so it is possible that some of the electrons that are lost from a GPS perspective move inward of L=4. But given the large shock that struck the magnetosphere, the magnetopause being pushed inside geosynchronous orbit, the most likely place the electrons went is outward. MINIS results show insignificant precipitation in either an average, campaign long sense or an instantaneous sense to explain the number of electrons lost from L~4.

6. Future Work on Balloons

The MINIS balloon campaign flew during a unique time period. Although it made observations of high energy precipitating electrons from multiple points for the first time, it is difficult to determine the source of these electrons or relate them to events in the magnetosphere. This difficulty stems from three principal sources: 1) the magnetosphere was being dramatically reshaped in response to the strong compression on the dayside due to the shock arrival which may move precipitation boundaries and modulate precipitation in such a way as to mask underlying processes. 2) There were insufficient measurements in the heart of the radiation belts conjugate to the observations to identify plasma and wave parameters which might account for scattering of electrons. 3) There were only two observation points conjugate to the radiation belts during the most interesting relativistic precipitation both of which were in the outer zone SAA. Having only two points means the determination of the overall scale size can only be a lower limit and drift loss effects can confuse the interpretation of precipitation data.

6.1 BARREL

In order to address the issues that MINIS faced in determining the cause and significance of the observed DREP a significantly more thorough set of balloon observations was proposed to fly in conjunction with the Radiation Belt Storms Probe mission (RBSP). This project, the Balloon Array for RBSP Relativistic Electron Loss (BARREL), was proposed as a mission of opportunity in late 2005 approximately 10 months after the MINIS observations of relativistic electron precipitation. The project is led by Dr. Robyn Millan at Dartmouth College, but includes significant effort at UCB which I have led. BARREL was selected for a phase-A year in July 2006. That study concluded in early fall of 2007, and BARREL was selected in December of that year. The BARREL proposal relied heavily on both the initial results of MINIS and the MINIS demonstration of feasibility of launching a balloon array of small spectrometers to study REP. BARREL is MINIS on a grand scale, with an order of magnitude increase in the number of balloons launched over two primary field seasons and several test flights. The first field season, where I led one of the field teams, has recently concluded (December 2012 into February 2013). Initial data analysis is just beginning, although a large part of the BARREL team is already busy working towards having payloads ready for the next major field campaign at the end of this year.

BARREL solves all three of the problems of MINIS. The goal is to launch 40 balloon payloads across two field seasons (the first field season successfully launched 19 payloads). In order to launch this many payloads and furthermore to get broader L-shell and MLT coverage the payloads are launched from 2 separate Antarctic launch sites. SANAE is again used as a launch site, and Halley Bay Station of the British Antarctic Survey which is at slightly higher L and ~1.5 hours earlier local time is used as well. Even taking an estimate of the BARREL average flight duration as low as 6 days, the majority of the season will consist of ~4 payloads making measurements at a given time. In practice the BARREL payloads from the first field season stayed aloft significantly longer than this 6 day figure. This significantly improves the difficulties of point 3 above in actually measuring the scale size (and therefore the number of electrons lost and importance to the radiation belts). As part of the BARREL concept study, I took expected balloon tracks and launch frequency and modeled them in a simple magnetic field model. This study demonstrated the additional advantage of having two launch sites. In addition to easing the

launch burden on one site, the multiple launch sites increased the average number of payloads aloft as well as the L-MLT extent at any given time.

BARREL's sheer number of payloads in a given campaign allows for frequent payload to payload comparisons of timing, as well as looking at L and MLT gradients in precipitation. BARREL attempted to launch two payloads from one site on a single day, separated by ~3.5 hours. This would result in a payload separation that was at least initially ~125 km, just outside the field-of-view of one payload. This tandem set of observations has overlaping fields of view and could coneceivably separate out the coherence scale of ULF modulation in the precipitation, something that MINIS was unable to confirm. It would also likely allow for definitive determination of the drift advance of a precipitation region. As the payloads drift apart a range of scales will be sampled. Unfortunately this effort in the first campaign included one of the shortest lived BARREL payloads at ~1/2 day. And the close pair of payloads did not observe any precipitation, although the surviving payload did several days later.

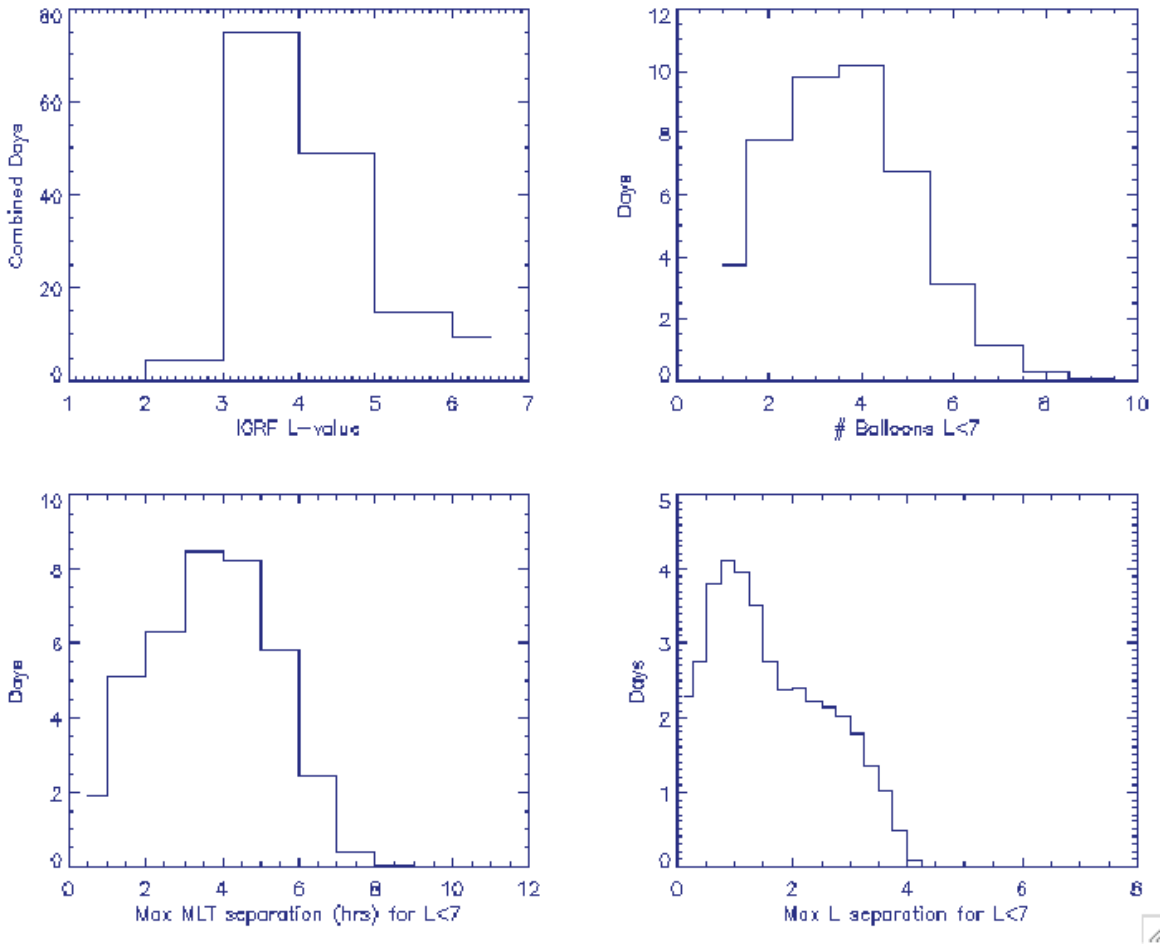

Figure 6.1: Simulations of (clockwise from top left) L-shell of observations, number of balloons aloft, Max MLT separation in the array, and maximum L shell separation in the array. The simulated payloads were launched 5 from Halley Bay, 15 from SANAE.

The second issue that MINIS had in determining the underlying mechanism which scatters high energy electrons into the loss cone had to do with the lack of plasma and wave measurements in the heart of the radiation belts. BARREL is flying in association with the most thoroughly well instrumented multi-point measurement that the radiation belts have ever been studied with, RBSP. The Radiation Belt Storm Probes mission consists of two identically instrumented spacecraft launched into ~600 x 30,500 km orbits with inclination of 10° and a magnetic inclination that peaks around 0°. This means they spend more observing time around L=5 than anywhere else. The spacecraft orbits are slightly different, such that they lap each other every 90 days. This means that although they are similar to a string of pearls arrangement, they actually vary the separation along that string dramatically, covering a wide range of spatial-temporal scales. The RBSP spacecraft were launched on my birthday, August 30, 2012, such that apogee was at dawn local times in early

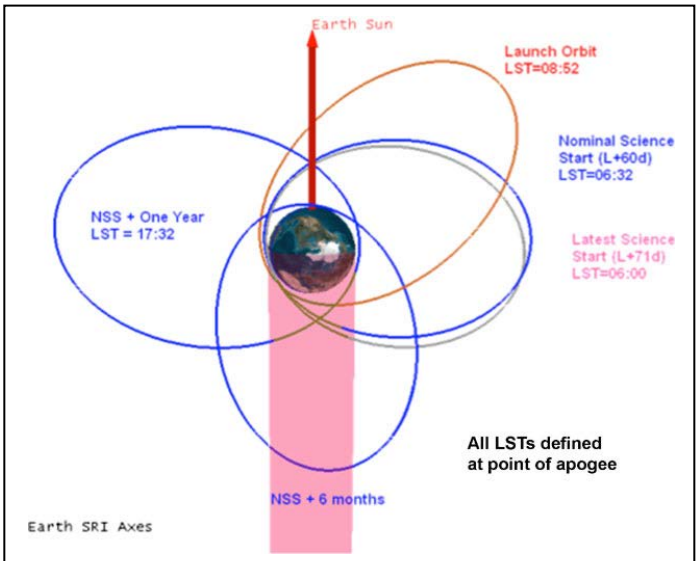

Figure 6.2: The RBSP orbit precesses such that apogee is at Dawn ~60 days after launch and apogee is at dusk local times 1 year later. after [Stratton 2013]

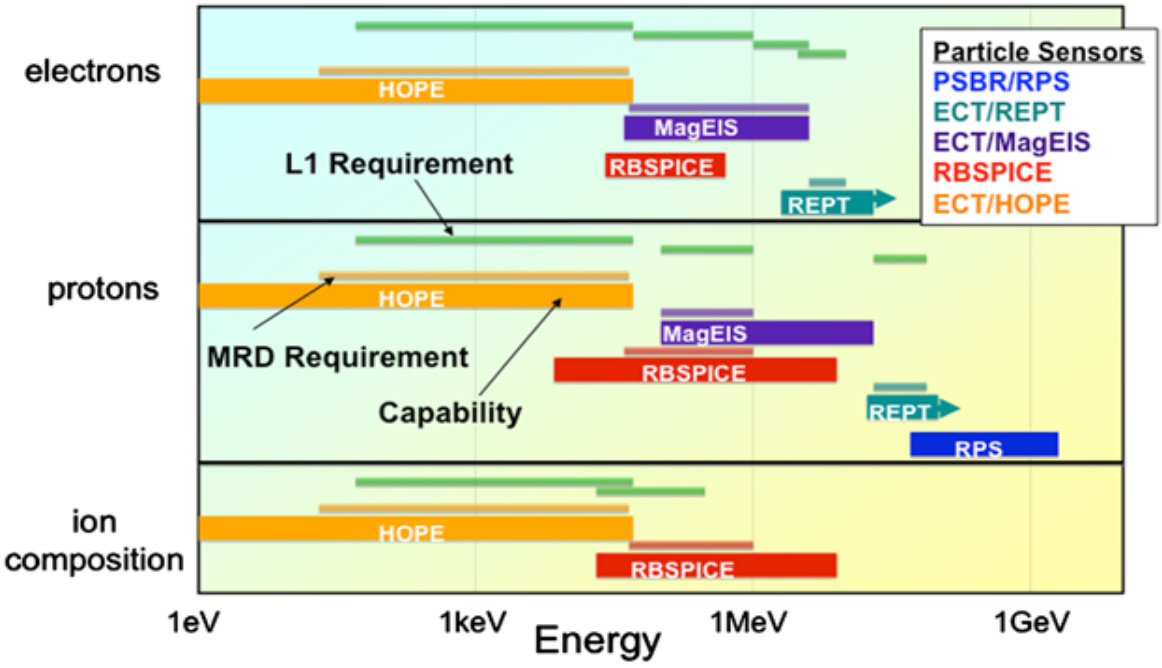

Figure 6.3: RBSP covers the radiation belt particle population over more than 9 orders of magntidue. Figure courtesy RBSP Science Working Group.

November. The orbits precess form there towards midnight local time approximately six months later and then towards dusk, the following November. The precession of the RBSP orbit in local time allows studies of the various processes which only occur at specific local times. Recall that chorus (and likely related microbursts) occurs primarily on the dawn side of the radiation belts. The BARREL campaigns in January of 2013 and January of 2014 are designed to make observations of precipitation in conjunction with RBSP's observation of the plasma, waves, and

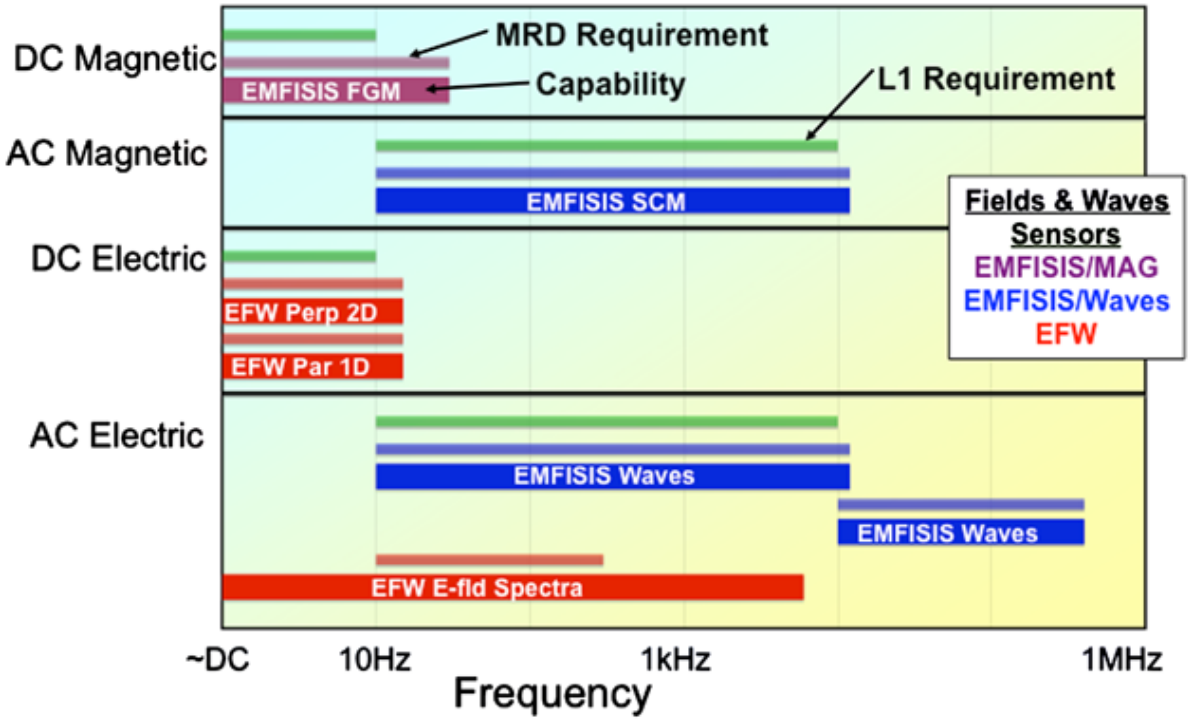

Figure 6.4: RBSP will be able to observe all the necessary wave modes that accelerate and scatter relativistic electrons. Observations of waves, plasma parameters, and the energetic particle population are the measurements BARREL needs in conjunction to actually understand the physics behind various precipitation mechanisms. Figure courtesy RBSP Science Working Group.

energetic particles found in the heart of the radiation belts. Since the two most significant competing loss processes are found in the dawn and dusk sectors, it is fortunate that RBSP's apogees in these sectors occur near the austral summer when balloon campaigns are feasible. Although BARREL makes observations at all local times, conjunctions are largely limited to the times when RBSP is at apogee, so the local time of apogee is an important parameter of the RBSP spacecraft for BARREL.

RBSP is thoroughly instrumented to study the Earth's Radiation Belts, a graphical summary of the range of energies and frequencies covered by the various instrument groups is shown here as Figures 6.3 and 6.4. While the pitch angle coverage of RBSP's energetic particle detectors is a remarkable achievements and significant effort will go into attempting to filter out the loss cone fluxes from surrounding particles, it is unlikely that RBSP will be able to measure the electrons which are bound for precipitation in the atmosphere. The loss cone at L=5 is ~4° wide,

(counting the drift loss cone~ 4.5°), which is well finer than the native 20° resolution of the instrument even when operated in a burst mode. BARREL fills in the electron part of this vital piece of information for times when it is in conjunction with RBSP. When the RBSP mission was first defined, the proposed project included the addition of a dedicated precipitation Low Earth Orbit spacecraft for studying loss cone physics. This part of the mission definition was cut, leaving a hole that BARREL could fill for a few key months out of the RBSP 2 year mission.

The BARREL payloads are very similar to the MINIS payloads, and the NaI detector is essentially the same. The BARREL payloads do not make electric field measurements, which simplifies the payload somewhat and allows them to be lighter weight than MINIS. Lighter weights should help contribute to higher initial float altitudes and potentially longer flights. BARREL uses a substantially less noisy magnetometer and the payload is not rotated. This should allow for observation of waves in the 10s of mHz range, frequencies that are often present in DREP precipitation. While analyzing the magnetometer data is nontrivial, the improved design should allow for more significant use of that data element. The BARREL telemetry scheme has been revised somewhat to include a spectral products at 4 second cadence, an improvement over MINIS 8 second cadence and at only slightly lower energy resolution. Significant testing went into the telemetry system to try to reduce the number and length of data gaps that MINIS suffered from. While the system is significantly better, data gaps still exist in the BARREL data stream. The heavy lithium primary cells were dropped as the power source and a system employing solar panels and a much smaller rechargeable battery was added as the primary power system. This proved useful in allowing some of the first year flights to extend as long as 19 days. Finally, the BARREL flight computer should not be paralyzeable due to excessive count rates as was the case on a few occasions for MINIS.

While BARREL will be a substantial improvement to observations of Relativistic Electron Precipitation, the exciting opportunities afforded by conjunctions with RBSP represent the most rewarding potential science. As part of the phase-A study I modeled balloon positions as a

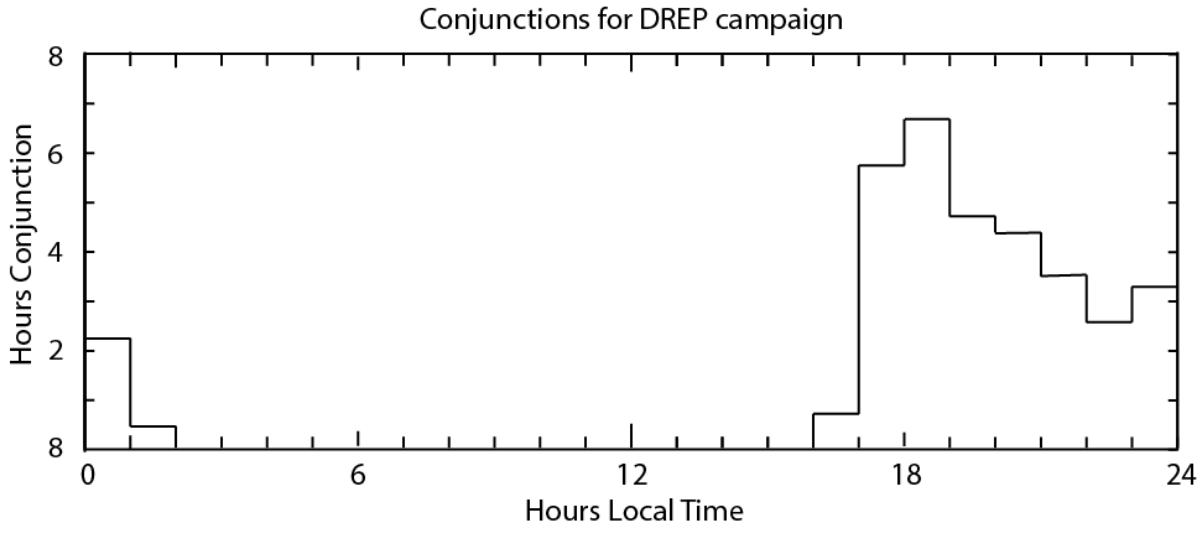

Figure 6.5: Originally planned on being the first campaign, the duskside campaign is now scheduled to occur in January 2014.

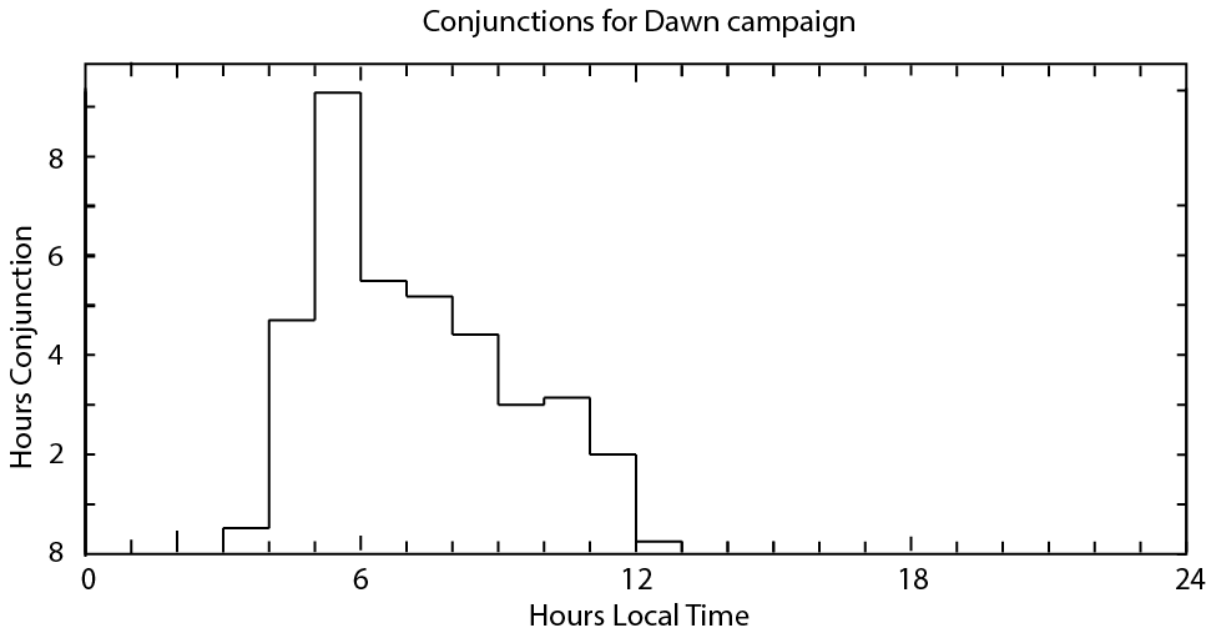

Figure 6.6: The same as the previous figure detailing hours of conjunctions for 15 payloads launched from SANAE during a timeframe when RBSP apogee is near local dawn (instead of dusk).

function of time and used magnetic field models to estimate conjunctions with the RBSP spacecraft. The results assumed what was then a slightly different nominal orbit, but are generally robust. The precession of the RBSP orbit strongly influences the local time of conjunctions, and thus it is important to have multiple balloon campaigns separated by 1 year. Conjunctions are defined as L shell separations less than 0.5 and local time separations of 0.5 hours as well. These definitions are reasonable given the scale size observed by MINIS for DREP. For Microburst, dawnside conjunctions, the conjunction conditions are substantially larger than the size of an individual burst, however they are smaller than the size of microburst regions as observed by SAMPEX. Since magnetic field maps even during quiet times can disagree by up to almost 0.5 L, confidence in conjunctions with individual microbursts is impossible anyway. The conjunction simulation assumed 1 spacecraft and 15 balloons launched from SANAE, and did not include any launches from Halley Bay. The first campaign launched 12 balloons from SANAE and 7 from Halley Bay. In all cases having two spacecraft flying through the region will certainly double the individual conjunctions, it will also allow for more broadly defined conjunctions where spacecraft bracket and/or subsequently traverse a region of conjunction. Applying knowledge of the Drift Loss Cone allows for a more loosely defined conjunction, one in which the spacecraft is at earlier local times to a balloon or balloons but on the same L-shell. Observations at the spacecraft will still be related to observations of precipitation, albeit with a small drift delay.

The first BARREL campaign involved significant planning for conjunctions, since the EFW (Electric Fields and Waves) instrument is able to play back burst data after the fact. This meant that if the BARREL payloads made any interesting observations of precipitation we could then request particularly high resolution measurements from that time period. Although I was

instrumental in the planning of this collaboration, lack of communication from Antarctica prevented me from playing a large part in its execution. The stateside BARREL team was quite successful at organizing burst playback and high resolution conjunction data during precipitation is available. This will be one of the roles that I fulfill next year as the collaboration with EFW will continue for the next BARREL campaign as apogee moves to the dusk side. The collaboration emphasizes the usefulness of the BARREL being telemetered in real time and quickly viewable by the stateside science team.

During magnetically quieter times when precipitation is still able to occur (if less frequently), and large scale motions of the magnetosphere are not occurring, having multi point observations in the drift loss cone can actually very accurately determine the pitch angle diffusion rate. Given three balloons on approximately the same L-shell, but at different points in the drift loss cone, each balloon's field of view of the sky samples:

$$\frac{d\alpha}{d\varphi} * (\Delta\varphi_{FOV})$$

Where $\frac{d\alpha}{d\varphi}$ (the slope of the equatorial pitch angle change with magnetic latitude) can be as high as 0.5° equatorial pitch angle per degree magnetic longitude (as seen in Figure 5.1 chapter 5) and the field of view of a typical payload at L=4 is ~4.5° magnetic longitude. This means that each payload is observing ~2° of equatorial pitch angle, which is far more sensitive a pitch angle measurement than can be made at the equator. By combining spectral estimates of the electron energy (and thus the drift rate) the model results from simulations such as the one shown in chapter 1 Figure1.30 can actually be verified, something that has not been achieved with spacecraft. Above ~300 keV this would be the most direct, sensitive measurement of the pitch angle diffusion rate that has ever been achieved (for results below that energy, see Lee et al. 2003). Even a pair of balloons east of 180° magnetic longitude can, during quiet times, provide limits on this measurement. Motions of the magnetosphere, separations in L, or any isotropization (strong scattering) that occurs between the payloads will have the ability to

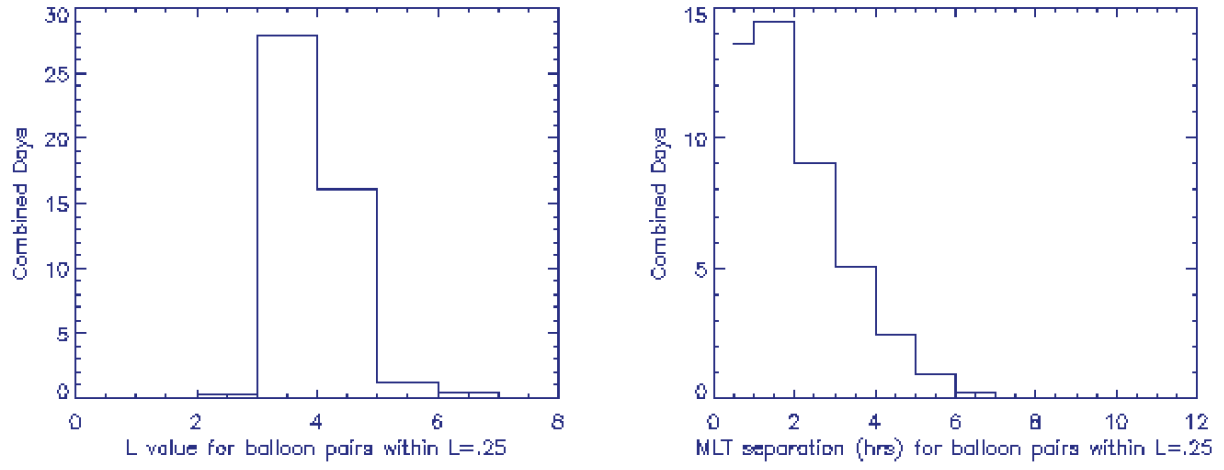

Figure [closeinL]: The left figure shows the total number of days with balloon L separations of less than 0.25 and the right figure shows the L-separations of those balloons.

confuse the measurement, so more than one pair is strongly preferred. With common launch sites and ~2 day launch separations which are the average, these close in L balloons are actually quite common and do in fact show a range of MLT separations (Figure 6.7).

While dramatic magnetic storms may be the driver of interest in REP, it may prove useful to consider what quiet time observations can provide as far as thoroughly understanding the processes involved. Considering the rarity of events like the time period in which MINIS flew, BARREL will likely make a significant percentage of its observations during relatively quiet magnetic conditions.

7- Proposed future work: Orbital

MINIS made the first measurements of the geographic (and therefore magnetic) scale size of relativistic electron precipitation. Although MINIS is only able to put a lower limit on that precipitation scale size because of the limited number of balloons that were up during a precipitation event, the ongoing BARREL project will do far better. Even given the scale of BARREL and the power of conjunctions with RBSP there are limitations to what can be accomplished from a balloon campaign. These limits are imposed from a variety of sources: accessibility of various locations in the drift and bounce loss cones from available launch sites, often seeing a superposition of drift-loss and bounce loss precipitation, limitations on the flight duration, and the flight time frame (geomagnetic storms exhibit seasonal modulation in geo-effectiveness due to the tilt in the Earth's field, and Antarctica is only accessible to balloons in ~January) There are also more direct measurement issues: inability to determine pitch angle, difficulty in measuring low energy precipitation in the presence of high energy precipitation and the relative insensitivity to small spatial scale precipitation structures like microbursts. There are further difficulties with associated measurements including the near impossibility of measuring ion precipitation which may be relevant to studying EMIC wave scattering of electrons, and clear

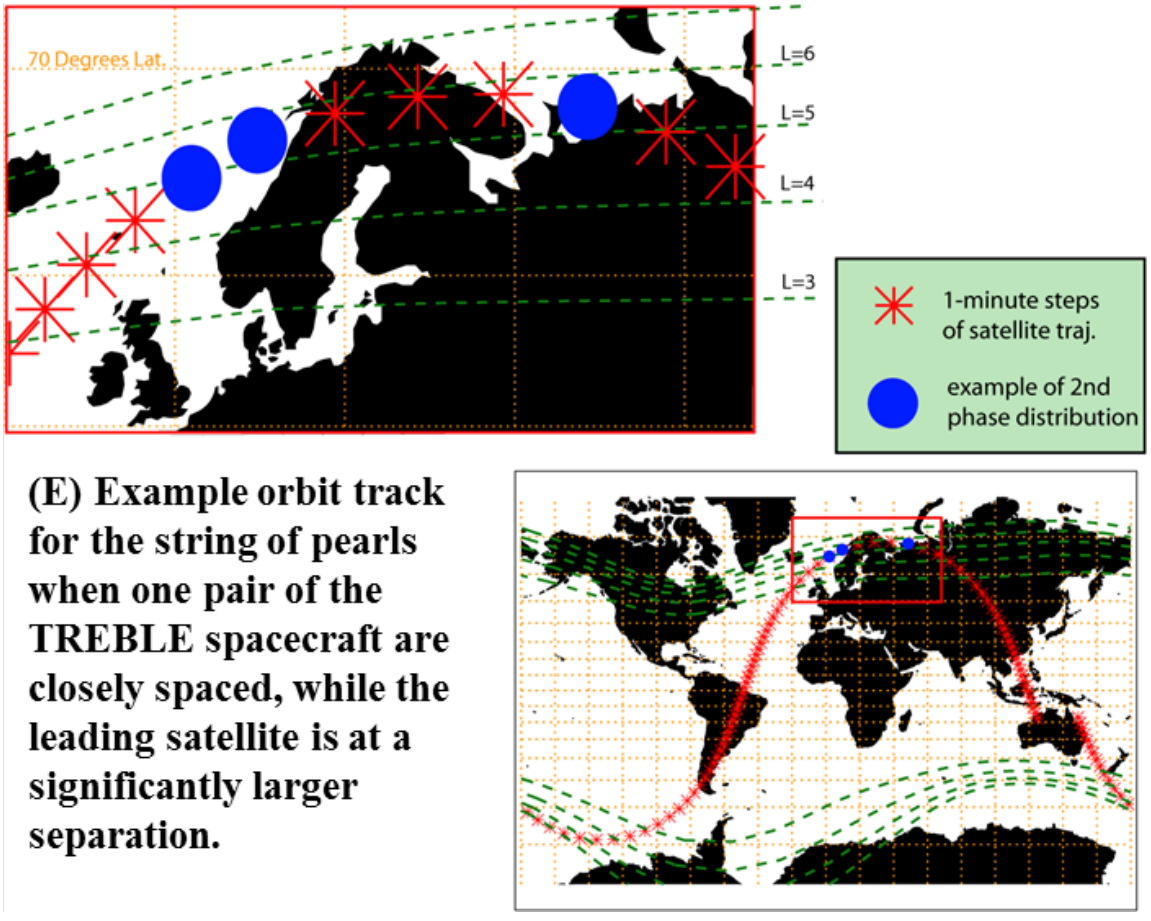

Figure 7.1: Showing the TREBLE string of pearls in a region where they are able to make extended measurements at appropriate L-shells while still separating out spatial and temporal structure and measuring multiple scales of precipitation.

difficulty making sensitive and/or direction-resolved measurements of the magnetic field.

While balloon based observations have significant merit, especially when considered in a restricted funding environment, it is useful to consider what an explorer mission dedicated to understanding precipitation could accomplish from Low Earth Orbit. While exisiting LEO measurements are instructive, none has been designed to study REP. For instance, the general purpose POES satellites have two pitch angle look directions and information from multiple satellites, but only include 3 energy channels, >30, >100, and >300 keV electrons, and these channels suffer from significant proton contamination. And while SAMPEX served the radiation belt community for ~20 years, it has now de-orbited and its usefulness in understanding the radiation belts was a secondary concern in its design; that it did so much despite this is in some ways a testament to the rich environment that LEO is for understanding the radiation belts.

A proposed mission, TREBLE (the Terrestrial Relativistic Electron Belt Loss Explorers) is a mission to LEO that would focus on and answer many of the questions of relativistic electron precipitation. TREBLE will focus on *losses* of high-energy electrons from the belts into Earth's atmosphere, similar to the goals of MINIS and BARREL, but from a different perspective. It will resolve two long-standing questions: the nature of the wave-particle interactions that cause these losses, and the role these loss processes play in controlling the global balance of relativistic electrons in the belts. Earth's radiation belts provide a unique laboratory for studying the physics of particle acceleration and wave-particle interactions that occur in a wide range of astrophysical plasma environments including solar flares, Jupiter's magnetosphere, and accretion disks. Whistler-mode chorus waves and EMIC have both been nominated as the dominant mechanism for scattering electrons into the loss cone. Chorus may also be an important acceleration mechanism [e.g. Horne, 2005b]. Although scattering by waves may often be taking place near the equatorial part of the radiation belt at several Earth radii, particle losses cannot be measured there because the loss cone is extremely small.

To date, spacecraft measurements [e.g. O'Brien, 2004] and balloon measurements have given strikingly different pictures of the cause of losses around 1 MeV. Spacecraft show strong losses from dawnside microbursts (associated with chorus), while balloons have never observed microbursts to extend above a few hundred keV; instead, balloons see prominent loss MeV events on the duskside, with different temporal patterns, that may be associated with EMIC waves. TREBLE is designed to resolve and reconcile these contradictions. Because TREBLE will last much longer than a balloon campaign, TREBLE will characterize losses from the magnetosphere in all space-weather conditions, including the most severe.

Mission Overview: TREBLE consists of three identically instrumented spacecraft orbiting at an altitude of 600 km and inclination of 69^{o}. By flying three spacecraft in a "string-of-pearls" configuration, TREBLE will be the first mission to not only observe, but cleanly disentangle, complex spatial and temporal variations and determine precipitation spatial scales. An example of the orbit tracks during a phase of the mission looking at multiple scales is shown in Figure 7.1. TREBLE's relativistic electron detectors, a new yet simple design, will for the first time measure these particles (> 500 keV) at high sensitivity and cleanly resolved in both energy and arrival angle – a prerequisite to understanding the mechanism and location of scattering. The spacecraft position at the footpoints of the outer-belt field lines will allow our detectors to distinguish between trapped particles and particles at the edge and center of the loss cone with modest instrumental angular resolution (Figure7.2). The orbital inclination maximizes the

amount of time the spacecraft will spend where precipitation of relativistic electrons occurs (simulation results are presented in Figure 7.3).

The detailed physics of the precipitation will be deduced from these new measurements, supported by measurements of ULF and EMIC waves and field-aligned currents with an onboard magnetometer (0.1 nT sensitivity) and by measurements of lower-energy electrons and protons by a separately optimized detector. Again, these measurements cannot be adequately made from a balloon platform. The particle measurements will include electrons from 40 keV to 5 MeV and ions from 40 keV to 10 MeV in five pitch-angle ranges centered at 0^o, 45^o, 90^o, upward moving populations at 135^o, and 180^o are sampled by the double ended nature of the telescopes. The spacecraft will be aligned to the local magnetic field so that these angles can be sampled by fixed detectors at all times. Since the spacecraft axis is tied to Earth's magnetic field to within 18^o, about 1/2 of the field of view of the particle detectors, attitude data are not required to interpret the particle measurements.

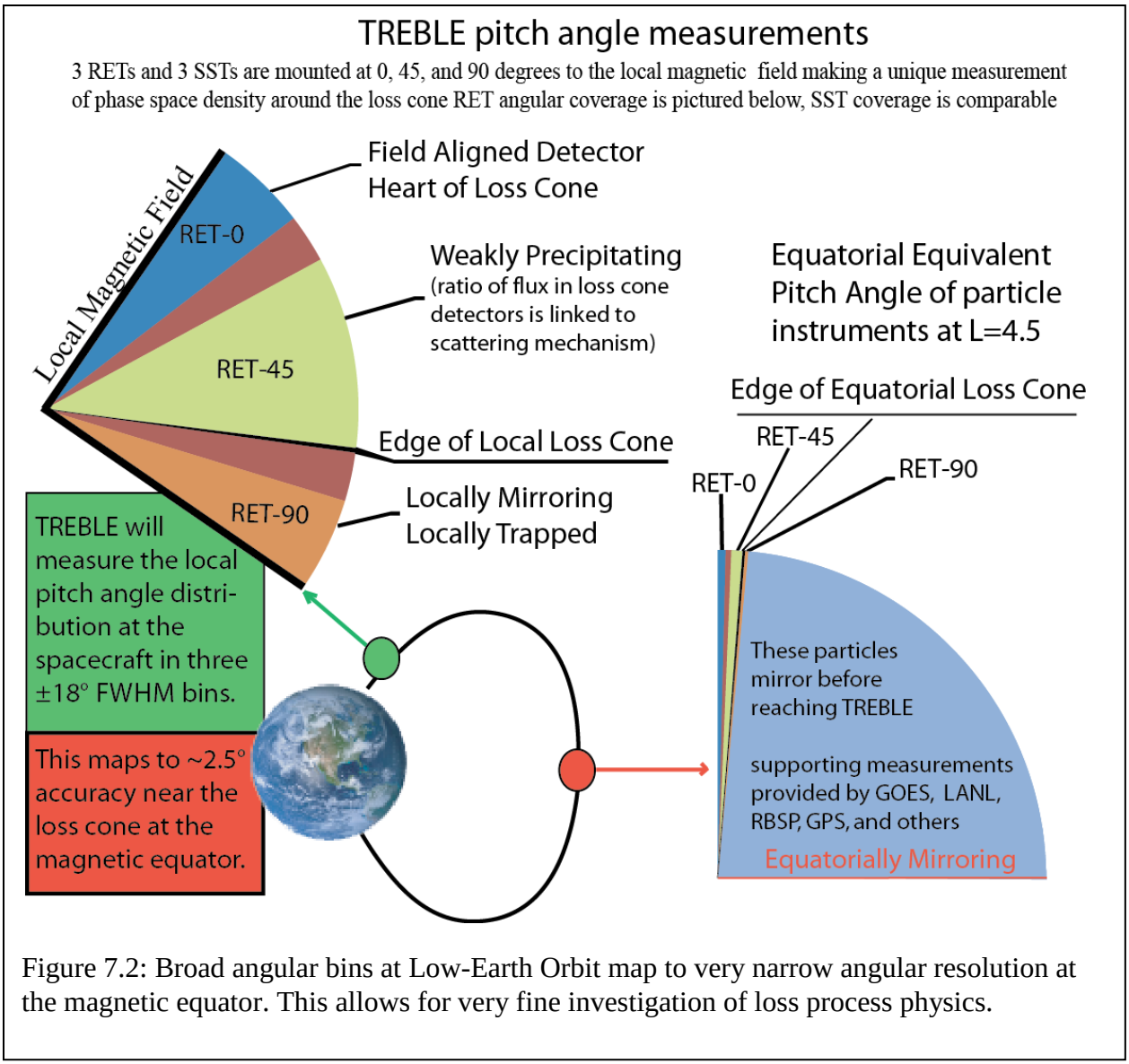

Figure 7.2: Broad angular bins at Low-Earth Orbit map to very narrow angular resolution at the magnetic equator. This allows for very fine investigation of loss process physics.

Being magnetically aligned allows the three particle detectors to make continuous measurements of the electron population at key pitch angles. The 90° detectors focus on locally mirroring electrons which are generally in the drift loss cone, or are more permanently trapped (depending on spacecraft location). Marginally precipitating electrons will be found in the 45° detector and strongly scattered electrons will be measured by the field-aligned detector. Depending on the position in the orbit, the 0° detector measures equatorial pitch angles from approximately 0° to 2°, the 45° detector from 2° to 6°, and the 90° detector from 6° to 8°. A schematic of the angular coverage of the TREBLE instruments in both local and equatorial pitch angle is shown on Figure 7.2. The equatorial pitch-angle measurements made by the TREBLE spacecraft will measure gradients in phase-space density near the loss cone which are identifiable with candidate physical processes for scattering loss of radiation belt electrons.

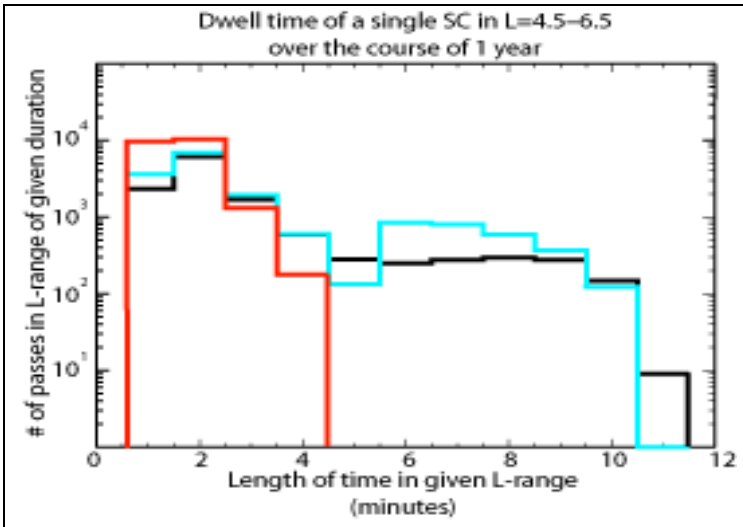

Figure 7.3: This plot compares the number of passes under the outer-belt precipitation as a function of the time spent in that region. An inclination of 69° is plotted in cyan and gives the highest average dwell time in the region. 65° (black) gives a few very long passes, but has a lower average duration. Red shows the limited duration passes for the inclination of SAMPEX (82 °). Near-polar orbits are less suitable for separating spatial and temporal variations.

As shown in Chapter 1 the important role played by *losses* in controlling relativistic electron variability in the radiation belts has become increasingly clear over the last few years. Radiation-belt models that solve the time-dependent radial diffusion equation typically assume an empirically determined decay lifetime; the simulation results crucially depend on the assumed losses. Physics-based loss rates that have been validated with observations are a critical next step in improving these models. Catastrophic depletions of the radiation belts are routinely observed by spacecraft, but it is not clear which processes are involved, nor their dynamics and evolution. While BARREL will produce observations of the loss rate, the potential lack of microburst observations at high energies and the inability to resolve the pitch angle information that gets at the underlying physics make a space based measurement more detailed as well as longer lasting and more broad.

As described in Chapter 1 and elsewhere in this dissertation, past observations show that there are at least two distinct classes of relativistic electron precipitation in the outer radiation belts, one on the morning side (microbursts) and the other on the dusk side [Lorentzen, 2000]. Though this may be a false dichotomy, with relatively sparse observation sets it could easily be the case that during some periods one type of precipitation does dominate and during other periods a different mechanism is most important. It may be a false dichotomy in another sense as well.

Given the limited spectral information of SAMPEX, it may be the case that MeV microbursts dominate when considered > 1 MeV but that DREP dominates when considering > 2 MeV or some other energy. Better energy resolution than SAMPEX provided combined with better observing statistics than balloons give are needed to resolve the question.

In the slot and near the outer edge of the *inner* radiation belt, however, losses of radiation belt electrons from lightning-generated whistler-mode waves and VLF transmitters may be dominant. The source location of plasma waves excited by these can be easily identified, thus providing a unique opportunity to study the details of wave-particle interactions causing precipitation.

Although previous missions, such as SAMPEX, have advanced our understanding of electron precipitation, they have also hinted at clear inconsistencies between theory and measurement. Previous measurements have not provided the necessary data for studying the physics of the processes involved and resolving these outstanding questions

7.1 Observational goals

7.1.1 TREBLE observations of Electron Microburst Precipitation

Microbursts are observed near the nightside trapping boundary and on the dayside at L-shells outside the plasmapause. There is evidence that the dayside microbursts are truly temporal [Blake, 1996; also their similarity to lower-energy microbursts seen by balloons], but the nightside events may well be another phenomenon altogether that produces fine spatial structures along thin drift shells that mimic bursts as a single spacecraft flies through them. A multi-spacecraft mission with narrow spacing is needed to separate these phenomena.

Models of electron scattering by chorus generally predict gradual diffusion, so that precipitation

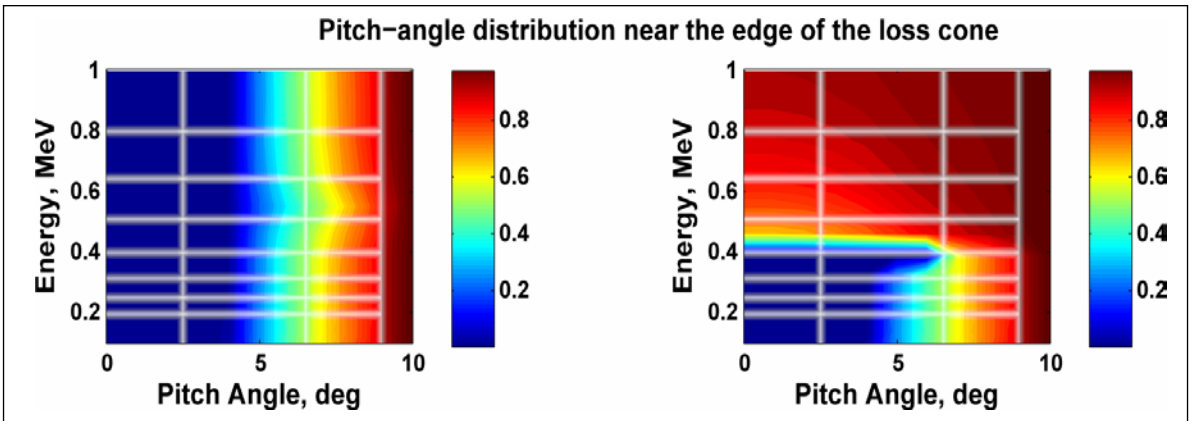

Figure 7.3: The phase space density near the loss cone (as a function of equatorial pitch angle), and its evolution, reveal distinct signatures from different scattering mechanisms. The panel on the left is from a model of scattering by chorus waves. The right panel shows EMIC-wave-induced precipitation. TREBLE will measure this distribution with the approximate resolution indicated by the overlying grid. For clarity flux has been made uniform at 10 degrees and the color scale is relative to that value.

occurs only near the edge of the loss cone. Figure 7.3 shows the results obtained by adapting a model provided by Shprits (described in Shprits [2006]) to higher resolution near the loss cone. Data comparing fluxes observed in low- and high-Earth orbit, however, suggest that pitch-angle distributions might actually isotropize during large events [e.g. Kanekal, 2005]. No platform to date, however, has actually measured losses at the edge and center of the loss cone simultaneously. TREBLE will resolve this controversy by directly measuring fluxes at the edge and center of the loss cone, immediately distinguishing between slow diffusion and strong isotropization.

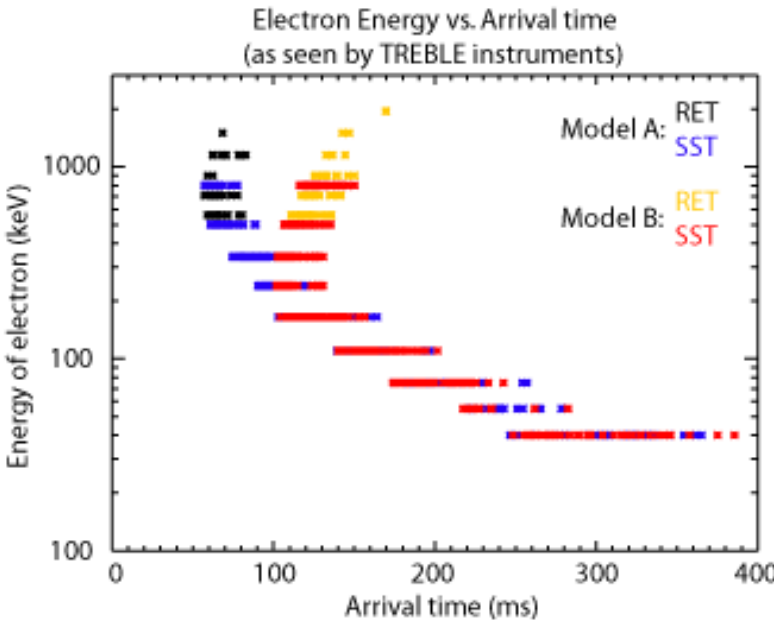

Figure 7.4: Electrons as seen by TREBLE as predicted by two different models of high energy microburst scattering vs. latitude. In both cases electrons below 200 keV scatter near the equator, but the scattering location of higher energies is a function of latitude. By measuring pitch angle and energy at high time resolution TREBLE can measure the position along the field line where scattering occurred, as a function of energy.

Most wave-particle interactions are resonant with electrons at particular energies. Electron-energy measurements are therefore at the heart of the physics involved, and can both reveal the particular wave responsible and pin down the physical conditions (such as plasma density and field strength) at the scattering site. Most spacecraft to date, however, have measured energy in only a handful of channels, or, when at higher resolution, over a very limited energy range [e.g. Lee, 2005]. Observations made with SAMPEX and S81-1 show that high energy (>1 MeV) microbursts sometimes appear without lower energy (~100 keV) microbursts, and vice versa [Nakamura, 1995; Blake, 1996,]. Although the high-energy end of this process has been recently modeled and compared with SAMPEX observations [Bortnik and Thorne, 2007], current models do not capture this complex energy-dependent scattering process. And since there is currently very limited spectral information there is little incentive for physics based models to fill in the gap between a few hundred keV and >1 MeV. TREBLE will measure the energy spectrum of electrons from microbursts and other interactions across two orders of magnitude in energy at high resolution. These measurements will drive the development and validation of more realistic models.

TREBLE will address a long-standing disagreement between balloon and satellite observations of microbursts. Although satellite observations suggest [O'Brien, 2004] that relativistic microbursts (> 1 MeV) can be the dominant loss mechanism during storm times, balloon payloads like MAXIS have *never* observed microburst emission to extend above about 500 keV

[Millan., 2002]. Instead, balloons have seen MeV emission *only* in duskside events with slower time variations as described throughout this dissertation. By measuring the pitch-angle distribution, energy spectrum, and spatial scale of relativistic microbursts accurately for the first time, TREBLE will allow us to build a complete model of exactly what these events ought to look like when seen from balloon payloads, leading to a resolution of the apparent disagreement.

O'Brien [2004] found that although microbursts occur frequently during the recovery phase of a storm, losses due to microbursts are much stronger during the main phase, capable of emptying the radiation belts in a day or less. However, they also point out, "Large uncertainties still remain in the MLT scales and time duration of microbursts extrapolated from measurements by a single spacecraft... Such uncertainties cannot be resolved easily without multipoint or nearly stationary measurements of precipitation at high time resolution (~100 ms)." As discussed in Chapter 3, MINIS and likewise BARREL will have difficulty observing MeV microbursts, but TREBLE will provide the multi-point measurements necessary to determine the spatial extent and temporal evolution of the microburst precipitation region, which is critical for quantifying the electron loss rate. Rocket launches into microburst regions have also been explored as possibilities but logistical issues have prevented significant advancement of these proposals. TREBLE will further determine whether nightside microbursts are temporal or spatial in nature, helping to distinguish their cause.

The scattering location along the field line combined with the size distribution as a function of energy of individual microbursts is a key to microburst physics. Non-relativistic microbursts have dimension varying from 40–200 km [Brown, 1973; Parks, 1967], while individual relativistic microbursts have been estimated to have scale sizes as small as 'several tens of gyroradii' [Blake, 1996]. A 1 MeV electron at SAMPEX at L=5 has a gyroradius of 80 meters. Thus a microburst may be as small as 1 km. These scales should be related to chorus elements in the equatorial source region which have a scale of ~200 km perpendicular to the magnetic field [Santolik, 2004]. This equatorial scale size maps to only ~2 km at high-latitude, low-Earth orbit. However, chorus scales are expected to become larger as the waves propagate off the equator to higher latitudes where scattering of relativistic electrons is expected to occur [Lorentzen, 2001a]. In addition to the chorus scale size being larger, the field strength is increased so the LEO footprint will be larger by two factors

These models exist now in a relatively sparse data space, but two leading models are easily distinguishable with a set of instruments like TREBLE. Shown in Figure 7.4 is the result of propagating model electrons along the field line to the position of TREBLE in low-Earth orbit. Time resolution of ~10 ms and energy resolution of ~20% are more than adequate to distinguish between the models as long as data are available up to 2 MeV with adequate sensitivity.

Individual microbursts are believed to be driven by a single chorus element [Lorentzen, 2001a]. The recent discovery of whistler-mode waves with amplitudes >200 mV/m, ten times larger than previously observed in the radiation belts, indicates that the quasi-linear theory most commonly used is inadequate for understanding microburst precipitation. [Cattell, 2008] The observed waves resulted in rapid (~hours) energization of electrons, and SAMPEX observed strong microburst precipitation during this time period [C. Cattell, private comm.]. A nonlinear analysis is required in these cases [Albert, 2002; Katoh and Omura, 2007]. Realistically assessing the role of these mechanisms requires extended measurements with greater spatial, temporal and energy resolution than currently available. Developing and testing new models of wave-particle

interactions that include these non-linear effects requires the very data that TREBLE will provide.

7.1.2 TREBLE meets DREP

Balloon observations have shown that the entire outer zone could be depleted of relativistic electrons by the DREP mechanism in a few days [Millan, 2002]. DREP observed during a rapid depletion of the relativistic electron flux at GOES and GPS was sufficient to account for the observed decrease in trapped flux [Millan, 2007]. Thus, this class of precipitation may rival microbursts as a dominant loss process at relativistic energies. The relative importance of these must be quantified. In particular, DREP is often observed during relatively quiet geomagnetic conditions [Foat, 1998] as well as during storms. TREBLE can better determine the loss rate as a function of geomagnetic activity due to its longer mission lifetime than a balloon campaign.

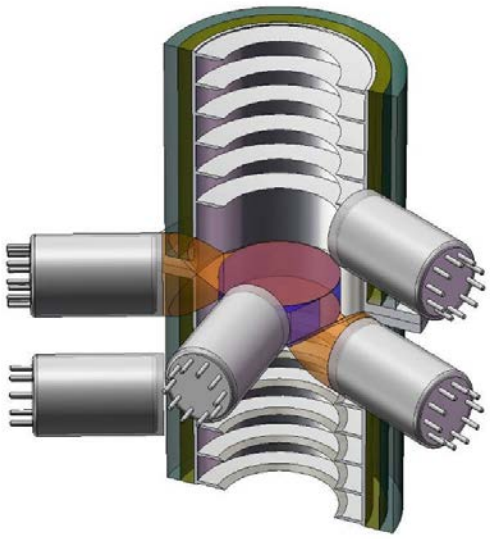

Figure 7.5: The RET detector: shown in dark green is the active collimator, which serves as an anticoincidence shield for fine pitch-angle resolution and as a large-area detector with coarse energy resolution and no inherent pitch-angle information

DREP nearly always shows temporal variations on much slower (~minutes) timescales than the dawnside microbursts. The nature of these ULF (Ultra Low Frequency) temporal modulations is currently unknown but may provide a key to understanding the physics of the interactions causing the electron scattering. TREBLE will measure ULF waves that may be responsible for the temporal variations that have been observed in DREP.

For EMIC-wave scattering, pitch-angle distributions reach the strong diffusion regime with a filled loss cone at higher energies, while below the minimum resonance energy pitch-angle distributions are unaffected by the wave and only weakly diffuse into the loss cone (see earlier Figure 7.3). TREBLE will distinguish scattering in the strong and weak diffusion limits by measuring the pitch angle distribution across the loss cone as a function of energy. TREBLE will also measure the EMIC waves and ion precipitation to identify electron scattering due to EMIC waves, it will therefore resolve the long-standing question of the importance of this mechanism. Theoretical studies indicate that the electron loss rate is highly sensitive to the particle distribution near the edge of the loss cone [Bortnik, 2006a]. TREBLE will measure the pitch-angle distribution there, the loss rate as a function of electron energy, and the spatial region over which particles are lost.

7.2 Instrumentation

Since models of different scattering mechanisms (chorus, EMIC, etc.) predict different dependencies on energy and equatorial pitch angle, the TREBLE science objective for understanding precipitation physics drives us to new instrumentation with time, energy and

pitch-angle resolution superior to previous missions. Figure 7.3 illustrates particle distributions expected for chorus and EMIC, with a grid of angle and energy bands superimposed that will both unambiguously distinguish between the two and provide a quantitative test of the models. The angular grid will be accomplished via three identical sets of detectors constantly oriented at 0^o, 45^o, and 90^o to the local B field using passive magnetic alignment of the spacecraft spin axis to the magnetic field. These angular bins correspond to pitch angles up to 9^o at the outer-belt equator

Each TREBLE spacecraft carries three types of instrument: three relativistic electron telescopes (RET), three solid state telescopes (SST) for lower energy electrons and ions, and a fluxgate magnetometer (FGM). The RETs and SSTs provide pitch-angle-resolved measurements of electrons from 40 keV to ~5 MeV and ions from 40 keV to ~10 MeV.

7.2.1 RET

The RETs provide electron measurements from 500 keV to several MeV. Each RET is double ended and uses three stacked scintillators: plastic, $LaBr_3$, and plastic. The detectors are collimated to ±18° FWHM by a collimator of passive baffles inside an active layer of plastic scintillator surrounded by passive material (figure7.5. The three RETs will be oriented relative to the local magnetic field at 0, 45, and 90° providing measurements of the center of the loss cone, marginally precipitating, and locally mirroring electrons, respectively as well as electrons moving *upward* along the field line at 135 and 180°.

Plastic scintillators are easy to form and handle and have very fast pulses (~few ns) allowing for large areas with fast counting during precipitation peaks. The $LaBr_3$ scintillator has higher light output than the plastic, is higher density for increased stopping power and is almost as fast (~20 ns). This scintillator will be subject to lower count rates than the plastic because only higher-energy electrons will penetrate into it. Each RET scintillator is read out by a PMT operated at ~10^4 gain for low quiescent currents and stable performance at high count rates. The output of each PMT is passed through an analog signal chain near the sensor. This front end includes a preamp similar to the RHESSI design, shapers of 150 ns, similar to those flown on the Nuclear Compton Telescope (a UCB Long Duration Balloon payload) and electronics to carry out pulse-height analysis. For the active collimator, the event is binned into commandable high and low energy

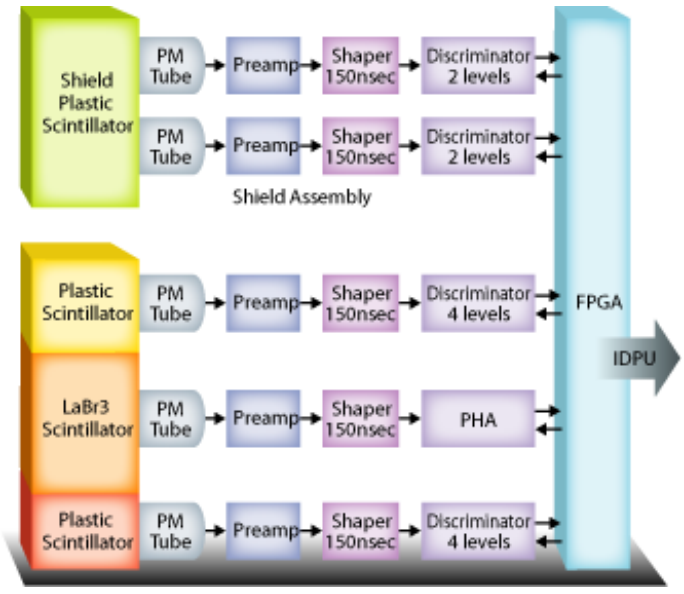

Figure 7.6 The RET electronics chain is uniquely tailored for the requirements of the TREBLE mission. It balances high throughput, low power, and moderate energy resolution. Each RET detector has one copy of the above chain

channels, for the front and rear plastic detectors a commandable 4-level discriminator is used, and for the $LaBr_3$ detector a 10-bit PHA is used. An FPGA time tags each event and prepares it for the instrument computer (IDPU). A block diagram of the RET electronics is shown in Figure 7.6.

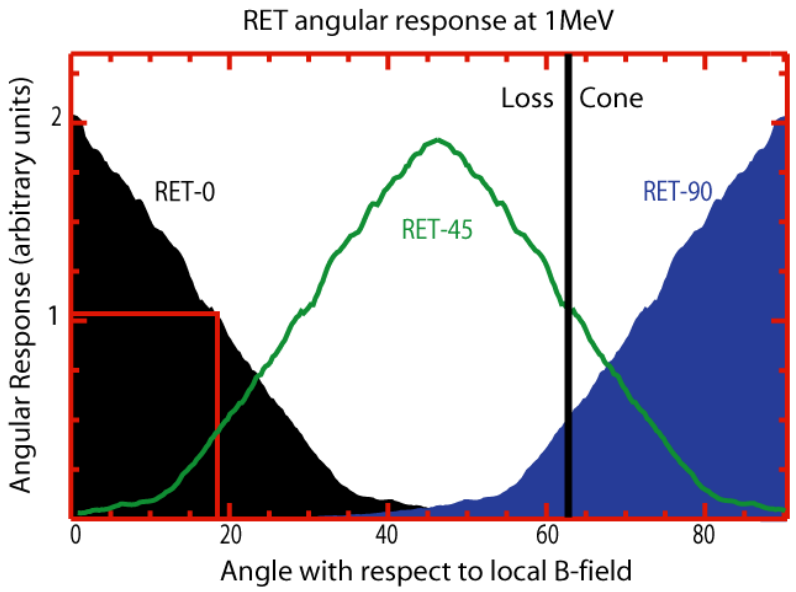

Figure 7.7: The angular response of the RET to 1MeV electrons. High energy electrons scatter easily off passive material. The RET's active shield and thin passive baffles are designed to make a clean measurement of the local pitch angle distribution. All counts beyond 36°. in the RET-0 response are from scatters which did not trigger the active collimator.

A small amount of passive shielding is placed in front of both front and rear plastic scintillators. This excludes protons below 12MeV, and electrons below 500keV. This prevents the RET's large geometric factor from being saturated by lower-energy counts, a significant design driver for such a large instrument since false coincidences can undermine the determination of electron energy and direction. The shielding also serves to make the plastic scintillator light-tight and will act as a thermal control surface. The central $LaBr_3$ will also be sensitive to protons above >18 MeV which can penetrate the path surrounding that detector. Channels in both the plastic and $LaBr_3$ detectors will be reserved for identifying the >12 and >18 MeV protons.

Each stack of RET scintillators has an electron geometric factor of ~6.5 cm^2sr at 1 MeV, determined by a Monte Carlo simulation of the detector response. The geometric factor is effectively constant across the energy range of interest. The RET active shield will also act as a large geometry detector (~100 cm^2sr each) with limited energy and pitch angle resolution. The shield count rate provides a large dynamic range to the RET. Using a survey of earlier data and detector simulated response we have made estimates of the anticipated count rates in various energy bins and compared this to our expected background counting rate. Minimum detectable signals above MeV are comparable to SAMPEX HILT's solid state detectors. However, because TREBLE will always be able to distinguish electrons which are locally trapped from those truly precipitating, expected background for measurements of precipitating flux will frequently be significantly lower than in SAMPEX. Also of note are those counts in the 500 keV to 1 MeV range where fluxes are expected to be ~4 times higher than >1 MeV.

7.2.2 Additional measurements:

Given the need for a LEO spacecraft, we must measure as many of the waves that relate to the precipitation as we can from that position. EMIC waves require magnetic-field measurements with a noise floor of approximately 0.1 nT and 10 Hz temporal resolution. ULF waves are then obtained automatically, since their sensitivity requirements are less severe. EMIC waves will propagate effectively along the field line between TREBLE and the equatorial regions, while ULF waves are globally detectable. VLF chorus propagates obliquely, so the precipitation seen by TREBLE would not be directly related to any VLF seen on the spacecraft. Thus VLF instrumentation is not part of the TREBLE design.

The expected association of EMIC waves with ion precipitation as well as precipitation of relativistic electrons leads us to require measurements of precipitating ions as well. Going down to 40 keV will allow us to reach the regime of ring-current ions. Electron measurements down to 40 keV will also be required, in order to compare our results with many previous missions, going all the way back to Injun III [e.g. Brown 1966] (which, incidentally, was also a magnetically-oriented satellite).

SST

In order to cover low and moderate energy electrons even in the presence of higher energy precipitation (a limitation of balloon observations) TREBLE will carry the compact SST (the same unit as those used on THEMIS [Larson, 2008]), and give lower-energy particle data than RET. SSTs are smaller than RETs since count rates are higher at lower energies. SSTs additionally measure a wide range of ion energies including those energies that will be scattered simultaneously with EMIC wave scattering of relativistic electrons. The SSTs measure electrons from 40 keV to ~1 MeV and ions from 40 keV to ~10 MeV. The SSTs will be mounted with similar look directions to the RETs so that across a wide energy range the angular resolved spectrum of energetic electron precipitation will be measured. Since the SST is an established instrument it will not be discussed further.

Flugate Magnetometer

Likewise, the details of the FGM are unimportant to this description of the TREBLE mission concept. It is important that it be able to measure EMIC and ULF waves as described earlier. As an aside, the multi spacecraft nature of TREBLE opens up significant new science goals with the magnetometer: Field Aligned Currents, accurate determination of ULF mode number and other areas that are generally beyond the scope of this dissertation.

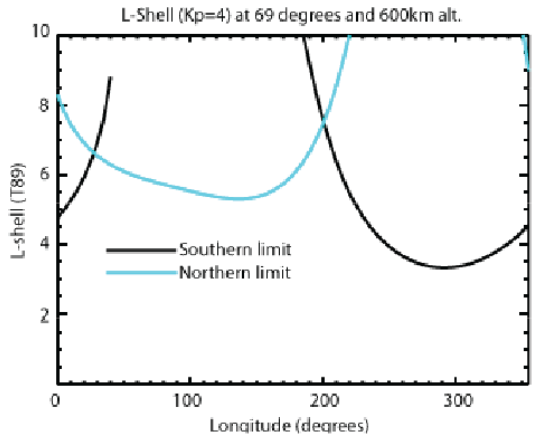

Figure 7.8: this shows the L-shell in the northern and southern hemispheres when |latitude| =69° as a function of longitude.

7.3 Mission Design

TREBLE is designed to make pitch-angle and energy-resolved observations of relativistic electrons near and in the equatorial loss cone. The measurement of the pitch-angle distribution is constantly provided by the magnetic alignment

of the three TREBLE spacecraft. TREBLE will also make definitive measurements of the spatial scale and time evolution of electron precipitation using three identical spacecraft. Each of these measurements is tied to understanding the precipitation and loss of these highly energetic electrons.

Orbit: Each TREBLE spacecraft will be placed in a 69^{o} inclination low earth (600 km) circular orbit. This orbit has been chosen to maximize observation time at L-shells from L=4.5 to L=6.5 (see Figure 7.8) where atmospheric precipitation is thought to be most important as a loss process. The orbit also maximizes time in conjunction with orbits near geosynchronous equatorial altitudes. The orbit choice also allows for spacecraft to move across L-shells slowly in the region of interest, in contrast to polar orbits that cut through them rapidly. This observation tactic allows for easier separation of spatial and temporal structures in the precipitation (Figure 7.3). Because spacecraft frequently move along contours of constant L-shell, trailing spacecraft can make simultaneous observations at similar L-shells but with separation in Magnetic Local Time.

Spacecraft Separations: The TREBLE spacecraft will naturally begin to separate upon launch. This will let them sample a range of spatial scales for precipitation. During the first six months of orbit, the three spacecraft oscillate in along-track and cross-track separations in their orbits. This spread gradually increases to approximately 60 km (or 9 seconds) from leading to trailing. Although this has been modeled in great detail, the results are similar to a simple physics based model that I developed by perturbing the orbit by an amount of energy similar to that imparted by the initial separation velocity. The close separations allow us to study the fine spatial structure of microbursts as well as the ULF oscillations found in DREP. The separation in L-shell is shown here in Figure 7.9. The equatorial mapped separations allow for comparison to known equatorial structures in waves and density which can tie observed precipitation to particular physical processes. For instance, measurements can easily be made during the traversal of a region conjugate to plasmaspheric plumes which have transverse structural sizes on the order of 1Re.

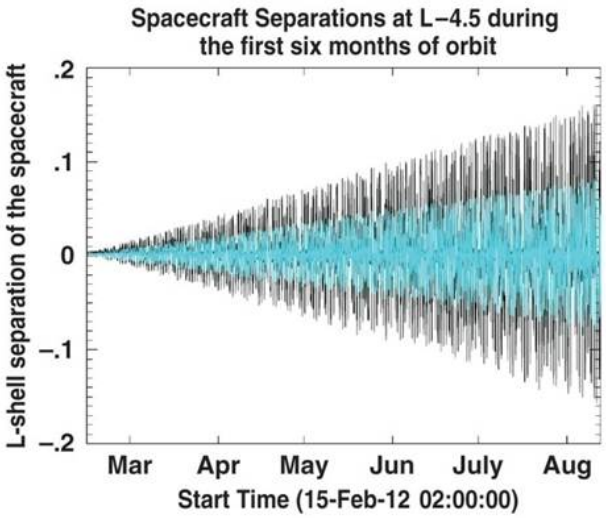

Figure 7.9: Shows the evolution of spacecraft separations in the equatorial plane over the course of the first 6 months. The data is filtered to times when the spacecraft are at an interesting outer- radiation-belt location. Blue is one of the interior pairs, black is leading to trailing.

At 6 months into the mission, one of the TREBLE spacecraft will eject a mass of ~1.5 kg. This will produce both an instantaneous, small change in velocity and a change in the ballistic coefficient of that satellite and therefore its continuous relative acceleration to the others. The separation rate will average ~100

km/month over the following year. During this time range, one pair of the TREBLE spacecraft are closely spaced, while the leading satellite is at a significantly larger separation. This scheme allows us to study multiple spatial scales in the precipitation region simultaneously. It also allows us to observe time variation at separate time scales from seconds for the close pair to minutes for the furthest separated. For example, the close pair can look for fine structure associated with chorus risers or density plumes, while the large separation gives us a measure of the precipitation's extent.

At one year into the mission, a second spacecraft will eject a mass so that the whole constellation is spaced widely by the end of the 2-year Phase E. In this last stage, we will get better coverage of slower time variations and larger spatial scales necessary to observe global precipitation and the ULF modulated precipitation found in DREP. The three stages of spacecraft separation are pictured in Figure 7.10.

7.4 Complementary Missions

TREBLE is designed to stand alone and make all the measurements necessary to achieve its baseline science objectives. However, it will suffer some of the same ambiguity as MINIS does in connecting loss processes to the conditions in the heart of the radiation belt which foster those loss processes. While BARREL will fly during RBSP (the first campaign already has as described in Chapter 6), that is unlikely to be an option for a mission as far out on the horizon as TREBLE. Still, I performed a magnetic conjunction study with the RBSP orbits as a proof of concept. When TREBLE and RBSP spacecraft are in conjunction (on nearly the same field line),

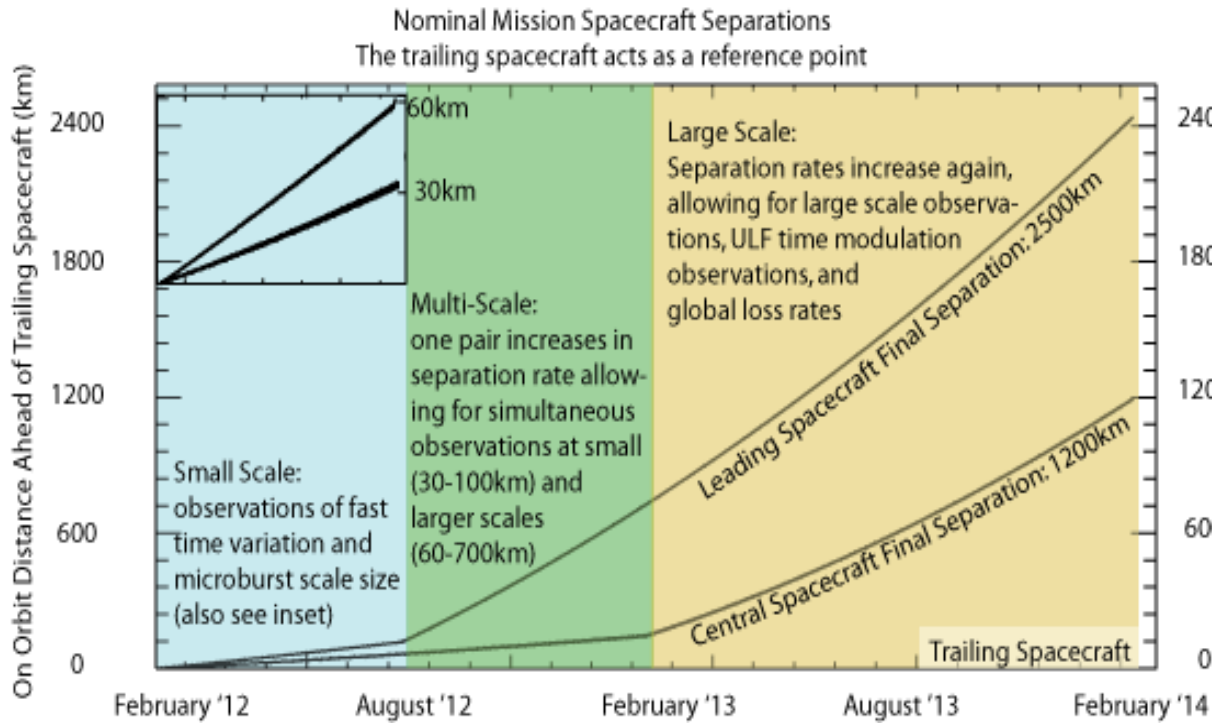

Figure 7.10: The TREBLE mission is broken into 3 phases of gradually increasing separation rates. This allows the string-of-pearls configuration to sample numerous spatial and temporal scales. Section E3 describes how each of the changes in separation rate are accomplished by the ejection of a mass.

equatorial waves, plasma conditions, and equatorially trapped particles measured at RBSP can be compared directly and quantitatively with TREBLE measurements of the flux, energy spectrum, and pitch-angle distribution of trapped and precipitating particles at low-Earth orbit. Indeed when RBSP was first conceived, the importance of measuring losses was called out as a top priority, but that measurement was unfortunately dropped. During a one year period, conjunctions between TREBLE and RBSP spacecraft, defined as being within 1 hour of local time and 0.5 L-shell, will occur an average of 60 times per day. However, many of these conjunctions are at low L-shell. If we include only conjunctions under the outer radiation belt, we have ~2 conjunctions a day lasting ~2 minutes on average. If we remove the local-time constraint, the number of outer-belt-coincident observations on the same drift shell increases to several hundred hours over the course of the year.

Conjunctions between TREBLE and a balloon array such as the previously detailed BARREL will be nearly as valuable as those between TREBLE and equatorial spacecraft, but in a different way. Balloon and satellite observations of precipitation have produced very different answers as to what mechanism dominates the loss of MeV electrons: microbursts or DREP. With simultaneous measurements of the same events by TREBLE particle sensors and balloon X-ray sensors, we will resolve two mysteries: why balloons never see microburst emission extending to 1 MeV, and why few DREP events appear distinctively in spacecraft data despite being so bright and distinctive in balloon data [see Millan and Thorne 2007 for a review]. Conjunctions between a TREBLE spacecraft and a balloon array like BARREL have been estimated using the same definition as above (1hr MLT, 0.5 L-shell), though a finer resolution is possible because of the close proximity of the balloons and spacecraft and magnetic field model mapping is not required. Conjunctions will occur roughly seven times per day during the ~2 month balloon campaign in the Antarctic summer. Conjunctions will last, on average, about 3 minutes. The ~3% occurrence rate for DREP precipitation between L=4 and 6 suggests that there will be ~12 conjunctions during DREP events. A similar number of observation opportunities occur at precipitation points conjugate to the balloons. These conjugate conjunctions will allow us to make unique observations of north-south differences.

8. Summary

The MINIS balloon campaign of late January 2005 flew during a unique time period for the Earth's magnetosphere. Payloads were aloft for solar flares, Solar Energetic Particles, the largest Ground Level Event in more than 50 years, and the impact and aftermath of a Coronal Mass Ejection shock that drove the magnetopause and perhaps even the bow shock inside of geosynchronous orbit. This shock came as two fronts, separated by 93 minutes, which started a moderate geomagnetic storm (Dst = -99 nT) with a substantial Storm Sudden Commencement. During the SSC, the MINIS balloons made observations, on the duskside, of relativistic electron precipitation. MINIS had 3 payloads returning data for at least part of the precipitation event, making it the first multipoint balloon observation of Relativistic Electron Precipitation (REP).

MINIS set out to capture the scale size of REP using multiple payloads that were launched sequentially over several days to achieve separation. MINIS was particularly interested in the duskside REP (DREP) which had previously (the MAXIS balloon campaign) been shown to be an important loss mechanism for the radiation belts. MAXIS showed DREP's significance largely through the average loss rate that the single point measurement recorded over the course of 8 days observing in the L =3.7-6.8 range of latitudes. Determining an instantaneous as opposed to average loss rate requires an estimate of the scale size of the precipitation region. MINIS had two payloads separated by more than hour of magnetic local time and ~0.5 L-shells that simultaneously observed precipitation of >500 keV electrons. The two payloads' separation establishes a scale size for this type of precipitation on the order of 10^{15} cm^2. Since MINIS had only two payloads aloft at the time, the direct measurement of scale size is a minimum area.

Although these precipitation events were as intense or more intense than all but one MAXIS event and the area of precipitation was substantial, the MINIS observations find a loss rate that is not as significant as MAXIS, either when considered as an instantaneous loss rate across the region of observation or when considered as an average over the course of the flight. This is true even if an extended local time (up to 9 hours) of precipitation is assumed. Important assumptions that go into loss rate calculations (both average and instantaneous) have been explored in this dissertation. Some of these assumptions are: duration, scale size, frequency, distribution across the sky and estimation of the pitch angle distribution of the precipitating electrons. MINIS also aimed to use its multiple, quasi-stationary balloons to separate out spatial and temporal variations in the precipitation. Although this was only successful in determining limits, it was demonstrated how limits on the expansion rates and limits on the drift rates could be determined from the X-ray data of an individual payload as well as from using inter-payload timing.

The variability in the response of the Earth's radiation belts to geomagnetic storms is documented as substantial [Reeves, 2004], so it should be no surprise that two separate balloon campaigns each of which saw one geomagnetic storm might observe substantially different loss rates to the atmosphere. In the case of MINIS, satellites making measurements of the trapped flux near the magnetic equator see far more electrons lost than MINIS observed as precipitation. Because MINIS was in the region of the Drift Loss Cone, it should at least some observe most precipitation, even if the cause of that precipitation is acting at a different local time. The lack of observed precipitation with sufficient intensity to explain the loss from the belts points to magnetopause shadowing as a likely sink for many of the energetic electrons.

Upcoming, and now ongoing, missions dramatically expand on the MINIS observations. The BARREL balloon array is an order of magnitude larger and makes observations in conjunction with a much more thorough set of equatorial instruments than MINIS or MAXIS. These observations come from the 2 RBSP (designed specifically for studying the radiation belts) and 3 remaining THEMIS satellites. BARREL has already flown one of its two balloon campaigns and observed two geomagnetic storms and more widespread precipitation than MINIS. Although MINIS observed a unique time period, it can be difficult to extrapolate from such a period, difficult to trace particle trajectories with magnetic field models and it may a time when atmospheric precipitation is not the principal loss mechanism. Quiet time observations of precipitation and conjunctions when payload and satellite are reliably thought to be on the same field line might be the best opportunity yet for elucidating the physics that cause electron scattering into the atmosphere. Having more than two payloads observing precipitation will also put a far greater limit on scale size, and thus instantaneous losses, and having longer duration campaigns should alleviate questions regarding the variability of the response.

REFERENCES

Albert, J. M. (2002), Nonlinear interaction of outer zone electrons with VLF waves, *Geophys. Res. Lett*., 29(8), 1275, doi:10.1029/2001GL013941.

Albert, J. M., and S. L. Young (2005), Multidimensional quasi-linear diffusion of radiation belt electrons, *Geophys. Res. Lett*., 32, L14110, doi:10.1029/2005GL023191.

Apostolakis et al., 1993. Apostolakis, J., et al., 1993. GEANT – Detector Description and Simulation Tool, CERN Program Library Long Writeup W5013, CERN Geneva, Switzerland

Baker, D. N., R. Belian, P. R. Higbie, R. W. Klebesadel, and J. B. Blake (1987), Deep dielectric charging effects due to high energy electrons in the Earth′s outer magnetosphere, *J. Electrost., 20*, 3–19.

Baker, D.N. R.A. Goldberg, F.A. Herrero, J.B. Blake, L.B. Callis, Satellite and rocket studies of relativistic electrons and their influence on the middle atmosphere, *J. of Atm. and Terr. Phys*., Volume 55, Issue 13, November 1993, Pages 1619-1628, ISSN 0021-9169, DOI: 10.1016/0021-9169(93)90167-W.

Berkey, F. T., V. M. Driatsiy, K. Henriksen, B. Hultqvist, D. H. Jelly, T. I. Shchuka, A. Theander, and J. Ylindemi (1974), A synoptic investigation of particle precipitation dynamics for 60 substorms in IQSY (1964–1965) and IASY (1969), *Planet. Space Sci.*, 22, 255.

Blake, J. B., et al. (1996), New high temporal and spatial measurements by SAMPEX of the precipitation of relativistic electrons, *Adv. Space Res*., 18(8), 171.

Bortnik, J. , U. S. Inan, and T. F. Bell (2006a), Temporal signatures of radiation belt electron precipitation induced by lightning-generated MR whistler waves: 1. Methodology, *J. Geophys. Res*., 111, A02204, doi:10.1029/2005JA011182.

Bortnik,J. and R.M. Thorne (2007) The dual role of ELF/VLF chorus waves in the acceleration and precipitation of radiation belt electrons, J. Atmos. & Solar-Terr. Phys., Vol. 69, pp. 378-386

Brown, R. R. (1966), Electron Precipitation in the Auroral Zone, Space Science Reviews, 5(3), 311-387.

Brown, R. R., Observations of narrow microburst trains in the geomagnetic storm of August 4–6, 1972, *J. Geophys. Res*., 78, 1727, 1973c.

Cattell, C., et al. (2008), Discovery of very large amplitude whistler-mode waves in Earth's radiation belts, *Geophys. Res. Lett., 35*, L01105, doi:10.1029/2007GL032009.

Chappell, C. R. (1972), Recent Satellite Measurements of the Morphology and Dynamics of the Plasmasphere, *Rev. Geophys.*, *10*(4), 951–979.

Chen, Y., R. H. W. Friedel, G. D. Reeves, T. G. Onsager, and M. F. Thomsen (2005), Multisatellite determination of the relativistic electron phase space density at geosynchronous orbit: Methodology and results during geomagnetically quiet times, *J. Geophys. Res*., 110, A10210, doi:10.1029/2004JA010895.

Chen, Y.; Reiner, F. H.; Geoffrey, R. D.; Cayton, T.; Christensen, R. (2008), Differentiating Loss Mechanisms of Outer Radiation Belt Relativistic Electrons from Multi- point Satellite Observations, AGU, Fall Meeting 2008, abstract #SM43B-04

Clilverd, M. A., et al. (2008), Energetic electron precipitation during substorm injection events: High-latitude fluxes and an unexpected midlatitude signature, *J. Geophys. Res*., 113, A10311, doi:10.1029/2008JA013220.

Clilverd, M. A., C. J. Rodger, R. J. Gamble, T. Ulich, T. Raita, A. Seppälä, J. C. Green, N. R. Thomson, J.-A. Sauvaud, and M. Parrot (2010), Ground-based estimates of outer radiation belt energetic electron precipitation fluxes into the atmosphere, *J. Geophys. Res*., 115, A12304,

Cornwall, J. M., F. V. Coroniti, and R. M. Thorne**,** Turbulent loss of ring current protons, *J. Geophys. Res.*, *75*, 4699, 1970.

Datta, S., R. M. Skoug, M. P. McCarthy, G. K. Parks, Analysis and modeling of microburst precipitation *Geophys Res. Lett.*,23,1729-1732, 1996

Dessler, A. J., and R. Karplus, Some effects of diamagnetic ring currents on Van Allen radiation, *J. Geophys. Res*., 66, 2289-2295, 1961.

Elkington, S. R. (2006), A review of ULF interactions with radiation belt electrons, in Magnetospheric ULF Waves: Synthesis and New Directions, *Geophys. Monogr. Ser*., vol. 169, edited by K. Takahashi et al., pp. 177–193, AGU, Washington, D. C.,

Farris, M., and C. Russell (1994), Determining the Standoff Distance of the Bow Shock: Mach Number Dependence and Use of Models, *J. Geophys. Res*., 99(A9), 17681-17689.

Foat, J. E., R. P. Lin, D. M. Smith, F. Fenrich, R. Millan, I. Roth, K. R. Lorentzen, M. P. McCarthy, G. K. Parks, and J. P. Treilhou (1998), First detection of a terrestrial MeV X-ray burst, *Geophys. Res. Lett*., 25(22), 4109–4112.

Fraser, B. J., H. J. Singer, W. J. Hughes, J. R. Wygant, R. R. Anderson, and Y. D. Hu (1996), CRRES Poynting vector observations of electromagnetic ion cyclotron waves near the plasmapause, *J. Geophys. Res*., 101(A7), 15331–15343, doi:10.1029/95JA03480.

Fraser, B. J., and T. S. Nguyen, Is the plasmapause a preferred source region of electromagnetic ion cyclotron waves in the magnetosphere?, *J. Atmos. Terr. Phys.*, *63*, 1225, 2001.

Friedel, R. H. W., et al. (2000), A multi-spacecraft synthesis of relativistic electrons in the inner magnetosphere using LANL, GOES, GPS, SAMPEX, HEO, and POLAR, *Adv. Space. Res.*, 26, 93–98.

Friedel, R. H. W., G. D. Reeves, and T. Obara **(**2002), Relativistic electron dynamics in the inner magnetosphere-a review, *J. Atmos. Solar Terr. Phys.*, *64*, 265.

Gannon, J. L., X. Li, and D. Heynderickx (2007), Pitch angle distribution analysis of radiation belt electrons based on Combined Release and Radiation Effects Satellite Medium Electrons A data, *J. Geophys. Res*., 112, A05212, doi:10.1029/2005JA011565.

Glassmeier, K.H., Lester, M., Mier-Jedrzejowicz, W.A.C., Green, C.A., Rostoker, G., Orr, D.,Wedeken, U., Junginger, H., and Amata, E.: 1984a, 'Pc5 pulsations and their possible source mechanism: A case study', *J. Geophys*. *Res*. 55, 108.

J. C. Green, T. G. Onsager, T. P. O'Brien, and D. N. Baker (2004a), Testing loss mechanisms capable of rapidly depleting relativistic electron flux in the Earth's outer radiation belt, *J. Geophys. Res*., 109, A12211, doi:10.1029/2004JA010579.

Green, J., and M. Kivelson (2004b), Relativistic electrons in the outer radiation belt: Differentiating between acceleration mechanisms, *J. Geophys. Res*., 109, A03213, doi:10.1029/2003JA010153.

Horne, R. B., S. A. Glauert, and R. M. Thorn**e** (2003), Resonant diffusion of radiation belt electrons by whistler-mode chorus, *Geophys. Res. Lett.*, *30*(9), 1493, doi:10.1029/2003GL016963.

Horne, R. B., R. M. Thorne, Y. Shprits, N. P. Meredith, S. A. Glauert, A. J. Smith, S. G. Kanekal, D. N. Baker, M. J. Engebretson, J. L. Posch, M. Spasojevic, U. Inan, J. S. Pickett, and P. M. E. Decreau (2005), Wave acceleration of electrons in the Van Allen radiation belts, *Nature*, 437, 227.

Imhof, W., G. Nakano, R. Johnson, and J. Reagan (1974), Satellite Observations of Bremsstrahlung From Widespread Energetic Electron Precipitation Events, *J. Geophys. Res*., 79(4), 565-574.

Imhof, W. L., H. D. Voss, J. Mobilia, D. W. Datlowe, E. E. Gaines, J. P. McGlennon, and U. S. Inan (1992), Relativistic electron microbursts, *J. Geophys. Res*., 97(A9), 13829–13837, doi:10.1029/92JA01138.

Imhof, W.L., H.D. Voss, J.B. Reagan, D.W. Datlowe, E.E. Gaines and J. Mobilia, Relativistic electron and energetic ion precipitation spikes near the plasmapause, Journal of Geophysical Research 91 (1986), pp. 3077–3088.

Jackson, J. D. , Classical Electrodynamics, 3rd ed. (Wiley, New York, 1998)

Johns, C. M., & Lin, R. P. (1992), The derivation of parent electron spectra from bremsstrahlung hard X-ray spectra, *Sol. Phys.*, 137, 121

Jordanova, V. K., C. J. Farrugia, R. M. Thorne, G. V. Khazanov, G. D. Reeves, and M. F. Thomsen, Modeling ring current proton precipitation by electromagnetic ion cyclotron waves during the May 14–16, 1997, storm, *J. Geophys. Res.*, *106*, 7, 2001

Kanekal, S. G., Friedel, R. H. W, Reeves, G. D., Baker, D. N., and Blake, J. B. 2005, Relativistic electron events in 2002: Studies of pitch angle isotropization, *J. Geophys. Res*., 110: 12,224-12,232

[Katoh and Omura, 2007] Katoh, Y., and Y. Omura (2007), Relativistic particle acceleration in the process of whistler-mode chorus wave generation, *Geophys. Res. Lett*., 34, L13102, doi:10.1029/2007GL029758.

Kim, H.-J., and A. A. Chan (1997), Fully adiabatic changes in storm time relativistic electron fluxes, *J. Geophys. Res.*, *102*(A10), 22, 107–22, 116.

Kippen R. Marc, The GEANT low energy Compton scattering (GLECS) package for use in simulating advanced Compton telescopes, New Astronomy Reviews, Volume 48, Issues 1-4, Astronomy with Radioactivities IV and Filling the Sensitivity Gap in MeV Astronomy, February 2004, Pages 221-225, ISSN 1387-6473, DOI: 10.1016/j.newar.2003.11.039.

Kivelson, M.G. Russell, C.T., 1995. *Introduction to Space Physics* , Cambridge University Press.

Koch, H. W., & Motz, J. W. 1959, *Rev. Mod. Phys.*, 31, 920

Kokorowski, M., (2008) Energetic Particle Precipitation Effects on the Electrodynamics of the Coupled Magnetosphere-Ionosphere-Atmosphere, [Dissertation] - University of Washington

Larson, D., et al. (2009), Solid state telescope for THEMIS, *Space Sci. Rev*., in press.

Lee, J.-J., et al. (2005), Energy spectra of 170 – 360 keV electron microbursts measured by the Korean STSAT-1, *Geophys. Res. Lett*., 32, L13106, doi:10.1029/2005GL022996.

Li, X., D. Baker, M. Temerin, T. Cayton, E. Reeves, R. Christensen, J. Blake, M. Looper, R. Nakamura, and S. Kanekal (1997), Multisatellite observations of the outer zone electron variation during the November 3–4, 1993, magnetic storm, *J. Geophys. Res*., 102(A7), 14123-14140.

Li, X., Baker, D. N., O'Brien, T. P., Xie, L., & Zong, Q. G. (2006). Correlation between the inner edge of outer radiation belt electrons and the innermost plasmapause location. *Geophysical research letters*, *33*(14).

Lorentzen, K. R., M. P. McCarthy, G. K. Parks, J. E. Foat, R. M. Millan, D. M. Smith, R. P. Lin, and J. P. Treilhou (2000), Precipitation of relativistic electrons by interaction with electromagnetic ion cyclotron waves, *J. Geophys. Res.*, 105(A3), 5381–5390.

Lorentzen, K. R., J. B. Blake, U. S. Inan, and J. Bortnik (2001a), Observations of relativistic electron microbursts in association with VLF chorus, *J. Geophys. Res.*, *106*, 6017–6027.

Lorentzen, K. R., M. D. Looper, and J. B. Blake **(**2001b), Relativistic electron microbursts during the GEM storms, *Geophys. Res. Lett.*, *28*, 2573–2576.

Lyons, L. R., R. M. Thorne, and C. F. Kennel (1972), Pitch-angle diffusion of radiation belt electrons within the plasmasphere, *J. Geophys. Res*., 77(19), 3455–3474, doi:10.1029/JA077i019p03455.

Lyons, L. R., and D. A. Williams**,** *Quantitative Aspects of Magnetospheric Physics*, D. Reidel, Norwell, Mass., 1984.

A. Markowicz, R. Van Grieken, Composition dependence of bremsstrahlung background in electron-probe X-ray microanalysis, *Anal. Chem.*, 56 (1984), pp. 2049–2051

McIlwain, C. E., Processes acting upon outer zone electrons, Radiation Belts: Models and Standards, Geophys. Monogr. Ser., 97J. F. Lemaire, D. Heynderickx, D. N. Baker, 15–26, AGU, Washington, D.C., 1996.

Mende, S. B., et al., Far ultraviolet imaging from the IMAGE spacecraft, 1, System design, *Space Sci. Rev.*, *91*, 243, 1999.

Meredith, N. P., R. B. Horne, and R. R. Anderson (2001), Substorm dependence of chorus amplitudes: Implications for the acceleration of electrons to relativistic energies, *J. Geophys. Res*., 106(A7), 13165–13178, doi:10.1029/2000JA900156.

Meredith, N. P., R. M. Thorne, R. B. Horne, D. Summers, B. J. Fraser, and R. R. Anderson (2003), Statistical analysis of relativistic electron energies for cyclotron resonance with EMIC waves observed on CRRES, *J. Geophys. Res*., 108, 1250, doi:10.1029/2002JA009700, A6.

Millan, R. M., R. P. Lin, D. M. Smith, K. R. Lorentzen, and M. P. McCarthy (2002), X-ray observations of MeV electron precipitation with a balloon-borne germanium spectrometer, *Geophys. Res. Lett.*, *29*(24), 2194, doi:10.1029/2002GL015922.

Millan, R. M., R. P. Lin, D. M. Smith, and M. P. McCarthy (2007), Observation of relativistic electron precipitation during a rapid decrease of trapped relativistic electron flux, *Geophys. Res. Lett.*, *34*, L10101, doi:10.1029/2006GL028653.

Millan, R. M. and R. M. Thorne (2007), Review of radiation belt relativistic electron losses, *Journal of Atmospheric and Solar-Terrestrial Physics*,69(3), 362-377.

Moldwin, M. B., L. Downward, H. K. Rassoul, R. Amin, and R. R. Anderson, A new model of the location of the plasmapause: CRRES results, *J. Geophys. Res.*, *107*(A11), 1339, doi:10.1029/2001JA009211, 2002.

Nakamura, R., D. N. Baker, J. B. Blake, S. Kanekal, B. Klecker, and D. Hovestadt (1995), Relativistic electron precipitation enhancements near the outer edge of the radiation belt, *Geophys. Res. Lett*., 22(9), 1129–1132.

Nicholson, D. R., Introduction to Plasma Theory (1983) Wiley, New York

O'Brien, B. J. (1964), High-latitude geophysical studies with satellite Injun 3: 3. Precipitation of electrons into the atmosphere, *J. Geophys. Res*., 69(1), 13–43, doi:10.1029/JZ069i001p00013.

O'Brien, T. P., K. R. Lorentzen, I. R. Mann, N. P. Meredith, J. B. Blake, J. F. Fennell, M. D. Looper, D. K. Milling, and R. R. Anderson (2003), Energization of relativistic electrons in the presence of ULF power and MeV microbursts: Evidence for dual ULF and VLF acceleration, *J. Geophys. Res.*, *108*(A8), 1329, doi:10.1029/2002JA009784.

O'Brien, T. P., M. D. Looper, and J. B. Blake (2004), Quantification of relativistic electron microburst losses during the GEM storms, *Geophys. Res. Lett*., 31, L04802, doi:10.1029/2003GL018621.

Onsager, T. G., et al. (2002), Radiation belt electron flux dropouts: Local time, radial, and particle-energy dependence, *J. Geophys. Res.*, *107*(A11), 1382, doi:10.1029/2001JA000187.

Onsager, T., A. Chan, Y. Fei, S. Elkington, J. Green, and H. Singer (2004), The radial gradient of relativistic electrons at geosynchronous orbit, *J. Geophys. Res.*, *109*, A05221, doi:10.1029/2003JA010368.

Parks G. K., H. S. Hudson, D. W. Milton, and K. A. Anderson, Spatial asymmetry and periodic time variations of X-ray microbursts in the auroral zone, *J. Geophys. Res*., 70, 4976- 4978, 1965.

Parks, G. K. (1967), Spatial Characteristics of Auroral-Zone X-Ray Microbursts, *J. Geophys. Res*., 72(1), 215–226.

Parks, G. K., T. J. Freeman, M. P. McCarthy, and S. H. Werden (1993), The discovery of auroral X-rays by balloon-borne detectors and their contributions to magnetospheric research, in Auroral Plasma Dynamics, *Geophys. Monogr. Ser*., vol. 80, edited by R. L. Lysak, pp. 17–23, AGU, Washington, D. C., doi:10.1029/GM080p0017.

Parks, G. K.: 2004, Physics of Space Plasmas, An Introduction, Second Edition, Perseus Publishing Company, Boulder, Colorado.

Randall, C. E., V. L. Harvey, C. S. Singleton, S. M. Bailey, P. F. Bernath, M. Codrescu, H. Nakajima, and J. M. Russell III (2007), Energetic particle precipitation effects on the Southern Hemisphere stratosphere in 1992–2005, *J. Geophys. Res*., 112, D08308,doi:10.1029/2006JD007696.

Reeves, G. D., L. A. Weiss, M. F. Thomsen, and D. J. McComas, Quantitative Experimental Verification of the Magnetic Conjugacy of Geosynchronous Orbit and the Auroral Zone, in Substorms 3, ESA SP-339, 187-192, 1996.

Reeves, G. D., K. L. McAdams, R. H. W. Friedel, and T. P. O'Brien, Acceleration and loss of relativistic electrons during geomagnetic storms, *Geophys. Res. Lett*. ,30 (10), 1529 , doi: 10.1029/2002GL016513, 2003.

Roederer, J. G. (1967), On the Adiabatic Motion of Energetic Particles in a Model Magnetosphere, *J. Geophys. Res*., 72(3), 981-992.

Roederer, 1970 J.G. Roederer Dynamics of Geomagnetically Trapped Radiation, Springer, New York (1970).

Roelof, E. C. (1997), ENA emission from nearly mirroring magnetospheric ions interacting with the exosphere, *Adv. Space Res.*, *20*(3), 361–366, doi:10.1016/S0273-1177(97)00692-3.

Santolík, O., D. A. Gurnett, and J. S. Pickett (2004), Multipoint investigation of the source region of storm-time chorus, *Ann. Geophys*., 22, 2555–2563.

Schulz and Lanzerotti 1974 M. Schulz and L.J. Lanzerotti Particle Diffusion in the Radiation Belts, Springer, Berlin (1974).

Selesnick, R. S., M. D. Looper, and J. M. Albert (2004), Low-altitude distribution of radiation belt electrons, *J. Geophys. Res*., 109, A11209, doi:10.1029/2004JA010611.

Share, G. H., R. J. Murphy, B. R. Dennis, R. A. Schwartz, A. K. Tolbert, R. P. Lin, and D. M. Smith (2002), RHESSI observation of atmospheric gamma rays from impact of solar energetic particles on 21 April 2002, *Solar Phys.*, *210*, 357–372.

Shprits, Y. Y., W. Li, and R. M. Thorne (2006a), Controlling effect of the pitch angle scattering rates near the edge of the loss cone on electron lifetimes, *J. Geophys. Res*., 111, A12206, doi:10.1029/2006JA011758.

Shprits, Y. Y., R. M. Thorne, R. Friedel, G. D. Reeves, J. Fennell, D. N. Baker, and S. G. Kanekal (2006b), Outward radial diffusion driven by losses at magnetopause, *J. Geophys. Res*., 111, A11214, doi:10.1029/2006JA011657.

Shue, J.-H., et al. (1998), Magnetopause location under extreme solar wind conditions, *J. Geophys. Res*., 103(A8), 17691–17700, doi:10.1029/98JA01103.

Stratton, J. M., Harvey, R. J., & Heyler, G. A. (2013). Mission Overview for the Radiation Belt Storm Probes Mission. *Space Science Reviews*, 1-29.

Summers, D., C. Ma, and T. Mukai (2004), Competition between acceleration and loss mechanisms of relativistic electrons during geomagnetic storms, *J. Geophys. Res*., 109, A04221, doi:10.1029/2004JA010437.

Thorne, R.M., and Andreoli, L. J. (1980.), Mechanisms for intense relativistic electron precipitation. In: Exploration of the Polar Atmosphere. Reidell Publishing Co., pp. 381–39.

Tsyganenko, N. A., and M. I. Sitnov (2005), Modeling the dynamics of the inner magnetosphere during strong geomagnetic storms, *J. Geophys. Res*., 110, A03208, doi:10.1029/2004JA010798.

Ukhorskiy, A. Y., B. J. Anderson, P. C. Brandt, and N. A. Tsyganenko (2006), Storm time evolution of the outer radiation belt: Transport and losses, *J. Geophys. Res*., 111, A11S03, doi:10.1029/2006JA011690.

Vampola, A. L. (1996), Outer zone energetic electron environment update, Final Report of ESA/ESTEC/WMA/P.O. 151351, ESA-ESTEC, Noordwijk, The Netherlands.

Weimer, D.R., D.M. Ober, N.C. Maynard, M.R. Collier, D.J. McComas, N.F. Ness, C.W. Smith, and J. Watermann, Predicting interplanetary magnetic field (IMF) propagation delay times using the minimum variance technique, *J. Geophys. Res*., 108, 10.1029/2002JA009405, 2003.

Winckler, J. R., Peterson, L., Arnoldy, R., & Hoffman, R. (1958). X-rays from visible aurorae at Minneapolis. P*hysical Review*, 110(6), 1221.